
Isvector One-Quadrupole-Phonon Excitations of Heavy Vibrational Nuclei

Isvektorielle Quadrupoleinphonon-Anregungen schwerer vibrationeller Kerne

Zur Erlangung des Grades eines Doktors der Naturwissenschaften (Dr. rer. nat.)
genehmigte Dissertation von Ralph Kern aus Alzenau in Unterfranken
Tag der Einreichung: 12. April 2021, Tag der Prüfung: 3. Mai 2021

1. Gutachten: Prof. Dr. Dr. h.c. mult. Norbert Pietralla
2. Gutachten: Prof. Dr. Joachim Enders
Darmstadt



TECHNISCHE
UNIVERSITÄT
DARMSTADT

Fachbereich Physik
Institut für Kernphysik
AG Pietralla

Isvector One-Quadrupole-Phonon Excitations of Heavy Vibrational Nuclei
Isovektorielle Quadrupoleinphonon-Anregungen schwerer vibrationeller Kerne

genehmigte Dissertation von Ralph Kern

1. Gutachten: Prof. Dr. Dr. h.c. mult. Norbert Pietralla
2. Gutachten: Prof. Dr. Joachim Enders

Tag der Einreichung: 12. April 2021

Tag der Prüfung: 3. Mai 2021

Darmstadt

Bitte zitieren Sie dieses Dokument als:

URN: urn:nbn:de:tuda-tuprints-185816

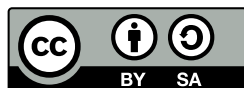
URL: <https://tuprints.ulb.tu-darmstadt.de/id/eprint/18581>

Dieses Dokument wird bereitgestellt von tuprints,

E-publishing-Service der TU Darmstadt

<http://tuprints.ulb.tu-darmstadt.de>

tuprints@ulb.tu-darmstadt.de



Die Veröffentlichung steht unter folgender Creative Commons Lizenz:

Namensnennung - Weitergabe unter gleichen Bedingungen 4.0 International

<https://creativecommons.org/licences/by-sa/4.0/deed.de>

Erklärungen laut Promotionsordnung

§8 Abs. 1 lit. c PromO

Ich versichere hiermit, dass die elektronische Version meiner Dissertation mit der schriftlichen Version übereinstimmt.

§8 Abs. 1 lit. d PromO

Ich versichere hiermit, dass zu einem vorherigen Zeitpunkt noch keine Promotion versucht wurde. In diesem Fall sind nähere Angaben über Zeitpunkt, Hochschule, Dissertationsthema und Ergebnis dieses Versuchs mitzuteilen.

§9 Abs. 1 PromO

Ich versichere hiermit, dass die vorliegende Dissertation selbstständig und nur unter Verwendung der angegebenen Quellen verfasst wurde.

§9 Abs. 2 PromO

Die Arbeit hat bisher noch nicht zu Prüfungszwecken gedient.

Darmstadt, 12. April 2021

Ralph Kern



Zusammenfassung

Die Untersuchung und Identifikation gemischt-symmetrischer Zustände steht im Fokus dieser Arbeit. Sie werden aus kollektiven Vibrationen und Rotationen der Valenzneutronen und -protonen geformt, wobei die zwei Nukleonengruppen zum Teil außer Phase zueinander oszillieren. In vibrationellen Kernen ist der $2_{1,\text{ms}}^+$ -Zustand das am niedrigsten gelegene gemischt-symmetrische Level.

Es wurde ein signifikanter Effekt des Unterschalenabschlusses bei $Z = 58$ auf den $2_{1,\text{ms}}^+$ -Zustand für die $N = 80$ Isotone beobachtet. Während die Isotone bis $Z = 56$ einen isolierten $2_{1,\text{ms}}^+$ -Zustand aufweisen, ist dieser für ^{138}Ce ($Z = 58$) stark fragmentiert. Das wird mit der Valenzschalen-Stabilisierung begründet, die am Unterschalenabschluss bei $Z = 58$ fehlt. Um die $2_{1,\text{ms}}^+$ -Zustände der $N = 80$ Isotone beim Überqueren des Protonen-Unterschalenabschlusses zu studieren, wurden Coulomb-Anregungs-Experimente durchgeführt. Diese fanden mit den radioaktiven Strahlen der $N = 80$ Isotone ^{140}Nd und ^{142}Sm an HIE-ISOLDE am CERN mit Nutzung des γ -Spektrometers Miniball statt. Die erhöhte $B(M1; 2_3^+ \rightarrow 2_1^+) = 0.26^{+0.11}_{-0.10} \mu_N^2$ Stärke und das niedrige obere Limit $B(M1; 2_4^+ \rightarrow 2_1^+) < 0.04 \mu_N^2$ von ^{140}Nd weist auf eine Wiederherstellung der Valenzschalen-Stabilisierung bei $Z = 60$ hin. Von dieser $M1$ -Stärke-Verteilung wird die Qualität des F -Spins von ^{140}Nd anhand des F -Spin-Mischungs-Matrixelements $V_{F-\text{mix}} < 7_{-7}^{+13}$ keV bestimmt. Das verringerte Mischungs-Matrixelement unterstützt die Annahme der wiederhergestellten Valenzschalen-Stabilisierung. Für ^{142}Sm lieferte die Analyse der Coulomb-Anregung das obere Limit $B(M1; 2_3^+ \rightarrow 2_1^+) < 0.14^{+0.37}_{-0.01} \mu_N^2$, welches nicht in Konflikt mit den Schlussfolgerungen des ^{140}Nd -Experiments steht. Eine komplementäre γ - γ Korrelationsmessung nach einem β^+/ϵ -Zerfall wurde entworfen um das notwendige $E2/M1$ Multipol-Mischungsverhältnis δ des $2_3^+ \rightarrow 2_1^+$ -Übergangs von ^{142}Sm zu erhalten. Dieses Experiment wurde bereits vom PAC am Heavy Ion Laboratory in Warschau akzeptiert.

Für ^{202}Hg wurde ebenfalls ein Projektil-Coulomb-Anregungsexperiment am ATLAS Beschleuniger am ANL unter Verwendung des γ -Spektrometers Gammasphere durchgeführt. Gleichzeitig wurden Winkelverteilungen der γ -Emissionen gemes-

sen, mit dem Ziel δ zu bestimmen. Es wurde eine erhöhte $B(M1; 2_7^+ \rightarrow 2_1^+) = 0.18(8) \mu_N^2$ Stärke mit $\delta = 0.06(4)$ gefunden, während ein oberes Limit für den Zerfall des benachbarten 2^+ -Zustands erhalten wurde, $B(M1; 2_8^+ \rightarrow 2_1^+) < 0.027 \mu_N^2$. Somit wurde das erste Mal in der Massenregion um den doppelt-magischen Kern ^{208}Pb die F -Spin-Mischungsstärke für ^{202}Hg und ^{204}Hg bestimmt mit $V_{F\text{-mix}} = 9(2)_{-3}^{+3}$ keV bzw. $11(1)_{-5}^{+4}$ keV.

Die Ergebnisse zeigen die hohe Güte des F -Spins als Quantenzahl für die untersuchten Atomkerne bei $N, Z = 80$ nahe doppelt-magischen Isotopen.

Abstract

The investigation and identification of mixed-symmetry states stand in the focus of this work. They are formed from collective vibrations and rotations of valence neutrons and protons, where the two nucleon groups oscillate partly out-of-phase with respect to each other. In vibrational nuclei, the $2_{1,\text{ms}}^+$ state is the lowest-lying mixed-symmetry level.

For the $N = 80$ isotones, the sub-shell closure at $Z = 58$ highly effects the structure of the $2_{1,\text{ms}}^+$ state. Up to $Z = 56$, the isotones have isolated $2_{1,\text{ms}}^+$ states, but for ^{138}Ce ($Z = 58$), it is strongly fragmented. This behaviour is explained by the valence-shell stabilization, which is lacking at the proton sub-shell closure $Z = 58$. For addressing the question how the $2_{1,\text{ms}}^+$ state behaves while going beyond the proton sub-shell closure, projectile Coulomb-excitation experiments were performed. They took place at HIE-ISOLDE at CERN using the γ -ray spectrometer Miniball with the radioactive ion beams of the $N = 80$ isotones ^{140}Nd and ^{142}Sm . The enhanced $B(M1; 2_3^+ \rightarrow 2_1^+) = 0.26_{-0.10}^{+0.11} \mu_N^2$ strength and the low upper limit $B(M1; 2_4^+ \rightarrow 2_1^+) < 0.04 \mu_N^2$ of ^{140}Nd showed the restoration of the valence-shell stabilization at $Z = 60$. From the $M1$ strength distribution, the quality of the F spin of ^{140}Nd was determined by the F -spin mixing matrix element $V_{F-\text{mix}} < 7_{-7}^{+13}$ keV. The reduced mixing matrix element supports the proposed restoration of the valence-shell stabilization. For ^{142}Sm , the Coulomb-excitation analysis delivered an upper limit $B(M1; 2_3^+ \rightarrow 2_1^+) < 0.14_{-0.01}^{+0.37} \mu_N^2$, which is not in conflict with the conclusions from the ^{140}Nd experiment. A complementary γ - γ correlation measurement after β^+/ϵ decay to determine the indispensable $E2/M1$ multipole-mixing ratio δ of the $2_3^+ \rightarrow 2_1^+$ transition of ^{142}Sm was designed for the Heavy Ion Laboratory in Warsaw and accepted.

For the stable ^{202}Hg , a projectile Coulomb-excitation experiment was conducted at the ATLAS facility at the ANL using the γ -ray spectrometer Gammasphere. Simultaneously, angular particle- γ correlations were measured with the aim of deducing δ . In ^{202}Hg a pronounced $B(M1; 2_7^+ \rightarrow 2_1^+) = 0.18(8) \mu_N^2$ with $\delta = 0.06(4)$ was found, while an upper limit for the neighboring transition was obtained,

$B(M1; 2_8^+ \rightarrow 2_1^+) < 0.027 \mu_N^2$. For the first time in the mass region $A \approx 200$, the F -spin mixing quality was determined, for ^{202}Hg and ^{204}Hg , $V_{F\text{-mix}} = 9(2)_{-3}^{+3}$ keV and $11(1)_{-5}^{+4}$ keV, respectively.

Consequently, F spin can be considered a sufficiently good approximate quantum number in the investigated nuclei of $N, Z = 80$ near doubly-magic isotopes.

Contents

1. Introduction	1
2. Nuclear Structure Theory	7
2.1. Geometrical Model	7
2.1.1. Vibrational Nuclei	9
2.1.2. Rotational Nuclei	10
2.2. Nuclear Shell Model	13
2.3. Interacting Boson Model	17
2.3.1. Interacting Boson Model 2	18
2.4. Two-State Mixing	23
2.4.1. General Formalism	23
2.4.2. F -Spin Mixing	25
3. Experimental Techniques	27
3.1. Coulomb Excitation	27
3.1.1. Semi-Classical Description	28
3.1.2. Connection to Nuclear Structure	34
3.2. Angular Correlations of γ Rays	37
4. Experiments	41
4.1. Coulomb Excitation of ^{140}Nd and ^{142}Sm at HIE-ISOLDE Using Miniball	43
4.1.1. Data Preparation	45
4.1.2. γ -Ray Spectroscopy of ^{140}Nd	52
4.1.3. γ -Ray Spectroscopy of ^{142}Sm	58
4.1.4. GOSIA Analysis of HIE-ISOLDE CE Experiments	62
4.2. Coulomb Excitation of ^{202}Hg at ATLAS Using Gammasphere	73
4.2.1. γ -Ray Spectroscopy of ^{202}Hg	75
4.2.2. Angular Correlations	78
4.2.3. CE Analysis of ^{202}Hg	82



4.3. γ -Ray Spectroscopy after β^+/ϵ Decay at the Heavy Ion Laboratory (HIL)	89
5. Discussion	95
5.1. $N = 80$ Isotones ^{140}Nd and ^{142}Sm	95
5.2. $Z = 80$ Isotopes ^{202}Hg and ^{204}Hg	105
6. Summary	111
Appendices	113
A. HIE-ISOLDE CE Experiments	113
B. GOSIA Files	125
C. ATLAS CE Experiment	141
D. CLX Files	153
E. HIL β^+/ϵ Decay Experiment	163
List of Publications	192
Danksagung	193
Lebenslauf	195

1. Introduction

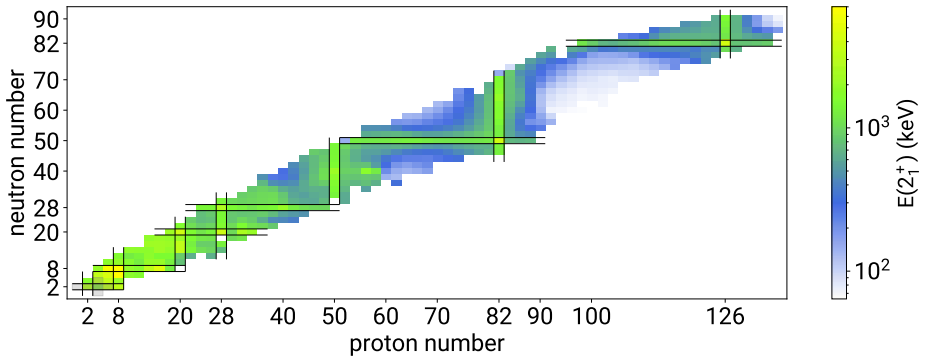


Figure 1.1.: The excitation energies of the first excited 2^+ states of even-even nuclei. The increased excitation energies at the marked nucleon numbers 2, 8, 20, 28, 50, 82 and 126 show the existing nuclear-shell closures. The energies were taken from Ref. [1].

A milestone of nuclear physics was set in 1949 by the development of the nuclear shell model [2–4]. The nucleons have a spin quantum number of $s = 1/2$. They are thus fermions and subject to the rules of the Pauli principle which is used to describe the structure of the atomic nucleus. Here, the excited nuclear states are depicted by the single-particle motions with the spin-particle interaction, which leads to discrete quantum states characterized by their total (j) and orbital (l) angular momenta. As a result, compositions with certain proton and neutron numbers exist, which are predicted to be very unreactive, analogously to noble gases in chemistry. These special nucleon numbers, 2, 8, 20, 28, 50, 82 and 126, are considered to represent shell closures and are called magic numbers. The nucleons outside these inert closed shells define the valence-space of an atomic

nucleus. The valence nucleons are responsible for the low-lying excitations of a nucleus. Besides single-nucleon excitations, there are also collective excitations where many nucleons are involved. The relevance of these collective excitations increases with a growing valence space. These collective motions can be interpreted as a homogeneous system, which vibrates or rotates [5].

The properties of collective excitations reveal information about the nuclear structure of an atomic nucleus. For even-even nuclei, their lowest-lying collective quadrupole excitations are sensitive on their shape or deformation [6]. An increase of the excitation energy and the lifetime of this state in respect to the neighboring isotopes indicates a shell closure at this nucleus. These observations reproduce the magic numbers, predicted from the shell model, see Figure 1.1. The doubly-magic nucleus has most commonly a spherical shape. The enlarged valence spaces of isotopes far away from shell closures lead to a serious axial deformation of the nucleus' shape. The enhanced collectivity is indicated by a lowered excitation energy and lifetime of the lowest-lying quadrupole excitation. That kind of excitation is interpreted as a collective motion of valence protons and valence neutrons, where the two types of nucleons are oscillating in phase, hence, they are indistinguishable. From that knowledge, the existence of further collective excitations where the protons and neutrons are oscillating out of phase is the logical conclusion. This class of collective excitations was firstly discussed in Refs. [7, 8].

The in-phase collective motions of even-even nuclei, the full-symmetry states, are also emerging from the framework of the Interacting Boson Model (IBM) [9]. The basic principle of the IBM is the coupling of valence-nucleon (or valence-hole) pairs to bosons, while the inert core is defined by the closest doubly-magic nucleus. The advanced version, the IBM-2, additionally distinguishes between proton and neutron bosons and, hence, is capable to describe also the out-of-phase collective excitations, the mixed-symmetry states, see Figure 1.2.

This work focuses in the following on the investigation of the mixed-symmetry states in heavy vibrational nuclei, where the collective quadrupole mixed-symmetry excitation, the $2_{1,ms}^+$ state, is the lowest-lying one of its type. To aim for the sought-for absolute $M1$ transition strength of the $2_{1,ms}^+ \rightarrow 2_1^+$ transition to identify the $2_{1,ms}^+$ states of the isotopes ^{140}Nd , ^{142}Sm and ^{202}Hg , it was and will be necessary to perform a combination of the Coulomb-excitation method and the angular γ - γ or particle- γ correlation method. The type of Coulomb excitation, where the excited states of the projectile nucleus is investigated, is especially qualified for the search of the $2_{1,ms}^+$ state of rare or radioactive heavy ions. Here, it is not necessary

- protons and neutrons

- protons
- neutrons

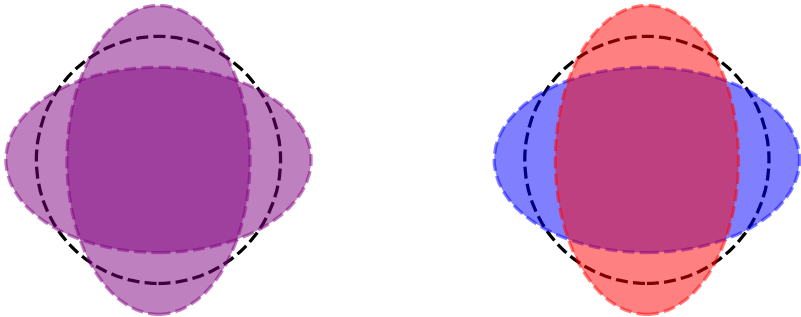


Figure 1.2.: Collective quadrupole excitations of vibrational nuclei. The right picture shows the motion of protons and neutrons in phase, while the right side represents the out-of-phase movements of protons and neutrons.

to produce a target of the desired isotope, which is simply not reasonable for the short-lived isotopes ^{140}Nd and ^{142}Sm ($T_{1/2} = 3.37\text{d}$ and $T_{1/2} = 72.49\text{ min}$). Furthermore, the Coulomb-excitation method suits the requirements to populate the $2_{1,\text{ms}}^+$ state with a significant excitation probability due to its moderate $E2$ connection to the ground state. However, additional information about the nature of the potential $2_{1,\text{ms}}^+ \rightarrow 2_1^+$ transition is indispensable, hence, a complementary measurement of the $E2/M1$ multipole-mixing ratio has to be performed. Here, this was done via the mentioned angular correlation methods for ^{140}Nd , ^{142}Sm and ^{202}Hg .

The $N = 80$ isotonic chain northwest of the doubly-magic isotope ^{132}Sn gained general interest with the postulation of a sub-shell closure at $Z = 58$. In ^{138}Ce , the fully-filled proton $g_{7/2}$ orbital is proposed as the reason for the fragmentation of the $2_{1,\text{ms}}^+$ state [10], see Figure 1.3 a). For ^{136}Ba with a partly filled $g_{7/2}$ proton orbital, the $M1$ strength is focused in the $2_{1,\text{ms}}^+ \rightarrow 2_1^+$ transition. From this point of view, a change of the characteristics of the low-lying collective excitations as

sudden and pronounced as from ^{136}Ba to ^{138}Ce is also expected from ^{138}Ce to ^{140}Nd .

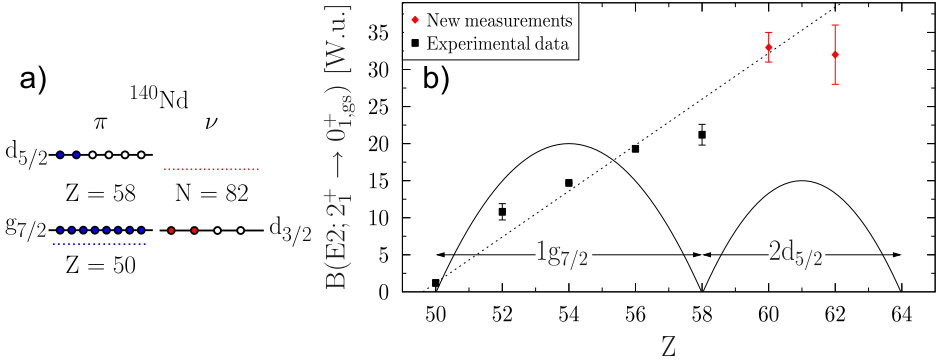


Figure 1.3.: a) shows the orbital structure of ^{140}Nd with its ten valence protons and two valence-neutron holes in respect to the doubly-magic ^{132}Sn (50 protons and 82 neutrons). b) represents the evolution of the $E2$ absolute transition strengths of the $2_1^+ \rightarrow 0_1^+$ transition of the $N = 80$ isotones from ^{130}Sn to ^{142}Sm . The experimental data are taken from Refs. [11–16]. Graphic b) was reprinted with permission from Ref. [15] and modified.

However, there was a lack of data about absolute transition strengths of the radioactive neutron-deficient $N = 80$ isotones ^{140}Nd and ^{142}Sm . In these nuclei, the valence protons also occupy the higher-lying $d_{5/2}$ orbital, see Figure 1.3 a). The examination of the isoscalar quadrupole excitations, the 2_1^+ states, of these isotones via projectile CE experiments at REX-ISOLDE [15, 16], showed also the effect of the sub-shell closure on the collectivity of the isoscalar quadrupole excitation, see the red diamonds in the Figure 1.3 b). The enhanced $B(E2; 2_1^+ \rightarrow 0_1^+)$ values of ^{140}Nd and ^{142}Sm intensify the indication of a suppression of the collectivity at ^{138}Ce . The effects of sub-shell structures on the low-lying isoscalar quadrupole excitations is clearly prominent in the $N = 80$ isotonic chain, i.e., the $B(E2; 2_1^+ \rightarrow 0_1^+)$ strength at the $Z = 58$ sub-shell closure, ^{138}Ce , is lowered, see Figure 1.3 b). So, the actual collectivity can be described by a superposition of the residual proton-neutron interaction (dashed line) and the influence of the seniority (curved line), while the

contribution from the seniority is significantly smaller. The residual proton-neutron interaction increases the collectivity proportional to the product of valence protons and neutrons [17]. This is applicable here, because the P -factor is less or equal five, $P = 0.5 \times (N_\pi N_\nu)/(N_\pi + N_\nu) \leq 5$, for all of the chosen isotones. This condition indicates a spherical behaviour of the nucleus, while a greater P -factor suggest characteristics of a deformed nucleus. The contribution from the seniority scheme is proportional to the term $\sqrt{f(1-f)}$, where f is the fractional filling of an orbital. Hence, the contribution peaks at a half-filled orbital and vanishes at a fully-filled orbital [17].

The effect of the sub-shell closure is even more pronounced regarding the low-lying isovector quadrupole excitations of the $N = 80$ isotones. The evolution of the $2_{1,ms}^+$ states of the $N = 80$ isotones from ^{132}Te up to ^{138}Ce [10, 12, 18, 19] is an example to show the effect of the sub-shell structure on the formation of collective excitations. Therefore a proton sub-shell closure at $Z = 58$ is postulated for the $N = 80$ isotones [10]. The question arose, how do the $2_{1,ms}^+$ states behave when passing the $Z = 58$ sub-shell closure, see Figure 1.4 a). To address this question, projectile Coulomb-excitation experiments were performed with the purpose of the identification of the $2_{1,ms}^+$ states of ^{140}Nd and ^{142}Sm [20–22]. The experiments were performed with a ^{140}Nd and a ^{142}Sm beam at $4.62 A \cdot \text{MeV}$ on a ^{208}Pb target while using the Miniball detector array [23] for the γ -ray spectroscopy. The mentioned complementary experiments were angular γ - γ -coincidence correlation measurements after β^+/ϵ decay, which were performed for ^{140}Nd [24] and will be performed for ^{142}Sm at the Heavy Ion Laboratory in Warsaw.

The existence of $2_{1,ms}^+$ states in vibrational nuclei were experimentally established more than two decades ago in the $A = 50$ [26–29] and $A = 90$ regions [30–38], and in the vicinity of the doubly-magic nucleus ^{132}Sn [10, 12, 18, 19, 39–45]. While in the vicinity of the doubly-magic atomic nucleus ^{208}Pb the investigation just recently started, for instance with the identifications of the $2_{1,ms}^+$ states in the radioactive isotopes $^{208,212}\text{Po}$ [46, 47] and the stable ^{204}Hg [48]. For the Po isotopes, the absolute $M1$ transition strengths were obtained by conducting direct lifetime measurements.

From the accumulated experimental information, the appearance of pronounced $2_{1,ms}^+$ states is suggested when the valence protons and neutrons occupy orbitals with high angular momenta. In ^{204}Hg , the valence nucleons are in orbitals with lower angular momenta than in its mirror isotope ^{212}Po , though, its $B(M1; 2_{1,ms}^+ \rightarrow 2_1^+)$ is more pronounced [48], see Figure 1.4 b). It is highly interesting whether this

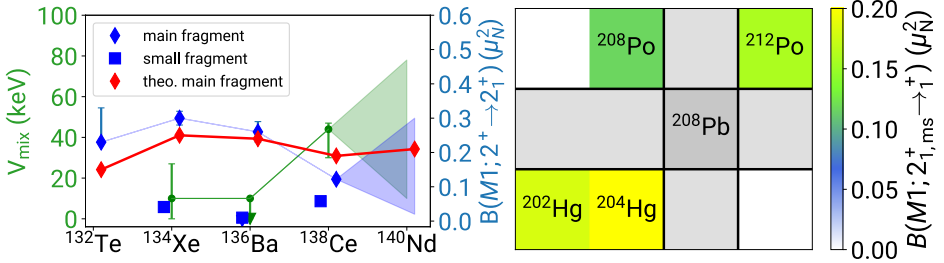


Figure 1.4.: The known $B(M1; 2_1^+ \rightarrow 2_1^+)$ values of the $N = 80$ isotones from ^{132}Te to ^{138}Ce [10, 12, 18, 19] compared to theory [25] and the corresponding F -spin mixing matrix elements are presented in a). They show the sub-shell closure at $Z = 58$ and a potential evolution towards ^{140}Nd . b) presents the situation in the vicinity of ^{208}Pb in respect to the $M1$ strength of the $2_{1,\text{ms}}^+ \rightarrow 2_1^+$ transitions. The value of ^{208}Po is a lower limit.

is the same for its neighboring isotope ^{202}Hg , or the increased valence-space leads to significant changes in the properties of the $2_{1,\text{ms}}^+$ state. A projectile Coulomb-excitation experiment at the Argonne National Laboratory was performed with a ^{202}Hg beam at $4.4 A \cdot \text{MeV}$ on a ^{12}C target using the γ -spectrometer Gammasphere [49] to solve this puzzle [50]. Simultaneously, an angular particle- γ correlation measurement was conducted to determine the nature of the $2_i^+ \rightarrow 2_1^+$ transitions.

Furthermore, the F spin will be probed as a quantum number in these heavy nuclei near doubly-magic isotopes. The F spin for bosons is analogous to the isospin for nucleons and is introduced in the framework of the IBM-2. On the basis of the F spin, fully- and mixed-symmetry states are distinguished. Hence, a weak mixing between fully and mixed-symmetry states indicates the F spin as a good approximate quantum number. The opposite was observed for the $N = 80$ isotones in ^{138}Ce , where the $2_{1,\text{ms}}^+$ state is strongly fragmented and, consequently, the F -spin mixing is extraordinarily high. The obtained $M1$ transition strengths distributions will be used to determine the F -spin mixing quantitatively.

2. Nuclear Structure Theory

The symbiosis of experimental and theoretical nuclear physics improves steadily the understanding of the universe we are living in.

There are various theoretical models describing the nuclear structure of excited states of the isotopes all over the chart of nuclides. Here, the intention of the reported experiments is the investigation of low-lying collective excitations of heavy nuclei near doubly-magic isotopes. A small selection of different approaches to describe low-lying excitations, i.e., single-particle or collective excitations, are presented in the following sections. The focus is on nuclear structure models to interpret the obtained results. Descriptions of the Geometrical Model [5], the Nuclear-Shell-Model and the Interacting-Boson-Model (IBM) [9, 51] will be presented.

2.1. Geometrical Model

The Geometrical Model [5] describes the nucleus as a homogeneous system of many nucleons, comparable to a drop of a liquid (Liquid Drop Model). Excitations of such a system are formed by collective motions of all nucleons, i.e., vibrations and rotations. These surface excitations can be mathematically described by a set of parameters $\alpha_{\lambda\mu}$ and spherical harmonics $Y_{\lambda\mu}^*(\theta, \phi)$. The distance between the origin of the nucleus and a certain spot of the surface is given by [5]

$$R(\theta, \phi) = R_0 \left(1 + \sum_{\lambda=0}^{\infty} \sum_{\mu=-\lambda}^{\lambda} \alpha_{\lambda\mu} Y_{\lambda\mu}^*(\theta, \phi) \right), \quad (2.1)$$

where R_0 is the radius of the system in the equilibrium. The type of the geometrical excitations varies in dependence of the shape of the nucleus. Near closed shells, the shape of the system is near-spherical and the nucleus can be excited to perform oscillations around the equilibrium shape. Away from closed shells, the

nucleus might take a deformed equilibrium shape [6]. The deformed shape of the nucleus enables additionally the rotation as a form of excitation. The dynamics of the system can be described by the Bohr Hamiltonian [5, 6]

$$H = -\frac{\hbar^2}{2D} \left[\frac{1}{\beta^4} \frac{\partial}{\partial \beta} \left[\beta^4 \frac{\partial}{\partial \beta} + \frac{1}{\beta^2} \frac{1}{\sin(3\gamma)} \frac{\partial}{\partial \gamma} \left[\sin(3\gamma) \frac{\partial}{\partial \gamma} \right] \right] \right] + \frac{\hbar^2}{2I} R^2 + V. \quad (2.2)$$

Here, R is the rotational angular momentum, I denotes the moment of inertia, D is the single mass parameter, and V denotes the nuclear potential.

The value $\lambda = 0$ in Eq. (2.1) describes the so-called breathing mode. The nucleus expands or compresses while keeping its shape. This kind of excitation happens at high energies and can be neglected for the description of low-lying collective states. The form of motion of the nucleus for $\lambda = 1$ is a simple oscillation around the origin and does not effect its internal structure. The quadrupole modes, $\lambda = 2$, are the lowest orders contributing to the collective surface excitations of the nucleus. This mode can be interpreted as an oscillation of the nucleus' shape, that means an oscillation of expansion and compression of the nuclear shape along alternating symmetry axes by a transitional restoring the original spherical shape. The third order, $\lambda = 3$, describes a pear-shaped octupole excitation, which is not uncommon for heavy nuclei in the vicinity of shell-closures [52–56].

In the case of quadrupole excitations, the parameters $\alpha_{2\mu}$ of Eq. (2.1) can be expressed via [5]

$$\alpha_{20} = \beta \cos(\gamma), \quad (2.3)$$

$$\alpha_{22} = \alpha_{2-2} = \frac{1}{\sqrt{2}} \beta \sin(\gamma). \quad (2.4)$$

In this notation the deformation parameters β and γ describe the degrees of the quadrupole deformation and of the axial symmetry, respectively. The extreme case $\beta = 0$ corresponds to a spherical shaped nucleus. $\beta > 0$ and $\gamma = 0^\circ$ describes an axially symmetric prolate deformed nucleus, while $\beta > 0$ and $\gamma = 60^\circ$ represents an axially symmetric oblate deformed nucleus. For values of γ in-between these limits, the nucleus is triaxially deformed.

2.1.1. Vibrational Nuclei

Most nuclei in the vicinity of shell closures have a near-spherical shape and vibrations around the spherical equilibrium form their collective excitations. The surface of a vibrating nucleus is described by Eq. (2.1) with an additional small modification. Now, the deformation parameters $\alpha_{\lambda\mu} = \alpha_{\lambda\mu}(t)$ are time dependent.

Here, the discussion focuses on the quadrupole collectivity, hence, all terms besides $\lambda = 2$ of Eq. (2.1) are neglected. Regarding the $\alpha_{\lambda=2,\mu}$ parameters, they vanish for odd μ and are symmetrical, $\alpha_{\lambda=2,\mu} = \alpha_{\lambda=2,-\mu}$. The Hamiltonian [6]

$$H = T + V = \frac{1}{2}B \sum_{\mu} \left| \frac{d\alpha_{2\mu}}{dt} \right|^2 + \frac{1}{2}C \sum_{\mu} |\alpha_{2\mu}|^2 \quad (2.5)$$

describes the quadrupole vibration of the surface. It has the form of a harmonic oscillator with the frequency of the term $\alpha_{2\mu}$:

$$\omega = \sqrt{\frac{C}{B}}, \quad (2.6)$$

with the vibrational energy $\hbar\omega$. Thus, the excitations of vibrational nuclei can be visualized as phonons with angular momentum λ and parity $(-1)^\lambda$, analogous to excitations in solid state physics. In the present case of $\lambda = 2$ excitations, the quadrupole phonons with positive parity, $J^\pi = 2^+$, are relevant.

The annihilation and creation of such phonons are equivalent to the excitation and the decay of excited nuclear states. This can be described in the language of second quantization with annihilation and creation operators

$$\mathbf{b}|n_b\rangle = \sqrt{n_b}|n_b - 1\rangle \quad (2.7)$$

$$\mathbf{b}^\dagger|n_b\rangle = \sqrt{n_b + 1}|n_b + 1\rangle, \quad (2.8)$$

respectively. Here, $|n_b\rangle$ is the multi-boson state where n_b is the number of bosons. The integer spins of the phonons lead to a boson-like treatment and, thus, they are not affected by the Pauli principle. Using Eq. (2.8), the N -phonon state $|N_{\text{ph}}\rangle$ can be constructed by applying the creation operator N times on the ground state $|0\rangle$:

$$|N_{\text{ph}}\rangle = (\mathbf{b}^\dagger)^N |0\rangle. \quad (2.9)$$

The angular momenta for the coupling of N phonons can be determined from the m -scheme. This leads to an angular momentum triplet, 0^+ , 2^+ and 4^+ , for two-phonon excitations and an angular momentum quintuplet, 0^+ , 2^+ , 3^+ , 4^+ and 6^+ , for three-phonon excitations, see Figure 2.1. In this simplified phonon picture, the ratio of the level energies of the two-phonon 4_1^+ state and the one-phonon 2_1^+ state, $R_{4/2}$, is expected to be 2. In reality, the states of multi-phonon excitation are not exactly degenerate, which is caused by a residual interaction between the phonons. Indeed, the accumulated data of nuclei near shell closures show a value of $R_{4/2} \approx 2.2$ due to these anharmonicities [6].

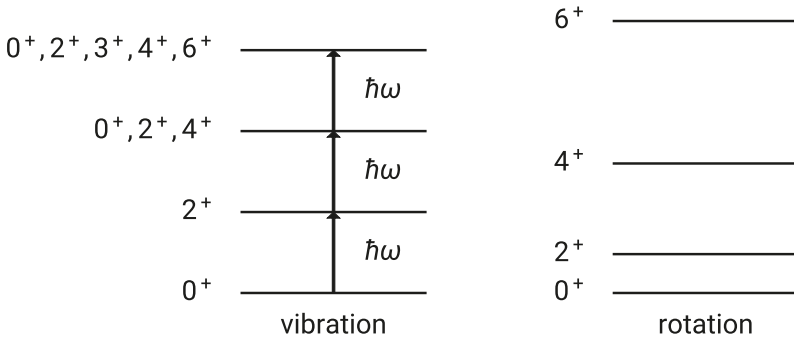


Figure 2.1.: Schematic level schemes of low-lying excitations of vibrational and rotational nuclei. The energies for the rotational states are obtained via Eq. (2.13).

2.1.2. Rotational Nuclei

As mentioned before, the mass distributions of some nuclei deviate from a near-spherical behaviour. This deformation is small in the vicinity of shell closures and increases while departing from shell closures. Hence, this non-spherical nucleus now exhibits an intrinsic quadrupole moment Q_0 due to a non-spherical distribution of the charged particles. It is connected to the equilibrium radius R_0 , the proton

number Z and the deformation parameter β by the relation

$$Q_0 = \frac{3}{\sqrt{5\pi}} R_0^2 Z \beta (1 + 0.16\beta). \quad (2.10)$$

Here, the intrinsic quadrupole moment is not equal, but connected to the experimentally observable spectroscopic quadrupole moment Q by the relation

$$Q = \frac{3K^2 - J(J+1)}{(J+1)(2J+3)} Q_0. \quad (2.11)$$

Here, the K -quantum number is the projection of the total angular momentum J on the intrinsic symmetry axis of the nucleus. For nuclear ground states of even-even nuclei, where $J = 0$, the measurable spectroscopic quadrupole moment vanishes. The 2_1^+ state exhibits the quantum number $K = 0$, because the state is part of the ground-state band. Thus, Eq. (2.11) evaluates to $Q = -2/7Q_0$. In the limit of the rigid rotor, there is a direct connection between the reduced transition strength of the $0_1^+ \rightarrow 2_1^+$ transition and the intrinsic quadrupole moment of the 2_1^+ state by the relation

$$B(E2; 0_1^+ \rightarrow 2_1^+) = \frac{5}{16\pi} e^2 Q_0^2 (2_1^+). \quad (2.12)$$

Furthermore, the rotational energy of the ground-state band ($K = 0$) of an even-even nucleus with the angular momentum J and the ground state $J^\pi = 0^+$ is given by

$$E_{\text{rot}}(J) = \frac{\hbar^2}{2I} J(J+1). \quad (2.13)$$

Here, I is the nucleus' moment of inertia. On top of the 0^+ ground state only even values of angular momenta $J = 2, 4, 6 \dots$ can be found for rotational bands in even-even nuclei [6], see Figure 2.1. It is shown by Eq. (2.13), that a ratio $R_{4/2} = (20\hbar^2)/(6\hbar^2) = 3.33$ is expected for the rigid rotor. A ratio of $2.91 < R_{4/2} < 3.33$ still indicates the rotational nature of the nucleus [6].

There is also the possibility of superpositions of rotational and vibrational excitations. In this case, a rotational band is normally built upon a vibrational

excitation, which can exhibit a non-vanishing angular momentum. Therefore, the level energy of Eq. (2.13) has to be generalized relative to the “base” energy to

$$E_{\text{rot}}(J, K) = \frac{\hbar^2}{2I} [J(J+1) - K(K+1)]. \quad (2.14)$$

This results in rotational bands equivalent to the ground state band ($K = 0$), but on top of $K \neq 0$ excitations. The angular momenta of these states can take values $J = K, K + 1, K + 2, \dots$, except when the “base” is a $K = 0$ state, in which case only even spins are allowed for J [6]. In deformed nuclei, two low-lying bands are commonly observed, i.e., the β and γ bands on top of the 0^+ and 2^+ vibrational excitations.

The standard geometrical model [5] with its great capability to describe collective motions of a homogeneous system lacks the ability to characterize single particle excitations or motions of a two-fluid system. Therefore, the nuclear shell model will be introduced in the following section.

2.2. Nuclear Shell Model

The original nuclear shell model was independently developed by Goeppert-Mayer [2, 3] and Haxel, Jensen and Suess [4]. It was able to theoretically justify the experimentally observed increased stability of nuclei with a certain number of protons or neutrons. These so-called magic numbers are 2, 8, 20, 50, 82, and 126.

The motion of a certain nucleon is determined by its initial momentum and the interaction with other nucleons. The interaction between the nucleons is assumed to be of two-body nature to simplify the Hamiltonian in a reasonable manner:

$$H = T + V = \sum_{i=1}^A \frac{\vec{p}_i^2}{2m_i} + \sum_{i < k=1}^A V_{ik}(\vec{r}_i - \vec{r}_k). \quad (2.15)$$

Here, A is the number of nucleons, \vec{p}_i , $\vec{r}_{i,k}$ and $m_{i,k}$ are the nucleon's momenta, coordinates, and masses, and V_{ik} is the interaction between two nucleons. With a rising number of nucleons A , this equation gets quickly hard to solve.

To overcome this obstacle, the interaction between the nucleons will be described through a central potential. In atomic physics, the electrons are affected by an external potential, while in the nucleus, the potential is generated by the $A - 1$ nucleons acting on the A -th nucleon. The Hamiltonian is modified by a one-body potential $U_i(\vec{r}_i)$ and given by

$$H = \underbrace{\sum_{i=1}^A \left[\frac{\vec{p}_i^2}{2m_i} + U_i(\vec{r}_i) \right]}_{\equiv H_0} + \underbrace{\sum_{i < k=1}^A V_{ik}(\vec{r}_i - \vec{r}_k) - \sum_{i=1}^A U_i(\vec{r}_i)}_{\equiv H_{\text{residual}}}. \quad (2.16)$$

The potential H_{residual} can be considered small in comparison to H_0 . Nevertheless, it is of great importance when it comes to collective excitations. The strength of the nucleon-nucleon interaction decreases rapidly with an increasing distance and the interaction is attractive. Although the harmonic oscillator shows the wrong asymptotic behaviour, it is a valid first approximation of the central nuclear potential,

$$V(\vec{r}) = \frac{1}{2} m \omega^2 \vec{r}^2. \quad (2.17)$$

From the three-dimensional harmonic oscillator follows the eigenvalues, which are single-particle excitation energies of modes of the harmonic oscillator,

$$E_N = \left(N + \frac{3}{2} \right) \hbar\omega, \quad (2.18)$$

where N is the oscillator shell number. The shells, which originate from the three-dimensional harmonic oscillator, reproduce the experimental magic numbers up to 20, see Figure 2.2. When a central potential is applied, the wave function can be divided into a radial and an angular part. Then, $n = 1, 2, 3, 4, \dots$ and $l = 0, 1, 2, 3, 4, \dots (s, p, d, f, g, \dots)$ are introduced as the radial quantum number, which is the number of nodes of the wave function, and as the angular momentum, respectively. The connection of N , n and l is given by $N = 2(n - 1) + l$. Different combinations of n and l lead to the same N and, consequently, to degenerate energy levels. For higher energies, the approximation of the nuclear potential with the harmonic oscillator fails. Hence, an attractive \vec{l}^2 term is included in the potential, $V_{l^2} = -V_l \vec{l}^2$, which splits the degeneracy and lowers the level energies with higher angular momentum l , see Figure 2.2. Though, the introduction of the \vec{l}^2 term does not improve the reproduction of the observed magic numbers. Hence, an additional coupling of the nuclear spin s and the angular momentum l is taken into consideration with the potential $V_{l.s} = -V_{l.s} \vec{l} \cdot \vec{s}$. Consequently, the levels are split into two levels with $j = l + s$ and $j = l - s$. The good quantum numbers after the $\vec{l} \cdot \vec{s}$ coupling are the absolutes of s , l and the total angular momentum j and its magnetic sub-state m . The energy splitting increases with higher values of l . The final Hamiltonian with the complete potential for the independent particle model

$$U(\vec{r}) = \frac{1}{2}m\omega^2\vec{r}^2 - V_l\vec{l}^2 - V_{l.s}\vec{l} \cdot \vec{s} \quad (2.19)$$

produces a shell scheme, see Figure 2.2 on the right side, which reproduces the observed magic numbers up to 126 nucleons. The parity quantum number of an orbital is determined by its angular momentum l : $\pi = (-1)^l$. The levels of a major shell generally inhabit the same parity, which is predetermined by the parity of the lowest-lying level. An exception occurs, when a level from a higher-lying shell intrudes the lower shell due to the $\vec{l} \cdot \vec{s}$ coupling term. Such an intruder orbit has the opposing parity in comparison to the levels of its new shell. Due to the Pauli principle, $2j + 1$ nucleons fill an orbit entirely and couple pairwise to

$J = 0$. Therefore, the properties of the atomic nucleus are mostly determined by the nucleons in partly-filled orbitals, so-called valence nucleons, and the residual interaction, which they are subject to. Valence nucleons of the same kind in the same orbital can couple to different total angular momenta J . The degeneracy, which is still present in Eq. (2.19), is broken by the residual interaction. The short-range attractive part of the nucleon-nucleon interaction can be modeled by the δ interaction

$$V_{\text{res}} = -V_0 \delta(\vec{r}_1 - \vec{r}_2). \quad (2.20)$$

The δ interaction increases with a growing overlap of the wave functions of two nucleons. The overlap maximizes with two anti-parallel aligned nucleons: $M = m_1 + m_2 = 0$. The consequence is that the $J^\pi = 0^+$ is the energetically most preferable configuration, followed by $2^+, 4^+, \dots$ configurations. Generally, configurations with the least number of pairs not coupled to $J^\pi = 0^+$ are favored by V_{res} . The number of pairs not coupled to $J^\pi = 0^+$ is measured by the seniority ν . Consequently, the ground-state total angular momentum is 0^+ or determined by the unpaired nucleons for even-even and other nuclei, respectively.

For the description of low-lying collective excitations of even-even nuclei, the promotions of several nucleons in the model space have to be considered. Here, the model space represents the involved orbitals of a performed shell-model calculation, e.g., the orbitals between two closed shells. In general, the most accurate reproduction of spectroscopic quantities is achieved by using a valence space as large as possible. However, the necessary computing power increases exponentially with a growing model space and the empirical hamiltonians are easier determined in a limited model space [57]. Hence, the balance between the quality of the calculations and the computational feasibility has to be found.

In contemporary nuclear physics, there are several successful approaches to solve the emerged many-body problem, e.g., coupled-cluster method [58], Greens function Monte Carlo method [59], Monte Carlo shell model [60] and large-scale shell model calculations using the m-scheme [61] and many others.

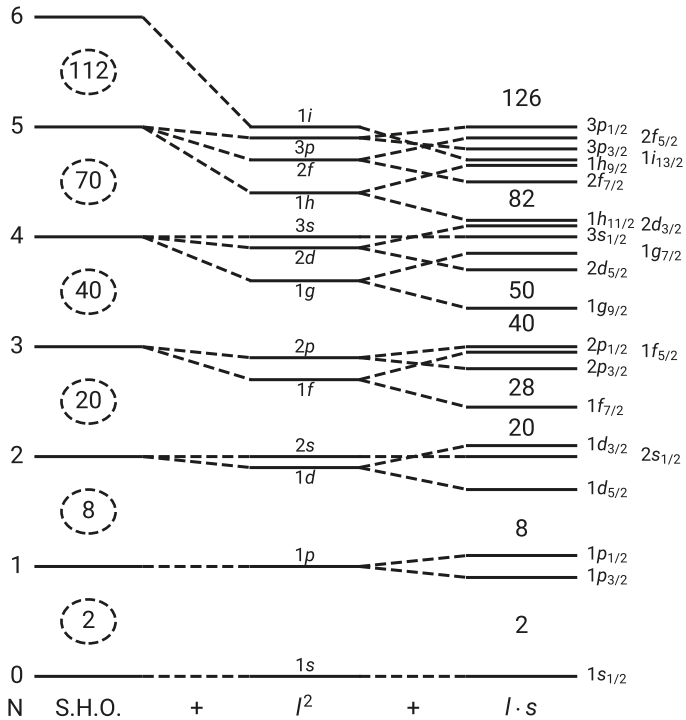


Figure 2.2.: The level scheme of the harmonic oscillator is presented, while taken into account the l^2 (mid) and $l \cdot s$ (right) corrections. The modified harmonic oscillator produces the experimental observed shell closures. The figure is based on Ref. [6].

2.3. Interacting Boson Model

The interacting boson model (IBM) [9] is an algebraic model with the purpose of describing collective phenomena of medium and heavy even-even atomic nuclei, i.e., energetically low-lying collective excitations. A fundamental idea of the IBM is, that an atomic nucleus consists of a doubly-magic inert core and, thus, the remaining valence nucleons form the collective excitations. Furthermore, the valence nucleons couple pairwise to bosons, reducing the degrees of freedom drastically. The total number of valence bosons N is given by $N = 1/2(N_p + N_n)$, where N_p and N_n are the numbers of valence protons (holes) and neutrons (holes), respectively, with respect to the closest-lying doubly-magic nucleus. Valence-nucleon holes are treated the same as real valence nucleons. In its original form, the sd -IBM-1, there is no distinction between the valence bosons composed of protons and neutrons. Furthermore, the bosons are meant to carry angular momenta of $L = 0$ (s boson) and $L = 2$ (d boson). The IBM is using the language of second quantization, so the bosons are given by the creation and annihilation operators

$$s^\dagger, s \quad \text{and} \quad d_\mu^\dagger, \tilde{d}_\mu, \quad (2.21)$$

respectively. Here, $\mu = -2, -1, 0, 1, 2$ corresponds to the magnetic sub-states of the d boson. The operator \tilde{d}_μ is defined as $\tilde{d}_\mu = (-1)^\mu d_{-\mu}$ in order to have spherical tensors for the annihilation and the creation operator, d_μ^\dagger and \tilde{d}_μ . The operators $s^\dagger s$, $s^\dagger \tilde{d}_\mu$, $d_\mu^\dagger s$, and $\left[d_\mu^\dagger \tilde{d}_\mu \right]_J$, where $J = 0, 1, 2, 3, 4$ and $\mu \leq J$, are the generators of the Lie Algebra $U(6)$. This set of generators spans a rich group structure. This means, that a new subset of generators closes under communication, i.e., the commutator of any two generators of the new subset is solely expressible in terms of generators of the new subgroup. Under the constraint, that subgroups of $U(6)$ have to include the rotational algebra $O(3)$, three different decompositions are found [9]:

$$U(6) \supset U(5) \supset O(5) \supset O(3) \supset O(2), \quad (2.22)$$

$\begin{matrix} N & n_d & \nu & L & M \end{matrix}$

$$U(6) \supset SU(3) \supset O(3) \supset O(2), \quad (2.23)$$

$\begin{matrix} N & (\lambda, \mu) & L & M \end{matrix}$

$$U(6) \supset O(6) \supset O(5) \supset O(3) \supset O(2). \quad (2.24)$$

$\begin{matrix} N & \sigma & \tau & L & M \end{matrix}$

The quantum numbers below the subgroups are the irreducible representations, where N is the total number of bosons, n_d is the number of d bosons, ν is the seniority, τ is the boson seniority, L is the angular momentum and M is its projection. The subgroups $U(5)$, $SU(3)$ and $O(6)$ represent the vibrational, rotational and γ -soft limits, respectively, and their eigenvalue relations are analytically solvable. A simplified Hamiltonian of the sd -IBM-1 is given by [62]

$$H = \epsilon \hat{n}_d + \kappa Q^\chi Q^\chi, \quad (2.25)$$

where $\hat{n}_d = d_\mu^\dagger \tilde{d}_\mu$ is the d boson number operator and Q^χ is the quadrupole operator with the structure parameter χ , $Q^\chi = d^\dagger s + s \tilde{d} + \chi [d^\dagger \tilde{d}]_2$.

In the framework of the sd -IBM-1, proton and neutron bosons are indistinguishable. Therefore, it is not capable to describe collective phenomena of the atomic nucleus, where protons and neutrons act differently. Thus, $M1$ transitions do not occur in the framework of the sd -IBM-1.

2.3.1. Interacting Boson Model 2

In contrast to its predecessor, the sd -IBM-1, the sd -IBM-2 distinguishes between neutron and proton bosons [7, 9, 51]. This innovation leads to the capability of describing states of mixed proton-neutron symmetry. The main features of the model and the properties of the so-called mixed-symmetry states will be introduced.

This model defines individual annihilation and creation operators for proton and neutron bosons as

$$s_\rho^\dagger, s_\rho \quad \text{and} \quad d_{\rho, \mu}^\dagger, \tilde{d}_{\rho, \mu}, \quad (2.26)$$

with $\rho = \pi, \nu$ for protons and neutron bosons, respectively, and $\mu = -2, -1, 0, 1, 2$. The resulting Hamiltonian contains specific proton and neutron terms, as well

as additional proton-neutron boson interaction terms. The extended Hamiltonian is given by [63]:

$$H = \epsilon_\pi \hat{n}_{d_\pi} + \epsilon_\nu \hat{n}_{d_\nu} + \kappa_{\pi\pi} Q_\pi^{\chi_\pi} Q_\pi^{\chi_\pi} + 2\kappa_{\pi\nu} Q_\pi^{\chi_\pi} Q_\nu^{\chi_\nu} + \kappa_{\nu\nu} Q_\nu^{\chi_\nu} Q_\nu^{\chi_\nu} + \hat{M}(\xi_1, \xi_2, \xi_3). \quad (2.27)$$

ϵ_π and ϵ_ν are the single d -boson energies and $Q_\pi^{\chi_\pi}$ and $Q_\nu^{\chi_\nu}$ are the proton and neutron quadrupole operators, respectively. The general three-parameter Majorana interaction \hat{M} can be defined as

$$\hat{M}(\xi_1, \xi_2, \xi_3) = \frac{1}{2} \xi_2 (s_\pi^\dagger d_\nu^\dagger - d_\pi^\dagger s_\nu^\dagger) \cdot (s_\pi \tilde{d}_\nu - \tilde{d}_\pi s_\nu) - \sum_{K=1,3} \xi_K \left([d_\pi^\dagger d_\nu^\dagger]^{(K)} \cdot [\tilde{d}_\pi \tilde{d}_\nu]^{(K)} \right). \quad (2.28)$$

The term of the Majorana interaction vanishes, if protons and neutrons are indistinguishable, e.g., in the case of IBM-1 states. The proton-neutron symmetry of a wave function of an IBM-2 state is quantified by the F -spin quantum number. The F spin for bosons is introduced analogously to the isospin for nucleons with its main properties shown in Table 2.1.

Table 2.1.: The F spin and its projection on the z -axis F_z of proton (π) and neutron (ν) bosons.

	π	ν
F	1/2	1/2
F_z	+1/2	-1/2

The total projection of a nucleus $F_z = \frac{1}{2}(N_\pi - N_\nu)$ follows from Table 2.1, with the proton and neutron boson number N_π and N_ν , respectively. The maximum F spin of a state is given by $F_{\max} = \frac{1}{2}(N_\pi + N_\nu)$. The F -spin quantum number quantifies the symmetry of a wave function with respect to the pairwise exchange of proton and neutron labels. The wave functions of states with maximum F spin, $F = F_{\max}$, are symmetric under that exchange. These states are labeled

fully-symmetric states (FSS) emerging from the framework of the IBM-1. States with partly anti-symmetric wave functions are called mixed-symmetry states (MSS) and exhibit a F spin less than the maximum, $F < F_{\max}$. However, only MSSs with $F = F_{\max} - 1$ have been observed until now, e.g., the 1^+ scissors mode [64] and the first 2^+ mixed-symmetry state in vibrational nuclei [63]. An exemplary level scheme of low-lying FSSs and MSSs of a nucleus in the $U(5)$ limit (vibrational) is presented in Figure 2.3 using the Hamiltonian

$$H = \epsilon (\hat{n}_{d\pi} + \hat{n}_{d\nu}) + \lambda \hat{M}, \quad (2.29)$$

with boson numbers $N_\pi = N_\nu = 1$ and energies $\epsilon = \epsilon_\pi = \epsilon_\nu$. Using these simplifications, the Majorana term reduces to

$$\hat{M} = [F_{\max}(F_{\max} + 1) - \hat{F}^2] / 2 \text{ with} \quad (2.30)$$

$$\hat{F}^2 \Psi_{\text{IBM-1}} = F_{\max}(F_{\max} + 1) \Psi_{\text{IBM-1}} \quad (2.31)$$

for IBM-1 states. For states outside the framework of the IBM-1, the Majorana term leads to a lowered excitation energy of the FSSs in comparison to the MSSs, see Figure 2.3.

Besides the energies of excited states, the structure of the wave functions and the corresponding decay behaviour are often of special interest. Here, the Q -phonon scheme is helpful to understand the main structural design in the formation of collectivity. It was introduced by Otsuka et al. [65] and developed by the Cologne-Tokyo collaboration [65–69]. The level scheme of Figure 2.3 is also emerging from the Q -phonon scheme. The states are formed by a combination of symmetric and mixed-symmetric quadrupole excitations from the ground state $|0_1^+\rangle$:

$$|2_1^+\rangle = Q_s |0_1^+\rangle, \quad (2.32)$$

$$|0_2^+\rangle = [Q_s Q_s]^{(0)} |0_1^+\rangle, \quad (2.33)$$

$$|2_2^+\rangle = [Q_s Q_s]^{(2)} |0_1^+\rangle, \quad (2.34)$$

$$|4_1^+\rangle = [Q_s Q_s]^{(4)} |0_1^+\rangle, \quad (2.35)$$

$$|2_{1,\text{ms}}^+\rangle = Q_m |0_1^+\rangle, \quad (2.36)$$

$$|1_{1,\text{ms}}^+\rangle = [Q_s Q_m]^{(1)} |0_1^+\rangle, \text{ and} \quad (2.37)$$

$$|3_{1,\text{ms}}^+\rangle = [Q_s Q_m]^{(3)} |0_1^+\rangle, \quad (2.38)$$

where $Q_s = Q_\pi + Q_\nu$ and $Q_m = [Q_\pi N/N_\pi - Q_\nu N/N_\nu]$ denote the F -scalar ($\Delta F = 0$) and the F -vector ($\Delta F = 1$) quadrupole operators, respectively.

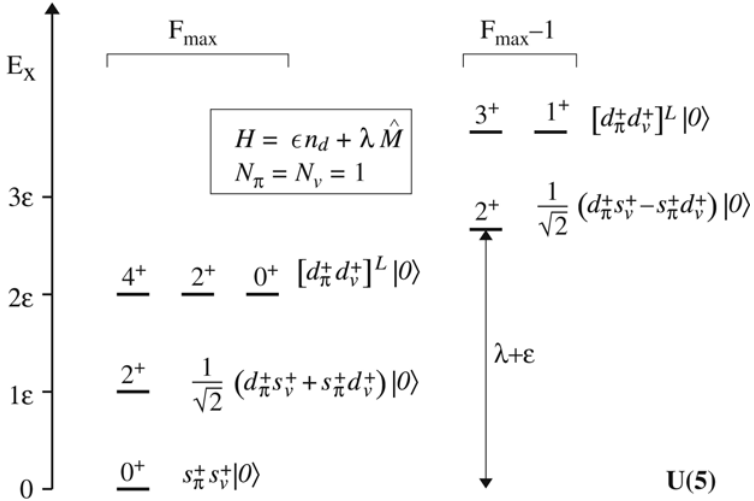


Figure 2.3.: A schematic level scheme of a simplified IBM-2 Hamiltonian $H = \epsilon n_d + \lambda \hat{M}$ in the limit of the vibrational $U(5)$ limit, with $N_\pi = N_\nu = 1$ and $\epsilon = \epsilon_\pi = \epsilon_\nu$. Reprinted figure with permission from Ref. [63].

Hence, the $2^+_{1,ms}$ states of vibrational nuclei exhibit experimental decay signatures, which are considered for its identification [63]:

- the lowest-lying MSS,
- an enhanced $B(M1; 2^+_{1,ms} \rightarrow 2^+_1) \approx 0.2 \mu_N^2$ strength,
- a short life time, typically in the range of 100 fs,
- an increased $B(E1; 3^-_1 \rightarrow 2^+_{1,ms})$ strength [37].

Especially, the observation of an enhanced $M1$ transition strength is an indispensable quantity for the reliable identification of the $2^+_{1,ms}$ state. The origin of the strong $M1$ transition is the F -vector nature of the $M1$ transition operator [63]:

$$T(M1) = \sqrt{\frac{3}{4\pi}} [g_\pi L_\pi + g_\nu L_\nu] \mu_N \quad (2.39)$$

$$= \sqrt{\frac{3}{4\pi}} \left[\frac{N_\pi g_\pi + N_\nu g_\nu}{N} L_{\text{tot}} + (g_\pi - g_\nu) \frac{N_\pi N_\nu}{N} \left(\frac{L_\pi}{N_\pi} - \frac{L_\nu}{N_\nu} \right) \right] \mu_N, \quad (2.40)$$

where $L_\rho = \sqrt{10} \left[d_\rho^\dagger \times \tilde{d}_\rho \right]_1$, with $\rho \in \pi, \nu$, is the angular momentum operator for proton and neutron bosons and $L_{\text{tot}} = L_\pi + L_\nu$ denotes the total angular momentum operator of the IBM-2 and g_π and g_ν are the effective boson g factors. This transition operator yields a vanishing matrix element for transitions between FSSs. Hence, in the framework of the IBM $M1$ transitions between FSSs are forbidden. Since nuclear states are in reality not entirely represented through theoretical IBM states, typically a small $M1$ strength in the order of $0.01\mu_N^2$, or less is observed between FFSs [10, 50, 63], when allowed by the selection rules. In the limits of the $U(5)$ symmetry, the following $M1$ and transition strength is expected:

$$B(M1; 2_{1,\text{ms}}^+ \rightarrow 2_1^+) = \frac{3}{4\pi} (g_\pi - g_\nu)^2 \frac{6}{N^2} N_\pi N_\nu. \quad (2.41)$$

Furthermore, the $E2$ transition operator,

$$T(E2) = e_\pi Q_\pi^{X_\pi} + e_\nu Q_\nu^{X_\pi}, \quad (2.42)$$

with e_π and e_ν as the effective quadrupole-boson charges, is of F -scalar nature, hence, it connects states with the same F spin ($\Delta F = 0$). Here, the $\Delta F = 1$ connections are suppressed for $E2$ transitions in the framework of the IBM-2.

2.4. Two-State Mixing

Regarding level schemes of real atomic nuclei, pure configurations as predicted in theoretical models are rarely found. The introduction of a simple two-state mixing takes account for the existing mixing between two states and enables a more realistic description or prediction of the nuclear excitation scheme. The presented discussion of this phenomenon is guided by Ref. [6].

2.4.1. General Formalism

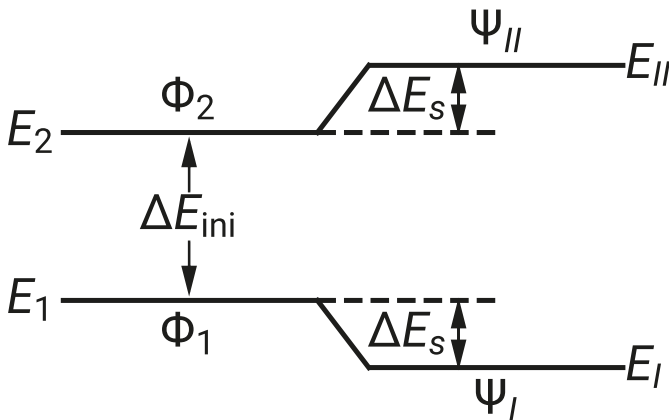


Figure 2.4.: A simple two-state mixing scenario with the initial states marked with 1, 2 and the final states marked with I, II.

The situation presented in Figure 2.4 is separated into two parts. The initial unperturbed levels are marked with energies E_1 and E_2 and wave functions Φ_1 and Φ_2 , and the final mixed levels with energies E_I and E_{II} and wave functions Ψ_I and Ψ_{II} . The mixing matrix element $\langle \Phi_1 | V | \Phi_2 \rangle$ of an arbitrary interaction V will be denoted in the following as V . The degree of mixing of the final states depends on the initial energy difference ΔE_{ini} and on the matrix element V . The energies and wave functions of the final states are deduced by the diagonalization

of the 2×2 matrix

$$\begin{pmatrix} E_1 & V \\ V & E_2 \end{pmatrix}. \quad (2.43)$$

The diagonalization leads to the following relations for the energies of the final states:

$$\begin{aligned} E_{I,II} &= \frac{E_1 + E_2}{2} \mp \frac{\sqrt{(E_1 + E_2)^2 - 4(E_1 E_2 - V^2)}}{2} \\ &= \frac{E_1 + E_2}{2} \mp \frac{\sqrt{(E_2 - E_1)^2 + 4V^2}}{2}. \end{aligned} \quad (2.44)$$

The ratio of the energy difference of the unperturbed states to the mixing matrix element $R = (\Delta E_{\text{ini}})/V$ is introduced to increase the comprehensibility of Eq. (2.44), resulting in

$$E_{I,II} = \frac{E_1 + E_2}{2} \mp \frac{\Delta E_{\text{ini}}}{2} \sqrt{1 + \frac{4}{R^2}}, \quad (2.45)$$

where the $-$ sign is meant for E_I and the $+$ sign for E_{II} . These equations show, that a large energy difference of the initial states ΔE_{ini} reduces the effect of a given matrix element V , but even a small matrix element may result in a large mixing if the energy spacing of the initial states ΔE_{ini} is small.

The wave functions of the mixed final states can be interpreted as superpositions of the unperturbed wave functions:

$$\Psi_I = \alpha \Phi_1 + \beta \Phi_2, \quad (2.46)$$

$$\Psi_{II} = -\beta \Phi_1 + \alpha \Phi_2 \quad \text{with} \quad \alpha^2 + \beta^2 = 1. \quad (2.47)$$

Here, the parameters α and β describe the contributions of the initial states $\Phi_{1,2}$ to the final states $\Psi_{I,II}$. These relations lead to the following system of linear equations, which connects α and β to the matrix Element V and the energies of the initial and final states E_1 , E_2 , E_I , and E_{II} :

$$\begin{pmatrix} E_1 & V \\ V & E_2 \end{pmatrix} \begin{pmatrix} \alpha \\ \beta \end{pmatrix} = E_I \begin{pmatrix} \alpha \\ \beta \end{pmatrix} \quad (2.48)$$

$$\begin{pmatrix} E_1 & V \\ V & E_2 \end{pmatrix} \begin{pmatrix} -\beta \\ \alpha \end{pmatrix} = E_{II} \begin{pmatrix} -\beta \\ \alpha \end{pmatrix}. \quad (2.49)$$

This is a generic mixing situation, which can be applied to any interaction.

2.4.2. F -Spin Mixing

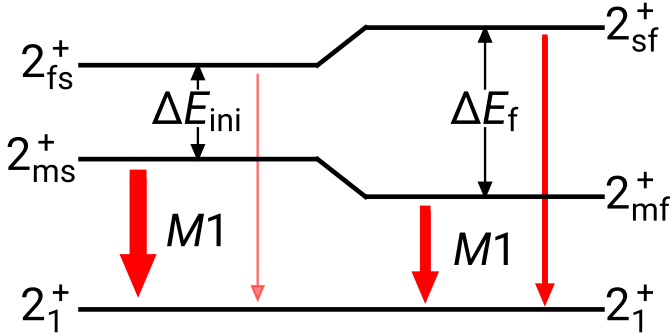


Figure 2.5.: A two-state mixing scenario regarding the F spin. The width of the arrows indicate the strength of the corresponding $M1$ transition. ΔE_f is the energy difference of the mixed states.

Here, this simple two-state mixing scenario was used to determine the degree of mixing between FSSs ($F = F_{\max}$) and MSSs ($F = F_{\max} - 1$). In this case, the initial levels are the theoretical unperturbed mixed-symmetry 2_{ms}^+ state and a neighboring fully-symmetric 2_{fs}^+ state. The fully-symmetric 2_1^+ state will remain unmixed, but is necessary to resolve the mixing scenario. Then, the final states are superpositions of the theoretical MSS and FSS, see Figure 2.5. The state with mainly mixed-symmetry character is called the main fragment (2_{mf}^+) and the mainly full-symmetric one is called the small fragment (2_{sf}^+) of the 2_{ms}^+ state. A characteristic of the transition between the 2_{ms}^+ state and the 2_1^+ state is its

strong $M1$ nature, which is forbidden for transitions between FSSs, see Section 2.3. These relations are getting useful, if the wave function of the 2_1^+ state and the $M1$ transition operator are applied to Eqs. (2.46) and (2.47):

$$\langle 2_1^+ || M1 || 2_{mf}^+ \rangle = \alpha \langle 2_1^+ || M1 || 2_{ms}^+ \rangle + \beta \langle 2_1^+ || M1 || 2_{fs}^+ \rangle, \quad (2.50)$$

$$\langle 2_1^+ || M1 || 2_{sf}^+ \rangle = -\beta \langle 2_1^+ || M1 || 2_{ms}^+ \rangle + \alpha \langle 2_1^+ || M1 || 2_{fs}^+ \rangle. \quad (2.51)$$

The $M1$ matrix elements of the transitions between realized states can be determined experimentally. In a sophisticated view, the unperturbed states should not be considered idealized IBM states, because transitions between predominantly FSSs carry in reality a small, but measurable, $M1$ transition strength. Hence, this $M1$ strength has its origin outside the framework of the IBM-2. In this thesis, this background $M1$ transition matrix element between FSSs $\langle 2_1^+ || M1 || 2_{fs}^+ \rangle$ is determined by the transition between the 2_1^+ and the 2_2^+ states. The latter has in the considered cases a sufficiently large energy difference to the main fragment of the $2_{1,ms}^+$ state to exclude mixing with it. The total strength from the unperturbed 2_{ms}^+ state is given by

$$B(M1; 2_{ms}^+ \rightarrow 2_1^+) = B(M1; 2_{mf}^+ \rightarrow 2_1^+) + B(M1; 2_{sf}^+ \rightarrow 2_1^+) - B(M1; 2_{fs}^+ \rightarrow 2_1^+). \quad (2.52)$$

Finally, α and β can be determined and, then, inserted in Eqs. (2.48) and (2.49) to obtain the mixing matrix element for F spin, V_{F-mix} .

3. Experimental Techniques

The successful determination of the sought-for observables is seriously dependent on the right choice of experimental method. In many cases, it is necessary to combine highly complex measurements to obtain the desired quantities. In this chapter, the theory of Coulomb excitation and its connection to nuclear observables, and the origin of the angular dependence of particle- γ and γ - γ correlations and their connection to the multipole-mixing ratio will be discussed briefly.

3.1. Coulomb Excitation

Since the 1950s, Coulomb excitation (CE) has been a well-established experimental technique to study a wide variety of stable isotopes [70] and its mathematical description has been documented in several review articles by Alder and Winther [71–73]. The continuous progress in accelerator science, the development of radioactive-ion beam facilities, and the constant evolution of instrumentation have never let CE go out-of-fashion. Especially, the projectile CE with high-resolution γ -ray detectors in combination with a high-efficiency particle detection is a powerful tool to face the obstacles of in-flight measurements. Using such an experimental set-up enables the deduction of information about the structure, e.g., the deformation, of exotic nuclei, which is in some cases hardly to access otherwise.

The basic principle of CE is the excitation of the target nucleus by the intrusion of the Coulomb field of a passing projectile and vice versa. The excitation process can be considered as a transfer of one or more virtual photons. The probability of CE increases with decreasing distance of both reaction partners. To prevent nuclear reactions, e.g., transfer and fusion reactions, the velocity v of the projectile has to be sufficiently low to hinder the penetration of the target nucleus by the projectile.

3.1.1. Semi-Classical Description

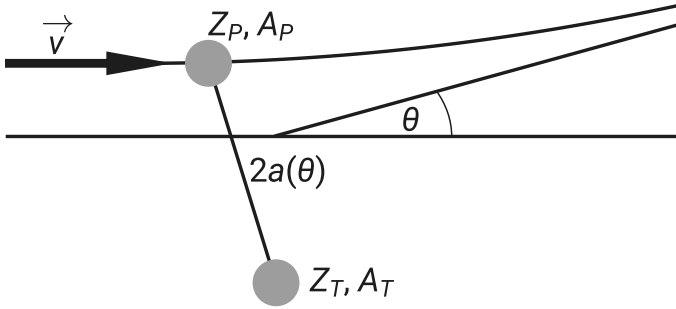


Figure 3.1.: The scattering process of a Coulomb excitation in a classical picture. $Z_{P,T}$ and $A_{P,T}$ are the proton and mass numbers of the projectile and target particles, respectively. $2a(\theta)$ is the smallest approach of both reaction partners depending on the scattering angle θ .

In the semi-classical approach of CE, the projectile is deflected by the electromagnetic force stemming from the interaction of the electric fields of the projectile and target. The classical trajectory of an elastic scattering, see Figure 3.1, is a good approximation of the semi-classical description when agreeing on two assumptions. Here, the scattering cross section of the classical trajectory of a heavy ion collision is described by the well-known Rutherford cross section

$$\left(\frac{d\sigma}{d\Omega}\right)_R = \frac{1}{4} \frac{a^2}{\sin^4(\theta/2)}, \quad (3.1)$$

with a being half of the smallest distance between the surfaces of the target and the projectile particle

$$a = \frac{Z_P Z_T e^2}{m_0 v}, \quad (3.2)$$

where v is the velocity of the projectile, Z_P and Z_T are the proton numbers of the projectile and the target, respectively, e is the elementary charge, and m_0 is the reduced mass.

The first assumption is, that the interaction of the reaction partners is purely electromagnetic and the nuclear force only contributes in a negligible way. This is achieved by ensuring a sufficiently large distance between the surfaces of the reaction partners, determined by the dimension-less Sommerfeld parameter η ,

$$\eta = \frac{2\pi a}{\lambda} = \frac{Z_P Z_T e^2}{\hbar v}, \quad (3.3)$$

where λ is the deBroglie wavelength. The second assumption is, that the energy loss of the projectile is small in comparison to the bombarding energy. This is measured through the adiabaticity parameter

$$\xi = \frac{a}{\hbar v} \Delta E, \quad (3.4)$$

where ΔE is the excitation energy. It has been proven that the semi-classical approach is a legitimate approximation for CE at low bombarding energies, if the conditions, $\eta \gg 1$ and $\xi \rightarrow 0$, are full-filled [73].

Furthermore, a good measure of restricting nuclear forces is the Coulomb barrier

$$V_C = \frac{1}{4\pi\epsilon_0} \frac{Z_P Z_T e^2}{d}, \quad (3.5)$$

where d is the distance between the centers of both reaction partners. The distance d is approximated by the sum of the radii of two spherical nuclei, while the radius is estimated to be

$$r \approx 1.2 \text{ fm} \times A^{1/3}, \quad (3.6)$$

where A is the nucleon number of the nucleus. A valid estimation for heavy ion collisions is Cline's "safe" CE criterion [74]. It says, if the distance between the surfaces of both reaction partners is greater than 5 fm, it is legitimate to neglect other forces besides CE. This leads to an upper limit for the kinetic energy of the projectile in the laboratory frame, given in MeV,

$$E_P[\text{MeV}] \leq 1.44 \times \left(1 + \frac{A_P}{A_T}\right) \frac{Z_P Z_T}{1.2 \times (A_P^{1/3} + A_T^{1/3}) + 5}. \quad (3.7)$$

In this framework, the CE cross section of a state $|n\rangle$ is determined by the Rutherford cross section and the excitation probability P_n

$$\left(\frac{d\sigma}{d\Omega}\right)_n = \left(\frac{d\sigma}{d\Omega}\right)_R P_n. \quad (3.8)$$

For the determination of the excitation probability P_n , a perturbation calculation has to be carried out. A simplified Schrödinger equation describes the state of one nucleus, either the projectile or the target, $|\psi(t)\rangle$:

$$i\hbar \frac{\partial}{\partial t} |\psi(t)\rangle = [H_0 + V(t)] |\psi(t)\rangle. \quad (3.9)$$

H_0 is the Hamiltonian of the free nucleus with its eigenstates $|n\rangle$ and the eigenvalues E_n , and $V(t)$ is the time-dependent external potential at the position of the nucleus. The electromagnetic interaction $V(t)$ can be written in terms of a multipole expansion,

$$V(t) = \sum_{\lambda, \mu} \frac{4\pi Z e}{2\lambda + 1} (-1)^\mu S_{E/M\lambda\mu} M_{E/M}(\lambda, \mu), \quad (3.10)$$

with the orbital integrals for electric and magnetic excitations,

$$S_{E\lambda\mu} = r(t)^{-\lambda-1} Y_{\lambda\mu}[\theta(t), \phi(t)], \quad (3.11)$$

$$S_{M\lambda\mu} = \frac{i}{\lambda} \frac{1}{r(t)^{\lambda+1}} \frac{\vec{r}(t) \cdot \hat{L}}{c} Y_{\lambda\mu}[\theta(t), \phi(t)]. \quad (3.12)$$

$\theta(t)$, $\Phi(t)$ and $r(t)$ are the coordinates and Z is the proton number of the nucleus, and $Y_{\lambda\mu}[\theta(t), \Phi(t)]$ denotes the spherical harmonics. λ denotes the multipolarity and μ its projection on the symmetry axis. $M_{E/M}(\lambda, \mu)$ are the multipole operators and are defined as

$$M_E(\lambda, \mu) = \int \rho(\vec{r}) r^\lambda Y_{\lambda\mu}[\theta(t), \phi(t)] \left(\frac{\vec{r}}{r}\right) d\vec{r}, \quad (3.13)$$

$$M_M(\lambda, \mu) = \frac{-i}{c(\lambda+1)} \int \vec{j}(\vec{r}) r^\lambda \hat{L} Y_{\lambda\mu}[\theta(t), \phi(t)] \left(\frac{\vec{r}}{r}\right) d\vec{r}. \quad (3.14)$$

Here, \hat{L} is the angular momentum operator and $\rho(\vec{r})$ is the charge density. From Eq. (3.9), the time-dependent excitation amplitude can be defined as

$$a_n(t) = \langle n | \psi \rangle e^{iE_n t / \hbar}. \quad (3.15)$$

Using the boundary condition where the nucleus is in its ground state at $t \rightarrow -\infty$, meaning $a(-\infty) = \delta_{0n}$, leads to the excitation probability of the state $|n\rangle$ from the initial state $|i\rangle$ with spin J_i

$$P_n = \frac{1}{2J_i + 1} \sum_{m_i, m_n} |a_n|^2, \quad (3.16)$$

where m_i and m_n are the magnetic sub states of $|i\rangle$ and $|n\rangle$, respectively. The Eqs. (3.15) and (3.9) lead to a set of coupled differential equations:

$$i\hbar \dot{a}_n(t) = \sum_n \langle n | V(t) | m \rangle e^{i(E_n - E_m)t/\hbar} a_m(t). \quad (3.17)$$

The whole CE process is defined by this set of coupled differential equations. Hence, solving these equations will deliver the cross sections of all Coulomb excited states of a nucleus in a given reaction. Pure one-step excitations are often reasonable estimations for, e.g., 2^+ and 3^- states. However, for a detailed examination, higher order excitations, especially two-step excitations, can't be neglected. For one-step excitations, the CE cross sections of certain states are given by

$$\sigma_{E\lambda} = \left(\frac{Ze}{\hbar v} \right)^2 a^{-2\lambda+2} B(E\lambda) f_{E\lambda}(\xi), \quad (3.18)$$

$$\sigma_{M\lambda} = \left(\frac{Ze}{\hbar c} \right)^2 a^{-2\lambda+2} B(M\lambda) f_{M\lambda}(\xi), \quad (3.19)$$

where a is again half the distance of the closest approach and the functions $f_{E/M\lambda}(\xi)$ are listed in Ref. [71]. The $B(E/M\lambda)$ values are the reduced transition probabilities for electric and magnetic transitions. They are defined by the multipole operators and the corresponding states

$$\begin{aligned}
B(E/M\lambda; J_i \rightarrow J_n) &= \sum_{\mu, m_n} |\langle J_n m_n | M_{E/M}(\mu, \lambda) | J_i m_i \rangle|^2 \\
&= \frac{1}{2J_i + 1} |\langle J_n || M_{E/M}(\lambda) || J_i \rangle|^2.
\end{aligned} \tag{3.20}$$

The cross section decreases rapidly, approximately two orders of magnitude, with an increasing multipolarity. A theoretical example is shown in Figure 3.2. From the Eqs. (3.18) and (3.19), it is shown, that the magnetic excitations are suppressed by a factor of β^2 , which is also visible in Figure 3.2. Hence, it is negligible for low-energy CE which is subject of this thesis. Consequently, the excitation paths are predominantly $E2$ transitions and, with a significantly smaller influence, $E3$ transitions. Thus, CE is the ideal method to investigate collective quadrupole and octupole states. In despite of the plots of Figure 3.2, $E1$ transitions do not play a role in CE. The $E1$ transition matrix elements are usually some orders of magnitudes smaller on a single-particle scale than the $E2$ and $E3$ ones and, thus, negligible. Although the cross section of a $E1$ excitation with a comparable matrix element might be significantly enhanced in comparison to higher multiplicities.

A significant role in the excitation process is played by multi-step excitations, especially two-step excitations. Two-phonon states, i.e., the 2_2^+ and especially the 4_1^+ states, are even predominantly populated in a two-step path. Furthermore, multi-step excitation plays also a role for one step-excitations as the 2_1^+ state. Here, the “reorientation effect” [73], where a transition between the different magnetic sub states takes place, is present and is seen as a two-step excitation. This effect is dependent on the static quadrupole moment of this state. Hence, the diagonal $E2$ matrix element, which is proportional to the static quadrupole moment, may be crucial for the state’s excitation process.

All kind of multi-step excitations are taken into account by the here used CE calculation codes, GOSIA and CLX. If a state is predominantly excited via a certain excitation path, the sign of the matrix element $\langle J_n || M_{E/M}(\lambda) || J_i \rangle$ does hardly effect the state’s population yield. However, when two different excitation paths contribute relevantly to the population of a state, the relative sign decides whether the two excitation probabilities interfere constructively (+) or destructively (–). In these cases, the relative sign highly affects the CE population yields.

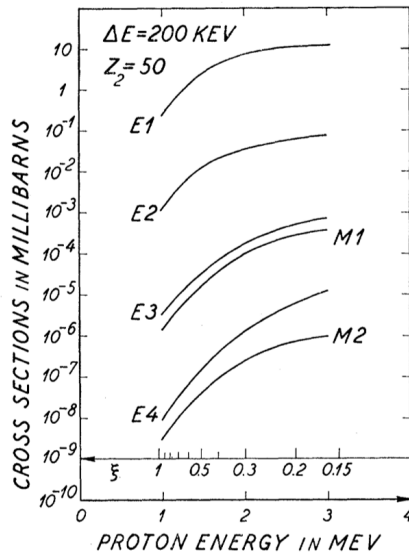


Figure 3.2.: Theoretical cross sections of CE of transitions with different multipolarities and a transition probability of 1 W.u.. The projectile, a proton, impinged on a Sn target with bombarding energies from 1 to 3 MeV. Reprinted figure with permission from Ref. [71].

3.1.2. Connection to Nuclear Structure

The wave function of the excited state provides the desired information about its structure, which is not directly measurable. However, the overlap of wave functions of two states is given by the transition matrix element connecting these two states. The transition matrix elements have a decisive influence on the CE process, which was outlined in Section 3.1, as well as they dictate the de-excitation process via a γ -ray decay.

Here, the access to nuclear structure variables is the decay of the Coulomb-excited states via γ -ray emission. The energy difference of the initial and the final state is equal to the γ -ray energy E_γ . The γ -ray energies and the intensities of γ rays are recorded by γ -ray spectrometers, which are most commonly position sensitive, hence, the emission angles of the γ rays are also measured. Finally, the CE theory links the measurable γ -ray properties to the sought-for transition matrix elements. The decay and the excitation of nuclear states via electromagnetic transition underlie the electro-magnetical transition selection rules

$$\left| J_i^{\pi_i} - J_f^{\pi_f} \right| \leq \lambda \leq J_i^{\pi_i} + J_f^{\pi_f} \quad (3.21)$$

$$\pi_\gamma = \pi_i \pi_f = \begin{cases} (-1)^\lambda & \text{for electric transitions} \\ (-1)^{\lambda+1} & \text{for magnetic transitions,} \end{cases} \quad (3.22)$$

where $J_i^{\pi_i}$, π_i , and $J_f^{\pi_f}$, π_f are the spins and the parities of the initial and the final state, respectively. λ and π_γ are the transition's multipolarity and parity, respectively. The previous equations show, that the nature and multipolarity of a transition is rarely restricted to one possible combination. Transitions, where states with spin $J = 0$ are involved, are exceptions and exhibit an unmixed character. Otherwise, the multipole-mixing ratio δ defines the multipole composition of a transition,

$$\delta^2 = \frac{\Gamma_i(\lambda + 1)}{\Gamma_i(\lambda)}, \quad (3.23)$$

where Γ_i is the partial width of the transition i . The partial widths Γ_i are proportional to the observed γ -ray intensities. The sum of the partial widths of transitions from a state is the natural line width, which is directly connected to the lifetime τ of the excited state

$$\Gamma = \sum_i \Gamma_i \text{ and} \quad (3.24)$$

$$\Gamma = \frac{\hbar}{\tau}. \quad (3.25)$$

The partial widths, on the other hand, are defined by nuclear structure properties, notably the sought-for reduced transition strengths:

$$\Gamma_i(\sigma\lambda) = 8\pi \frac{\lambda + 1}{\lambda [(2\lambda + 1)!!]^2} \left(\frac{E_\gamma}{\hbar c} \right)^{2\lambda+1} \times B(\sigma\lambda; J_i - J_f)_\downarrow, \quad (3.26)$$

the equation is in Gaussian units and its constant factor in front changes to $2/(\epsilon_0 \hbar)$, if it is expressed in SI units [75]. It is useful to merge the parameter which are only dependent on the multipolarity and whether it is an electric or magnetic transition. This leads to the following equations [75]

$$\Gamma(E\lambda) = 5.498 \times 10^{22} \times f(\lambda) \left(\frac{E_\gamma [\text{MeV}]}{197.33} \right)^{2\lambda+1} \times B(E\lambda)_\downarrow [e^2 \text{fm}^{2\lambda}] \frac{1}{\text{s}}, \quad (3.27)$$

$$\Gamma(M\lambda) = 6.080 \times 10^{20} \times f(\lambda) \left(\frac{E_\gamma [\text{MeV}]}{197.33} \right)^{2\lambda+1} \times B(M\lambda)_\downarrow [(\mu_N/c)^2 \text{fm}^{2\lambda-2}] \frac{1}{\text{s}}, \quad (3.28)$$

$$f(\lambda) = \frac{\lambda + 1}{\lambda [(2\lambda + 1)!!]^2}. \quad (3.29)$$

The relation $\hbar c = 197.33 \text{ MeV fm}$ was used for the simplification of the equations for $\Gamma(\sigma\lambda)$. The absolute transition strength $B(\sigma\lambda)$ is given in $e^2 \text{fm}^{2\lambda}$ and $(\mu_N/c)^2$ for $E\lambda$ and $M1$ transitions, respectively. Here, Gaussian units are commonly used, therefore the $B(M1)$ strength is often given in μ_N^2 . A different way to present reduced transition strengths, especially $B(E\lambda)$, is the single-particle unit, Weisskopf unit (W.u.). One W.u. is an estimate for an excitation, where only one nucleon is involved. The transition strength $B(E\lambda) \gg 1 \text{ W.u.}$, thus, indicates a participation of many nucleons in that particular excitation. Consequently, the presentation of a reduced transition probability in W.u. is a measure of the

collectivity of this excited state. The conversion into W.u. for electric transitions is dependent on the mass number of the nucleus [75] and given by

$$B_W(E\lambda) = \frac{1.2^{2\lambda}}{4\pi} \times \left(\frac{3}{\lambda + 3} \right)^2 A^{2\lambda/3} e^2 \text{fm}^{2\lambda}. \quad (3.30)$$

3.2. Angular Correlations of γ Rays

The angular intensity distribution of the γ -ray emission of a certain transition exhibits information about the angular momenta and the multiplicities of the transition. The extraction of this information will be introduced on the basis of Refs. [76, 77]. Two specific cases will be discussed. The angular distributions of a particle- γ coincidence after CE and of a γ - γ coincidence after β^+/ϵ decay.

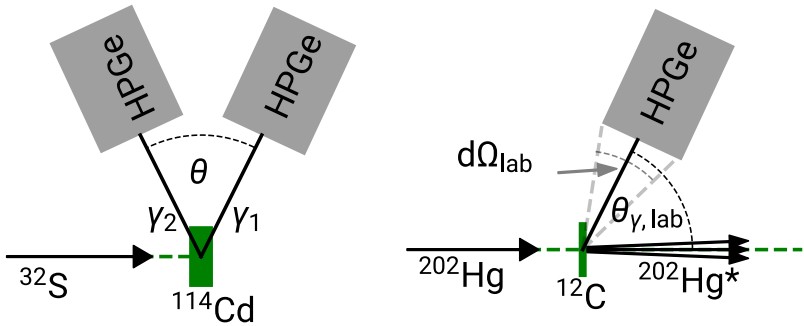


Figure 3.3.: Two scenarios of measuring angular distributions of γ - γ (left) and of particle- γ (right) coincidences. For more information, see text.

In the case of the projectile CE using Gammasphere for the detection of γ rays, the angular distribution was determined by ring-wise measurements of the γ -ray intensities. The detectors of a ring share the same polar angle with respect to the beam axis. A schematic drawing of the situation describes the angles in laboratory frame, see Figure 3.3. Due to the beam velocity of approximately 10 % of the speed of light in the reported experiments, relativistic effects have to be taken into account. So, it is necessary to transform the laboratory angle of the γ -ray emission $\theta_{\gamma, \text{lab}}$ to the frame of the emitting nucleus $\theta_{\gamma, \text{nuc}}$. This transformation is given by

[78]

$$\cos \theta_{\gamma,\text{nuc}} = \frac{\cos \theta_{\gamma,\text{lab}} - \beta}{1 - \beta \cos \theta_{\gamma,\text{lab}}}. \quad (3.31)$$

The so-called Lorentz boost also effects the solid angle of the detectors. In the frame of the nucleus, the detectors in forward angles appear to be bigger and the ones in backwards angles to be smaller. This directly effects the intensities measured in a detector, because the intensities are proportional to the solid angle of the detector. The transformation is given by [78]

$$d\Omega_{\text{nuc}} = \frac{(1 + \beta \cos \theta_{\gamma,\text{nuc}})^2}{1 - \beta^2} d\Omega_{\text{lab}}, \quad (3.32)$$

where $d\Omega_{\text{nuc}}$ and $d\Omega_{\text{lab}}$ are the solid angles in the frame of the nucleus and of the laboratory, respectively.

The statistical ensemble of oriented nuclear levels promoted via Coulomb excitation is axially symmetric with respect to the beam axis, if the outgoing nucleus is not detected [76]. These conditions lead to a population of the magnetic sub-states of the initial states with the angular momentum J_i described by the statistical tensor $\rho_k(J_i)$. The statistical tensor is directly correlated to the statistical angular distribution of the γ -ray emission of the $J_i \rightarrow J_f$ transition. The angular distribution is given by [77]

$$W(\theta) = \sum_k A_k P_k(\cos \theta). \quad (3.33)$$

For an aligned ensemble of states, e.g., axially symmetric oriented, where the population of a magnetic sub state is equal to its negative counterpart, the equation simplifies to

$$W(\theta) = A_0 [1 + a_2 P_2(\cos \theta) + a_4 P_4(\cos \theta)], \quad (3.34)$$

where $P_{2,4}$ are Legendre polynomials, the coefficients $a_k = A_k/A_0$ cover the angular momentum coupling, and A_0 is a normalization factor. The coefficients

a_k are given by [77]

$$a_k = \rho_k(J_i) \alpha_k(\delta, J_f L L' J_i) \quad \text{with} \quad (3.35)$$

$$\alpha_k(\delta J_f L L' J_i) = \frac{1}{1 + \delta^2} [F_k(J_f L L' J_i) + 2\delta F_k(J_f L L' J_i) + \delta^2 F_k(J_f L' L' J_i)] \quad (3.36)$$

with

$$F_k(J_f L L' J_i) = (-1)^{J_f - J_i - 1} \sqrt{(2L + 1)(2L' + 1)(2J_i + 1)} \times \underbrace{\begin{pmatrix} L & L' & k \\ 1 & -1 & 0 \end{pmatrix}}_{\text{Clebsch-Gordan}} \underbrace{W(J_i J_f L L'; k J_f)}_{\text{Racah}}. \quad (3.37)$$

Here, L and L' are the multipolarities of the mixed transition, i.e., $L = 1$ for $M1$ and $L' = 2$ for $E2$, and δ is the multipole-mixing ratio given by

$$\delta = \frac{\langle J_f || M_{E/M}(L') || J_i \rangle}{\langle J_f || M_{E/M}(L) || J_i \rangle}, \quad (3.38)$$

where $\langle J_f || M_{E/M}(L/L') || J_i \rangle$ are the transition matrix elements from Eq. (3.20). The multipole-mixing ratio δ measures the mixture of the transition $J_i \rightarrow J_f$. It is obvious from Eq. (3.36), that the coefficients a_k simplify if $J_i \rightarrow J_f$ is a pure transition ($\delta = 0$):

$$a_k = \rho_k(J_i) F_k(J_f L L J_i) \quad (3.39)$$

This happens if a state $J = 0$ is involved in the investigated transition, e.g., a ground state for an even-even nucleus $J_f = 0^+$. Then the statistical tensor $\rho_k(J_i)$ can be obtained from the angular distribution of the ground state transition $J_i \rightarrow 0_1^+$. If the ground state transition is not observed, an iterative method can be applied to determine the statistical tensor, this method was utilised in various publications, e.g., Refs. [48, 50]. The coefficients a_k can be determined by the angular distribution of the intensity of the $J_i \rightarrow J_f$ transition. The combination of the coefficients a_k and the statistical tensor leads ultimately to the multipole-mixing ratio δ .

In the case of the angular distribution of the γ -ray emission after a β/ϵ decay, there are a few differences how to obtain the multipole-mixing ratio. For the

unoriented β/ϵ decays, the ion beam axis can't be used as the quantization axis. However, the detection of a first γ ray serves as quantization axis. Then, the detection of a second coincident γ ray can be used to determine the angular distribution of this γ - γ coincidence. Therefore, θ is in the following not longer meant to be the polar angle between the beam axis and the γ -ray emission, but the angle between two γ -ray emissions of a coincidence event, see Figure 3.3. In this case, Eq. (3.34) is also used to obtain the coefficients a_k , but they are now defined slightly different:

$$a_k = \alpha_k(J_{\text{int}}\delta_1 L_1 L'_1 J_i) B_k(\delta_2 J_f L_2 L'_2 J_{\text{int}}). \quad (3.40)$$

The equation corresponds to the γ - γ cascade $J_i \xrightarrow{\delta_1} J_{\text{int}} \xrightarrow{\delta_2} J_f$. The coefficients α_k are given by Eq. (3.36) and B_k is given by [76]

$$B_k(\delta J_f L L' J_i) = \frac{1}{1 + \delta^2} [F_k(J_f L L' J_i) + (-1)^{L+L'} 2\delta F_k(J_f L L' J_i) + \delta^2 F_k(J_f L' L' J_i)], \quad (3.41)$$

where the coefficients F_k are determined by Eq. (3.37) and are also tabulated in Ref. [77] for several combinations of angular momenta.

4. Experiments

The four performed or planned experiments have different requirements on the beam-producing facilities. The projectile CE of ^{202}Hg was performed at the Argonne Tandem Linac Accelerator System (ATLAS) facility at the Argonne National Laboratory (ANL), with the 4π high-purity germanium (HPGe) array Gammasphere [49]. The extreme-inverse kinematics experiment, where the mass of the projectile is much greater than the one of the target particle, could be processed without particle detection, which is often the limiting factor of the beam current. The projectile CE experiments of the radioactive $N = 80$ isotones, ^{140}Nd and

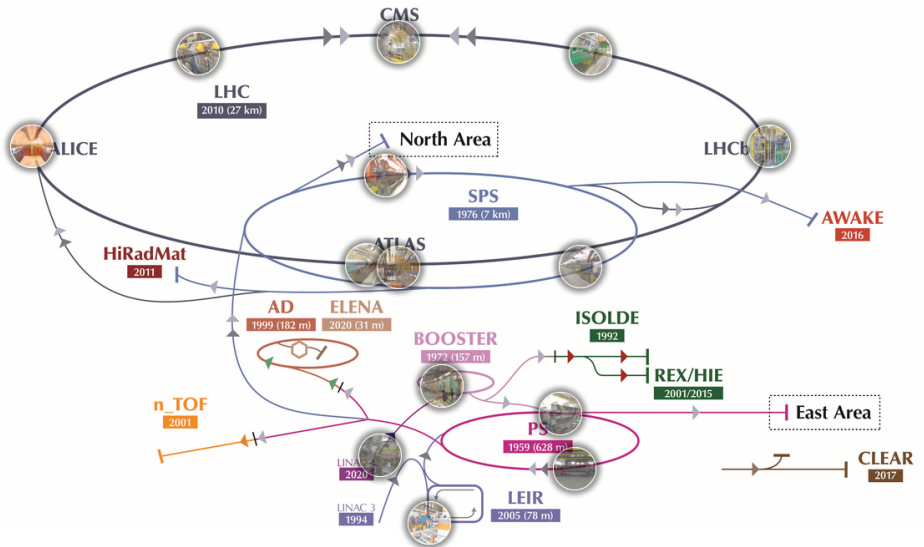


Figure 4.1.: Overview of the beam lines of CERN [79].

^{142}Sm , were challenging in terms of the isotope production and the necessary post acceleration up to $\approx 4.5 A \cdot \text{MeV}$. After the upgrade from REX- to HIE-ISOLDE, the radioactive-ion beam facility at CERN with the six-fold segmented HPGe array Miniball [23] was capable to face these challenges. The γ -ray spectroscopy of ^{142}Sm after β^+/ϵ decay was designed with a ^{32}S beam with an energy of $\approx 4.7 A \cdot \text{MeV}$. The Warsaw Cyclotron at the Heavy Ion Laboratory provides the requested beam energy with the necessary high resolution HPGe array EAGLE (European Array for Gamma Levels Evaluation) [80] belonging to the local experimental setup. An overview of all experiments and their durations are shown in Table 4.1.

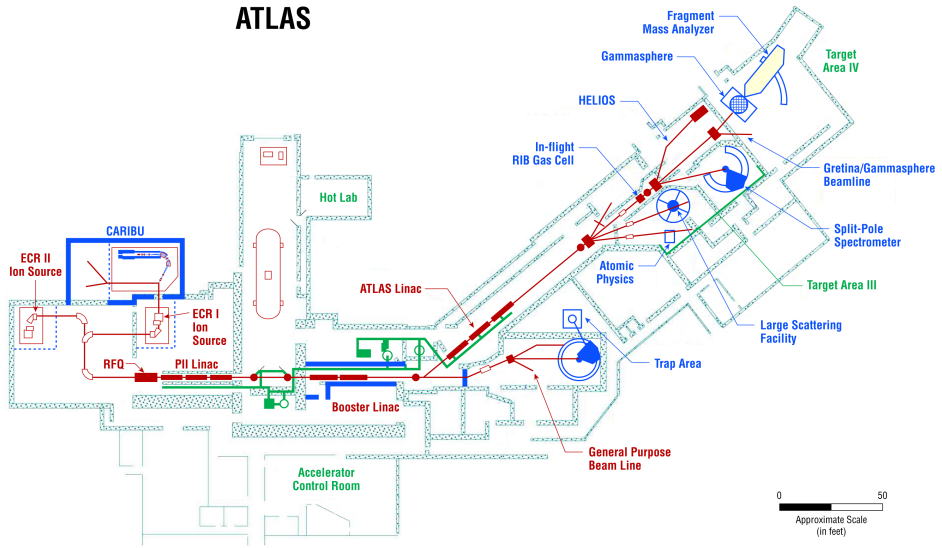


Figure 4.2.: Floorplan of the beam lines of the ATLAS facility [81] at the Argonne National Laboratory (USA).

Table 4.1.: An overview of the reported experiments with the utilized reaction processes. CE, FE and II are abbreviations for Coulomb excitation, fusion evaporation and investigated isotope, respectively.

Facility	Beam	Target	Beam energy	Reaction	II	Duration
HIE-ISOLDE	^{140}Nd	^{208}Pb	$4.62 A \cdot \text{MeV}$	CE	^{140}Nd	1 day
HIE-ISOLDE	^{142}Sm	^{208}Pb	$4.62 A \cdot \text{MeV}$	CE	^{142}Sm	5 days
ATLAS	^{202}Hg	^{12}C	$4.4 A \cdot \text{MeV}$	CE	^{202}Hg	20 h
HIL	^{32}S	^{114}Cd	$4.7 A \cdot \text{MeV}$	FE	^{142}Sm	10 days ^a

^aPlanned and accepted.

4.1. Coulomb Excitation of ^{140}Nd and ^{142}Sm at HIE-ISOLDE Using Miniball

Two of the reported projectile-CE experiments were performed at the radioactive-ion beam (RIB) facility ISOLDE [82, 83], which is part of CERN, see Figure 4.1. The ISOLDE facility is provided with 1.4 GeV protons from the PS Booster. The high-energy protons impinged on a thick tantalum production target, which was embedded in a hot surface ion source. The proton-induced spallation, fusion and fission in the target produced a large variety of neutrally charged isotopes. The isotopes were subsequently ionized at the hot surface (up to 2400°C) of the transfer line of the ion source. The material of the transfer line had to be more likely to absorb an electron than the newly-produced atoms were. The ionization properties of the ion source could be varied by adjusting the temperature. The Resonance Ionization Laser Ion Source (RILIS) [84] was additionally used to improve the selectivity of the ionization process. RILIS ionizes atoms by exciting electrons of a certain element in a multi-step process by using an element specific customized laser scheme, see Figure 4.3. Consequently, the ratio of the desired element to all other ions was increased. The extracted ions with a kinetic energy of 30 keV were led to the General Purpose Separator (GPS), a one-dipole-magnet mass separator. Afterwards, the beam is cooled, accumulated and bunched in REXTRAP [86]. The trapped bunch of ions was transferred to REXEBIS [87]. REXEBIS uses a strongly focused electron beam to increase the charge state of the trapped ions

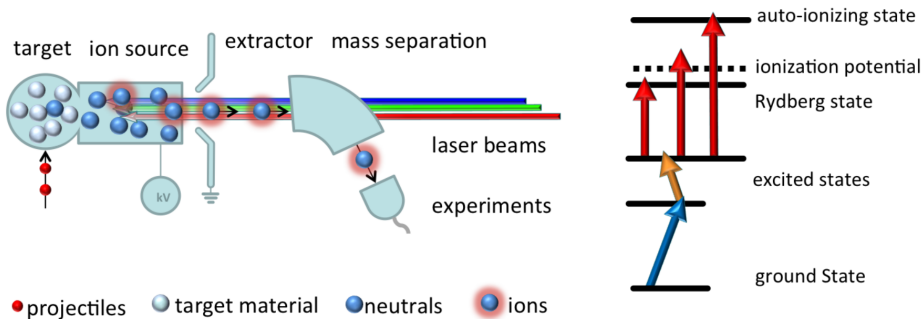


Figure 4.3.: A schematic drawing of the functionality of RILIS in combination with the hot surface ion source. The figure is adopted from Ref. [85] and modified.

to a higher charge-state. The favoured charge-state was, then, selected by the following mass-over-charge separator, see Figure 4.4.

Since the energy and resolution upgrade from REX- to HIE-ISOLDE, the ions can be post-accelerated up to $10 A \cdot \text{MeV}$. The post-accelerated ions were led to the Miniball experimental station [23]. At that time, Miniball consisted of 24 sixfold-segmented high-purity germanium (HPGe) detectors arranged to eight triple clusters on a variable spherical detector frame. The positions of the clusters during the experiments are listed in Table 4.2. The segmentation of the HPGe crystals was used to improve the correction for the Doppler shift of the γ -ray energies. The Miniball clusters are focused onto the target chamber, where a target wheel and a particle detector were mounted. The following targets were mounted on the wheel, a 2.5 mg/cm^2 -thick ^{208}Pb foil, a 3 mg/cm^2 -thick ^{92}Mo foil, a stopper foil, a small and a big hole for the tuning of the ion beam, and a 1.5 mg/cm^2 -thick ^{208}Pb foil. The latter one was used for both CE experiments. The mentioned particle detector was a double-sided silicon strip detector (DSSD), which was placed in forward direction in respect to the beam axis. The DSSD is segmented in four quadrants, each quadrant is divided in 16 rings at the front side and 24 stripes at the back side. Technical details are shown in Figure 4.5 and a detailed description is found in Ref. [89].

After the post-acceleration in the REX- and HIE-cavities, the ^{140}Nd and ^{142}Sm

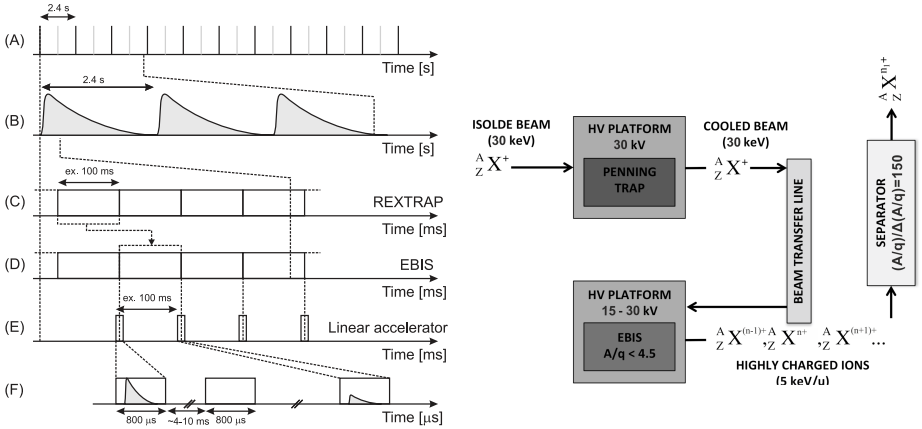


Figure 4.4.: Left: the time structure from the proton bunches from the PS-Booster (A) to the timing of the beam at the linear accelerator (F). Right: the schematic layout of the charge breeding and bunching components at REX-ISOLDE. The figures are adopted from [88] and modified.

ions impinged with an kinetic energy of $4.62 A \cdot \text{MeV}$, meaning approximately eight percent of the speed of light, on the $1.5 \text{ mg/cm}^2 \text{ }^{208}\text{Pb}$ target. The energy was chosen sufficiently low, 76 % and 74 % of the Coulomb barrier of ^{208}Pb with ^{140}Nd and ^{142}Sm , respectively, to ensure “safe” CE [74].

4.1.1. Data Preparation

The calibration and the data acquisition were conducted analogously for both reported CE experiments at HIE-ISOLDE. The sorting code MiniballCoulexSort [90] was used to build the particle- γ and particle- γ - γ events. For the energy and the efficiency calibration of the HPGe detectors, radioactive sources of ^{133}Ba , ^{152}Eu and ^{66}Ga were used. The combination of these sources enables a calibration of Miniball for γ -ray energies from 40 keV up to 5 MeV. The γ -ray energies and intensities of the γ -ray transitions were taken from Ref. [91] and denoted in Table A.1.

The energy calibration was done for every detector separately, by applying second

Table 4.2.: The parameters of the Miniball clusters during the reported experiments. The scattering angle θ describes the angle of the center of the cluster in respect to the beam axis. ϕ is the azimuthal angle and α is a intrinsic rotation of the cluster. r is the distance between the center of the cluster's surface and the target.

#	θ	ϕ	α	r
0	135.05°	125.75°	319.50°	102.62 mm
1	50.15°	56.85°	52.75°	105.70 mm
2	44.35°	132.87°	300.75°	104.25 mm
3	136.45°	55.79°	245.75°	104.20 mm
4	134.50°	236.50°	292.25°	99.99 mm
5	43.35°	233.35°	238.94°	107.04 mm
6	136.15°	312.01°	78.85°	109.15 mm
7	42.85°	315.44°	121.85°	113.94 mm

degree polynomials to the raw γ -ray energies. Although the Miniball detectors are segmented, it is common to use the core signal of the crystal for the γ -ray energy with addback, while the segment signal with the highest energy serves for the position determination. Addback means here, that the deposited energy of a neighboring crystal is added to the deposited energy of the initial crystal, if this scenario happened in a short time gate. Consequently, the energy of a detected photon could be reconstructed correctly even though it did not deposit its whole energy in one crystal.

The photo-peak efficiency of a γ -ray detector is the ratio of the amount of γ -rays of a certain energy which deposit their complete energy in the detector to the total number of these γ -rays hitting the detector. The γ -rays of the used radioactive sources, see Table A.1, are taken to determine the efficiency I_γ/I_{eff} , where I_γ is the summarised intensity of the whole Miniball array of a certain transition and I_{eff} is its known intensity relative to the activity of the source. The activities of the three sources, ^{133}Ba , ^{152}Eu and ^{66}Ga , were partly unknown, so it was necessary to scale the experimental efficiencies of each source by a constant factor to compensate the different activities and durations of the source measurements.

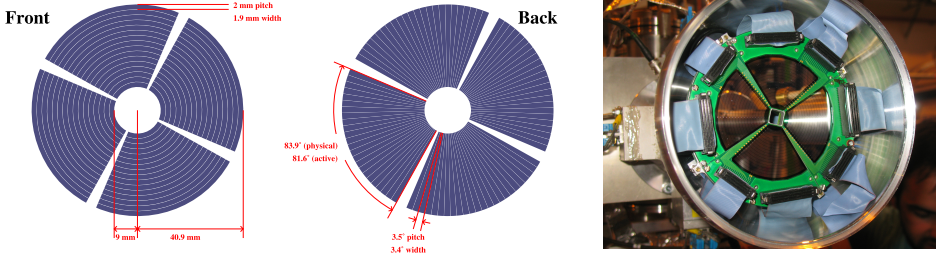


Figure 4.5.: Left: a schematic drawing of the DSSD including the associated distances and angles. Right: a photograph of the DSSD mounted in the target chamber. Both pictures are adopted from Ref. [89].

The phenomenological energy-dependent function,

$$\epsilon(E_\gamma) = a \times e^{-b \ln(E_\gamma - c + d e^{e E_\gamma})}, \quad (4.1)$$

was fitted to the combined data set. The resulting relative efficiency of Miniball with its one- σ band is shown in Figure 4.6. The relative efficiency is sufficient for the performed CE measurements, because the calculations are relative to the $2_1^+ \rightarrow 0_1^+$ transition of the investigated nucleus. The DSSD was used for the heavy particle detection and was mounted 21.5 cm downstream from the target. This placement led to a total coverage of the DSSD from 23.5° to 63° in the laboratory frame in respect to the beam axis regarding the target. The scattered heavy particles, beam and target like, hit the DSSD and deposited kinetic energy in the silicon layers. This energy loss ΔE is proportional to the incoming kinetic energy and was recorded by the DSSD. The energy and local resolution of the DSSD enabled to differentiate between three types of particles by their deposited energy in dependence of the scattering angles, see Figure 4.8 d). The energy of stripes and rings of the DSSD were not calibrated with an external source, but with the calculated energy of the scattered particles of the CE reaction. The time difference of a DSSD hit and a hit of a γ ray in a Miniball detector shows a pronounced peak due to the pulsed nature of the beam, see Figure 4.7. This time structure is used to reduce the random-time background by setting a prompt and a random gate. The events inside the prompt gate are good events coming from the beam, while the events outside this time gate do not have any correlation to the beam and are seen as random. The random, non-beam related γ rays have their source in activated

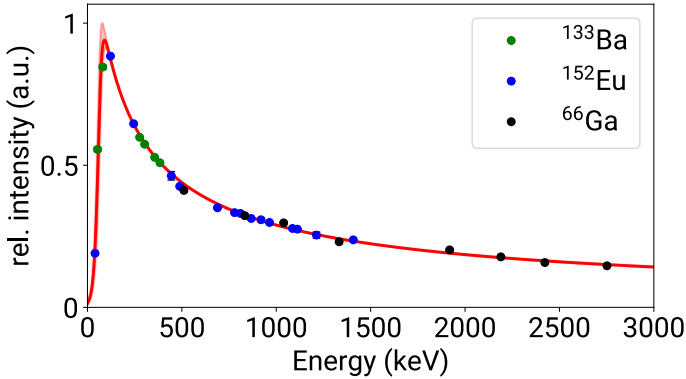


Figure 4.6.: The relative efficiency of Miniball was determined by using three different calibration sources ^{133}Ba (green), ^{152}Eu (blue) and ^{66}Ga (red). The best fit of the function (4.1) to the data set is shown in red with its one- σ band. The absolute efficiency of Miniball in this configuration is 7.8 % at 1.3 MeV [23].

material or are natural radioactivity. These are subtracted with a scaling factor, which depends on the ratio of the width of the background gate to the width of the prompt gate.

In Figure 4.8 a), the kinematic calculations of two possible scattering reactions are presented, the planned CE of $^{140}\text{Nd}(^{208}\text{Pb}, ^{208}\text{Pb}^*)^{140}\text{Nd}^*$ at $4.62 \text{ A} \cdot \text{MeV}$ on a 1.5 mg/cm^2 -thick lead target and the elastic scattering of the ^{140}Nd ions at $4.62 \text{ A} \cdot \text{MeV}$ impinging on a 0.1 mg/cm^2 -thick oxygen layer are shown. The energy losses in the targets were determined by using Atima [92] and are dependent on the total kinetic energy E and the neutron and proton numbers of the beam and target particles.

Comparing the experimental results with the kinematic calculations, one can clearly identify the beam-like, mainly ^{140}Nd , and the target-like, ^{208}Pb , particles. An appearance at lower energies was more challenging to identify. The energy spread is significantly smaller, which points to a thin contamination of the target. A thinner material means less energy loss of the beam particles in the target, which results in a smaller energy spread of the outgoing beam and target particles. The

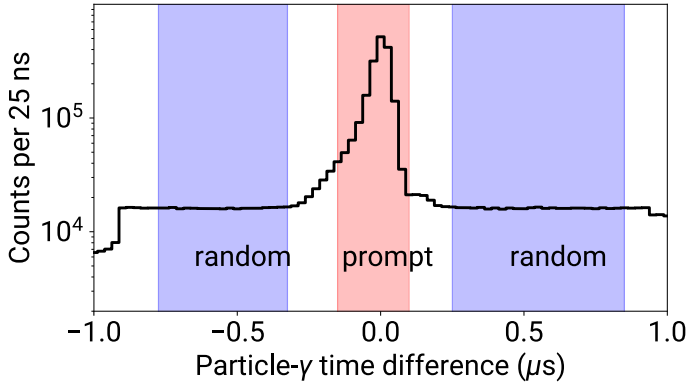


Figure 4.7.: The time difference spectrum of γ -ray hits in Miniball in respect to the corresponding particle hits on the DSSD. The origin of the x axis was shifted to the peak of prompt particles.

assumption of a thin target contamination is supported by looking at the coinciding γ rays of the associated excited beam particles, whose energy is rightly corrected for the Doppler shift by assuming them as target-like particles. Furthermore, the kinematic calculations of the reaction of ^{140}Nd on a thin ^{16}O layer, 0.1 mg/cm^2 , showed a similar behaviour, see Figure 4.8. However, the decrease of the particle energies at the inner rings was probably caused by difficulties of the energy calibration at low energies for the damaged ring segments. Nevertheless, another light target contamination, like ^{12}C , could not be excluded, because there are no γ rays of the target particles visible, which is again an argument for ^{16}O or ^{12}C , whose first excited states are at such high energies, that no population would be expected with this beam energy. Also, no corresponding beam-like reaction partners of the thin contamination are detected by the DSSD. That also suits the suspicion of ^{16}O or ^{12}C , because they would be scattered in extreme forward direction ($< 10^\circ$) due to inverse kinematics and, consequently, would not hit the DSSD. The received information of the scattering process from the DSSD was used to set three separate gates, where the target- and beam-like particles are expected, see Figure 4.8 d). Two different types of events for the target detection had to be taken in consideration, one- and two-particle hits. Regarding the two-particle hits, when

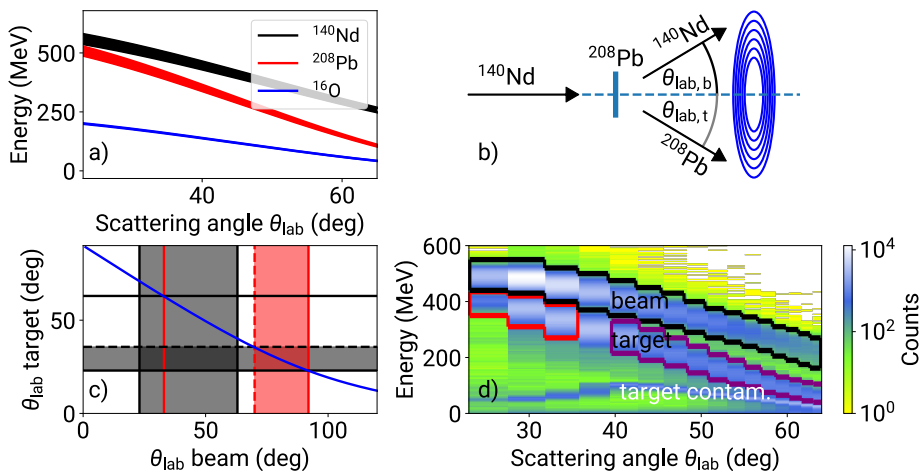


Figure 4.8.: a) presents the calculations of the reaction kinematic of the ^{140}Nd CE experiment. b) shows an exemplary scattering process to introduce the general setting. c) presents the co-dependency of the scattering angles of both reaction partners, target- and beam-like particles (blue) and the corresponding scattering angles of the particle gates (red and black fields). d) shows the experimental particle energies in dependence of the scattering angle measured by the DSSD. Three different particle types can be separated. The used gates for the particle- γ coincidences are marked. For more information, see text.

a particle is inside the beam gate and the reaction partner could be expected in the target-two-hits gate, marked in purple in Figure 4.8 d). All of the two-particle events, where both gates were hit, were solely added to the beam-gated events to avoid double counting.

There are two scenarios, where one-hit events happen. The first case, when one reaction partner is scattered outside the range of the DSSD and the second case, where a potential two-hit event may end up as a one-hit. The latter case happens, when only one of the reaction partners makes it properly to the DSSD, while the other one is doubly scattered or hits a dead part of the DSSD, for instance the separator between the ring segments of the DSSD.

Regarding one-hit events, the beam gate remained the same, because there are also two-hit events included. However, the target-gate had to be restricted, that only real one-hit events are kinematically possible to avoid the corruption by one hit-events which are potential two-hit events. The resulting target-one-hit gate is marked in red in Figure 4.8 d).

In Figure 4.8 c), the vertical and horizontal black lines mark the scattering angles for the beam and target particles, respectively, corresponding to the boundaries of the DSSD. The dashed black line represents the changed boundary due to the modified target-one-hit gate. The red vertical lines mark the scattering angles of the beam particles, which correspond to the target-one-hit gate. There is not any overlap between the scattering angles of the beam particles of the beam gate (black field) and of the modified target one-hit gate (red field) due to the restrictions of the target-one-hit gate, see Figure 4.8 c).

The in-flight emission of γ rays causes the Doppler-shift of the γ -ray energies,

$$E_{\gamma} = \frac{1 - \cos \theta_{p,\gamma}}{\sqrt{1 - \beta^2}} E_{D,\gamma}. \quad (4.2)$$

The shift is dependent on the velocity of the emitting ion β and on the angle between the ion and the γ ray, $\theta_{p,\gamma}$. The emission angle is determined by the distance between target and the DSSD, and the Miniball geometry (see Table 4.2) in respect to the target position. The Miniball geometry is pre-calibrated, but the fine adjustments are done by varying the parameters until the Doppler-shift corrections are optimized for the $2_1^+ \rightarrow 0_1^+$ transition, meaning its width in the preliminary γ -ray spectrum is minimized. The velocity, or energy, of the beam particles hitting the target is well known, but the velocity at the moment of the γ -ray emission can't be measured. Hence, a velocity has to be assumed by taking the energy loss in the target into account by using SRIM [93]. This leads to a non-resolvable uncertainty of the beam-particle's velocity at the emission which increases with the thickness of the target material, and is dependent on the length of the path the beam particles are taking through the target.

The data preparation for the $^{142}\text{Sm}(^{208}\text{Pb}, ^{208}\text{Pb}^*)^{142}\text{Sm}^*$ experiment was done analogously and the corresponding graphics are shown in Figure A.1.

4.1.2. γ -Ray Spectroscopy of ^{140}Nd

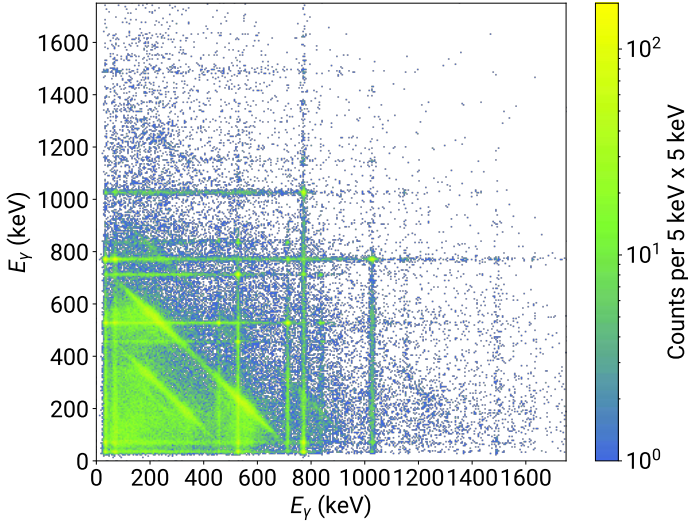


Figure 4.9.: The E_γ - E_γ matrix of the ^{140}Nd CE experiment with the conditions of the detection of at least one particle on the DSSD inside the beam energy gate and of more than one γ ray in Miniball inside the prompt time gate. The spectrum is mirrored at the E_γ - E_γ axis for visibility.

The ^{140}Nd CE experiment was separated in two sub experiments, the beam-particles and target-particles gated spectra. For both sub experiments a particle- γ (p - γ) spectrum and p - γ - γ coincidences spectra were produced. Two p - γ - γ spectra for each sub experiment were sorted by setting γ -energy gates on the $2_1^+ \rightarrow 0_1^+$ and $4_1^+ \rightarrow 2_1^+$ transitions in the E_γ - E_γ matrices (see Figure 4.9 for the beam-gated and Figure A.2 for the target-gated data). The matrices were filled with events, if a particle hit on the DSSD is coincident with two or more γ -ray hits on Miniball inside the prompt gate (see Figure 4.7). The visible lines orthogonal to the $E_\gamma = E_\gamma$ axis are Compton-scattering events. The γ -ray spectra of both sub experiments were Doppler-shift corrected for the scattered beam particles. The following section concentrates on the beam-gated spectra. The procedure was

performed analogously for the target-gated spectra.

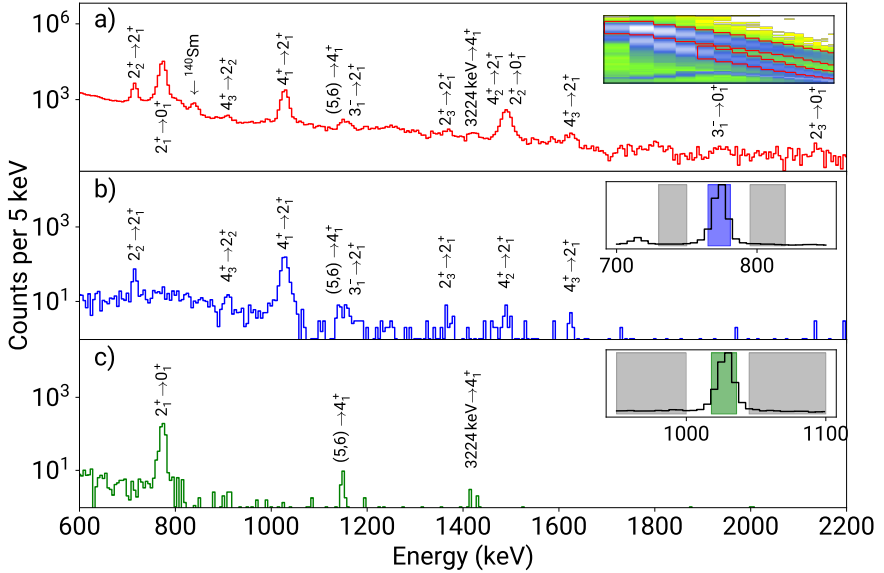


Figure 4.10.: Three beam-particles gated spectra are presented. The γ -singles spectrum in a) and b), c) show the coincidence spectra from gating in the E_γ - E_γ matrix on the $2_1^+ \rightarrow 0_1^+$ and $4_1^+ \rightarrow 2_1^+$ transitions of ^{140}Nd , respectively.

The p- γ - γ coincidences spectra are of special interest, when it comes to resolving doublets of γ -ray peaks in the p- γ spectrum and one of the doublet's transitions can be excluded by setting smart γ -ray gates. It is also useful to get rid of transitions of the isobaric beam contaminant ^{140}Sm . The resulting intensities of the p- γ - γ coincidence spectra had to be scaled to the p- γ intensities. This was done for the $2_1^+ \rightarrow 0_1^+$ coincidence spectra, beam and target gated, by the determination of the ratio of the peak areas of the $4_1^+ \rightarrow 2_1^+$ transition in the p- γ and the corresponding $2_1^+ \rightarrow 0_1^+$ coincidence spectra. This is a legitimate method for transitions whose final state completely decays via the gated transition. Otherwise the branching ratio of different decay paths has to be considered which did not occur in the

reported experiment. Here, the resulting scaling factors from the γ -ray gated to γ -ray singles intensities, 14.1(7) and 16.1(16) for the beam- and target-gated spectra, respectively, are equal to the inverse of the absolute efficiency for the detection of the $2_1^+ \rightarrow 0_1^+$ transition. Here, the detection of this γ ray is the only additional condition for the mentioned p- γ - γ coincidence. For the $4_1^+ \rightarrow 2_1^+$ coincidence spectrum, the ratio of the relative efficiencies at the energies of the $4_1^+ \rightarrow 2_1^+$ and $2_1^+ \rightarrow 0_1^+$ transitions was introduced as an additional factor to the coincidences efficiency. After these conversions, the observed intensities in the three different spectra (see Figure 4.10 for the beam- and Figure A.3 for the target-gated spectra) were comparable.

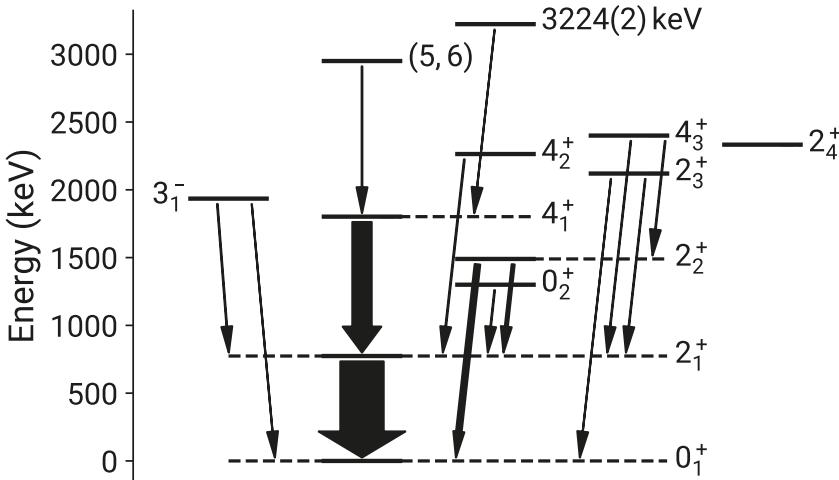


Figure 4.11.: The partial level scheme of ^{140}Nd shows the excited states of the here observed transitions. The widths of the arrows indicate the intensities of the transitions. The width of the $2_1^+ \rightarrow 0_1^+$ transition is reduced by a factor of 5 for visibility. Decays of the 2_4^+ state were not observed, though it is presented, because the state plays an important role in the further analysis. Reprinted figure with permission from Ref. [21].

From these spectra, 14 transitions of ^{140}Nd were identified. The statistics of

the target-gated spectra were much lower than the beam-gated spectra, therefore, fewer transitions were observed in the target-gated spectra. Most of the identified γ -ray peaks did not directly interfere with other transitions. However, there were three doublets of transitions which hindered the determination of the peak areas of the involved transitions.

The first doublet d_1 at 717 keV was identified as a sum of the $2_2^+ \rightarrow 2_1^+$ transition of ^{140}Nd at 716 keV and the $4_1^+ \rightarrow 2_1^+$ transition of ^{140}Sm at 717 keV. They were detangled by using the $2_1^+ \rightarrow 0_1^+$ (^{140}Nd) coincidence spectrum, where the transition of ^{140}Sm was not longer present. The second doublet, d_2 , at ≈ 1155 keV, $(5, 6) \rightarrow 4_1^+$ at 1148 keV and $3_1^- \rightarrow 2_1^+$ at 1162 keV, was also present in the $2_1^+ \rightarrow 0_1^+$ coincidence spectrum. However, the $3_1^- \rightarrow 2_1^+$ transition vanished in the $4_1^+ \rightarrow 2_1^+$ coincidence spectrum and the intensity of the $(5, 6) \rightarrow 4_1^+$ transition was measured undoubtedly. Due to the energy difference of 14 keV, it was also feasible to determine separated peak areas for both transitions of the doublet in the other two spectra. The independently measured intensities of the three different spectra were consistent. The third doublet d_3 consisted of the $4_2^+ \rightarrow 2_1^+$ transition at 1491 keV, which was previously observed in Ref. [94], and the ground state transition of the 2_2^+ state. The transitions were resolved by using the $2_1^+ \rightarrow 0_1^+$ coincidence spectrum and the associated vanishing of the ground state transition. The origin of the peak at 639 keV is ambiguous. The γ rays of the $0_2^+ \rightarrow 2_1^+$ transition and the transition connecting the 2^+ state at 1414 keV [95, 96] and the 2_1^+ state share the same energy. However, the transition of 639 keV of ^{140}Nd was identified in recent studies [24, 94] as the $0_2^+ \rightarrow 2_1^+$ transition and no γ ray decays are assigned to the 2^+ state at 1414 keV [95]. Consequently, in the later analysis this peak is assumed to be the $0_2^+ \rightarrow 2_1^+$ transition.

The peak areas were corrected for the Miniball efficiency to determine the final relative γ -ray intensities, see Table 4.3. The partial level scheme of the identified γ -ray transitions of ^{140}Nd was deduced, see Figure 4.11, by using the obtained coincidence information.

This experiment was designed for the investigation of $2_i^+ \rightarrow 2_1^+$ transitions and their resulting absolute $B(M1; 2_i^+ \rightarrow 2_1^+)$ strengths. The multipole-mixing ratios of $2_{2,3,4}^+ \rightarrow 2_1^+$ transitions were already measured in a γ - γ -correlation measurement after β^+ decay [24]. It shows, that the $2_2^+ \rightarrow 2_1^+$ is predominantly a $E2$ transition [$\delta = -1.22(14)$], while the $2_{3,4}^+ \rightarrow 2_1^+$ transitions showed a strong $M1$ character [$\delta = -0.08(8)$ and $-0.19(9)$, respectively] [24], which is a strong indication for being a fragment of the $2_{1,\text{ms}}^+$ state of ^{140}Nd . A detailed list of signatures of the

$2_{1,ms}^+$ state in vibrational nuclei is presented in Section 2.3. In this experiment, the depopulating transitions of the 2_3^+ state were observed in the beam-gated spectra but not the decays of the 2_4^+ state. Consequently, only upper limits for the intensities of the depopulating transitions of the 2_4^+ state were determined.

It was observed, that the different ranges of the scattering angles of the beam particles (see Figure 4.8) without any overlap led to expected unequal relative excitation yields of the same state for each experiment. The resulting γ -ray intensities of transitions of ^{140}Nd and were used to perform CE calculations with GOSIA to investigate the total sought-for transition strengths.

Table 4.3.: The measured counts with statistical uncertainties of the identified transitions of ^{140}Nd in the beam-particle gated spectra, see Figure 4.10. The transitions, which formed doublets, are marked with $d_{1,2,3}$. I_γ is the efficiency-corrected intensity relative to the intensity of the $2_1^+ \rightarrow 0_1^+$ transition.

E_{level} (keV)	J^π	E_γ (keV)	J_f^π	$A_{p-\gamma}$	$A_{p-\gamma-\gamma}$ $2_1^+ \rightarrow 0_1^+$	$A_{p-\gamma-\gamma}$ $4_1^+ \rightarrow 2_1^+$	I_γ
774	2_1^+	774	0_1^+	86140(320)		489(23)	100(1)
1413	0_2^+	639	2_1^+		18(7)		0.26(10)
1490	2_2^+ [24]	1490	0_1^+	d_3			2.1(1)
		716	2_1^+	d_1	101(12)		1.6(2)
1802	4_1^+	1028	2_1^+	6960(90)	495(23)		9.6(1)
1936	3_1^-	1936	0_1^+	42(11)			0.08(2)
		1162	2_1^+	d_2	d_2		0.25(4)
2140	2_3^+	2140	0_1^+	33(8)			0.073(18)
		1366	2_1^+	113(19)	12(4)		0.19(3)
2264	4_2^+ [94]	1491	2_1^+	d_3	16(4)		0.4(1)
2400	4_3^+	1626	2_1^+	112(16)	9(3)		0.21(4)
		910	2_2^+	240(16)	25(7)		0.31(5)
2950	(5,6)[94]	1148	4_1^+	d_2	d_2	16(5)	0.40(6)
3224		1422	4_1^+	101(17)		5(2)	0.17(3)
d_1				8050(130)			
d_2				391(41)	42(7)		
d_3				1450(40)			

4.1.3. γ -Ray Spectroscopy of ^{142}Sm

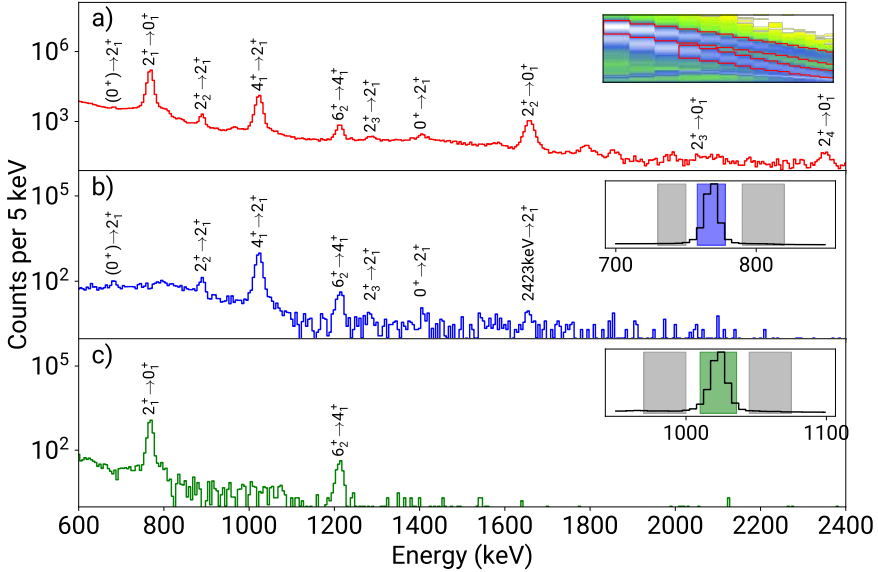


Figure 4.12.: Three spectra of beam-particle gated spectra, which were used to produce a level scheme and to determine the transitions' intensities of ^{142}Sm . a) shows the γ -singles spectrum and b), c) show the coincidence spectra from gating in the E_γ - E_γ matrix on the $2_1^+ \rightarrow 0_1^+$ and $4_1^+ \rightarrow 2_1^+$ transitions of ^{142}Sm , respectively.

The projectile-CE experiment of ^{142}Sm was performed using the same experimental setup as the previous described ^{140}Nd experiment and with the same purpose of investigating $2_i^+ \rightarrow 2_1^+$ transitions. The reaction kinematic of the scattering process was also similar due to the small mass difference of the beam particle $\approx 2u$ and the usage of the same ^{208}Pb target. No prominent contamination was identified. The RILIS laser-ionization scheme for Sm was extraordinary effective, because it consisted of one single wavelength to ionize the atom through a monochromatic two-step excitation path. This enhanced the chance of ionization drastically. Hence,

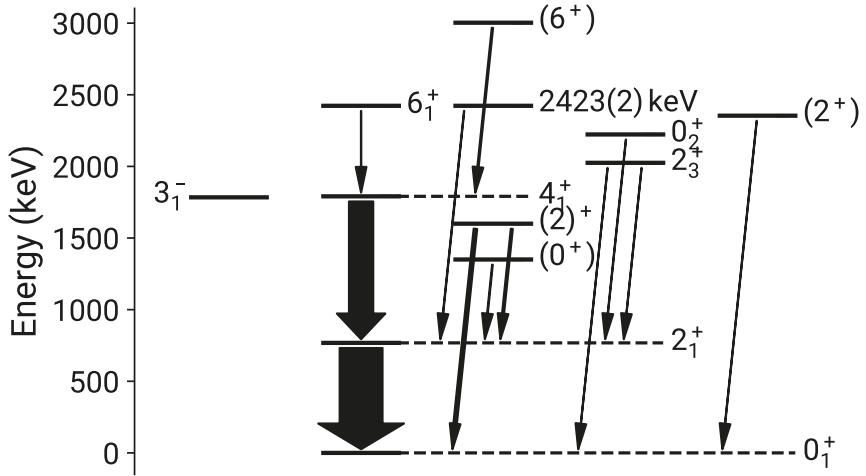


Figure 4.13.: The partial level scheme of ^{142}Sm with arrows symbolizing the observed transitions. The widths of the arrows are related to the transitions' intensities. The width of the $2_1^+ \rightarrow 0_1^+$ transition is reduced by a factor of 5 for visibility. The 3_1^- state was not observed, because of the domination of the decays of the 4_1^+ state in the same energy region, but included in the later analysis.

the rate of ionized Sm atoms was heavily increased due to the application of RILIS.

After performing the same calibrations as it was done for the ^{140}Nd experiment, γ -ray spectra of ^{142}Sm were produced, see Figure 4.12. For the ^{142}Sm experiment, the first inner ring of the DSSD was malfunctional and therefore it was dismissed in the later analysis. The same conditions as in the before mentioned experiment were used for building of the γ -ray spectra, see Figure A.1. The resulting γ -ray singles spectrum is presented in Figure 4.12 a). If the γ -ray multiplicity is higher than one, the events are sorted in a symmetrical E_γ - E_γ matrix, see Figure A.4. From this matrix, γ -ray coincidence spectra are obtained by setting gates on the γ -ray energy areas of the $2_1^+ \rightarrow 0_1^+$ and $4_1^+ \rightarrow 2_1^+$ transitions of ^{142}Sm , see Figure 4.12 b) and c). The same spectra were produced using the target-gated data, see Figure A.6.

From these spectra, 12 transitions of ^{142}Sm were identified, however a few puzzles of the spectra arose. At the energy of 1658 keV, the ground state transition of the 2_2^+ state is expected and observed. However, there is a peak at a very similar energy, 1655(2) keV, present in the $2_1^+ \rightarrow 0_1^+$ coincidence spectrum. Since this peak is not coincident with any other transition, it is considered to be a transition to the 2_1^+ state, although such a transition was previously unobserved. This reassembles the situation in ^{140}Nd , where a doublet of the $2_2^+ \rightarrow 0_1^+$ and the $4_2^+ \rightarrow 2_1^+$ transitions is present in the singles spectrum at 1490 keV. Consequently, the origin of the transition will be linked to a state at 2423(2) keV, which was unknown before. For the GOSIA calculations, it will be assumed as a 4^+ state due to the discussed similarities to the level scheme of ^{140}Nd .

Furthermore, a possible population of the 3_1^- state of ^{142}Sm is investigated in this CE due the experience from the ^{140}Nd experiment. The energy of the predominant γ -ray decay of the 3_1^- state, the $3_1^- \rightarrow 2_1^+$ transition ($E_\gamma = 1016$ keV), is quite close to the energy of the dominant $4_1^+ \rightarrow 2_1^+$ transition ($E_\gamma = 1023$ keV). Although the energy distance between both transitions is generally sufficiently large to distinguish them, it is impossible to achieve that due to the expected great imbalance of the two intensities of that doublet and due to the reduced energy-resolution of the present experiment from Doppler-shift corrections. Nevertheless, similar ratios as in ^{140}Nd are assumed, 0.038(10) and 0.030(11) for the beam- and target-gated spectra of ^{142}Sm , respectively, for the later analysis, because the 3_1^- state of ^{142}Sm is probably populated although it is not resolvable.

The intensities of the γ -ray energy gated spectra are scaled to the niveau of the singles spectra by the previously described coincidence factors, which are here 13.0(3) and 13.4(5) for the beam and target-gated spectra of ^{142}Sm . The measured peak areas and the corresponding γ -ray energies for the beam-gated and target-gated experiments are presented in Table 4.4 and Table A.3, respectively.

Table 4.4.: The measured counts with statistical uncertainties of identified transitions of ^{142}Sm in the beam-particle gated spectra, see Figure 4.12. The transitions, which formed a doublet, are marked with d_1 . I_γ is the efficiency-corrected intensity relative to the intensity of the $2_1^+ \rightarrow 0_1^+$ transition.

E_{level} (keV)	J^π	E_γ (keV)	J_f^π	$A_{p-\gamma}$	$A_{p-\gamma-\gamma}$ $2_1^+ \rightarrow 0_1^+$	$A_{p-\gamma-\gamma}$ $4_1^+ \rightarrow 2_1^+$	I_γ
768	2_1^+	768	0_1^+	409100(700)		3170(60)	100.0(5)
1450	(0_2^+)	683	2_1^+	1380(60)	114(21)		0.32(3)
1658	$(2)_2^+$	1658	0_1^+	d_1			1.64(4)
		890	2_1^+	3380(90)	248(21)		0.94(4)
1791	4_1^+	1023	2_1^+	39310(210)	3020(60)		11.32(4)
2055	2_3^+	2055	0_1^+	73(21)			0.034(10)
		1287	2_1^+	280(40)	28(6)		0.089(15)
2173	0_3^+	1405	2_1^+	313(34)	23(6)		0.14(1)
2354	$(2)_4^+$	2354	0_1^+	208(19)			0.099(9)
2420	6_1^+	629	4_1^+	650(150)			0.14(3)
2423		1655	2_1^+	d_1	28(6)		0.14(3)
3003	(6^+)	1212	4_1^+	1860(60)	148(13)	132(12)	0.61(3)
d_1				4500(70)			

4.1.4. GOSIA Analysis of HIE-ISOLDE CE Experiments

GOSIA is a multi-step CE code and a very powerful tool to analyze CE experiments in the "safe" CE regime [74]. It has the ability to fit a set of transitions matrix elements (ME) on experimental transition yields, see Table 4.5. The MEs are varied and the resulting calculated transition yields are compared to the experimental yields. Besides the γ -ray yields, the electron conversion is also taken into account by GOSIA using BRICC [97]. The fitting procedure is automatically repeated until the convergence criteria are full-filled. The quality of the fit is determined by the normalized χ^2 value. It is obtained by the sum of all deviations from the data points – transition yields, branching ratios, multipole-mixing ratios, etc. – in units of their standard deviations and divided through the number of data points. GOSIA needs diverse information as input to perform this kind of calculations, the most crucial are

- list of levels,
- list of transitions,
- geometry of particle and γ -ray detectors,
- reaction partners (beam and target),
- beam energy,
- observation limits relative to a certain transition,
- and additional spectroscopic quantities, e.g., branching ratios or multipole-mixing ratios.

It is necessary to normalize the CE yields to a known excitation. Here, the experiments were self-normalized to the 2_1^+ states of ^{140}Nd and ^{142}Sm . The required $E2$ MEs of the $2_1^+ \rightarrow 0_1^+$ transitions and the diagonal MEs of the 2_1^+ states of ^{140}Nd and ^{142}Sm were previously measured by Bauer et al. [16] and Stegmann et al. [15]. For further general information and a more detailed description of the CE experiment analysis using GOSIA, see Refs. [98, 99]. An example of the here used GOSIA-input file is presented in the Appendix in Listing B.2.

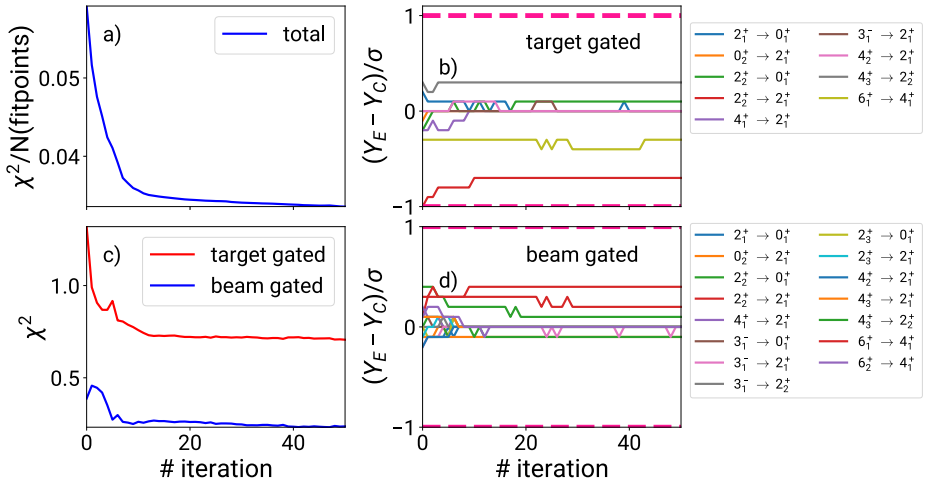


Figure 4.14.: The plots show the process in the GOSIA minimizations of the ^{140}Nd CE experiment. a) shows the evolution of the normalized χ^2 and c) of the total χ^2 values of the target- and beam-gated yields. b) and d) show the evolution of the deviation of the calculated and the experimental yields of individual transitions in units of the standard deviation.

GOSIA Analysis of ^{140}Nd

The known $E2/M1$ multipole-mixing ratios of $2_4^+ \rightarrow 2_1^+$ transitions and the branching ratio of the γ -ray decays of the 2_4^+ state [24] are included in the GOSIA calculations as well as the transitional and diagonal $E2$ MEs of the 2_1^+ state [16]. The diagonal ME was also applied to the higher lying 2^+ states and the 4_1^+ state. The quantities which were used as GOSIA input are also visible in Listing B.2.

After the initial minimization, each following minimization started with the best fit parameters of the previous minimization process as start parameters. This iterative procedure was stopped after 51 minimizations, because of the satisfying convergence with a normalized χ^2 value of 0.034 at 50 data points, see Figure 4.14 a), and total χ^2 of ≈ 0.8 and ≈ 0.2 for the target-gated and beam-gated yields, respectively, see Figure 4.14 c). The experimental yields of both experiments,

beam and target gated, were reproduced in such a good way, that each deviation was smaller than one σ , see Figures 4.14 b) and d). If a calculated yield of an unobserved transition was higher than the chosen observation limits an additional contribution to the total χ^2 arose.

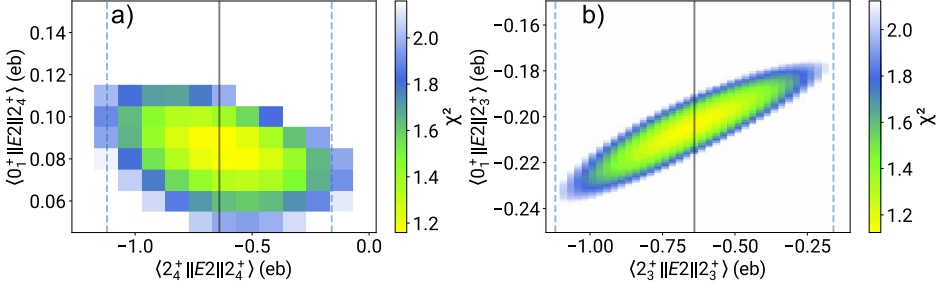


Figure 4.15.: The χ^2 distributions for the variations of the MEs, $\langle 2_4^+ || E2 || 0_1^+ \rangle$ and $\langle 2_4^+ || E2 || 2_4^+ \rangle$, and $\langle 2_3^+ || E2 || 0_1^+ \rangle$ and $\langle 2_3^+ || E2 || 2_3^+ \rangle$. For the GOSIA calculations of the transition from the 2_4^+ state, the intensities of its γ -ray decays were assumed at the edge of the detection limit.

A crucial issue when analyzing CE experiments with GOSIA is the determination of the uncertainties of the resulting MEs. GOSIA has in-built functions to determine uncorrelated and correlated uncertainties. The uncorrelated uncertainties are obtained by fixing every ME besides the investigated ME. This ME is then varied in such a way that the total χ^2 does not exceed the minimum plus one, meaning that it remains inside a one- σ environment. In reality, MEs may be highly correlated. These possible correlations can also be included in the uncertainty estimation in GOSIA. For the visualization of these correlations a method is used, where a χ^2 surface in dependence of these two correlating MEs is performed. All remaining MEs are fixed during the minimization process while scanning step-by-step through all possible pairs of the two investigated MEs. This is a reasonable method, if the investigated ME is dominantly correlated to a certain other ME.

The focus of this experiment was on the MEs $\langle 2_{3,4}^+ || E2 || 0_1^+ \rangle$. It was observed that the strongest correlation of these MEs were given to their diagonal MEs $\langle 2_{3,4}^+ || E2 || 2_{3,4}^+ \rangle$, like it was expected. Therefore, χ^2 -surface distributions of both ME pairs were performed to obtain the absolute uncertainties of the corresponding matrix elements. The diagonal matrix elements of the 2^+ states have a strong

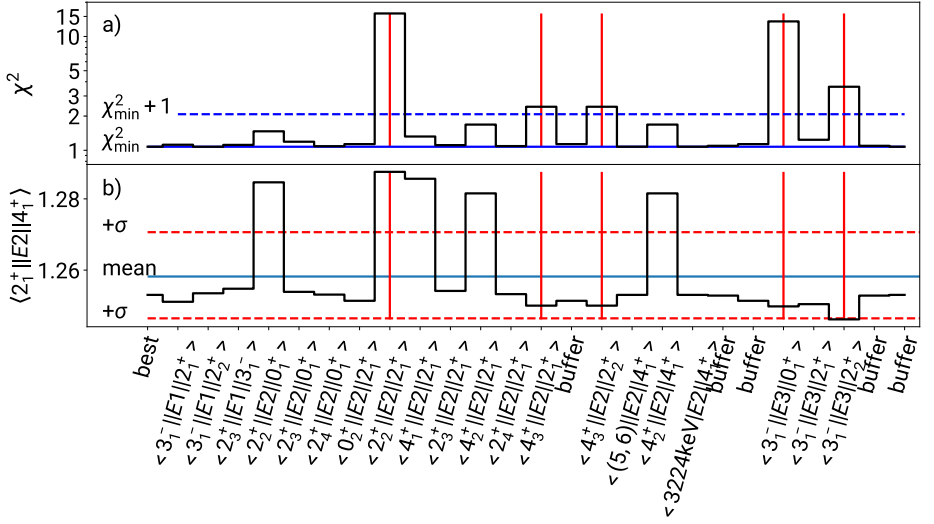


Figure 4.16.: The signs of the MEs are fixed by the “best” fit and later only one ME’s sign was switched, which is labeled on the x-axis. In a), the total χ^2 of the GOSIA calculation with the changed set of matrix elements is presented. b) shows the distribution of the values for the instance of the ME $\langle 2_1^+ || E2 || 4_1^+ \rangle$ of ^{140}Nd . For more information, see text.

impact of the excitation yields. Consequently, leaving the diagonal ME as a free parameter does here not lead to a defined minimum. Fortunately, the diagonal ME of the 2_1^+ state was measured [16], $\langle 2_1^+ || E2 || 2_1^+ \rangle = -0.64(48)$ eb, and was estimated the same for the higher lying 2^+ states. Especially for the potential $2_{1,\text{ms}}^+$ state, this is an adequate assumption due to the similar one-quadrupole-phonon structure of both states. The values were applied to the GOSIA calculations as data points.

In Figure 4.15, the correlation between the diagonal and transitional MEs was made clearly visible by using the previously described method. Nevertheless, a clearly defined minimum is found for the ME $\langle 2_3^+ || E2 || 0_1^+ \rangle$ for both potential signs of this ME. For the determination of the ME $\langle 2_4^+ || E2 || 0_1^+ \rangle$ fewer χ^2 values were

computed, because the distribution in Figure 4.15 a) is already sufficient to obtain the upper limit. The resulting transition strengths and their uncertainties are noted in Table 4.5. This well-established method was already utilised for the determination of the $B(E2; 2_1^+ \rightarrow 0_1^+)$ strength of ^{140}Nd [16] and for various other CE experiments [99–102].

The ground state transition ME $\langle 2_1^+ || E2 || 0_1^+ \rangle$ is directly connected with the sought-for $M1$ ME $\langle 2_1^+ || M1 || 2_1^+ \rangle$ via the Eqs. (3.28) and (3.27) for the partial transition width and the measured branching ratio. The resulting $B(M1)$ values are discussed in detail in Chapter 5.

A further critical point in the GOSIA analysis is the determination of the signs of the MEs. GOSIA does not tend to change the sign of a ME in the minimization process unless the value of the ME is near zero. Although, the sign of the ME does not effect the absolute transition strength in the first place, it influences the excitation process. The switch of the relative sign between different excitation paths of the same state leads to a significant change of its excitation yield. Hence, the absolutes of the MEs have to change to fit the fixed experimental yield. So, in the end, the relative sign indirectly effects the absolute MEs.

Therefore, the data may be sensitive to the signs of some MEs. Here, it was probed by switching one ME's sign and then fixing all remaining MEs' signs for the GOSIA minimization process. The procedure was performed for each ME, besides the previously determined MEs $\langle 2_1^+ || E2 || 0_1^+ \rangle$ and $\langle 2_1^+ || E2 || 2_1^+ \rangle$ [16], and the assumed diagonal MEs $\langle 2_i^+ || E2 || 2_i^+ \rangle$. The result is shown in Figure 4.16 a), where the horizontal and dashed blue lines represent the minimum χ_{\min}^2 from the “best” fit and $\chi_{\min}^2 + 1$, respectively. If the resulting χ^2 is greater than $\chi_{\min}^2 + 1$, the corresponding sign change is not a valid solution. Hence, the ME's sign is determined by the experimental data. This resulting set of MEs is in the further analysis neglected and marked by a vertical red line in Figures 4.16 a) and b).

It was shown, that this is the case for MEs involved in the excitation processes of the 4_3^+ and 3_1^- states, namely $\langle 2_1^+ || E2 || 2_2^+ \rangle$, $\langle 2_1^+ || E2 || 4_3^+ \rangle$, $\langle 2_2^+ || E2 || 4_3^+ \rangle$, $\langle 3_1^- || E2 || 0_1^+ \rangle$, and $\langle 3_1^- || E2 || 2_2^+ \rangle$. However, the signs of the remaining MEs are indefinite and each combination of signs is a valid solution. In Figure 4.16 b), the determination of an uncertainty is illustrated for $\langle 4_1^+ || E2 || 2_1^+ \rangle$. The vertical red and the dashed lines indicate the mean value and its corresponding one- σ deviation, respectively, determined by this sign-switch analysis. The additional systematical uncertainties of the MEs are included in the total uncertainties together with the statistical ones.

The checking of the signs of the matrix elements was the last step to finalize the transition MEs with their uncertainties. Table 4.5 presents the observed transition intensities and the corresponding absolute $E2$, $E3$ and $M1$ transition strengths. The interpretation of the obtained absolute transition strengths in the context of the $N = 80$ isotones is discussed in Chapter 5.

Table 4.5.: Measured properties of the levels and γ -ray transitions of ^{140}Nd . Level energies and spin assignments are adopted from Ref. [95] unless otherwise noted. The relative γ -ray intensities determined from the beam-gated (exp. 1) and the target-gated (exp. 2) γ -ray spectra are corrected for efficiency.

E_{level} (keV)	J^π	E_γ (keV)	J_f^π	I_γ exp. 1	I_γ exp. 2	δ from [24]	$\pi\lambda$	$B(\pi\lambda) \downarrow$ ^a
774	2_1^+	774	0_1^+	100(1)	100(1)		$E2$	$33.6(27)^b$
1413	0_2^+	639	2_1^+	0.3(1)	1.4(4)		$E2$	$7.5(16)^c$
1490	2_2^{+d}	1490	0_1^+	2.1(1)	5.5(6)		$E2$	$1.76(13)$
		716 ^e	2_1^+	1.6(2)	2.7(8)	-1.22(14)	$E2$	$33(3)$
							$M1$	$0.033(8)$
1802	4_1^+	1028 ^e	2_1^+	9.6(1)	21.4(6)		$E2$	$40(1)$
1936	3_1^-	1936	0_1^+	0.08(2)			$E3$	$6(2)$
		1162 ^e	2_1^+	0.25(4)	0.9(4)			
2140	2_3^+	2140	0_1^+	0.07(2)			$E2$	$1.9(6)$
		1366 ^e	2_1^+	0.19(3)		-0.08(8)	$E2$	$0.3_{-0.3}^{+0.6}$
							$M1$	$0.26_{-0.10}^{+0.11}$
2264	4_2^{+f}	1491 ^e	2_1^+	0.4(1)	1.2(5)		$E2$	$2.3(8)$
2333	2_4^+	2333	0_1^+	<0.03			$E2$	<0.8
		1560	2_1^+	<0.03		-0.19(9)	$E2$	<0.4
							$M1$	<0.04
2400	4_3^+	1626 ^e	2_1^+	0.21(4)			$E2$	$1.6(3)$
		910 ^e	2_2^+	0.31(5)			$E2$	$41(7)$
2950 ^g	$(5,6)^f$	1148 ^{hi}	4_1^+	0.40(6)	1.6(5)		$E2$	$30(3)$
3224 ^g		1422 ^{hi}	4_1^+	0.17(3)	1.0(2)		$E2$	$22(4)$

^a $B(M1)$ values are given in μ_N^2 , $B(E2)$ and $B(E3)$ values are given in W.u. ($E2$: 1 W.u. = $4.32 \times 10^{-3} \text{ e}^2\text{b}^2$; $E3$: 1 W.u. = $1.16 \times 10^3 \text{ e}^2\text{b}^3$)

^bTransition strength adopted from Ref. [16]

^cThis value is extracted without considering $E0$ excitation. It has to be considered as an estimate only

^dSpin adopted from Ref. [24]

^eObserved in coincidence spectrum of the $2_1^+ \rightarrow 0_1^+$ transition

^fSpin and parity adopted from Ref. [94]

^gAssumed as a 6^+ state in the GOSIA analysis

^hObserved in coincidence spectra of the $4_1^+ \rightarrow 2_1^+$ and $2_1^+ \rightarrow 0_1^+$ transitions

ⁱTransition energy adopted from Ref. [103]

GOSIA Analysis of ^{142}Sm

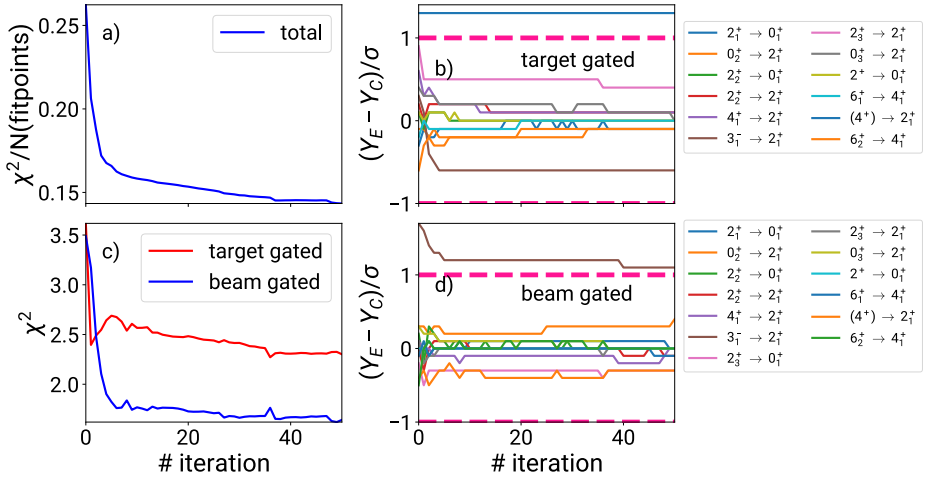


Figure 4.17.: The plots show the process in the GOSIA minimizations of the ^{142}Sm CE experiment. a) shows the evolution of the normalized χ^2 and c) of the total χ^2 values of the target- and beam-gated yields. b) and d) show the evolution of the deviation of the calculated and the experimental yields of individual transitions in units of the standard deviation.

The GOSIA analysis of the CE experiment with a ^{142}Sm beam was basically performed analogously to the analysis of ^{140}Nd , but a few differences occur. Obviously, there is a lack of $E2/M1$ multipole-mixing ratios of the $2_2^+ \rightarrow 2_1^+$ transitions. Hence, at this point it is impossible to determine the $M1$ strengths of $2_2^+ \rightarrow 2_1^+$ transitions on the base of the reported CE experiment. A further crucial difference is the missing knowledge of the diagonal $E2$ ME of the 2_1^+ state. The previous work on the isoscalar collectivity of ^{142}Sm [15, 104] assumed the diagonal $E2$ ME of the 2_1^+ state to be inside the rigid rotor limits and was not able to make a further statement about it. Consequently, the quadrupole moments in this GOSIA-analysis procedure were free parameters, while the one of the 2_3^+ state was coupled by being equal to the one of the 2_1^+ state. As mentioned before, this a legitimate

estimation due the one-phonon structure of both states. Fortunately, the branching ratio of the γ -ray decays of the 2_3^+ state of ^{142}Sm is known and added to the GOSIA-input file. The calculations are relative to the $E2$ transition strength $B(E2; 2_1^+ \rightarrow 0_1^+) = 32(4)$ W.u., or as ME: $\langle 2_1^+ || E2 || 0_1^+ \rangle = 0.837(54)$ eb. The used level scheme and set of transition MEs are noted in the GOSIA-input file, see Listing B.4 and the experimental yields or intensities of the target- and beam-gated experiments are noted in Listing B.5.

The kinematics of the $^{208}\text{Pb}(^{142}\text{Sm}, ^{142}\text{Sm})^{208}\text{Pb}^*$ reaction is similar to the one of $^{208}\text{Pb}(^{140}\text{Nd}, ^{140}\text{Nd}^*)^{208}\text{Pb}^*$ within the energy and angular resolution of the DSSD. However, the angular ranges of the scattered particles change, because the innermost ring of the DSSD was corrupted during that experiment and, hence, excluded from the analysis. The general GOSIA minimization for the CE of ^{142}Sm was performed in the same way as it was done for ^{140}Nd and the agreement between calculated and experimental yields is also quite accurate with a normalized χ^2 equal to 0.14 after 51 minimizations. However, there are two out of in total observed 25 transitions, whose differences between calculated and experimental yields are slightly greater than one standard deviation, see Figure 4.17. Hence, the CE calculation is a good reproduction of the experiment.

Although, it is not possible to determine the sought-for $M1$ strengths of the $2_i^+ \rightarrow 2_1^+$ transitions, an estimation of the upper limit can be done. Four 2^+ states of ^{142}Sm were excited in this experiment. The spin and parity assignments of two of them are definite, while it was not for the two others. The $(2)^+$ state at 1658 keV has the spin $J^\pi = 2^+$ with a high probability, because of the similarities of the level scheme of ^{142}Sm and ^{140}Nd and the observed high population via CE. The assumption of the spin and parity of the state at 2354 keV, (2^+) , is also strongly supported by the strong population via the ground state transition, which points to a $E2$ connection.

Regarding the accumulated data, the 2_3^+ state is expected to be the most promising candidate for the $2_{1,ms}^+$ state of ^{142}Sm . Hence, a predominant $M1$ transition to the 2_1^+ state is assumed by applying a near-zero multipole-mixing ratio $\delta = 0.01$ to obtain an upper limit of the $B(M1; 2_3^+ \rightarrow 2_1^+) < 0.14_{-0.01}^{+0.37} \mu_N^2$ strength. Furthermore, upper and lower limits of the $E2$ transition strengths of the γ -ray decays of the 2_3^+ state were obtained by assuming a $M1$ and $E2$ character of the $2_3^+ \rightarrow 2_1^+$ transition ($\delta = 0.01$ and 1, respectively). To determine the δ of the $2_3^+ \rightarrow 2_1^+$ transition, a β^+/ϵ -decay experiment was designed, which is described in Section 4.3.

However, the set of the resulting transition strengths from the GOSIA calculations are preliminary, because the important $E2/M1$ multipole-mixing ratios are missing, see Table 4.6. This directly affects the MEs of the $2_i^+ \rightarrow 2_1^+$ transitions and indirectly, but not as intensive, all other MEs. Therefore, especially the $E2$ strengths of the $2_{2,3}^+ \rightarrow 2_1^+, 0_1^+$ transitions may change tremendously when $E2/M1$ multipole mixing ratios will be included in the CE calculations in the future. Later, the upper limit of the $B(M1)$ strength and the $B(E2)$ values are discussed in context of the $N = 80$ isotonic chain in Chapter 5.

Table 4.6.: Measured properties of the levels and γ -ray transitions of ^{142}Sm . Level energies and spin assignments are adopted from Ref. [105] unless otherwise noted. The relative γ -ray intensities determined from the beam-gated (exp. 1) and the target-gated (exp. 2) γ -ray spectra are corrected for efficiency.

E_{level} (keV)	J^π	E_γ (keV)	J_f^π	I_γ exp. 1	I_γ exp. 2	δ	$\pi\lambda$ ^a	$B(\pi\lambda) \downarrow$
768	2_1^+	768 ^b	0_1^+	100(1)	100(1)		$E2$	32(4) ^c
1451	(0^+)	683 ^e	2_1^+	0.29(4)	1.2(1)		$E2$	10(3) ^d
1658	$(2)^+$	1658	0_1^+	1.66(5)	2.8(3)		$E2$	2.9(3)
		890 ^e	2_1^+	0.89(4)	1.4(2)		$E2$	30(7)
1784	3_1^-	1784	0_1^+				$E3$	$0.3^{+7.7}_{-0.3}$
		1016	2_1^+	0.4(1)	0.7(2) ^f			
1791	4_1^+	1023 ^e	2_1^+	11.2(1)	23.2(3)		$E2$	51(3)
2055	2_3^+	2055	0_1^+	0.03(1)			$E2$	$>0.33^{+0.05g}_{-0.11}$
							$E2$	$<0.95^{+1.5}_{-0.02} h$
		1287 ^e	2_1^+	0.10(2)	0.10(4)		$E2$	$<4.5^{+1.4g}_{-0.9}$
						$M1$	$<0.14^{+0.37}_{-0.01} h$	
2174	0_2^+	1405 ^e	2_1^+	0.11(2)	0.55(8)		$E2$	21(6) ^d
2353	(2^+)	2353	0_1^+	0.10(1)	0.13(4)		$E2$	1.0(2)
2420	6_1^+	629 ^{bde}	4_1^+	0.14(3)	0.5(1)		$E2$	8(3)
2423	$(4^+)^i$	1655 ^{ej}	2_1^+	0.16(3)	0.6(2)		$E2$	2.2(12)
3003	(6^+)	1212 ^{bde}	4_1^+	0.64(3)	2.5(2)		$E2$	56(5)

^a $B(M1)$ values are given in μ_N^2 , $B(E2)$ and $B(E3)$ values are given in W.u. ($E2$: 1 W.u. = $4.4 \times 10^{-3} \text{ e}^2\text{b}^2$; $E3$: 1 W.u. = $1.20 \times 10^3 \text{ e}^2\text{b}^3$)

^bObserved in coincidence spectrum of the $4_1^+ \rightarrow 2_1^+$ transition

^cTransition strength adopted from Ref. [15]

^dThis value is extracted without considering $E0$ excitation. It has to be considered as an estimate only

^eObserved in coincidence spectrum of the $2_3^+ \rightarrow 0_1^+$ transition

^fIntensity assumption due to similarities in ^{140}Nd

^g $M1$ strength was estimated with predominant $E2$ character of the $2_3^+ \rightarrow 2_1^+$ transition ($\delta = 1$)

^h $M1$ strength was estimated with predominant $M1$ character of the $2_3^+ \rightarrow 2_1^+$ transition ($\delta = 0.01$)

ⁱSpin assignment due to similarities to ^{140}Nd

^jNewly observed

4.2. Coulomb Excitation of ^{202}Hg at ATLAS Using Gammasphere

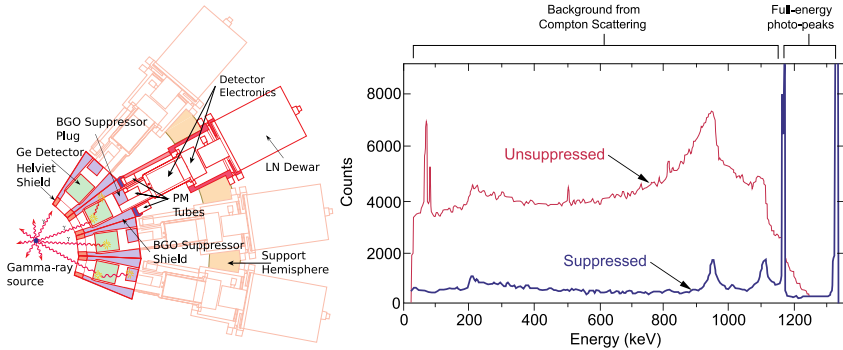


Figure 4.18.: Left: a schematic drawing of the Gammasphere detectors. The HPGe detectors are surrounded by BGO scintillators for the purpose of Compton suppression. Right: the effect of the Compton suppression on the γ -ray energy spectra are shown. The pictures are adopted from Ref. [106].

The reported projectile-CE experiment was performed at the Argonne Tandem Linear Accelerator System (ATLAS) facility [107]. The heavy ion beam of the stable isotope ^{202}Hg was produced in an electron cyclotron resonance (ECR) ion source. In general, ECR ion sources are made of a metallic box filled with a low-pressure plasma, where a magnetic field is applied to create its minimum potential in the center of the metallic box and its maximum near the wall. Between the center and the walls of the box, a so-called ECR surface exists. There, the Larmor frequency of the electrons is equal to the frequency of the injected microwaves. The electrons are energized each time they pass the ECR surface and consequently the plasma is heated [108] and the ions are ionized multiple times. Then, the ions can be extracted by applying an electrical field.

The extracted continuous ion beam is delivered to the the radio-frequency quadrupole (RFQ). Inside the RFQ, the ion beam is accelerated, focused, and bunched, leading to a pulsed beam with a frequency of 12 MHz. The further

Table 4.7.: The polar angles of the 17 rings of Gammasphere in respect to the beam axis.

#	θ	#	θ	#	θ	#	θ	#	θ
1	17.3°	5	58.3°	9	90.0°	13	121.7°	17	162.7°
2	31.7°	6	69.8°	10	99.2°	14	129.9°		
3	37.4°	7	79.2°	11	100.8°	15	142.6°		
4	50.1°	8	80.7°	12	110.2°	16	148.3°		

acceleration of the ion bunches happens in the linear accelerators (linac), i.e., the Positive Ion Injector (PII, 12 MV) linac, the Booster linac (20 MV), and the ATLAS linac (20 MV). The ^{202}Hg ions were accelerated up to $4.4 \text{ A} \cdot \text{MeV}$ before they were delivered to a 1 mg/cm^2 -thick ^{12}C target surrounded by Gammasphere. The beam energy was chosen sufficiently low, approximately 85 % of the Coulomb barrier, to ensure “safe” CE [74].

Gammasphere consists generally of 110 HPGe detectors, which are individually equipped with a Bismuth Germanium Oxide (BGO) Compton-suppression shield. The BGO detectors are used as a veto detector. That means, if γ -ray hits are recognized in the HPGe detector and in the linked BGO detector at the same time, it is assumed that the initial γ ray did not deposit its total energy inside the HPGe detector, i.e., Compton scattering happens, and the event is dismissed. This method leads to a tremendous reduction of the background from Compton-scattered γ rays, which is prominent without Compton suppression, see Figure 4.18. The detectors are arranged in 17 rings, where the detectors of each ring share the same polar angles in respect to the beam line, see Table 4.7. The structure of an individual Gammasphere detector is shown in detail in Figure 4.18. At the time of the experiment, the ring at the most forward angles was dismantled due to geometrical reasons. Five additional detectors of the whole array were not working properly, thus, 100 detectors were in use in the present analysis.

The energy and efficiency calibrations of Gammasphere were done with sources of ^{152}Eu , ^{56}Co and ^{182}Ta . The Eq. (4.1) was utilized for the fit of the efficiency curve on the relative intensities of the sources’ γ rays for the whole Gammasphere array, see Figure C.1. For the efficiency calibration of each ring, a simplified exponential decay curve, valid for $E_\gamma > 200 \text{ keV}$, was utilized, see Figure C.2.

4.2.1. γ -Ray Spectroscopy of ^{202}Hg

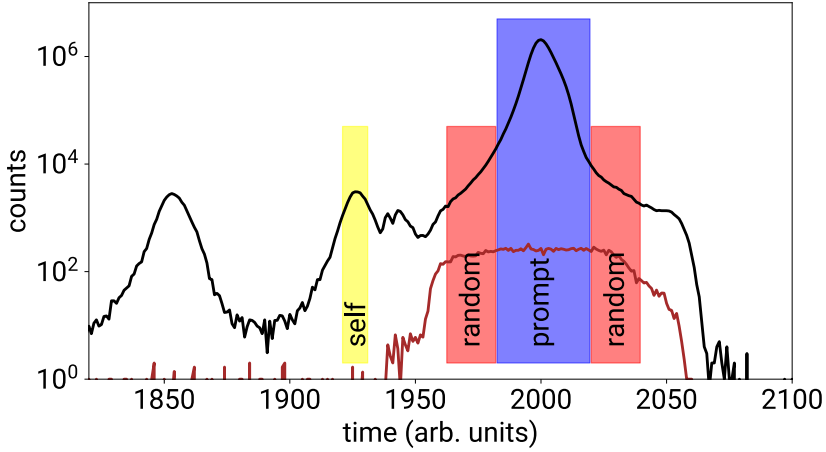


Figure 4.19.: The prompt (black) and random (red) time differences to radio frequency are produced by gating on the $2_1^+ \rightarrow 0_1^+$ transition of ^{202}Hg (prompt) and the 1461-keV line of the β^+ -decay of ^{40}K (red), respectively.

The extreme mass difference between beam and target particles [$m(^{202}\text{Hg}) \gg m(^{12}\text{C})$] led to the opportunity of measuring in-flight emitted γ rays without particle detection. This was feasible, because the beam particles were scattered into extreme forward angles ($> 3.5^\circ$). Hence, an averaged Doppler shift of γ rays emitted from ^{202}Hg particles is assumed for 0 degree particle scattering, which is a good approximation, see Figure 4.20 a). This enabled an event-by-event Doppler-shift correction of the γ -ray energies by using Eq. (4.2). The angle between the beam axis and the line from the target to the hit detector was consequently taken as the emission angle of the γ ray. The method of projectile CE in extreme inverse kinematics without particle detection was successfully utilized before several times [10, 18, 36, 39, 40, 48, 109].

Without a particle detector, which is often a limiting factor, the beam current could be increased up to the maximum performance of the accelerator or till the

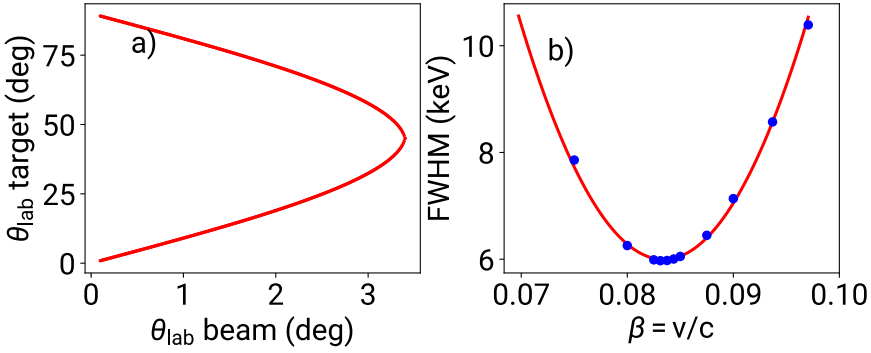


Figure 4.20.: The calculated angular correlation of the incoming beam and target particles is presented in a). The maximum scattering angle of the beam particles is less than 4° . The determination of the ion-beam velocity was done by minimizing the FWHM of the $2_1^+ \rightarrow 0_1^+$ peak and is presented in b). A second order polynomial was fitted on the data to obtain the right β .

maximum rate of HPGe detectors was reached. Hence, an average beam current of approximately 1-2 pA was achieved during the measurement with a duration of ≈ 20 hours. The pulsed nature of the beam was used to minimize the time-random background. The time structures of the random background and the beam events relative to the RF are displayed in Figure 4.19. The time background is produced by setting an energy gate on the 1461-keV line of ^{40}K , while a gate on the $2_1^+ \rightarrow 0_1^+$ transition of ^{202}Hg was set for the beam-related γ -rays. The random events were subtracted from the prompt events scaled with the ratio of the widths of the random and prompt gates. The time spectrum of beam events showed the pulsed shape of the beam. The “self” coincidences, see Figure 4.19, are associated with a following beam pulse.

After the time-random background subtraction, 8.4×10^8 events were counted with a γ -ray fold greater than one. The $2_1^+ \rightarrow 0_1^+$ transition of ^{202}Hg dominates the γ -ray singles spectrum with the extraordinarily high statistics of $\approx 2.5 \times 10^8$ counts, see Figure 4.21. This transition was used to optimize the Doppler-shift correction. The width of the peak is measured by a simultaneous variation of the velocity β

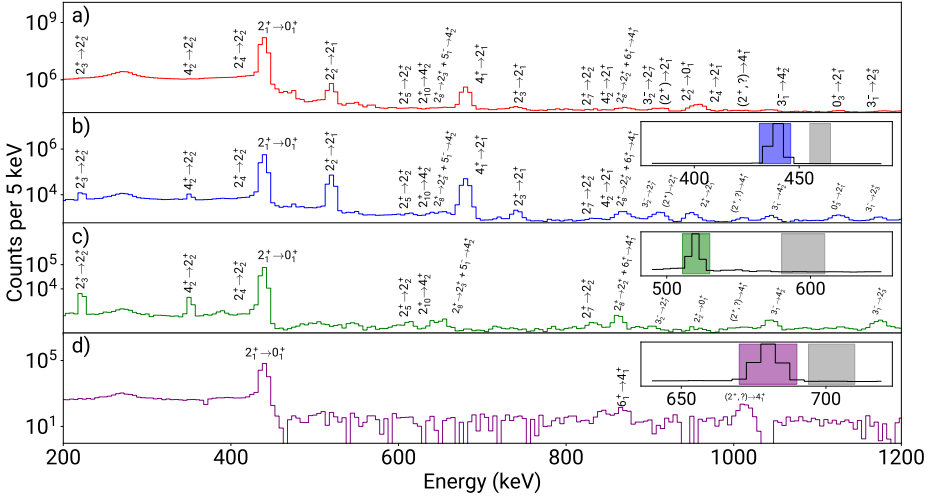


Figure 4.21.: The random-time-subtracted medium-energy γ -ray spectra of the $^{12}\text{C}(^{202}\text{Hg}, ^{202}\text{Hg}^*)$ CE experiment with Doppler-shift correction for the beam particles. γ -ray events with multiplicity ≥ 1 are shown in a), with multiplicity ≥ 2 and a gate on the γ -ray transitions $2_1^+ \rightarrow 0_1^+$, $2_2^+ \rightarrow 2_1^+$, and $4_1^+ \rightarrow 2_1^+$ are presented in b), c), and d), respectively.

$= v/c$, which is assumed for the Doppler-shift correction. The minimum width is achieved with $\beta = 0.0834(1)$, see Figure 4.20 b). About 2 % of the data were events with γ -ray fold greater than or equal two, which were sorted in a E_γ - E_γ matrix, see Figure 4.23. The γ -ray coincidence spectra, see Figure 4.21, which were produced by gating on an energy of a transition in the E_γ - E_γ matrix, were used to disentangle multiplets and prepare a level scheme, see Figure 4.25. The relevant γ rays of ^{202}Hg with a higher energy than 1200 keV are shown in Figure 4.22. This energy region was cut out in the spectra in Figure 4.21 to increase the visibility. In total, 39 transitions were assigned to 24 excited states of ^{202}Hg . For more information about the measured counts of the identified transitions, see Table C.1. The transition from and to the excited 2^+ states of ^{202}Hg are of special interest in this analysis and will be investigated further.

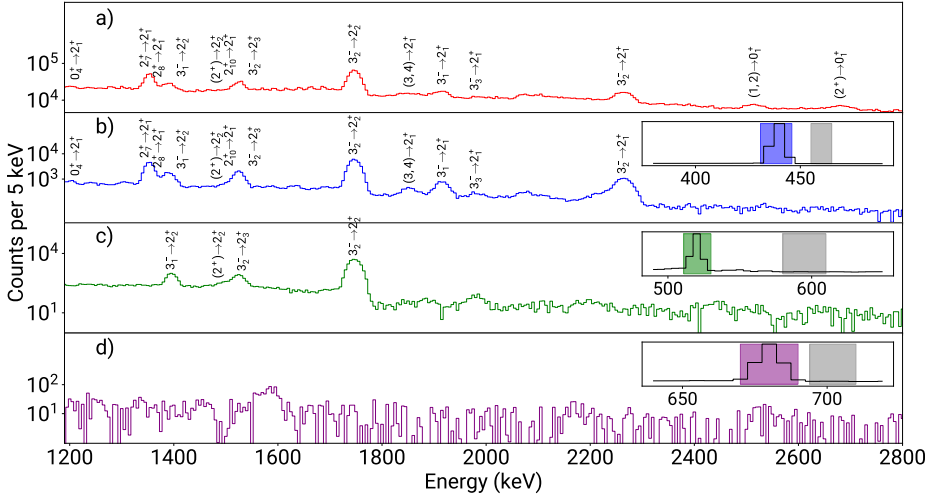


Figure 4.22.: The random-time-subtracted high-energy γ -ray spectra of the $^{12}\text{C}(^{202}\text{Hg},^{202}\text{Hg}^*)$ CE reaction with Doppler-shift correction for the beam particles. γ -ray events with multiplicity ≥ 1 are shown in a), with multiplicity ≥ 2 and a gate on the γ -ray transition $2_1^+ \rightarrow 0_1^+$ are presented in b).

4.2.2. Angular Correlations

The quest of the determination of $B(M1; 2_i^+ \rightarrow 2_1^+)$ values demands the knowledge of the $E2/M1$ multipole-mixing ratios δ . Here, the ultra-high statistics of this experiment gave the opportunity to perform a CE experiment to primarily obtain $E2$ and $E3$ transition strength and, simultaneously, an angular correlation measurement to determine the indispensable $E2/M1$ multipole-mixing ratios.

In the first place, angular intensity distributions have to be carried out by analyzing the γ -ray spectra ring-wise. Relativistic effects on polar angles have to be taken into account due to the ion-beam velocity of $\beta \approx 8\%$. The polar angles of the detectors in the center-of-mass frame of the emitting nucleus θ_{nuc} are the essential angles, when it comes to the angular distribution. The angles are determined from the angles in the laboratory system by Eq. (3.31). They are related to the polar

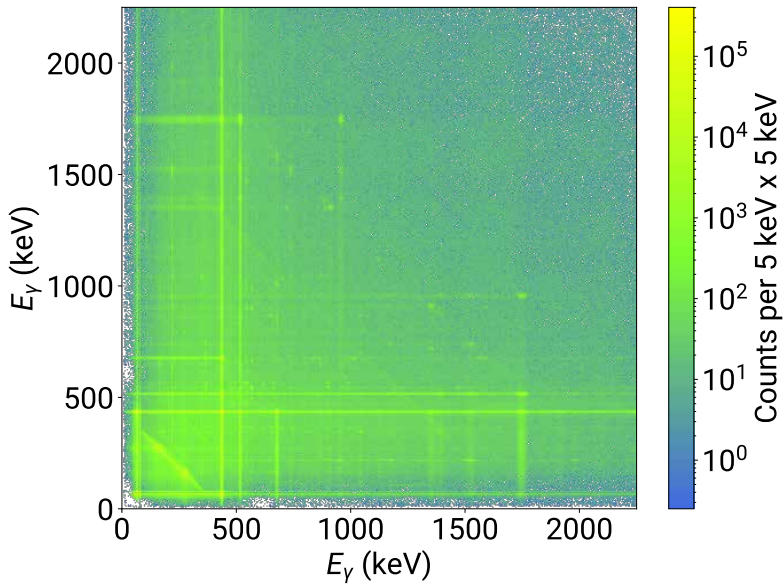


Figure 4.23.: The E_γ - E_γ matrix of the ^{202}Hg CE experiment. The condition is the detection of at least two γ rays in Gammasphere inside the prompt time gate.

angles in the laboratory frame θ_{lab} and the ion velocity β . This transformation consequently effects also the solid angles of the detectors for the center-of-mass frame of the in-flight ions Ω_{nuc} , which are, then, given by Eq. (3.32). It shows, that the detectors in forward direction appear larger than the ones in backwards direction for the accelerated ions.

Fortunately, the lifetime of the 2_1^+ state is relatively long ($\tau(2_1^+) = 39.3(3)$ ps), hence, the spin de-orientation led to an isotropic γ -ray emission of the $2_1^+ \rightarrow 0_1^+$ transition. This statement was supported by its angular distribution, see Figure 4.24. As a consequence, a γ -ray coincidence condition to the $2_1^+ \rightarrow 0_1^+$ transition was legitimately set for the purification of the ring-wise spectra.

In general, the statistical tensor of a certain state is determined by the angular distribution of its ground-state transition, see Eq. (3.39). Here, the ground-state

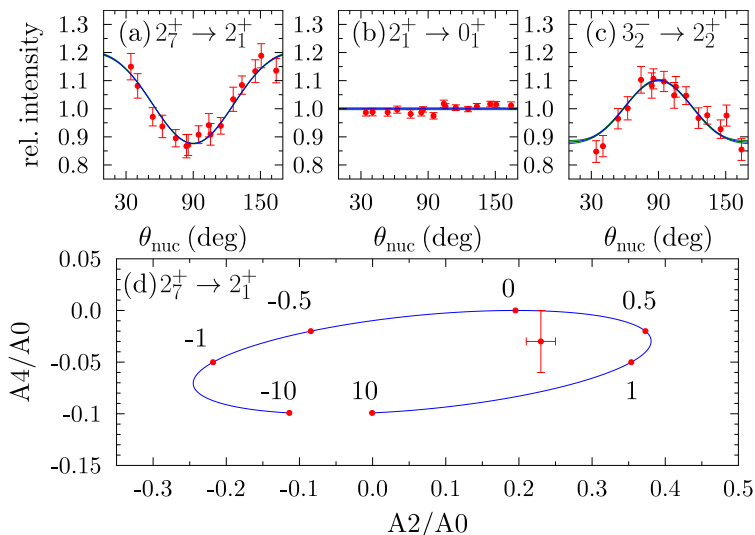


Figure 4.24.: The sub figures a), b), and c) show the ring-wise efficiency-corrected relative intensities of the transitions $2_7^+ \rightarrow 2_1^+$, $2_1^+ \rightarrow 0_1^+$, and $3_2^- \rightarrow 2_1^+$, respectively. It is obvious from b), that the assumption of an isotropic emission of the $2_1^+ \rightarrow 0_1^+$ transition is legitimate. Reprinted figure with permission from Ref. [50].

transition of the most promising candidate for the $2_{1,\text{ms}}^+$ state was not observed, hence, the statistical tensor was deduced in an iterative way using the Coulomb-excitation code GOSIA. The technique is documented in Ref. [48] and is based on the analysis of a subset of transition matrix elements and levels. Here, the γ -ray transitions of the 2^+ state of interest, the $2_{1,2,3}^+$ states, the most populated 3^- states ($3_{1,2}^-$), the 4_1^+ state and the ground state are included in the GOSIA calculations, see Code B.6. The statistical tensor ρ_k is newly determined by GOSIA in each iteration. Then, the statistical tensor is used to obtain the multipole-mixing ratio by Eq. (3.36). The obtained δ leads to $E2$ MEs of the $2^+ \rightarrow 2_1^+$ and $2^+ \rightarrow 0_1^+$ transitions, which serve in the next iteration again as GOSIA input. This iterative procedure is repeated until the change of the resulting δ becomes decisively small.

In Figure 4.24, three different angular distributions together with the fitted

Table 4.8.: The coefficients $a_{2,4}$ from the fits on the angular distributions are presented with the determined $E2/M1$ multipole-mixing ratios of selected γ -ray transitions of ^{202}Hg , if possible.

Transition	a_2	a_4	δ
$2_2^+ \rightarrow 2_1^+$	0.11(1)	0.012(16)	0.9(1)[110]
$4_1^+ \rightarrow 2_1^+$	0.16(2)	-0.010(28)	
$2_3^+ \rightarrow 2_1^+$	0.21(4)	-0.039(54)	(0.02(7)) & 2.1(4)
$2_3^+ \rightarrow 2_2^+$	0.12(2)	-0.007(22)	-0.13(3)
$2_7^+ \rightarrow 2_1^+$	0.23(2)	-0.028(25)	0.06(4)
$3_2^- \rightarrow 2_1^+$	-0.17(2)	0.048(30)	

function (3.34) and its uncertainties are presented. For the $E2/M1$ multipole-mixing ratio analysis, the plots a) and d) are relevant. The parameters a_2 and a_4 from the fitting procedure in a) are inserted in Figure 4.24 d). The ellipse in Figure 4.24 d) shows the relation from Eq. (3.36) of the coefficients a_2 and a_4 to the $E2/M1$ multipole-mixing ratio δ . This δ -determination procedure was performed for the transitions $2_7^+ \rightarrow 2_1^+$, $2_3^+ \rightarrow 2_2^+$, and $2_3^+ \rightarrow 2_1^+$, see Table 4.8 for the results, Figures 4.24 and C.6 for the angular distributions and Figures C.5, C.7 and C.8 for the corresponding ring-wise spectra.

The results revealed the pronounced $M1$ nature of the transitions $2_7^+ \rightarrow 2_1^+$ ($\delta = 0.06(4)$) and $2_3^+ \rightarrow 2_2^+$ ($\delta = -0.13(3)$). In the case of $2_3^+ \rightarrow 2_1^+$, δ could not be determined unambiguously, $\delta_1 = 0.02(7)$ and $\delta_2 = 2.1(4)$. For the identification of the $2_{1,\text{ms}}^+$ state, the $M1$ nature of the transition to the 2_1^+ state is not sufficient, the necessary deduction of the absolute $B(M1; 2_i^+ \rightarrow 2_1^+)$ strengths will be figured out by the CE calculations in the following section.

The relative long lifetimes of the states 4_1^+ [$\tau(4_1^+) = 20(4)$ ps] and 2_2^+ [$\tau(2_2^+) = 2.95(9)$ ps] also led to a de-orientation of the nuclear spins and, consequently, to a smear-out effect of the angular distributions of their γ -ray transitions $4_1^+ \rightarrow 2_1^+$ and $2_2^+ \rightarrow 2_1^+$, see Figure C.6 for the angular distributions and Figures C.3 and C.10 for the corresponding spectra, respectively. The angular distribution of the $3_2^- \rightarrow 2_1^+$ represents a typical electrical dipole distribution, see Figure 4.24 c). The counted events for the ring-wise analysis for certain transitions is presented in Table C.2. The statistics of the remaining transitions were insufficient for a proper

angular distribution analysis.

4.2.3. CE Analysis of ^{202}Hg

The directly-accessible observables of γ -ray spectroscopy are the intensities of the γ -ray transitions. For the calculation of the transition matrix elements from that, the multi-step CE code CLX [111] was utilized. CLX calculates the population yields of the excited states relative to a normalization state from a given set of transition matrix elements. It is important, especially for low γ -ray energies ($E_\gamma \approx 100$ keV), to consider electron conversion. The electron conversion coefficients were determined by using the code BRICC [97]. In this experiment, the 2_1^+ state was taken for the self-normalization, because it is the lowest-lying, most populated state and its transition strength to the ground state is well known, $B(E2; 2_1^+ \rightarrow 0_1^+) = 17.35(14)$ W.u. [112, 113], as well as its diagonal matrix element $\langle 2_1^+ || E2 || 2_1^+ \rangle = -1.33(17)$ eb. Further previously measured γ -ray transition strengths of ^{202}Hg , see Table 4.9, are not used as fixed parameters in the following CE analysis, but for testing the results.

The multi-step CE code CLX, as it is used in this work, needed some certain input parameters:

- a list of involved nuclear levels with their energy, spin and parity,
- the nucleon numbers of target and beam particle,
- the average beam energy,
- the scattering range of the beam particles in the center-of-mass system,
- and a set of transition matrix elements.

The spin and parity of the excited states is mostly known, otherwise educated assumptions were made. The ion-beam energy hitting the target is precisely determined, $E_{\text{beam}} = 4.4 A \cdot \text{MeV}$. However, it was necessary to determine the energy loss of the beam particle in the target [92] to obtain the remaining beam energy in the middle of the target, $E_{\text{av,beam}} = 4.1 A \cdot \text{MeV}$. That value was taken as the average kinetic energy of the γ -ray emitting ions. The experiment was performed without any heavy particle detection. Hence, all scattered ^{202}Hg particles were relevant regardless of their scattering angle. In reality, the range of the scattered beam particles is quite narrow, see Figure 4.20.

Table 4.9.: Previously measured absolute transition strengths of ^{202}Hg . Solely, the transition strength of the $2_1^+ \rightarrow 0_1^+$ transition was used as a fixed input parameter for the CLX calculations.

Transition	$E\lambda$	$B(E\lambda) \downarrow$ (W.u.) ^a
$2_1^+ \rightarrow 0_1^+$	$E2$	17.35(14)[112, 113]
$2_2^+ \rightarrow 0_1^+$	$E2$	0.087(21)[112, 114]
$2_2^+ \rightarrow 2_1^+$	$E2$	5.6(15)[112, 114]
$4_1^+ \rightarrow 2_1^+$	$E2$	26.5(8)[112, 114]
$6_1^+ \rightarrow 4_1^+$	$E2$	25[114]
$3_2^- \rightarrow 0_1^+$	$E3$	<25[115]

^a $B(E2)$ and $B(E3)$ values are given in Weisskopf units [$1 \text{ W.u.}(E2) = 70.4 \text{ e}^2\text{fm}^4$, $1 \text{ W.u.}(E3) = 2.42 \times 10^3 \text{ e}^2\text{fm}^6$].

Furthermore, the near- 4π coverage of Gammasphere led to the assumption of a γ -ray detection efficiency independent from the γ -ray emission angle. For a non- 4π detector array, the angular distribution of the γ -ray emission has to be taken into account, because the efficiency of the array might be highly angle-dependent, because the detectors may not be equally distributed in a spherical shape as it is the case for Gammasphere.

The sought-for variables in this procedure were the transition MEs, which were the essential input parameters for the CLX calculations. So, they were step-by-step varied until the CLX-calculated CE yields were equal to the experimental population yields. That procedure resulted in a final set of electric transition MEs.

For the final error estimation of the transition matrix elements, a python3 code using CLX was constructed, see Listing D.2. This code utilizes a set of random numbers to produce a set of input parameters, e.g., beam energy, known transition matrix elements, and experimental yields. These quantities are assumed as Gaussian distributions. There are also dependent MEs, which are predetermined by the corresponding ME, the branching ratio, the transition energies and the multipole-mixing ratios by the relation (3.26).

For each set of random numbers several iterations were performed to minimize the deviation from the calculated to the experimental yields. The final results after many sets of random numbers were probability distributions for every transition ME, see Figure 4.26. From those distributions, the mean values and the standard

deviations of the involved transition MEs were obtained. The efficiency-corrected γ -ray intensities are noted in Table 4.10 with the the absolute transitions strengths, which were determined by the transition MEs from Figure 4.26.

It is obvious from the decreased MEs connecting the 2_2^+ state with the 0_1^+ and 2_1^+ states, that the population yield of the 2_2^+ state is less than expected from its previously known $E2$ transition strengths. However, besides that, the known MEs were nicely reproduced in the CLX calculations, especially, the $B(E2)$ values of the yrast transitions $6_1^+ \rightarrow 4_1^+$ and $4_1^+ \rightarrow 2_1^+$, compare Tables 4.9 and 4.10. The precise agreement shows the quality of this CE calculation using CLX.

Table 4.10.: Measured properties of the levels and γ -ray transitions in ^{202}Hg . Level energies and spin assignments are adopted from Ref. [116], unless otherwise noted. The relative γ -ray intensities are corrected for efficiency.

E_{level} (keV)	J^π	E_γ (keV)	J_f^π	I_γ	$E\lambda$	$B(E\lambda) \downarrow^a$ (W.u.)	$B(M1) \downarrow$ μ_N^2
439	2_1^+	439	0_1^+	$1.00(1) \times 10^6$	$E2$		
960	2_2^+	960	0_1^+	620(13)	$E2$	0.039(3)	
		520	2_1^+	4444(44)	$E2$	2.7(3)	$43(8) \times 10^{-4}$
1120	4_1^+	680	2_1^+	4008(41)	$E2$	26.6(5)	
1182	2_3^+	1182	0_1^+	$< 50^b$	$E2$	< 0.015	
		743	2_1^+	183(4)	$E2$	$0.54^{+0.09}_{-0.47}$	$33^{+5}_{-29} \cdot 10^{-5}$
		222	2_2^+	356(15)	$E2$	9^{+5}_{-8}	$0.13^{+0.07}_{-0.12}$
1312	4_2^+	872	2_1^+	113(13)	$E2$	0.74(6)	
		352	2_2^+	221(9)	$E2$	137(17)	
		129	2_3^+	38(17)	$E2$	3413(1216)	
1348	$(2^+)^c$	908	2_1^+	73(7)	$E2$	1.52(4)	
1390	2_4^+	1390	0_1^+	$15(6)^b$	$E2$	0.013(1)	
		950	2_1^+	136(6)	$E2$	< 1	$< 6 \times 10^{-3}$
		429	2_2^+	39(4)	$E2$	12(4)	
		207	2_3^+	20(5)	$E2$	234(96)	
1564	0_3^+	1125	2_1^+	114(6)	$E2$	5.8(2)	
1575	2_5^+	1136	2_1^+	$15(5)^b$	$E2$	0.47(2)	
		615	2_2^+	26(3)	$E2$	17(6)	



1643	0_4^+	1204	2_1^+	44(6)	<i>E2</i>	2.6(1)	
1794	2_7^+	1794	0_1^+	30(14) ^b	<i>E2</i>	0.13(6)	
		1354	2_1^+	1086(17)	<i>E2</i>	0.1(1)	0.18(8)
		833 ^d	2_2^+	33(7)	<i>E2</i>	6(3)	
1823	2_8^+	1823	0_1^+	18(7) ^b	<i>E2</i>	0.052(3)	
		1384	2_1^+	221(13)	<i>E2</i>	< 4	< 0.027
		864	2_2^+	91(7)	<i>E2</i>	11(4)	
		641	2_3^+	37(3)	<i>E2</i>	19(7)	
1966	5_1^-	654	4_2^+	78(5)	<i>E1</i>		
1966	2_{10}^+	1527	2_1^+	171(30)	<i>E2</i>	10.0(3)	
		655	4_2^+	14(3)	<i>E2</i>	55(22)	
1989	6_1^+	868	4_1^+	21(2)	<i>E2</i>	24.9(1)	
2134	$(2^+)^c$	1014	4_1^+	94(6)	<i>E2</i>		
2293	$(3, 4)^e$	1853	2_1^+	117(8)	<i>E2</i>	3.40(5)	
2357	3_1^-	2357	0_1^+		<i>E3</i>	2.5(1)	
		1917	2_1^+	328(13)	<i>E1</i>		
		1396	2_2^+	247(16)	<i>E1</i>		
		1174 ^d	2_5^+	100(8)	<i>E1</i>		
		1045 ^d	4_2^+	100(9)	<i>E1</i>		
2456	$(2^+)^c$	1495 ^d	2_2^+	42(15)	<i>E2</i>		
2516	$(1, 2)^c$	2516	0_1^+	181(11)	<i>E2</i>	0.11(1)	
2681 ^d	$(2^+)^c$	2681 ^d	0_1^+	226(14)	<i>E2</i>	0.20(2)	
2709	3_2^-	2709	0_1^+		<i>E3</i>	21(1)	
		2264 ^d	2_1^+	611(23)	<i>E1</i>		
		1747 ^d	2_2^+	2431(51)	<i>E1</i>		
		1524 ^d	2_3^+	373(29)	<i>E1</i>		
		914 ^d	2_7^+	122(14)	<i>E1</i>		
3166	3_3^-	3166	0_1^+		<i>E3</i>	1.0(1)	
		1983 ^d	2_3^+	74(36)	<i>E1</i>		

^a $B(E2)$ and $B(E3)$ values are given in Weisskopf units [$1 \text{ W.u.}(E2) = 70.4 \text{ e}^2 \text{ fm}^4$, $1 \text{ W.u.}(E3) = 2.42 \times 10^3 \text{ e}^2 \text{ fm}^6$].

^b Calculated via literature branching ratio [116].

^c Assumed 2^+ state in the analysis.

^d Newly observed.

^e Assumed 4^+ state in the analysis.

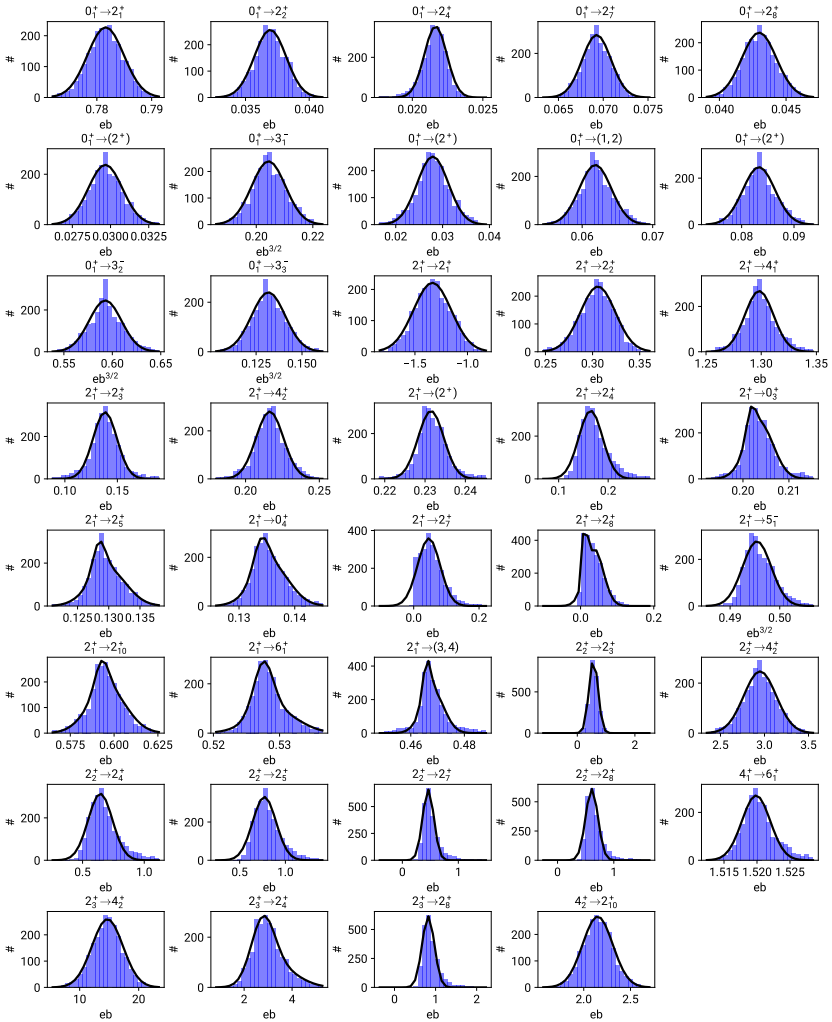


Figure 4.26.: The probability distributions of the transition matrix element using the python3 code which uses CLX, see Listing D.2.

4.3. γ -Ray Spectroscopy after β^+/ϵ Decay at the Heavy Ion Laboratory (HIL)

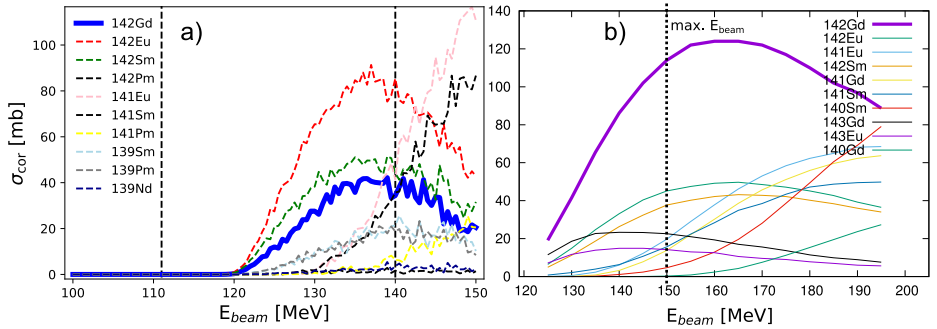


Figure 4.27.: The theoretical fusion evaporation cross sections of various reaction channels of the bombarding of a ^{114}Cd target with a ^{32}S beam. The reaction codes PACE4 and COMPA, a) and b), respectively, predict different relative cross sections of the various channels. The dashed vertical lines in a) represent the beam energy at the entrance of the target, 140 MeV, and the corresponding exit energy, ≈ 110 MeV, when using a 4 mg/cm 2 thick ^{114}Cd target.

The experiment at the Heavy Ion Laboratory (HIL) at Warsaw was designed to determine the $E2/M1$ multipole-mixing ratio δ of the $2_3^+ \rightarrow 2_1^+$ transition of ^{142}Sm . This multipole-mixing ratio is the missing piece of the MSS puzzle of ^{142}Sm . The sought-for δ will be determined through the measurement of the γ - γ angular correlation of the $2_3^+ \rightarrow 2_1^+$ and the $2_1^+ \rightarrow 0_1^+$ transitions of ^{142}Sm . The method is described in Section 3.2.

The primary goal is the population of the 2_3^+ state at 2055 keV of ^{142}Sm . It is directly populated by the β^+/ϵ decay of the short-lived isomer ($T_{1/2} = 2.34$ s) of ^{142}Eu [117, 118] with a probability of 1.6% per decay, but not at all from the decay of the long-lived one ($T_{1/2} = 1.223$ min) of ^{142}Eu [118]. Regarding the direct production of ^{142}Eu via fusion-evaporation reactions, solely the population of the long-lived isomer was measured so far [119–121]. However, the short-lived

isomer was observed via the β^+/ϵ decay of ^{142}Gd ($T_{1/2} = 70.2\text{ s}$) [117], which itself was produced in fusion-evaporation reactions.

Generally, the fusion of two nuclei may happen, if the kinetic energy of an incoming beam particle is high enough to overcome the Coulomb barrier of the target nucleus. The beam and target particles fuse to a new highly-excited compound nucleus, which de-excites via an emission of particles. In this way, a large variety of isotopes are produced. For an estimation of the cross sections of the different isotopes, fusion-evaporation codes are utilized, e.g., PACE4 [122, 123] and COMPA [124, 125].

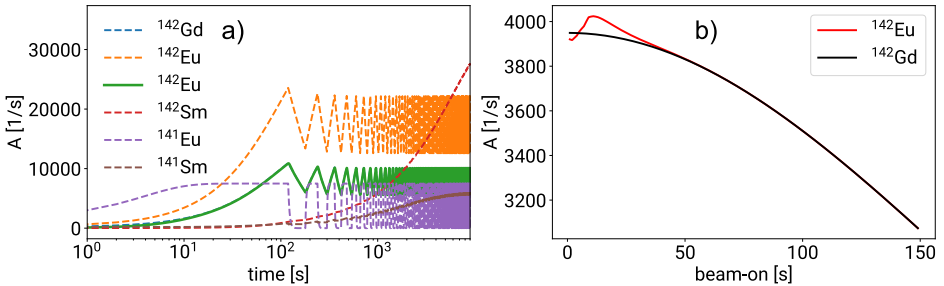


Figure 4.28.: The sub figure a) presents the evolution of the activities of isotopes in a beam-on and beam-off mode, 60 seconds periods, and an activation time of 60 seconds at the start. These isotopes are the most prominent ones in the presented fusion-evaporation reaction. b) shows the dependence of the activity of the short-lived isomer of ^{142}Eu on the period length, while the beam-on time equals the beam-off time.

The designed experiment aims for the $4n$ channel, meaning the evaporation of four neutrons after the fusion, $^{146}\text{Gd} \rightarrow ^{142}\text{Gd} + 4n$, and, hence, for the compound nucleus ^{146}Gd . Finally, for the production of the neutron-deficient ^{146}Gd , the combination of a ^{32}S beam on a ^{114}Cd target at the HIL was chosen.

The resulting cross sections of the various reaction channels in dependence of the beam energy are monitored by using PACE4. The PACE4 calculations show a maximum of the $4n$ reaction at a beam energy of ≈ 140 MeV near the Coulomb barrier ($V_C \approx 141$ MeV), see Figure 4.27 a). At this energy region and below, the $3n + p$ and $2n + 2p$ channels to ^{142}Eu and ^{142}Sm , respectively, are the predominant

reactions together with the desired $4n$ channel. For higher energies than 140 MeV, the cross section of the $4n$ channel decreases and the ones of the $4n+p$ and $3n+2p$ channels to ^{141}Eu and ^{141}Sm , respectively, increase rapidly. Hence, the PACE4 calculations lead to the conclusion of a beam energy of 140 MeV to suppress the production of ^{141}Eu and ^{141}Sm .

Calculations of our polish collaborators from the group of Julian Srebrny (HIL, University of Warsaw) using the nuclear reaction code COMPA [124, 125] indicate even a much higher relative production of our desired isotope ^{142}Gd , see Figure 4.27 b). Furthermore, they would allow higher beam energies up to 190 MeV before other reaction products' intensities would overcome the one of ^{142}Gd . The final conclusion of regarding both calculations and the energy loss in the target, see Figure 4.27 a), is the demand of a ^{32}S beam with an energy between 140 MeV and the maximum 150 MeV of the HIL cyclotron [126] to maximize the production of ^{142}Gd .

For the determination of the populations and activities of the various produced isotopes, it is important to know their population paths. While some are only directly produced by a fusion-evaporation reaction, i.e., ^{142}Gd , others are produced by the followed β^+/ϵ decay, i.e., the short-lived isomer of ^{142}Eu , and there are even some, which are populated through more than one channel, i.e., ^{142}Sm . For more information on how the activities were determined in detail, see the used python code in Listing E.1. Here, the ansatz $A(t) = \frac{d}{dt}N(t)$ was chosen, where A is the activity and N is the number of nuclei, and solved analytically for the different population paths. A second part of the code performs simulations with only the ansatz of the probability of the decay as an exponential distribution. Fortunately, the activities were reproduced with this computationally intensive method.

The experiment aims for the detection of the delayed γ -rays from the β^+/ϵ decay of ^{142}Eu . Hence, a method is needed to suppress the prompt γ -ray emission from especially CE. So, a beam-on-off mode of the accelerator has been designed specifically for our experimental request. Here, the beam is automatically blocked and released by an in-and-out driving Faraday cup. The period of this process is chosen to be ≈ 1 min. It is a compromise of the maximization of the activity of the mother nucleus ^{142}Eu ($T_{1/2} = 2.40$ s) and the sparing of the mechanics of the beam-chopping process, see Figure 4.28 b). The resulting activities for the main products are shown in Figure 4.28 a) assuming a maximum beam current of 2.7×10^{10} pps [126], the cross sections from Figure 4.27 a) and 60 s of beam-on-target and beam-off-target time, each.

Table 4.11.: Left: the amount of detector pairs of each angle group for a certain configuration of the 15 HPGe detectors of EAGLE and the corresponding estimated count rates per day, $r_{\gamma\gamma}$ [(see Eq. (4.3)], of the $2_3^+ \rightarrow 2_1^+ \rightarrow 0_1^+$ γ - γ coincidence. Right: the parameters used for the rate estimation in Eq. (4.3).

angle	# pairs	$r_{\gamma\gamma}$	parameter	
180°	5	51	$A_s(^{142}\text{Eu})$	7564 $\frac{1}{\text{s}}$
138°	15	153	T_{off}	60 s
110°	31	316	T_{off}	60 s
70°	35	357	$R(2_3^+)$	1.6%[118]
42°	19	194	$I_{\text{rel}}(2_3^+ \rightarrow 2_1^+)$	72%[118]
			$\epsilon_{\gamma 1, \gamma 2}$	1.5 & 1.9 % [127]
total	105	1073		

The γ -ray emission of the produced radioactive isotopes will be detected by the EAGLE array, which consists at the moment of 15 HPGe detectors with a total efficiency of 1.9 % and 1.5 % at the energies of the $2_3^+ \rightarrow 2_1^+$ and $2_1^+ \rightarrow 0_1^+$ transitions, 1.3 and 0.8 MeV, respectively [127]. For more information, see Ref. [80]. For the measurement of angular distributions of γ - γ coincidences, it is necessary to categorize the detector pairs in groups with similar angles. The angles are determined by the triangle set up by the first detector, the target and the second detector. In this way, it is possible to use 105 detector pairs representing the angles 42°, 70°, 110°, 138°, and 180° [127]. In any case, it is not possible to get more than five detector pairs with an angle of 180° with 15 usable detectors. The resulting distribution of the detector pairs to angle groups is shown in Table 4.11.

For the planning of a successful γ -spectroscopic experiment, it is inevitable to estimate the rates of the sought-for γ -ray transitions. Here, the rate of the γ - γ coincidence $2_3^+ \rightarrow 2_1^+ \rightarrow 0_1^+$ of ^{142}Sm is given by

$$\begin{aligned}
 r_{\gamma\gamma} &= A_s(^{142}\text{Eu}) \times \frac{T_{\text{off}}}{T_{\text{off}} + T_{\text{on}}} \times R(2_3^+) \times I_{\text{rel}}(2_3^+ \rightarrow 2_1^+) \times \epsilon_{\gamma_1}\epsilon_{\gamma_2} \\
 &= 0.012 \frac{1}{s}.
 \end{aligned}
 \tag{4.3}$$

$A_s(^{142}\text{Eu})$ is the activity of the short-lived isomer in the equilibrium and determined via Figure 4.28, T_{off} and T_{on} are the periods with beam off and on the target, respectively, and $R(2_3^+)$ is the relative population of the 2_3^+ state of ^{142}Sm from the β^+/ϵ decay of the short-lived isomer of ^{142}Eu . Furthermore, $I_{\text{rel}}(2_3^+ \rightarrow 2_1^+)$ is the relative intensity of the $2_3^+ \rightarrow 2_1^+$ transition with respect to all γ -ray decays of the 2_3^+ state and $\epsilon_{\gamma_1, \gamma_2}$ are the total γ -ray efficiencies at the γ -ray energies 1287 keV and 768 keV. The chosen values of these parameters are presented in Table 4.11.

This conservative estimation leads to ≈ 500 events for the lowest-statistics angle group (180°) for the full ten days of measurement, which ends up in a relative uncertainty of $\approx 5\%$ and a general good feasibility of such an experiment. However, the rates will increase by at least the factor three when the cross sections from J. Srebrny, see Figure 4.27 b), are adopted.

A successful execution of this experiment enables the determination of the multipole-mixing ratio of the $2_3^+ \rightarrow 2_1^+$ transition of ^{142}Sm . This additional spectroscopic observable will cause a distinct $B(M1; 2_3^+ \rightarrow 2_1^+)$ from the GOSIA calculations of the ^{142}Sm CE experiment at HIE-ISOLDE.

Besides that, a panoply of radioactive isotopes will be produced in this experiment. This γ - γ coincidences data may create an access to diverse unknown spectroscopic observables of the neutron deficient isotopes northwest of the doubly-magic nucleus ^{132}Sn .



5. Discussion

The obtained results will be discussed in context with previous measurements of neighboring isotopes and theoretical predictions. Additionally, the determined $M1$ -strength distributions will be used to identify the low-lying isovector quadrupole excitation, the $2_{1,\text{ms}}^+$ state, and to calculate the F -spin mixing matrix element of the corresponding isotopes.

5.1. $N = 80$ Isotones ^{140}Nd and ^{142}Sm

The visible effects of the sub-shell structure of the $N = 80$ isotones on the collective one-quadrupole-phonon excitations were introduced in Chapter 1. This effect is extraordinarily pronounced for the isovector quadrupole excitation causing an isolated $2_{1,\text{ms}}^+$ state for the isotones ^{132}Te , ^{134}Xe and ^{136}Ba [12, 18, 19], but a sudden fragmentation of this excitation for ^{138}Ce . At $Z = 58$, the total $B(M1; 2_i^+ \rightarrow 2_1^+)$ strength is almost equally distributed to the $2_3^+ \rightarrow 2_1^+$ and $2_4^+ \rightarrow 2_1^+$ transitions at 1354 and 1448 keV. This fragmentation of the $2_{1,\text{ms}}^+$ state was the first experimental evidence of a direct influence of the sub-shell structure on the characteristics of MSSs [10]. This effect is called valence-shell stabilization of the quadrupole isovector excitations and is not present at the $Z = 58$ sub-shell closure. The presence and the lacking of the valence-shell stabilization effects besides the $B(M1; 2_i^+ \rightarrow 2_1^+)$ distributions of the $N = 80$ isotones primarily the corresponding F -spin mixing matrix element $V_{F-\text{mix}}$. Hence, the investigation of the $2_{1,\text{ms}}^+$ states of the $N = 80$ isotones ^{140}Nd and ^{142}Sm is of exceptional importance to probe the effect of the valence-shell stabilization when exceeding the proton sub-shell closure at $Z = 58$.

For ^{140}Nd , the obtained $B(M1; 2_i^+ \rightarrow 2_1^+)$ distribution leads to the identification of the 2_3^+ state as the main fragment of the $2_{1,\text{ms}}^+$ state with $B(M1; 2_3^+ \rightarrow 2_1^+) = 0.26_{-0.10}^{+0.11} \mu_N^2$, see Figure 5.1 a). Furthermore, the weakly collective transition from the ground state, $B(E2; 2_3^+ \rightarrow 0_1^+) = 1.9(6)$ W.u., is in agreement with the mixed-symmetry one-phonon character of the $2_{1,\text{ms}}^+$ state (≈ 1 W.u. [63]). For

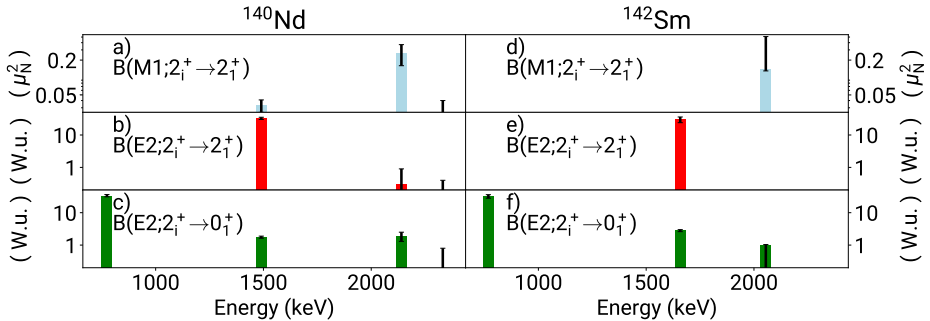


Figure 5.1.: The values for $B(M1; 2_i^+ \rightarrow 2_1^+)$, $B(E2; 2_i^+ \rightarrow 2_1^+)$ and $B(E2; 2_i^+ \rightarrow 0_1^+)$ strengths of ^{140}Nd and ^{142}Sm deduced in the reported CE experiments are displayed in a)-c) and d)-f), respectively. For ^{142}Sm , the $E2/M1$ multipole mixing ratios are unknown, hence, for the 2_3^+ state at 2055 keV, a pure $M1$ decay to the 2_1^+ state was assumed to estimate an upper limit for the $B(M1; 2_3^+ \rightarrow 2_1^+)$ strength.

the determination of the F -spin mixing matrix element $V_{F\text{-mix}}$, it is necessary to measure the absolute $M1$ transition strength of the decay of a potential minor fragment. Here, the 2_4^+ state is assumed to be the small fragment of the $2_{1,\text{ms}}^+$ state, because it is the closest-lying 2^+ state to the 2_3^+ state and shares also the decay properties with the $2_{1,\text{ms}}^+$ state: it exhibits a predominant $M1$ transition to the 2_1^+ state, $\delta = -0.19(9)$ [24]. Unfortunately, the known γ -ray transitions from the 2_4^+ state to the 2_1^+ and 0_1^+ states [95] were not observed in the reported CE experiment. Nevertheless, an upper limit of the value of $B(M1; 2_4^+ \rightarrow 2_1^+) < 0.04 \mu_N^2$ was determined by using experimental yields of the γ -ray decays of the 2_4^+ state at the edge of the detection limit for the GOSIA analysis.

Calculations of a two-state mixing scenario where $M1$ transitions are forbidden between FSSs yielded the upper limit of $V_{F\text{-mix}} < 79$ keV for ^{140}Nd . Regarding the obvious domination of the $B(M1; 2_3^+ \rightarrow 2_1^+)$ strength in the $B(M1)$ distribution of ^{140}Nd , see Figure 5.1 a), the deduced upper limit is not quite meaningful. Especially with respect to the mixing $V_{F\text{-mix}} = 44(3)_{-14}^{+3}$ keV of ^{138}Ce , where the $2_{1,\text{ms}}^+$ state is obviously highly fragmented. The ratio of the $B(M1; 2_i^+ \rightarrow 2_1^+)$ values of the main and small fragments of ^{140}Nd is greater or equal four, while it

is only approximately two for ^{138}Ce . Hence, the origin of this seemingly enhanced $V_{F\text{-mix}}$ of ^{140}Nd is the increased energy difference of $\Delta E = 193\text{ keV}$ between the potential two fragments of the $2_{1,\text{ms}}^+$ state, if any remnant $M1$ strength from outside of the model range may exist.

In reality, nuclear states are neither ideal FSSs nor MSSs. Even if a state comes very close to this theoretical construct, i.e., the 2_1^+ state, it is more complex than that. Consequently, there is a small part of experimental FSSs which may allow for $M1$ transitions between them, which are originated outside the framework of the IBM. In the following, this $M1$ strength between FSSs is called background $M1$ strength. In ^{140}Nd , it is determined by the value of $B(M1; 2_2^+ \rightarrow 2_1^+) = 0.033(8)\mu_N^2$, because the 2_2^+ state is considered as the fully-symmetric two-quadrupole-phonon 2^+ state. This is a legitimate assumption, because the 2_3^+ state as the main fragment of the $2_{1,\text{ms}}^+$ state is far away ($\Delta E = 650\text{ keV}$) and the decay to the 2_1^+ state is predominantly of $E2$ nature, $\delta = -1.22(14)$ [24]. The calculations of this specific scenario are described in Section 2.4 and result in a renewed upper limit for the F -spin mixing matrix element of ^{140}Nd , $V_{F\text{-mix}} < 7_{-7}^{+13}\text{ keV}$. This value is significantly smaller than the upper limit of the first scenario and the $V_{F\text{-mix}} = 94(12)\text{ keV}$ from Ref. [24], where the F -spin mixing matrix element was deduced only on the base of $E2/M1$ multipole-mixing ratios. The near-zero values of δ of both transitions lead to the conclusion of a mixing near the maximum ($V_{F\text{-mix}} = \Delta E/2 = 96\text{ keV}$), which could only be corrected by the measurement of the absolute $M1$ transition strengths.

The $V_{F\text{-mix}}$ and the $B(M1; 2_i^+ \rightarrow 2_1^+)$ strength distribution of ^{140}Nd in the context of the $N = 80$ isotonic chain, see Figure 5.2, are showing a restoration of the valence-shell stabilization at $Z = 60$. The observed enhanced $B(M1; 2_3^+ \rightarrow 2_1^+)$ strength and the decrease of $V_{F\text{-mix}}$ from ^{138}Ce to ^{140}Nd are caused by the partly filled $d_{5/2}$ proton orbital. Hence, the collective excitations are now formed by the valence nucleons without breaking the filled orbital structure as it the case for ^{138}Ce .

The interpretation of the reported ^{142}Sm CE experiment in terms of the low-lying isovector quadrupole excitation is ambiguous because of the lacking $M1/E2$ multipole-mixing ratios of the $2_i^+ \rightarrow 2_1^+$ transitions. The structure of the excited levels of ^{140}Nd is quite similarly observed for ^{142}Sm . Therefore, the 2_3^+ state is also assumed to be the main fragment of the $2_{1,\text{ms}}^+$ state of ^{142}Sm . The preliminary results of the CE experiment and the prior evolution of the $2_{1,\text{ms}}^+$ states of the $N = 80$ isotones lead to that conclusion.

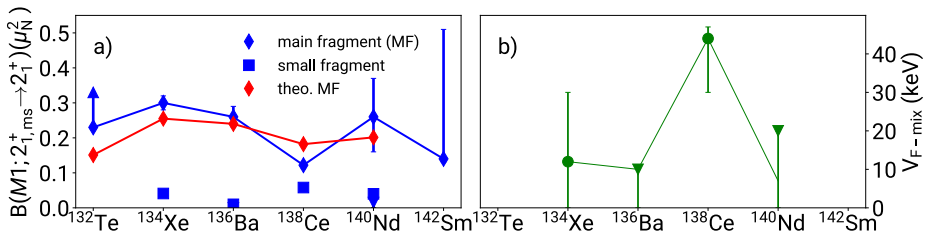


Figure 5.2.: The $M1$ transition strengths $B(M1; 2_i^+ \rightarrow 2_1^+)$ of the main and the small fragment of the $2_{1,ms}^+$ state of the $N = 80$ isotones are compared to a theoretical $B(M1; 2_{1,ms}^+ \rightarrow 2_1^+)$ systematic [red, Ref. [25)] in a)]. For ^{142}Sm , a multipole-mixing ratio of $\delta = 0.01$ for the $2_3^+ \rightarrow 2_1^+$ transition was assumed. The resulting F -spin mixing matrix elements (\circ) and upper limits (∇) are shown in b). $V_{F\text{-mix}}$ of ^{136}Ba and ^{138}Ce are taken from Ref. [10].

The remaining possible candidates, the $(2)^+$ state at 1658 keV, introduced as 2_2^+ state, and the (2^+) states at 2353 and 2374 keV [105], exhibit decay characteristics, which are unlikely for the $2_{1,ms}^+$ state.

The 2_2^+ state decays predominantly to the ground state and the similarities of the level structure to ^{140}Nd lead rather to the assumption that the 2_2^+ state is the two-phonon 2^+ state. However, due to its strong population, the 2_2^+ state remains a possible candidate for the $2_{1,ms}^+$ state unless rejected by the determination of $E2/M1$ multipole-mixing ratios.

The ground state decay of the (2^+) state at 2353 keV is prominent in the γ -ray spectra, while γ rays of the transition to the 2_1^+ state are not. Hence, this state can not have a sufficiently strong $M1$ connection to the 2_1^+ state for being the major fragment of the $2_{1,ms}^+$ state.

In a scenario, where the (2^+) state at 2374 keV is the main fragment of the $2_{1,ms}^+$, a similar $B(E2; (2^+) \rightarrow 0_1^+)$ would be expected as the (2^+) at 2354 keV ($\approx 1\text{W.u.}$). Since it is not excited while having a similar energy, it has consequently an even smaller excitation probability and, hence, the chances of being the $2_{1,ms}^+$ state are heavily decreased. This experiment is not sensitive on significantly higher-lying $2_{1,ms}^+$ states. Furthermore, this would also be very uncommon, regarding the

energies of the known $2_{1,\text{ms}}^+$ states of the lighter $N = 80$ isotones.

Table 5.1.: Determined $M1$ transition strengths of the unperturbed 2_{MS}^+ states and the $E2$ ratios $B_{4/2}$ and $B_{2/2}$ of the $N = 80$ isotones ^{140}Nd and ^{142}Sm .

	^{140}Nd	^{142}Sm
$B(M1; 2_{\text{MS}}^+ \rightarrow 2_1^+) [\mu_{\text{N}}^2]$	0.27(11)	$< 0.15_{-0.04}^{+0.37a}$
$B_{4/2}$	1.2(1)	1.6(3)
$B_{2/2}$	0.98(12)	0.97(23)

^aThe $M1$ strengths between FSSs and of the transition from the minor fragment from ^{140}Nd are applied to the calculations for ^{142}Sm .

The $M1$ strength's upper limit of the most promising candidate for the $2_{1,\text{ms}}^+$ state, $B(M1; 2_3^+ \rightarrow 2_1^+) < 0.14_{-0.01}^{+0.37} \mu_{\text{N}}^2$, was estimated by applying a realistic almost pure $M1$ $2_3^+ \rightarrow 2_1^+$ transition ($\delta = 0.01$) to the GOSIA calculations. The uncertainties were determined by the built-in error estimation of GOSIA. The obtained upper limit does not stand in conflict with the conclusion of the restoration of the valence-shell stabilization at $Z = 60$ from the ^{140}Nd CE experiment. However, on the basis of an upper limit of the $B(M1; 2_3^+ \rightarrow 2_1^+)$ with the 2_3^+ state as the potential main fragment, it is not feasible to determine a meaningful limit for $V_{\text{F-mix}}$ of ^{142}Sm .

Furthermore, the big energy difference of more than 300 keV between the 2_3^+ state and the nearest-lying 2^+ state makes it very challenging to determine a significant F -spin mixing matrix element. The calculations will result in an enhanced $V_{\text{F-mix}}$ due to the large energy difference unless the $B(M1; 2_i^+ \rightarrow 2_1^+)$ strength of the minor fragment is small with very high precision. Unfortunately, the accuracy of the transition strength of a radioactive isotope measured in CE is often suffering due to low statistics. Although, for the identification of the $2_{1,\text{ms}}^+$ state of ^{142}Sm , the determination of the $E2/M1$ multipole-mixing ratios are indispensable. Therefore an angular correlation measurement of γ - γ coincidences after β^+/ϵ decay is planned and was described in Section 4.3 in detail.

The evolution of the $B(M1; 2_i^+ \rightarrow 2_1^+)$ strengths for the $N = 80$ isotonic chain was subject of several theoretical publications using the quasi-particle phonon model (QPM) [103, 128] and the shell model [25, 129]. Solely the large-scale shell model calculations of Ref. [25] using the shell model codes NATHAN and ANTOINE [61, 130] were able to reproduce a re-rise of the $B(M1; 2_{1,\text{ms}}^+ \rightarrow 2_1^+)$

value passing the $Z = 58$ sub-shell closure, see Figure 5.2. The other mentioned calculations predicted a similar fragmentation of the $2_{1,ms}^+$ state of ^{140}Nd as for ^{138}Ce . In Ref. [25], the *gds* shell was used as model space and the utilized interaction (GCN5082) was obtained by a fit of the Hamiltonian on many low-lying states of a large variety of isotopes within the 50 – 82 valence space for protons and neutrons. This phenomenological corrected interaction enabled the reproduction of experimental excitation energies of ≈ 400 states in 80 nuclei within a root-mean-square deviation of 110 keV [25, 131]. However, calculations of the $M1$ strengths distribution of low-lying 2^+ states for ^{142}Sm are lacking.

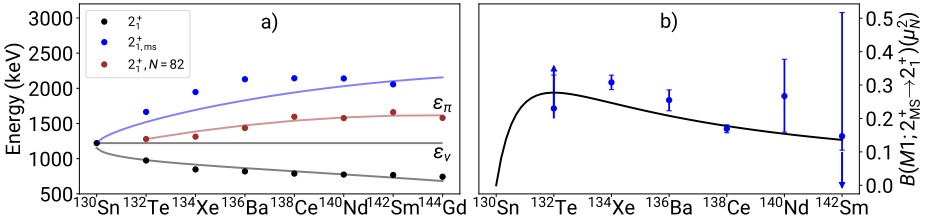


Figure 5.3.: a) presents the level energies of the 2_1^+ [95, 105, 132–136] and $2_{1,ms}^+$ [10, 12, 18, 19, 21] states of the $N = 80$ isotones, when available, and the ones of the 2_1^+ states of the semi-magical $N = 82$ isotonic chain [95, 105, 133–137] for comparison. The blue and black lines are determined by Eq. (5.2). b) shows the $B(M1; 2_{ms}^+ \rightarrow 2_1^+)$ strength evolution of the $N = 80$ isotones compared with the systematic [Eq. (2.41)] from the $U(5)$ symmetry for $\Delta g = |g_\pi - g_\nu| = 0.880(1) \mu_N^2$. The 2_{ms}^+ state is the theoretical unperturbed mixed-symmetry 2_{ms}^+ state.

The low-lying collective quadrupole excitations, namely the 2_1^+ and $2_{1,ms}^+$ states, can be interpreted as superpositions of two unperturbed valence-proton and valence-neutron 2^+ configurations. The proton-neutron quadrupole interaction increases with the valence space or more precisely, the product of the valence protons and neutrons $N_\pi N_\nu$. The resulting mixing interaction is given by [138]

$$V_{\nu\pi} = \beta_{\nu\pi} \sqrt{N_\pi N_\nu}, \quad (5.1)$$

where $\beta_{\nu\pi}$ is a scaling parameter for the mixing interaction. For the application of this model for the $N = 80$ isotonic chain, the energies of the unperturbed proton and neutron 2^+ excitations, ϵ_π and ϵ_ν , respectively, have to be determined analogously to the successful calculations for a shorter area of the $N = 80$ isotones [18] and the Xe isotopic chain [139]. The energy of the 2_1^+ state of semi-magic ^{130}Sn , which should be a pure neutron excitation ($\epsilon_\nu = 1221$ keV) due to its closed proton shell ($Z = 50$), determines the parameter ϵ_ν . Since the neutron number is the same for the nuclei of the $N = 80$ isotonic chain, ϵ_ν is applied to all of them as a constant. However, ϵ_π changes over the isotonic chain and is determined via a fit of the empirical function $\epsilon_\pi = \epsilon_0 + \epsilon_1(N_\pi - 1) + \epsilon_2(N_\pi - 1)^2$ to the energies of the 2_1^+ states of the semi-magic $N = 82$ isotones from ^{134}Te up to ^{146}Gd , see Figure 5.3 a). The 2_1^+ excitations of this isotonic chain should be pure proton excitations due to the closed neutron shell ($N = 82$). The parameter $\epsilon_0 = 1279$ keV is given by the 2_1^+ energy of semi-magic ^{134}Te , which has one valence-proton boson, and $\epsilon_{1,2} = 117, -10$ keV are determined via the fit process. The uncertainties are negligibly small. The resulting level energies of the 2_1^+ and $2_{1,\text{ms}}^+$ states of this two-state mixing scenario, see Eq. (2.44) in Section 2.4, are then given by

$$E(2_1^+, 2_{1,\text{ms}}^+) = \frac{\epsilon_\pi + \epsilon_\nu}{2} \mp \sqrt{\frac{(\epsilon_\pi - \epsilon_\nu)^2}{4} + \beta_{\nu\pi}^2 N_\pi N_\nu}, \quad (5.2)$$

where the - (+) sign corresponds to the energy of the 2_1^+ ($2_{1,\text{ms}}^+$) state. The data from ^{130}Sn up to ^{144}Gd were used to fit the energies of the 2_1^+ states and $\beta_{\nu\pi} = 0.27$ MeV was obtained and applied for predicting the energies of the $2_{1,\text{ms}}^+$ states from Eq. (5.2), see Figure 5.3 a).

The $2_{1,\text{ms}}^+$ levels are strongly affected by the sub-shell closure [10], but Eq. (5.2) is not sensitive to any sub-shell structures. Hence, Eq. (5.2) with $\beta_{\nu\pi}$ from the fit of the 2_1^+ states' energies can not describe the evolution of the energies of the isovector 2^+ states properly all along the isotonic chain. The trend of an increasing energy of the $2_{1,\text{ms}}^+$ level is in reality inverse from the sub-shell closure on.

The 2_1^+ levels are barely affected by the sub-shell closure and their energies are reproduced by Eq. (5.2). The energies of the low-lying one-quadrupole-phonon excitations show a similar behaviour as the transition probabilities. While the effect of the sub-shell closure is rather small on the isoscalar excitations, it is significant regarding isovector excitations.

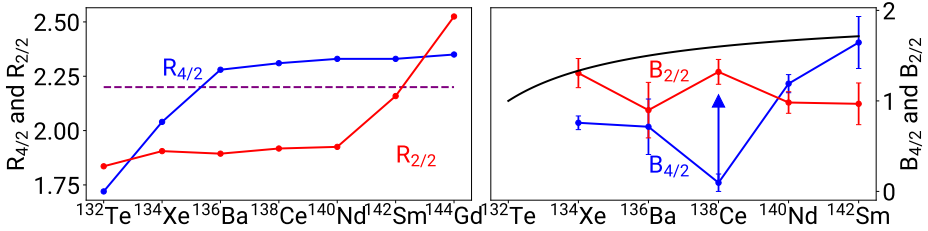


Figure 5.4.: a) presents the comparison of the ratios of the level energies of the two-phonon states 4_1^+ and 2_2^+ to the one-phonon state 2_1^+ , $R_{4/2}$ and $R_{2/2}$ [95, 105, 132–136], respectively, and the theoretical predictions from the $U(5)$ symmetry, $R_{4/2} \approx R_{2/2} \approx 2.2$ [6]. For ^{132}Te , the 2_3^+ state was assumed as the fully-symmetric two-phonon state, because the 2_2^+ state was identified as the $2_{1,\text{ms}}^+$ state [12]. b) shows the evolution of the ratios of the $E2$ transition strengths of the two- to one-phonon states transitions $4_1^+ \rightarrow 2_1^+$ and $2_2^+ \rightarrow 2_1^+$ and the $B(E2; 2_1^+ \rightarrow 0_1^+)$ strength [21, 132–136], $B_{4/2}$ and $B_{2/2}$. They are also compared to predictions from the $U(5)$ symmetry [Eq. (5.2) [140]].

Besides the $M1$ information giving an insight into the low-lying isovector valence-shell excitations of the $N = 80$ isotones, the $M1$ strength of the unperturbed 2_{ms}^+ states can be used to probe the $U(5)$ symmetry of the $N = 80$ isotones. The $B(M1; 2_{\text{ms}}^+ \rightarrow 2_1^+)$ strength of the unperturbed mixed-symmetry 2_{ms}^+ state is described in Section 2.4. The resulting values are noted in Table 5.1. The fit of the $B(M1)$ strengths originating from the $U(5)$ symmetry, see Eq. (2.41), on the available data of the $N = 80$ isotones is presented in Figure 5.3 b). $M1$ transition strength from Eq. (2.41) is only dependent on the number of valence bosons, N_ν and N_π , and the difference of the effective boson g -factors, g_π and g_ν . Figure 5.3 b) shows that the assumption of a $U(5)$ symmetry in the $N = 80$ is not in conflict with the obtained $B(M1; 2_i^+ \rightarrow 2_1^+)$ values. The upper and lower limit of the $B(M1)$ values of ^{132}Te and ^{142}Sm were used for the fit shown in Figure 5.3 b). The fit parameter $\Delta g = |g_\pi - g_\nu| = 0.880(1) \mu_N^2$ does not change significantly by excluding them from the fit. This is in good agreement with the general assumption of $g_\pi \approx 1$ and $g_\nu \approx 0$ [141].

The obtained CE data reveal also several $B(E2)$ values which are used to probe

the $U(5)$ symmetry for the $N = 80$ isotones. Here, transitions will be investigated which connect the two-quadrupole-phonon states (0_2^+ , 2_2^+ and 4_1^+) and the one-quadrupole-phonon state (2_1^+). In the simplified picture of the quadrupole-phonon model, these transitions are destructions of the symmetric quadrupole phonon as it is for the $2_1^+ \rightarrow 0_1^+$ transition. However, the two-phonon state has twice as many decay possibilities than the one-phonon state, because there are two phonons which can potentially be destroyed. Hence, the decay probability is doubled: $B(E2; 0_2^+, 2_2^+, 4_1^+ \rightarrow 2_1^+)/B(E2; 2_1^+ \rightarrow 0_1^+) = 2$ [6].

In the phonon model, the transition rate is solely related to the number of involved quadrupole phonons, but in the sd -IBM a destruction (or creation) of a d boson must involve a creation (or destruction) of an s boson. So, an increase of the number of d bosons leads to less available s bosons and, hence, a reduced probability to create (or destruct) one. Therefore, the ratio of transition strengths between full-symmetry two- and one-phonon states in $U(5)$ is given by [140]

$$\frac{B(E2; 0_2^+, 2_2^+, 4_1^+ \rightarrow 2_1^+)}{B(E2; 2_1^+ \rightarrow 0_1^+)} = 2 \frac{N-1}{N}, \quad (5.3)$$

where N is the number of valence bosons or holes. The ratios are smaller than two for a finite number of valence bosons and the spin of the fully-symmetric two-phonon state does generally not affect the transition strength. In Figure 5.4 b), the evolution of the ratios of the $E2$ strengths of the transitions between the two- and the one-phonon states are shown. The comparison of the predictions from the $U(5)$ symmetry, Eq. (5.3), which are related to the valence-boson number, shows conformity with the deduced transition strengths. The two ratios $B_{4/2}$ and $B_{2/2}$, which would be equal in a perfect $U(5)$ nucleus, are also in quite good agreement to each other.

A further indicator for the assignment of an isotope to a nuclear shape or symmetry is the ratio of the level energies of multi-phonon states to the ones of one-phonon states. In the rotational model and the harmonic vibrator phonon-model, the ratio of these level energies is two for vibrational nuclei, $R_{4/2} = E(4_1^+)/E(2_1^+) = R_{2/2} = E(2_2^+)/E(2_1^+) = R_{0/2} = E(0_2^+)/E(2_1^+) = 2$ [6]. However, the assumptions of additional two-body residual interactions may lead to a small increase and breaking of the degeneracy in the two-phonon energy levels. These energy additions are called anharmonicities and lead typically to an energy ratio of the two-phonon states to the one-phonon state slightly above two (≈ 2.2) [6].

The two energy ratios $R_{4/2}$ and $R_{2/2}$ of the $N = 80$ isotones fit in the predictions of the $U(5)$ symmetry and are far below the rotational limit ($R_{4/2} \approx 3.33$), which support the assumption of a vibrational shape of the nuclei along this isotonic chain, see Figure 5.4 a). For the $R_{2/2}$ of ^{132}Te , the 2_3^+ state was taken as the fully-symmetric two-phonon 2^+ state, because it was shown, that the 2_2^+ state was identified as the mixed-symmetry one-phonon 2^+ state. Summarized, the shapes of the $N = 80$ isotones from ^{132}Te up to ^{142}Sm can legitimately assumed to be vibrational and no significant effect of the sub-shell structure on the deformation was observed. It seems that the increase and decrease of the valence space have logically a significantly bigger influence on the shape of the nucleus than the sub-shell structure, when studying the energy ratios. The $R_{4/2}$ and the $R_{2/2}$ ratios are distant from the predicted value for ^{132}Te and ^{144}Gd , respectively. Additionally, the $R_{4/2}$ ratio is smaller than the $R_{2/2}$ ratio only for the two extreme isotones with the lowest and highest number of valence protons of the here regarded nuclei.

5.2. $Z = 80$ Isotopes ^{202}Hg and ^{204}Hg

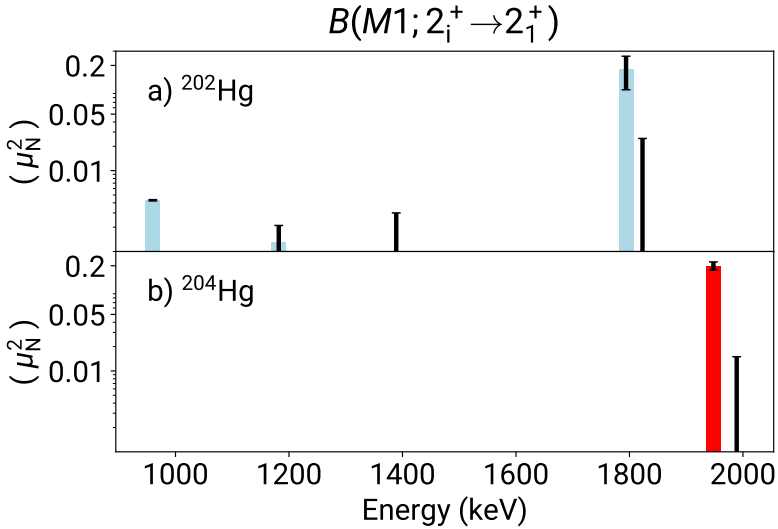


Figure 5.5.: $M1$ strength distributions $B(M1; 2_i^+ \rightarrow 2_1^+)$ of ^{202}Hg determined in the reported CE experiment a) and of ^{204}Hg b) [48]. Upper limits are illustrated by the errorbars extending to the bottom.

The identification of the low-lying isovector quadrupole excitation of ^{202}Hg was challenging due to the variety of excited 2^+ states and missing information about $E2/M1$ multipole-mixing ratios except for the $2_2^+ \rightarrow 2_1^+$ transition, which shows a balanced $M1$ and $E2$ nature [$\delta = 0.9(1)$ [110]]. In total eight states with a definitive and three states with a tentative 2^+ spin and parity assignment were excited in the ^{202}Hg CE experiment. Besides the 2_1^+ and 2_2^+ states, the most-populated 2^+ states were the third, seventh, eighth and tenth at 1182, 1794, 1823 and 1966 keV, respectively. For the 2_3^+ and 2_7^+ states, it was feasible to deduce the $E2/M1$ multipole-mixing ratios of their γ -ray decays to the 2_1^+ state, $\delta = 2.1(4)$ and $\delta = 0.06(4)$, respectively. In any other case, upper limits of the $B(M1; 2_i^+ \rightarrow 2_1^+)$ strengths were estimated by assuming a pure $M1$ transition. The highest of them,

$B(M1; 2_8^+ \rightarrow 2_1^+) < 0.027\mu_N^2$, was significantly smaller than the $M1$ strength of the designated main fragment of the $2_{1,ms}^+$ state, $B(M1; 2_7^+ \rightarrow 2_1^+) = 0.18(8)\mu_N^2$. Besides the strong $M1$ transition to the 2_1^+ state and the weakly collective excitation from the ground state, $B(E2; 2_7^+ \rightarrow 0_1^+) = 0.13(6)$ W.u., the 2_7^+ state exhibits a further signature of the $2_{1,ms}^+$ state.

From the *sdf*-IBM-2 [142], where additional octupole (f) bosons are introduced, an enhanced $E1$ strength between the fully-symmetric octupole 3^- state and the $2_{1,ms}^+$ state relative to the $E1$ transition to the 2_1^+ state is expected.

Due to the seemingly enhanced collectivity of the second 3^- state, $B(E3; 3_2^- \rightarrow 0_1^+) = 21(1)$ W.u., in comparison to the first and third 3^- states, $B(E3; 3_{1,3}^- \rightarrow 0_1^+) = 2.5(1), 1.0(1)$ W.u., the 3_2^- state was assigned as the dominant fragment of the fully-symmetric octupole vibration. The two neighboring $3_{1,3}^-$ states may be minor fragments of this octupole vibration and, thus, may indicate its fragmentation. The phenomenon of an enhanced collectivity of an off-yrast 3^- state was already observed previously, e.g., in even- A Pt isotopes [143, 144].

Unfortunately, this experiment was not sensitive of $B(E1)$ strengths, because $E1$ transitions do not contribute significantly to the CE process and the multipole-mixing of these transitions was unknown. However, the measured γ -ray intensities allowed to determine the $E1$ ratio $R_{E1} = B(E1; 3_2^- \rightarrow 2_7^+)/B(E1; 3_2^- \rightarrow 2_1^+) \approx 3$. Such an enhanced $E1$ transition of the octupole vibration to the mixed-symmetry 2^+ state was also observed in the $A \approx 90$ [31, 33, 37], 130 [37, 41] regions and in the $A \approx 208$ mass region in ^{204}Hg [48]. These accumulated indications lead to the conclusion that the 2_7^+ state is the mixed-symmetry one-quadrupole-phonon $2_{1,ms}^+$ state of ^{202}Hg .

Table 5.2.: Orbital structures of $^{202,204}\text{Hg}$ and $^{208,212}\text{Po}$ with respect to the doubly-magic ^{208}Pb were derived from Ref. [48] and the corresponding $B(M1; 2_{1,ms}^+ \rightarrow 2_1^+)$ values are taken from Refs. [46–48, 50]

isotope	π	ν	$B(M1; 2_{1,ms}^+ \rightarrow 2_1^+)$
^{202}Hg	$(d_{3/2})^{-2}$	$(f_{5/2})^{-4}$	$0.18(8)\mu_N^2$
^{204}Hg	$(d_{3/2})^{-2}$	$(f_{5/2})^{-2}$	$0.20(2)\mu_N^2$
^{208}Po	$(h_{9/2})^2$	$(f_{5/2})^{-2}$	$> 0.112(13)\mu_N^2$
^{212}Po	$(h_{9/2})^2$	$(g_{9/2})^2$	$0.126(16)\mu_N^2$

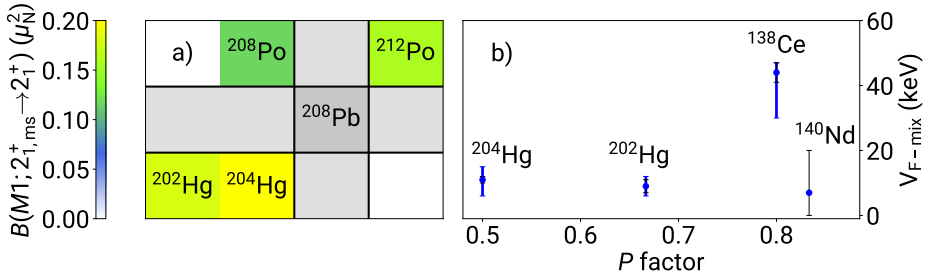


Figure 5.6.: a) shows the known $M1$ strengths of $2_{1,ms}^+ \rightarrow 2_1^+$ transitions in the vicinity of the doubly-magic ^{208}Pb . The value of ^{208}Po is a lower limit. b) presents the determined F -spin mixing matrix elements $V_{F\text{-mix}}$ of the $Z = 80$ isotopes $^{202,204}\text{Hg}$ [50] and of the $N = 80$ isotones ^{140}Nd [21] and ^{138}Ce [10] in dependence of the P factor.

The resulting $B(M1; 2_i^+ \rightarrow 2_1^+)$ strengths distributions of ^{202}Hg and ^{204}Hg [48, 50], see Figure 5.5, are used to determine the F -spin mixing $V_{F\text{-mix}}$ of the Hg isotopes. This is the first measurement of the F -spin mixing in the $A = 208$ mass region. The closest-lying 2^+ states with respect to the main fragments of the $2_{1,ms}^+$ states of ^{202}Hg and ^{204}Hg are the 2_8^+ and the 2_3^+ states, respectively. They are assumed to be the minor fragments in the two-state mixing calculations. The $B(M1; 2_2^+ \rightarrow 2_1^+) = 43(8) \times 10^{-4} \mu_N^2$ value of ^{202}Hg is taken as the background $M1$ transition strength connecting FSSs of ^{202}Hg . It is also applied to the calculations of ^{204}Hg , because the second 2^+ state of ^{204}Hg is identified as the $2_{1,ms}^+$ state. The $B(M1)$ values of ^{204}Hg of the main and minor fragments' γ -ray decays are $0.200(23) \mu_N^2$ and $< 0.018 \mu_N^2$ [48, 50], respectively. The analogous procedure as it was used for the $N = 80$ isotones will be applied. The resulting upper limits of the F -spin mixing matrix elements of $^{202,204}\text{Hg}$, $V_{F\text{-mix}} < 9(2)_{-3}^{+3}$ keV, $11(1)_{-4}^{+4}$ keV, show the suppressed mixing of FSSs with MSSs in these isotopes. The values are quite comparable to the ones of the $N = 80$ isotones, except for the sub-shell closure at $Z = 58$, see Figure 5.6 b). Consequently, the F spin qualifies as an approximately good quantum number, also, near doubly-magic nuclei, like ^{132}Sn and ^{208}Pb .

The identifications of the $2_{1,ms}^+$ states of ^{202}Hg [50] and recently of ^{208}Po [47],

expand the knowledge of the MSSs in the vicinity of ^{208}Pb , see Figure 5.6 a). There is not any significant evidence visible, that one-phonon MSSs are more pronounced, when both protons and neutrons occupy orbitals with high angular momenta. The Hg isotopes exhibit slightly enhanced $B(M1; 2_{1,\text{ms}}^+ \rightarrow 2_1^+)$ values than the Po isotopes, although the valence nucleons of Po occupy orbitals with higher angular momenta, see Table 5.2. Here, the trend seems to be inverted. However, the prominent existence of the $2_{1,\text{ms}}^+$ state is clearly proven in vibrational nuclei in the nearest vicinity of the doubly-magic ^{208}Pb .

Although pronounced $B(M1; 2_{1,\text{ms}}^+ \rightarrow 2_1^+)$ values are found in the $A = 200$ mass region, it seems that nuclei near the heaviest stable doubly-magic isotope exhibit the least enhanced $B(M1; 2_{1,\text{ms}}^+ \rightarrow 2_1^+)$ strengths in comparison to nuclei in other regions near double shell closures, e.g., $A \approx 132$, $A \approx 100$ and $A \approx 56$, see Figure 5.7. However, solely the $N = 52$ isotones, ^{94}Mo and ^{96}Ru , show extraordinarily outstanding $M1$ strengths of the $2_{1,\text{ms}}^+ \rightarrow 2_1^+$ transitions.

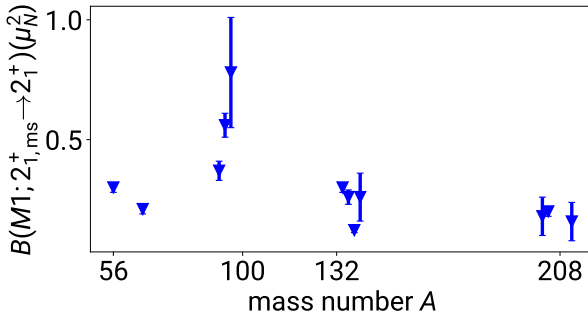


Figure 5.7.: The $B(M1; 2_{1,\text{ms}}^+ \rightarrow 2_1^+)$ strengths of nuclei in the mass regions near doubly-magic nuclei $A \approx 56$, ^{56}Fe [27, 28] and ^{66}Zn [29], $A \approx 100$, ^{92}Zr [38], ^{94}Mo [31] and ^{96}Ru [33, 36], $A \approx 132$, ^{134}Xe [18], ^{136}Ba [19], ^{138}Ce [10] and ^{140}Nd [21], and $A \approx 208$, ^{202}Hg [50], ^{204}Hg [48] and ^{212}Po [46].

Comparing the previously known transition strengths from Ref. [116], see Table 4.9, with the here obtained values, the deviations of the $B(E2; 2_2^+ \rightarrow 2_1^+, 0_1^+)$ strengths of about 50 % attract attention. These values from Ref. [116] are averaged results from two CE experiments [112, 114] using Hg as target material.

The later experiment [114] seems to obtain lower $B(E2)$ strengths than the previous one [112], see Table 5.3. Especially, the $B(E2; 2_2^+ \rightarrow 2_1^+)$ value shows a large decrease of 36% , while the corresponding transition strength to the ground state, $B(E2; 2_2^+ \rightarrow 0_1^+)$, was not newly determined in the CE analysis of Ref. [114]. Hence, the results from this analysis in combination with the already reduced value from Ref. [114] may indicate, that the 2_2^+ state of ^{202}Hg is significantly less collective than expected from Ref. [112].

Table 5.3.: Comparison of previously measured $E2$ absolute transition strengths of ^{202}Hg from Refs. [112, 114] and this work. The $B(E2)$ values are given in Weisskopf units [$1 \text{ W.u.}(E2) = 70.4 \text{ e}^2 \text{ fm}^4$].

Transition	this work	Ref. [112]	Ref. [114]
$B(E2; 2_2^+ \rightarrow 0_1^+)$	0.039(3)	0.10(3)	
$B(E2; 2_2^+ \rightarrow 2_1^+)$	2.7(3)	7.5(2.6)	4.8(1.0)
$B(E2; 4_1^+ \rightarrow 2_1^+)$	26.6(5)	27.1(10)	25.8(23)
$B(E2; 6_1^+ \rightarrow 4_1^+)$	24.9(1)		25(2)



6. Summary

The presented work concentrates on the low-lying collective isovector quadrupole excitations of heavy vibrational nuclei near doubly-magic isotopes. Furthermore, the obtained $E2$ transition strengths ratios were used to probe the $U(5)$ symmetry for the $N = 80$ isotones ^{140}Nd and ^{142}Sm . These observables were deduced by conducting projectile CE experiments at the HIE-ISOLDE facility at CERN and at the ATLAS facility at the ANL for the radioactive ^{140}Nd and ^{142}Sm , and the stable ^{202}Hg isotope, respectively. The high-resolution HPGe-detector arrays Miniball and Gammasphere were used for the γ -ray detection.

The main fragment of the $2_{1,\text{ms}}^+$ state of ^{140}Nd was identified by measuring a pronounced absolute $M1$ transition strength, $B(M1; 2_3^+ \rightarrow 2_1^+) = 0.26_{-0.10}^{+0.11} \mu_N^2$, while an upper limit, $B(M1; 2_4^+ \rightarrow 2_1^+) < 0.04 \mu_N^2$, was obtained for the potential minor fragment. This re-enhancement of the $M1$ strength after the fragmentation of the $2_{1,\text{ms}}^+$ state of ^{138}Ce at the $Z = 58$ sub-shell closure leads to the conclusion of the restoration of the valence-shell stabilization for ^{140}Nd . This special position for ^{138}Ce with its highly fragmented $2_{1,\text{ms}}^+$ state in the $N = 80$ is also supported by the decreased F -spin mixing matrix element of ^{140}Nd , $V_{F-\text{mix}} < 7_{-7}^{+13}$ keV.

The preliminary upper limit of the $B(M1; 2_3^+ \rightarrow 2_1^+) < 0.14_{-0.01}^{+0.37} \mu_N^2$ strength of ^{142}Sm is not in conflict with the conclusion made from the ^{140}Nd experiment. However, it is not reasonable to make a further statement until the designed β^+/ϵ -decay experiment will be performed with its purpose of measuring the angular γ - γ correlation of the $2_3^+ \rightarrow 2_1^+ \rightarrow 0_1^+$ γ - γ cascade of ^{142}Sm . The desired result of this measurement will be the $E2/M1$ multipole-mixing ratio and it will finalize the investigation of the low-lying isovector one-quadrupole-phonon excitation in ^{142}Sm .

Furthermore, the obtained decay characteristics of the fully-symmetric two-phonon states of ^{140}Nd and ^{142}Sm showed qualities of IBM's $U(5)$ limit. The ratios $B_{2/2} = B(E2; 2_2^+ \rightarrow 2_1^+)/B(E2; 2_1^+ \rightarrow 0_1^+) = 0.98(12)$, $0.97(23)$ and $B_{4/2} = B(E2; 4_1^+ \rightarrow 2_1^+)/B(E2; 2_1^+ \rightarrow 0_1^+) = 1.2(1)$, $1.6(3)$ indicate tendency towards

vibrational shapes of ^{140}Nd and ^{142}Sm , respectively. Furthermore, the measured $B(M1; 2_{1,\text{ms}}^+ \rightarrow 2_1)$ values of the $N = 80$ isotones also fulfill the predictions of the $U(5)$ limit. Summarized, the $N = 80$ isotones from ^{132}Te to ^{142}Sm show qualities of the $U(5)$ limit of the IBM.

Regarding the vicinity of the doubly-magic ^{208}Pb , the ultra-high statistics particle-detection-free experiment with a ^{202}Hg beam at ATLAS enabled the measurement of the $B(M1; 2_i^+ \rightarrow 2_1^+)$ strengths of several transitions. The $2_{7,8}^+$ states at 1794 keV and 1823 keV were identified as the main and the potential minor fragment of the $2_{1,\text{ms}}^+$ state with the corresponding $M1$ strengths $B(M1; 2_7^+ \rightarrow 2_1^+) = 0.18(8)\mu_N^2$ and $B(M1; 2_8^+ \rightarrow 2_1^+) < 0.027\mu_N^2$. Additionally, the enhanced $E1$ ratio $R_{E1} = B(E1; 3_2^- \rightarrow 2_7^+)/B(E1; 3_2^- \rightarrow 2_1^+) \approx 3$ was measured, which is a further indication for the 2_7^+ state being the main fragment of the $2_{1,\text{ms}}^+$ state [63, 142]. The resulting $B(M1; 2_i^+ \rightarrow 2_1^+)$ strengths of $^{202,204}\text{Hg}$ from Refs. [48, 50] were used to deduce the F -spin mixing matrix elements for the isotopes $^{202,204}\text{Hg}$, $V_{F-\text{mix}} = 9(2)_{-3}^{+3}$ keV and $11(1)_{-5}^{+4}$ keV, respectively. This was the first measurement of the F -spin mixing in the $A \approx 200$ mass region.

The obtained results of the F -spin mixing of the $N = 80$ isotones and $Z = 80$ isotopes showed the F -spin as an approximately good quantum number in $^{202,204}\text{Hg}$ and ^{140}Nd . All determined $V_{F-\text{mix}}$ values in the $N = 80$ isotonic and $Z = 80$ isotopic chains, two nucleons apart from a shell closure, showed a similar behaviour, except ^{138}Ce at the $Z = 58$ sub-shell closure.

A. HIE-ISOLDE CE Experiments

Table A.1.: The γ -ray transitions used for the energy and efficiency calibration for the HIE-ISOLDE experiments. I_γ is the measured peak area, I_{eff} is the intensity relative to the activity of the source.

E_γ (keV)	I_γ	ΔI_γ	I_{eff} (%)	ΔI_{eff}	source
53.2	50394	534	2.200	0.020	^{133}Ba
81.0	1186900	1300	34.060	0.270	^{133}Ba
302.9	433508	783	18.330	0.060	^{133}Ba
356.0	1349700	1200	62.050	0.190	^{133}Ba
383.8	187445	538	8.940	0.030	^{133}Ba
276.4	176647	616	7.164	0.022	^{133}Ba
40.1	1695800	1400	59.400	1.100	^{152}Eu
121.8	3789400	1100	28.580	0.060	^{152}Eu
244.7	734829	995	7.583	0.019	^{152}Eu
444.0	215231	550	3.100	0.100	^{152}Eu
488.7	26752	38	0.419	0.003	^{152}Eu
688.7	45043	342	0.857	0.008	^{152}Eu
779.0	646903	853	12.940	0.020	^{152}Eu
810.5	15864	278	0.320	0.003	^{152}Eu
867.4	199441	518	4.250	0.002	^{152}Eu
919.3	19739	264	0.427	0.006	^{152}Eu
964.1	654493	839	14.610	0.020	^{152}Eu
1085.8	425206	728	10.210	0.020	^{152}Eu
1112.1	562752	778	13.640	0.020	^{152}Eu
1212.9	54166	289	1.420	0.060	^{152}Eu
1408.0	748372	871	21.010	0.200	^{152}Eu
511.0	11928400	3700	1.1400	0.0800	^{66}Ga
833.5	483874	880	0.0590	0.0030	^{66}Ga

1039.2	2797900	1700	0.3700	0.0200	⁶⁶ Ga
1333.1	68677	362	0.0117	0.0006	⁶⁶ Ga
1918.3	102359	2592	0.0199	0.0011	⁶⁶ Ga
2189.6	239528	540	0.0530	0.0030	⁶⁶ Ga
2422.5	75361	375	0.0188	0.0010	⁶⁶ Ga
2751.8	844262	936	0.2270	0.0012	⁶⁶ Ga
3228.8	49111	253	0.0151	0.0008	⁶⁶ Ga
3380.9	45023	244	0.0147	0.0008	⁶⁶ Ga
4085.9	33469	218	0.0127	0.0007	⁶⁶ Ga
4295.2	119587	358	0.0404	0.0021	⁶⁶ Ga
4806.0	41680	206	0.0186	0.0010	⁶⁶ Ga

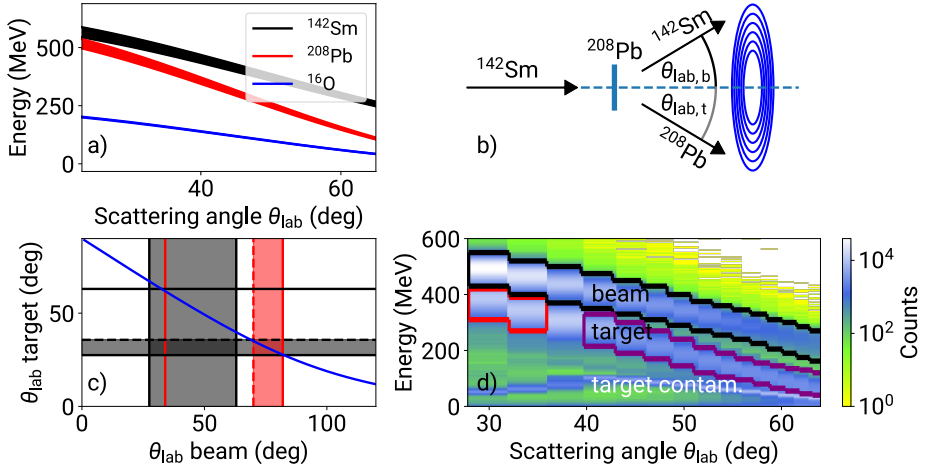


Figure A.1.: a) presents the calculations of the reaction kinematic of the ^{142}Sm CE experiment. b) shows an exemplary scattering process to introduce the general setting. c) presents the co-dependency of the scattering angles of both reaction partners, target- and beam-like particles (blue). d) shows the experimental particle energies in dependence of the scattering angle measured by the DSSD. Three different particle types can be separated. The used gates for the particle- γ coincidences are marked. For more information, see text in Chapter 4.

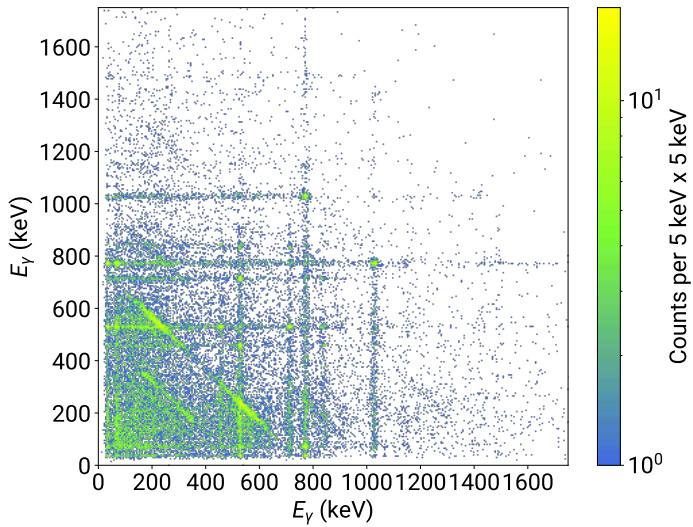


Figure A.2.: The E_γ - E_γ matrix of the ^{140}Nd CE experiment with the conditions of the detection of one particle on the DSSD inside the target (one hit) energy gate and of more than one γ ray in Miniball inside the prompt time gate. The spectrum is mirrored at the E_γ - E_γ axis for visibility.

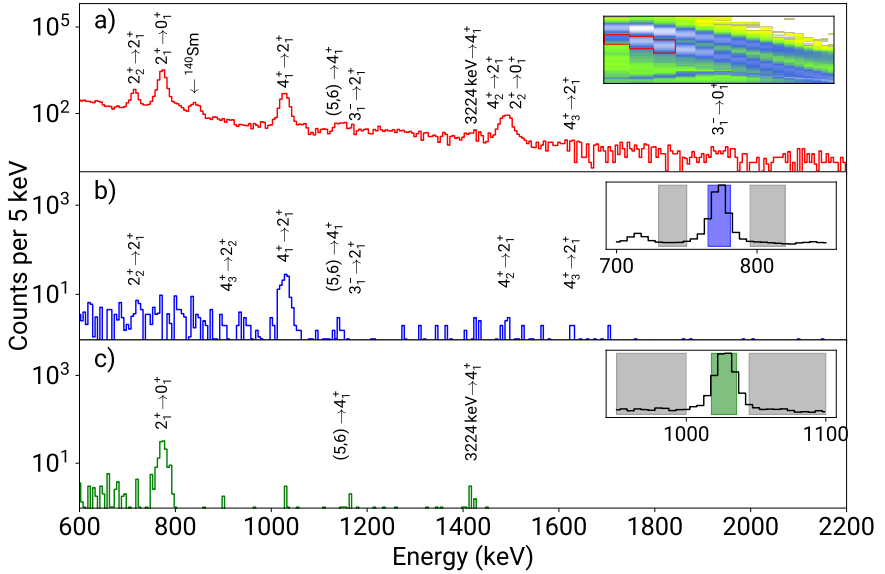


Figure A.3.: Three target-particles gated spectra are presented. The γ -singles spectrum in a) and b), c) show the coincidence spectra from gating in the E_γ - E_γ matrix on the $2_1^+ \rightarrow 0_1^+$ and $4_1^+ \rightarrow 2_1^+$ transitions of ^{140}Nd , respectively.

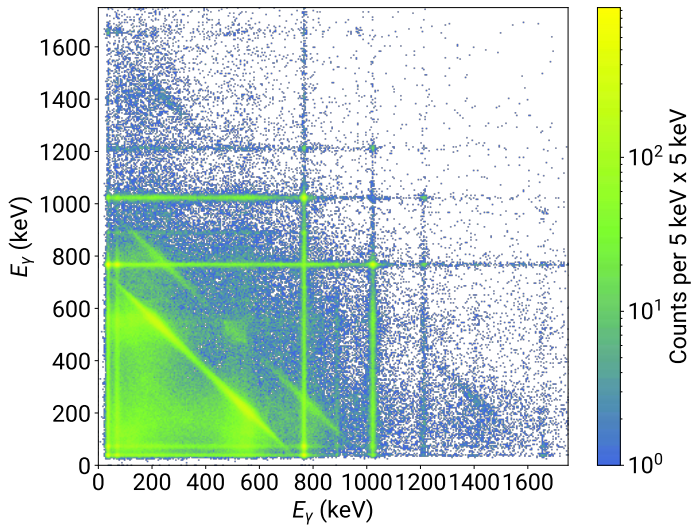


Figure A.4.: The E_γ - E_γ matrix of the ^{142}Sm CE experiment with the conditions of the detection of one particle on the DSSD inside the beam energy gate and of more than one γ ray in Miniball inside the prompt time gate. The spectrum is mirrored at the E_γ - E_γ axis for visibility.

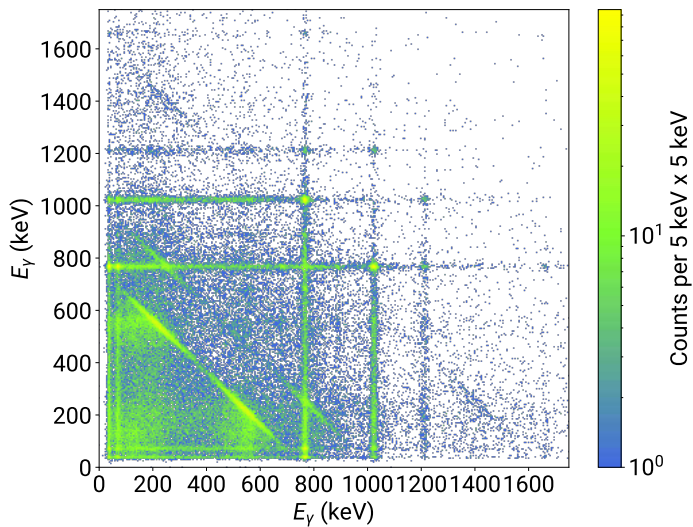


Figure A.5.: The E_γ - E_γ matrix of the ^{142}Sm CE experiment with the conditions of the detection of one particle on the DSSD inside the target (one hit) energy gate and of more than one γ ray in Miniball inside the prompt time gate. The spectrum is mirrored at the E_γ - E_γ axis for visibility.

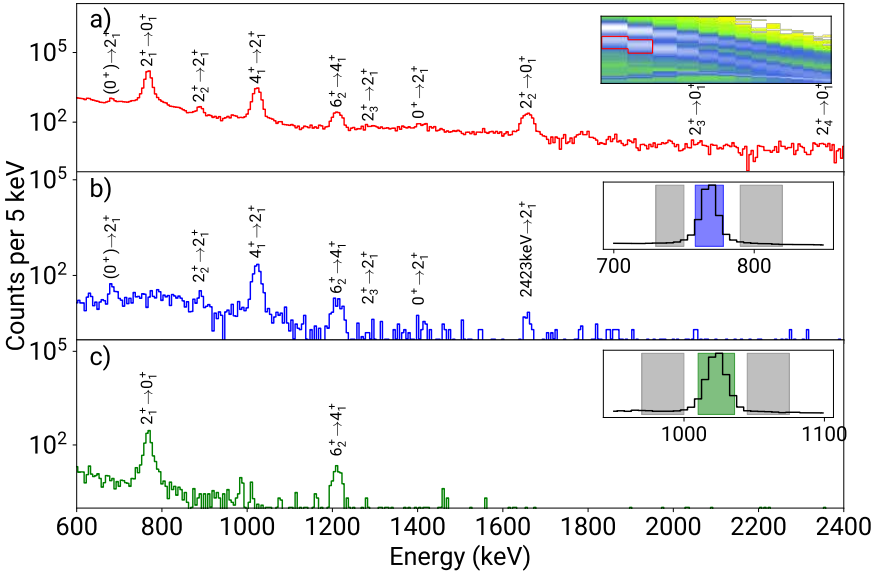


Figure A.6.: Three target-particles gated spectra of the ^{142}Sm CE experiment. a) shows the γ -singles spectrum and b), c) show the coincidence spectra from gating in the E_γ - E_γ matrix on the $2_1^+ \rightarrow 0_1^+$ and $4_1^+ \rightarrow 2_1^+$ transitions of ^{142}Sm , respectively.

Table A.2.: The measured counts with statistical uncertainties of the identified transitions of ^{140}Nd in the target-particle gated spectra, see Figure A.3. The transitions, which formed doublets, are marked with $d_{1,2,3}$. I_γ is the efficiency-corrected intensity relative to the intensity of the $2_1^+ \rightarrow 0_1^+$ transition.

E_{level} (keV)	J^π	E_γ (keV)	J_f^π	$A_{p-\gamma}$	$A_{p-\gamma-\gamma}$ $2_1^+ \rightarrow 0_1^+$	$A_{p-\gamma-\gamma}$ $4_1^+ \rightarrow 2_1^+$	I_γ
774	2_1^+	774	0_1^+	10220(120)		119(11)	100(1)
1413	0_2^+	639	2_1^+	160(40)			1.4(3)
1490	2_2^+ [24]	1490	0_1^+	d_3			5.5(6)
		716	2_1^+	d_1	18(5)		2.7(8)
1802	4_1^+	1028	2_1^+	1840(50)	114(11)		21.4(6)
1936	3_1^-	1936	0_1^+				
		1162	2_1^+	d_2	d_2		0.9(4)
2264	4_2^+ [94]	1491	2_1^+	d_3	5(2)		1.2(5)
2950	(5,6)[94]	1148	4_1^+	d_2	d_2	3(1.7)	1.6(4)
3224		1422	4_1^+	70(13)		5.8(2.4)	1.0(2)
d_1				145(60)			
d_2				193(51)	10(3)		
d_3				451(24)			

Table A.3.: The measured counts with statistical uncertainties of the identified transitions of ^{142}Sm in the target-particle gated spectra, see Figure A.6. The transitions, which formed a doublet, are marked with d_1 . I_γ is the efficiency-corrected intensity relative to the intensity of the $2_1^+ \rightarrow 0_1^+$ transition.

E_{level} (keV)	J^π	E_γ (keV)	J_f^π	$A_{p-\gamma}$	$A_{p-\gamma-\gamma}$ $2_1^+ \rightarrow 0_1^+$	$A_{p-\gamma-\gamma}$ $4_1^+ \rightarrow 2_1^+$	I_γ
768	2_1^+	768	0_1^+	53220(250)		918(31)	100.0(7)
1450	(0_2^+)	683	2_1^+	700(70)	73(12)		1.2(1)
1658	$(2)_2^+$	1658	0_1^+	d_1			2.8(3)
		890	2_1^+	710(50)	47(10)		1.4(2)
1791	4_1^+	1023	2_1^+	10630(110)	792(29)		23.2(3)
2055	2_3^+	1287	2_1^+	74(26)			0.096(38)
2173	0_3^+	1405	2_1^+	197(24)	15(4)		0.55(8)
2354	(2_4^+)	2354	0_1^+	36(11)			0.13(4)
2420	6_1^+	629	4_1^+	270(60)	26(8)	15(7)	0.45(9)
2423		1655	2_1^+	d_1	14(6)		0.57(20)
3003	(6^+)	1212	4_1^+	1020(40)	75(9)	74(9)	2.5(2)
d_1				1100(40)			

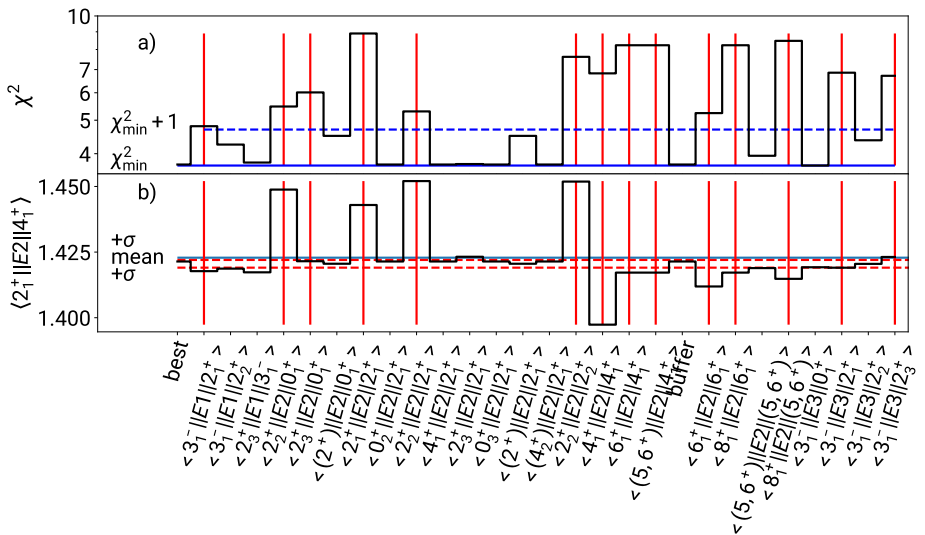


Figure A.7.: The signs of the MEs are fixed by the “best” fit and later only one ME’s sign was switched, which is labeled on the x-axis. In a) the total χ^2 of the GOSIA calculation with the changed set of matrix elements is presented. b) shows the distribution of the values for the instance of the ME $\langle 2_1^+ || E2 || 4_1^+ \rangle$ of ^{142}Sm . For more information, see text in Section 4.1.4.



B. GOSIA Files

GOSIA, a semi-classical coupled-channel CE code, has been developed to simulate experiments or analyze experimental CE data to determine electromagnetic transition MEs. The normalization is performed onto a selected transition ME of the investigated isotope itself. The presented GOSIA-input files were used to analyze the data of the CE experiments investigating the $N = 80$ isotones and to determine the statistical tensor of the 2_7^+ state of ^{202}Hg from the CE data. The large variety of options of GOSIA are described in detail in the GOSIA user manual [98].

Listing B.1: GOSIA-input file to define the HPGe detectors of Miniball.

```
1 OP, TITLE
2 MINIBALL ARRAY
3 OP, GDET
4 -24
5 0.1,5.0,7.8,12.3
6 0.2,0,0,0,0,0
7 0.1,5.0,7.8,12.3
8 0.2,0,0,0,0,0
9 0.1,5.0,7.8,12.3
10 0.2,0,0,0,0,0
11 0.1,5.0,7.8,11.2
12 0.2,0,0,0,0,0
13 0.1,5.0,7.8,11.2
14 0.2,0,0,0,0,0
15 0.1,5.0,7.8,11.2
16 0.2,0,0,0,0,0
17 0.1,5.0,7.8,11.7
18 0.2,0,0,0,0,0
19 0.1,5.0,7.8,11.7
20 0.2,0,0,0,0,0
21 0.1,5.0,7.8,11.7
22 0.2,0,0,0,0,0
23 0.1,5.0,7.8,11.2
24 0.2,0,0,0,0,0
25 0.1,5.0,7.8,11.2
26 0.2,0,0,0,0,0
27 0.1,5.0,7.8,11.2
28 0.2,0,0,0,0,0
29 0.1,5.0,7.8,12.4
30 0.2,0,0,0,0,0
```

```

31 0.1,5.0,7.8,12.4
32 0.2,0,0,0,0,0,0
33 0.1,5.0,7.8,12.4
34 0.2,0,0,0,0,0,0
35 0.1,5.0,7.8,11.1
36 0.2,0,0,0,0,0,0
37 0.1,5.0,7.8,11.1
38 0.2,0,0,0,0,0,0
39 0.1,5.0,7.8,11.1
40 0.2,0,0,0,0,0,0
41 0.1,5.0,7.8,11.6
42 0.2,0,0,0,0,0,0
43 0.1,5.0,7.8,11.6
44 0.2,0,0,0,0,0,0
45 0.1,5.0,7.8,11.6
46 0.2,0,0,0,0,0,0
47 0.1,5.0,7.8,12.0
48 0.2,0,0,0,0,0,0
49 0.1,5.0,7.8,12.0
50 0.2,0,0,0,0,0,0
51 0.1,5.0,7.8,12.0
52 0.2,0,0,0,0,0,0
53 OP, EXIT

```

Listing B.2: GOSIA-input file for the $^{208}\text{Pb}(^{140}\text{Nd}, ^{140}\text{Nd}^*)^{208}\text{Pb}^*$ CE experiment.

```

1 OP, FILE
2 22,3,1
3 140nd_208pb.out
4 25,3,1
5 140nd_208pb.inp
6 3,3,1
7 140nd_208pb.yld
8 4,3,1
9 140nd_208pb.cor
10 7,3,1
11 140nd_208pb.map
12 12,3,1
13 140nd_208pb.bst
14 15,3,1
15 140nd_208pb.err
16 17,3,1
17 140nd_208pb.sev
18 99,13,1
19 140nd_208pb.amp
20 0,0,0
21 OP, TITLE
22 140ND_208PB
23 OP, GOSI
24 LEVE
25 1,1,0,0
26 2,1,2,0.774
27 3,1,0,1.413

```

28 4,1,2,1.490
 29 5,1,4,1.802
 30 6,-1,3,1.935
 31 7,1,2,2.140
 32 8,1,4,2.264
 33 9,-1,5,2.276
 34 10,1,2,2.332
 35 11,1,4,2.400
 36 12,1,6,2.950
 37 13,1,6,3.224
 38 14,1,8,3.685
 39 15,-1,5,2.480
 40 16,1,2,3.036
 41 0,0,0,0
 42 ME
 43 1,0,0,0
 44 2,6,-0.00020,-0.0100,0.0100
 45 4,6,0.00048,-0.0100,0.0100
 46 6,7,0.00048,-0.0100,0.0100
 47 2,0,0,0,0
 48 1,2,0.850,0.82,0.88
 49 1,4,-0.195,-0.450,0.450
 50 1,7,-0.20257,-0.40,0.400
 51 1,10,-0.018,-0.40,0.500
 52 2,2,-0.62,-1.2,-0.04
 53 2,3,0.1803,-0.500,0.500
 54 2,4,0.8227,-4.1000,4.000
 55 2,5,-1.2549,-3.000,3.000
 56 2,7,0.0825,-0.150,0.150
 57 2,8,0.3029,-1.500,1.500
 58 2,10,-0.0065,-0.500,0.500
 59 2,11,-0.2489,-0.500,0.500
 60 3,16,0.680,-10.0,10.0
 61 4,4,-.62,-1.0,1.0
 62 4,11,-1.27,-3.500,3.500
 63 5,5,-.62157,-1.0,1.0
 64 5,12,1.311,-5.500,5.500
 65 5,8,-0.548,-5.000,5.000
 66 5,13,1.1288,-5.000,5.000
 67 6,9,0.1880,-5.000,5.000
 68 7,7,-.62,-1.0,1.0
 69 7,16,0.2990,-5.000,5.000
 70 12,-14,1.5,5,12
 71 3,0,0,0,0
 72 1,6,0.23335,-2.600,2.600
 73 2,6,0.5660,-3.000,3.000
 74 4,6,-0.960,-4.000,4.000
 75 5,9,1.845,-3.0,3.0
 76 5,15,1.65,-2.000,2.000
 77 7,0,0,0,0
 78 2,4,-0.40,-1.000,1.000
 79 2,7,-1.16,-2.000,2.000
 80 2,10,0.05,-2.000,2.000
 81 0,0,0,0,0

```

82 EXPT
83 2,60,140
84 -82,208,623,45.5,3,1,0,0,360,0,1
85 -82,208,623,-75.5,3,1,0,0,360,0,2
86 CONT
87 1,3
88 2,3
89 INT,4
90 1,1000
91 2,1000
92 SPL,1.
93 CRF,
94 SEL,
95 PRT,
96 1,1
97 2,1
98 5,1
99 11,0
100 12,0
101 13,1
102 14,0
103 15,1
104 16,0
105 0,0
106 END,
107
108 OP, BRIC
109 /home/ralli/Physik/hieisolde/gosia_isolde/BrIccFOV22.idx
110 /home/ralli/Physik/hieisolde/gosia_isolde/BrIccFOV22.icc
111 OP, YIELD
112 1
113 -1,0
114 0.010
115 24,24
116 1,2,3,4,5,6,7,8,9,10,11,12,13,14,15,16,17,18,19,20,21,22,23,24
117 135.5,147.0,152.9,44.1,59.6,67.8,42.8,56.2,65.3,126.3,138.8,149.6,141.9,
118 148.6,149.8,59.7,59.4,55.4,124.3,135.2,147.1,42.9,32.0,27.5
119 127.2,117.7,109.2,56.6,47.9,52.4,104.3,111.5,121.2,78.4,85.0,82.8,261.9,
120 257.5,252.2,235.3,242.6,252,310.8,307.9,297.2,309.2,298.3,290.8
121 1,2,3,4,5,6,7,8,9,10,11,12,13,14,15,16,17,18,19,20,21,22,23,24
122 135.5,147.0,152.9,44.1,59.6,67.8,42.8,56.2,65.3,126.3,138.8,149.6,141.9,
123 148.6,149.8,59.7,59.4,55.4,124.3,135.2,147.1,42.9,32.0,27.5
124 127.2,117.7,109.2,56.6,47.9,52.4,104.3,111.5,121.2,78.4,85.0,82.8,261.9,
125 257.5,252.2,235.3,242.6,252,310.8,307.9,297.2,309.2,298.3,290.8
126 2,1
127 1
128 9e-4
129 1.0
130 1
131 1e-2
1.0
3 !ntap = 4 for minimization
1,1,0
10,2,10,1,0.54,0.18

```

132 0,1,0
133 3,1,0
134 4,2,-1.22,0.14
135 7,2,-0.08,0.08
136 10,2,-0.19,0.09
137 5,1,0
138 2,1,2,0.85,0.03
139 2,2,2,-0.64,0.41
140 2,4,4,-0.64,0.41
141 2,5,5,-0.64,0.41
142 2,7,7,-0.64,0.41
143 OP,RAW
144 1
145 0,0,0,0,0,0,-50,0
146 0,0,0,0,0,0,-50,0
147 0,0,0,0,0,0,-50,0
148 0,0,0,0,0,0,-50,0
149 0,0,0,0,0,0,-50,0
150 0,0,0,0,0,0,-50,0
151 0,0,0,0,0,0,-50,0
152 0,0,0,0,0,0,-50,0
153 0,0,0,0,0,0,-50,0
154 0,0,0,0,0,0,-50,0
155 0,0,0,0,0,0,-50,0
156 0,0,0,0,0,0,-50,0
157 0,0,0,0,0,0,-50,0
158 0,0,0,0,0,0,-50,0
159 0,0,0,0,0,0,-50,0
160 0,0,0,0,0,0,-50,0
161 0,0,0,0,0,0,-50,0
162 0,0,0,0,0,0,-50,0
163 0,0,0,0,0,0,-50,0
164 0,0,0,0,0,0,-50,0
165 0,0,0,0,0,0,-50,0
166 0,0,0,0,0,0,-50,0
167 0,0,0,0,0,0,-50,0
168 0,0,0,0,0,0,-50,0
169 1
170 24
171 1,2,3,4,5,6,7,8,9,10,11,12,13,14,15,16,17,18,19,20,21,22,23,24
172 2
173 0,0,0,0,0,0,-50,0
174 0,0,0,0,0,0,-50,0
175 0,0,0,0,0,0,-50,0
176 0,0,0,0,0,0,-50,0
177 0,0,0,0,0,0,-50,0
178 0,0,0,0,0,0,-50,0
179 0,0,0,0,0,0,-50,0
180 0,0,0,0,0,0,-50,0
181 0,0,0,0,0,0,-50,0
182 0,0,0,0,0,0,-50,0
183 0,0,0,0,0,0,-50,0
184 0,0,0,0,0,0,-50,0
185 0,0,0,0,0,0,-50,0

```

186 0,0,0,0,0,0,-50,0
187 0,0,0,0,0,0,-50,0
188 0,0,0,0,0,0,-50,0
189 0,0,0,0,0,0,-50,0
190 0,0,0,0,0,0,-50,0
191 0,0,0,0,0,0,-50,0
192 0,0,0,0,0,0,-50,0
193 0,0,0,0,0,0,-50,0
194 0,0,0,0,0,0,-50,0
195 0,0,0,0,0,0,-50,0
196 0,0,0,0,0,0,-50,0
197 1
198 24
199 1,2,3,4,5,6,7,8,9,10,11,12,13,14,15,16,17,18,19,20,21,22,23,24
200 0
201 OP,INTI
202 10,10,599,647,27.9,63
203 599,604,609,615,622,627,632,637,642,647
204 27.9,30,32,35,39,43,48,53,58,63
205 10,10,599,647,27.9,35.9
206 599,604,609,615,622,627,632,637,642,647
207 27.9,28.5,29.5,30,31,32,33,34,35,35.9
208 10
209 599,604,609,615,622,627,632,637,642,647
210 32.19,32.22,32.25,32.27,32.29,32.31,32.34,32.36,32.38,32.42
211 50,50
212 10
213 599,604,609,615,622,627,632,637,642,647
214 32.19,32.22,32.25,32.27,32.29,32.31,32.34,32.36,32.38,32.42
215 50,50
216 OP,CORR
217 OP,EXIT
218
219 OP,MAP
220 OP,EXIT
221
222 OP,MINI
223 2100,40,1e-05,1e-04,1.1,1,1,0,0,1e-04
224 OP,EXIT
225 !After the first minimization process OP,REST is inserted before OP,INTI to load
      corrected yields
226 OP,REST
227 0,0
228
229 !OP,SELE is necessary for the error estimation
230 OP,SELE
231
232 !diagonal errors need different flags in CONT
233 CONT
234 1,3
235 2,3
236 INT,4
237 1,1000
238 2,1000

```

```

239 SPL,1.
240 CRF,
241 1,1
242 2,1
243 4,0
244 5,1
245 11,0
246 12,0
247 13,1
248 14,0
249 15,1
250 16,0
251 18,1
252 0,0
253 END,
254
255 OP,REST
256 0,0
257 OP,RE,F
258 OP,ERRO
259 1,0,0,1,0,1e+308
260 OP,EXIT
261
262 !uncorellated errors need different flags in CONT
263 INT,4
264 1,1000
265 2,1000
266 SPL,1.
267 CRF,
268 SMR,
269 1,1
270 2,1
271 4,0
272 5,1
273 11,0
274 12,0
275 13,1
276 14,0
277 15,1
278 16,0
279 18,1
280 0,0
281 END,
282
283 OP,REST
284 0,0
285 OP,RE,F
286 OP,ERRO
287 1,0,0,1,0,1e+308
288 OP,EXIT

```

Listing B.3: Experimental yields of the excited nuclear states of ^{140}Nd .

```

1 1,1,60,140,647,14,1.0
2 2,1,1694,10 !774
3 3,2,4.4,1.7 !639
4 4,1,36,2 !1490
5 4,2,26.6,3.4 !716
6 5,2,163.1,2.2 !1028
7 6,1,1.4,0.4 !1935
8 6,2,4.2,0.7 !1161
9 7,1,1.24,0.3 !2140
10 7,2,3.2,0.5 !1366
11 8,2,6.7,1.7 !1491
12 11,2,3.6,0.6 !1626
13 11,4,5.2,0.8 !910
14 12,5,6.7,1.0 !1148
15 13,5,2.9,0.5 !1422
16 2,1,60,140,647,8,1.0
17 2,1,201,2.5 !774
18 3,2,2.8,0.7 !639
19 4,1,11,1.2 !1490
20 4,2,5.4,1.6 !716
21 5,2,43,1.2 !1028
22 6,2,1.8,0.8 !1161
23 8,2,2.4,1 !1491
24 12,5,3.3,0.9 !1148
25 13,5,2,0.4 !1422

```

Listing B.4: GOSIA-input file for the $^{208}\text{Pb}(^{142}\text{Sm},^{142}\text{Sm}^*)^{208}\text{Pb}^*$ CE experiment.

```

1 OP, FILE
2 22,3,1
3 142sm_208pb.out
4 25,3,1
5 142sm_208pb.inp
6 3,3,1
7 142sm_208pb.yld
8 4,3,1
9 142sm_208pb.cor
10 7,3,1
11 142sm_208pb.map
12 12,3,1
13 142sm_208pb.bst
14 15,3,1
15 142sm_208pb.err
16 17,3,1
17 142sm_208pb.sev
18 99,13,1
19 142sm_208pb.amp
20 0,0,0
21 OP, TITLE
22 142sm_208pb
23 OP, GOSI
24 LEVE
25 1,1,0,0

```

```

26 2,1,2,0.768
27 3,1,0,1.450
28 4,1,2,1.658
29 5,1,4,1.791
30 6,-1,3,1.784
31 7,1,2,2.055
32 8,1,0,2.173
33 9,1,2,2.354
34 10,1,6,2.420
35 11,1,4,2.423
36 12,1,2,2.374
37 13,1,6,3.003
38 14,1,8,3.227
39 0,0,0,0
40 ME
41 1,0,0,0
42 2,6,0.00020,0.000011,0.01
43 4,6,0.00048,0.000011,0.0100
44 6,7,0.00048,0.000011,0.0100
45 2,0,0,0
46 1,2,0.826267,0.82,0.88
47 1,4,0.247255,0.000011,0.450
48 1,7,-0.14943,-0.4,-0.00001
49 1,9,-0.14321,-0.50,-0.00001
50 2,2,-1.03107,-1.2,-0.00001
51 2,3,0.206909,0.000011,0.500
52 2,4,-0.805185,-1.10,-0.00001
53 2,5,1.4283,0.000011,3.000
54 2,7,0.00795607,0.000011,0.50
55 2,8,0.3004090,0.000011,1.500
56 2,9,-0.153296,-.5,-0.00001
57 2,11,0.293028,0.000011,5.0
58 4,4,-0.6903094,-1.0,-0.00001
59 5,5,-0.6867484,-1.2,-0.00001
60 5,10,0.635091,0.000011,5.500
61 5,13,1.843757,0.000011,5.500
62 7,-7,-1.03107,2,2
63 7,12,0.336634,0.000011,1.5
64 10,10,-1.81902,-3.5,-0.00001
65 10,14,-3.49929,-5.5,-0.00001
66 13,13,0.0029,0.000011,4.2
67 13,14,1.1473478,0.000011,2.5
68 3,0,0,0
69 1,6,0.03601616,0.000011,1.600
70 2,6,-0.845681,-3.000,-0.00001
71 4,6,-0.6338648,-4.000,-0.00001
72 6,7,-0.5761796,-1.5,-0.00001
73 7,0,0,0
74 2,4,-0.243666,-1.000,1.000
75 2,7,0.84421499,-2.000,2.000
76 0,0,0,0
77 EXPT
78 2,62,142
79 -82,208,632,45.5,3,1,0,0,360,0,1

```

```

80 -82,208,632,-75.5,3,1,0,0,360,0,2
81 CONT
82 1,3
83 2,3
84 INT,4
85 1,1000
86 2,1000
87 SPL,1.
88 CRF,
89 SEL,
90 PRT,
91 1,1
92 2,1
93 5,1
94 11,0
95 12,0
96 13,1
97 14,0
98 15,1
99 16,0
100 0,0
101 END,
102
103 OP, BRIC
104 /home/ralli/Physik/hieisolde/gosia_isolde/BrIccFOV22.idx
105 /home/ralli/Physik/hieisolde/gosia_isolde/BrIccFOV22.icc
106 OP, YIELD
107 1
108 -1,0
109 0.010
110 24,24
111 1,2,3,4,5,6,7,8,9,10,11,12,13,14,15,16,17,18,19,20,21,22,23,24
112 135.5,147.0,152.9,44.1,59.6,67.8,42.8,56.2,65.3,126.3,138.8,149.6,141.9,
    148.6,149.8,59.7,59.4,55.4,124.3,135.2,147.1,42.9,32.0,27.5
113 127.2,117.7,109.2,56.6,47.9,52.4,104.3,111.5,121.2,78.4,85.0,82.8,261.9,
    257.5,252.2,235.3,242.6,252,310.8,307.9,297.2,309.2,298.3,290.8
114 1,2,3,4,5,6,7,8,9,10,11,12,13,14,15,16,17,18,19,20,21,22,23,24
115 135.5,147.0,152.9,44.1,59.6,67.8,42.8,56.2,65.3,126.3,138.8,149.6,141.9,
    148.6,149.8,59.7,59.4,55.4,124.3,135.2,147.1,42.9,32.0,27.5
116 127.2,117.7,109.2,56.6,47.9,52.4,104.3,111.5,121.2,78.4,85.0,82.8,261.9,
    257.5,252.2,235.3,242.6,252,310.8,307.9,297.2,309.2,298.3,290.8
117 2,1
118 1
119 8e-4
120 1.0
121 1
122 1.25e-3
123 1.0
124 4 !ntap
125 1,1.0
126 7,1,7,2,0.37,0.06
127 0,1.0
128 1,1.0
129 7,2,0.01,0.01

```

```
130 1,1,0
131 2,1,2,0.837,0.054
132 OP,RAW
133 1
134 0,0,0,0,0,0,-50,0
135 0,0,0,0,0,0,-50,0
136 0,0,0,0,0,0,-50,0
137 0,0,0,0,0,0,-50,0
138 0,0,0,0,0,0,-50,0
139 0,0,0,0,0,0,-50,0
140 0,0,0,0,0,0,-50,0
141 0,0,0,0,0,0,-50,0
142 0,0,0,0,0,0,-50,0
143 0,0,0,0,0,0,-50,0
144 0,0,0,0,0,0,-50,0
145 0,0,0,0,0,0,-50,0
146 0,0,0,0,0,0,-50,0
147 0,0,0,0,0,0,-50,0
148 0,0,0,0,0,0,-50,0
149 0,0,0,0,0,0,-50,0
150 0,0,0,0,0,0,-50,0
151 0,0,0,0,0,0,-50,0
152 0,0,0,0,0,0,-50,0
153 0,0,0,0,0,0,-50,0
154 0,0,0,0,0,0,-50,0
155 0,0,0,0,0,0,-50,0
156 0,0,0,0,0,0,-50,0
157 0,0,0,0,0,0,-50,0
158 1
159 24
160 1,2,3,4,5,6,7,8,9,10,11,12,13,14,15,16,17,18,19,20,21,22,23,24
161 2
162 0,0,0,0,0,0,-50,0
163 0,0,0,0,0,0,-50,0
164 0,0,0,0,0,0,-50,0
165 0,0,0,0,0,0,-50,0
166 0,0,0,0,0,0,-50,0
167 0,0,0,0,0,0,-50,0
168 0,0,0,0,0,0,-50,0
169 0,0,0,0,0,0,-50,0
170 0,0,0,0,0,0,-50,0
171 0,0,0,0,0,0,-50,0
172 0,0,0,0,0,0,-50,0
173 0,0,0,0,0,0,-50,0
174 0,0,0,0,0,0,-50,0
175 0,0,0,0,0,0,-50,0
176 0,0,0,0,0,0,-50,0
177 0,0,0,0,0,0,-50,0
178 0,0,0,0,0,0,-50,0
179 0,0,0,0,0,0,-50,0
180 0,0,0,0,0,0,-50,0
181 0,0,0,0,0,0,-50,0
182 0,0,0,0,0,0,-50,0
183 0,0,0,0,0,0,-50,0
```

```

184 0,0,0,0,0,0,-50,0
185 0,0,0,0,0,0,-50,0
186 1
187 24
188 1,2,3,4,5,6,7,8,9,10,11,12,13,14,15,16,17,18,19,20,21,22,23,24
189 0
190 OP,REST
191 0,0
192 OP,INTI
193 10,10,608,656,27.9,63
194 608,613,618,623,628,632,638,644,650,656
195 27.9,30,32,35,39,43,48,53,58,63
196 10,10,608,656,27.9,35.9
197 608,613,618,623,628,632,638,644,650,656
198 27.9,28.5,29.5,30,31,32,33,34,35,35.9
199 10
200 608,613,618,623,628,632,638,644,650,656
201 33.33,33.36,33.39,33.42,33.45,33.47,33.50,33.53,33.56,33.58
202 50,50
203 10
204 608,613,618,623,628,632,638,644,650,656
205 33.33,33.36,33.39,33.42,33.45,33.47,33.50,33.53,33.56,33.58
206 50,50
207 OP,CORR
208 OP,EXIT
209
210 OP,MAP
211 OP,EXIT
212
213 OP,MINI
214 2100,40,1e-05,1e-04,1.1,1,1,0,0,1e-04
215 OP,EXIT
216 !After the first minimization process OP,REST is inserted before OP,INTI to load
    corrected yields
217 OP,REST
218 0,0
219
220 !OP,SELE is necessary for the error estimation
221 OP,SELE
222
223 !diagonal errors need different flags in CONT
224 CONT
225 1,3
226 2,3
227 INT,4
228 1,1000
229 2,1000
230 SPL,1.
231 CRF,
232 1,1
233 2,1
234 4,0
235 5,1
236 11,0

```

```

237 12,0
238 13,1
239 14,0
240 15,1
241 16,0
242 18,1
243 0,0
244 END,
245
246 OP,REST
247 0,0
248 OP,RE,F
249 OP,ERRO
250 1,0,0,1,0,1e+308
251 OP,EXIT
252
253 !uncorellated errors need different flags in CONT
254 INT,4
255 1,1000
256 2,1000
257 SPL,1.
258 CRF,
259 SMR,
260 1,1
261 2,1
262 4,0
263 5,1
264 11,0
265 12,0
266 13,1
267 14,0
268 15,1
269 16,0
270 18,1
271 0,0
272 END,
273
274 OP,REST
275 0,0
276 OP,RE,F
277 OP,ERRO
278 1,0,0,1,0,1e+308
279 OP,EXIT

```

Listing B.5: Experimental yields of the excited nuclear states of ^{142}Sm .

```

1 1,1,62,142,656,13,1.0
2 2,1,7937,40 !768
3 4,1,132,4 !1658
4 7,1,2.7,0.8 !2055
5 9,1,8.3,.8 !2354
6 3,2,23,3 !683
7 4,2,71,3.2 !890

```

```

8 5,2,885,6.5 !1023
9 6,2,33,10 !1016
10 7,2,8.1,1.2 !1287
11 8,2,8.8,1.2 !1405
12 10,5,11.3,2.3 !629
13 11,2,12.4,2.5 !1655
14 13,5,51,2.4 !1212
15 2,1,62,142,656,12,1.0
16 2,1,1041,7 !768
17 4,1,29,3 !1658
18 9,1,1.4,.44 !2354
19 3,2,12.8,1.3 !683
20 4,2,14.4,1.6 !890
21 5,2,241,3 !1023
22 6,2,7.2,2.6 !1016
23 7,2,1.0,0.4 !1287
24 8,2,5.7,0.8 !1405
25 10,5,4.7,1.0 !629
26 11,2,5.9,2.1 !1655
27 13,5,26.4,2 !1212

```

Listing B.6: GOSIA-input file used for the iterative procedure to determine the statistical tensor of the 2_7^+ state and δ of the $2_7^+ \rightarrow 2_1^+$ transition of ^{202}Hg .

```

1 OP, FILE
2 22,3,1
3 202Hg_subset_Transition.out      !Definition of output files
4 17,3,1
5 202Hg_subset_Transition.statTensor
6 0,0,0
7 OP,TITL
8 CE 202H on 12C
9 OP,GOSI
10 LEVE                               !Declaration of a subset of the level scheme
11 1 1 0.0 0.0
12 2 1 2.0 0.439
13 3 1 2.0 0.960
14 4 1 4.0 1.120
15 5 1 2.0 1.182
16 6 1 2.0 1.793                               !Level of interest
17 7 -1 3.0 2.356
18 8 -1 3.0 2.709
19 0 0 0 0
20 ME                               !Declaration of involved transitions
21 2 0 0 0 0
22 1 2 0.7815      0.78 0.79
23 1 3 0.03618     -5.0 5.0
24 1 5 0.0001      -5.0 5.0
25 1 6 0.0659      -5.0 5.0
26 2 2 -1.33       -5.0 5.0
27 2 3 0.300       -5.0 5.0

```

```

28 2 4 1.228      -5.0 5.0
29 2 5 0.160      -5.0 5.0
30 2 6 0.0498     -5.0 5.0      !Transition of interest
31 3 5 0.66       -5.0 5.0
32 3 0 0 0 0
33 1 7 0.1927     -5.0 5.0
34 1 8 0.5428     -5.0 5.0
35 0 0 0 0 0
36 EXPT          !Definition of the reaction partners
37 1 80 202
38 -6, 12, 829., -1.8, 6, 1, 0, 0.0, 360.0, 0, 1
39 CONT          !Switches and flags
40 INT,1.
41 1,1000
42 SPL,1.
43 PRT,
44 1,1
45 2,1
46 3,1
47 4,-2
48 5,1
49 6,1
50 7,1
51 8,1
52 10,1
53 11,1
54 12,1
55 13,1
56 14,1
57 15,1
58 16,1
59 17,3
60 18,1
61 19,1
62 20,1
63 0,0
64 TEN,
65 END,
66
67 OP,STAR
68 OP,EXIT

```



C. ATLAS CE Experiment

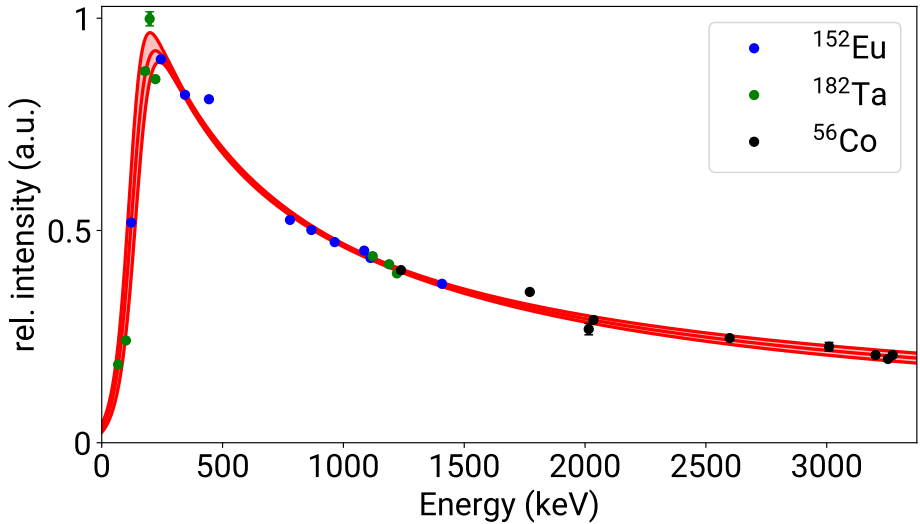


Figure C.1.: The relative intensities of the γ rays of the calibration sources ^{152}Eu , ^{182}Ta and ^{56}Co measured by Gammasphere are presented. The function (4.1) was used to fit the calibration data for the efficiency correction of the $^{12}\text{C}(^{202}\text{Hg}, ^{202}\text{Hg}^*)^{12}\text{C}$ experiment.

Table C.1.: The measured counts with statistical uncertainties of identified transitions of the ^{202}Hg CE experiment determined in four γ -ray spectra.

E_{level} (keV)	J^π	E_γ (keV)	J_f^π	$A(\text{Singles})$ $\times 10^3$	$A(\gamma\text{-gate})$ $2_1^+ \rightarrow 0_1^+$ $\times 10^3$	$A(\gamma\text{-gate})$ $2_2^+ \rightarrow 2_1^+$ $\times 10^3$	$A(\gamma\text{-gate})$ $4_1^+ \rightarrow 2_1^+$
439	2_1^+	439	0_1^+	$253.22 \times 10^3(2)$		272.9(6)	$223.3 \times 10^3(5)$
960	2_2^+	960	0_1^+	86.7(6)			
	2_2^+	520	2_1^+	1037(1)	270.9(5)		
1120	4_1^+	680	2_1^+	810(1)	225.3(5)		
1182	2_3^+	743	2_1^+	45.8(6)	7.6(1)		
	2_3^+	222	2_2^+	97.1(16)	27.3(2)	242.6(17)	
1312	4_2^+	872	2_1^+	34.7(6)	5.4(2)		
	4_2^+	352	2_2^+	56.8(18)	14.8(2)	133.7(14)	
	4_2^+	129	2_3^+			10.9(5)	
1348	(2^+)	908	2_1^+	d_1	d_1		
1390	2_4^+	950	2_1^+	38.3(6)	6.1(1)		
	2_4^+	429	2_2^+			24.8(9)	
	2_4^+	207	2_3^+			9.5(7)	
1564	0_3^+	1125	2_1^+	17.0(4)	5.1(1)		
1575	2_5^+	615	2_2^+			13.5(7)	
1643	0_4^+	1204	2_1^+		1.7(1)		
1794	2_7^+	1354	2_1^+	143.7(6)	36.2(2)		
	2_7^+	833	2_2^+			12.8(7)	
1823	2_8^+	1384	2_1^+	28.8(5)	7.7(2)		
	2_8^+	864	2_2^+	10.6(6)	4.6(2)	34.9	
	2_8^+	641	2_3^+			11.5(5)	
1966	5_1^-	654	4_2^+			15.8(6)	
1966	2_{10}^+	1527	2_1^+	d_2	d_2	d_2	
	2_{10}^+	654	4_2^+			15.8(6)	
1989	6_1^+	868	4_1^+				1335(64)
2134	(2^+)	1014	4_1^+		2.6(1)		784(55)
2293	$(3, 4)$	1853	2_1^+		3.4(1)		
2357	3_1^-	1917	2_1^+	34.2(5)	7.5(1)		
	3_1^-	1396	2_3^+	29.8(5)	7.2(3)	69.3(10)	
	3_1^-	1174	2_5^+		2.8(1)	24.3(10)	
	3_1^-	1045	2_3^+	24.4(5)	4.0(1)	21.6(8)	
2456	(2^+)	1495	2_2^+			11.2(11)	
2516	$(1, 2)$	2516	0_1^+	15.5(4)			
2681	(2^+)	2681	0_1^+	18.4(4)			
2357	3_2^-	2264	2_1^+	56.5(5)	16.0(1)		
	3_2^-	1747	2_2^+	270.0(7)	64.4(3)	567.3(25)	
	3_2^-	1524	2_3^+	d_2	d_2	d_2	
	3_2^-	914	2_7^+	d_1	d_1		
3166	3_3^-	1983	2_3^+			10.8(6)	
d_1				33.2(4)	6.4(1)		

Table C.2.: Peak areas of selected transitions of ²⁰²Hg determined in ring spectra in coincidence with the 2₁⁺ → 0₁⁺ transition unless otherwise noted.

ring	2 ₁ ⁺ → 0 ₁ ⁺ ^a ×10 ³	2 ₂ ⁺ → 2 ₁ ⁺	4 ₁ ⁺ → 2 ₁ ⁺	2 ₇ ⁺ → 2 ₁ ⁺	3 ₂ ⁻ → 2 ₂ ⁺	2 ₃ ⁺ → 2 ₁ ⁺	2 ₃ ⁺ → 2 ₂ ⁺
2	9997(3)	5911(79)	4741(71)	910(34)	1148(37)	205(24)	743(48)
3	12178(4)	6935(86)	5616(78)	990(36)	1348(40)	216(22)	908(43)
4	25433(5)	13844(122)	11473(112)	1887(54)	3201(62)	434(55)	1791(63)
5	11949(4)	6515(83)	5178(75)	861(34)	1580(44)	181(22)	803(41)
6	27371(5)	14856(127)	11802(113)	1972(54)	4174(69)	415(31)	1707(63)
7	10924(3)	5743(70)	4477(70)	734(33)	1566(42)	160(28)	699(44)
8	13884(4)	7267(88)	5777(80)	923(38)	2014(48)	176(22)	929(48)
9	19773(5)	10848(108)	8326(94)	1392(44)	2891(56)	299(27)	1368(56)
10	12814(4)	6879(88)	5623(78)	940(38)	1785(46)	223(22)	803(47)
11	13677(4)	7290(90)	5920(79)	941(38)	1920(47)	224(23)	890(45)
12	26183(5)	14440(127)	11615(112)	1880(54)	3599(65)	423(33)	1723(66)
13	10375(3)	5893(79)	4978(73)	830(33)	1335(39)	178(19)	695(38)
14	23619(5)	13316(119)	11147(109)	1909(51)	2941(59)	418(32)	1728(63)
15	13191(4)	7795(90)	6553(83)	1100(37)	1532(41)	234(20)	925(49)
16	12446(4)	7296(88)	6309(81)	1120(37)	1574(43)	216(21)	861(43)
17	12306(4)	7573(89)	6424(82)	1965(36)	1364(39)	248(22)	899(45)

^aMeasured in γ singles

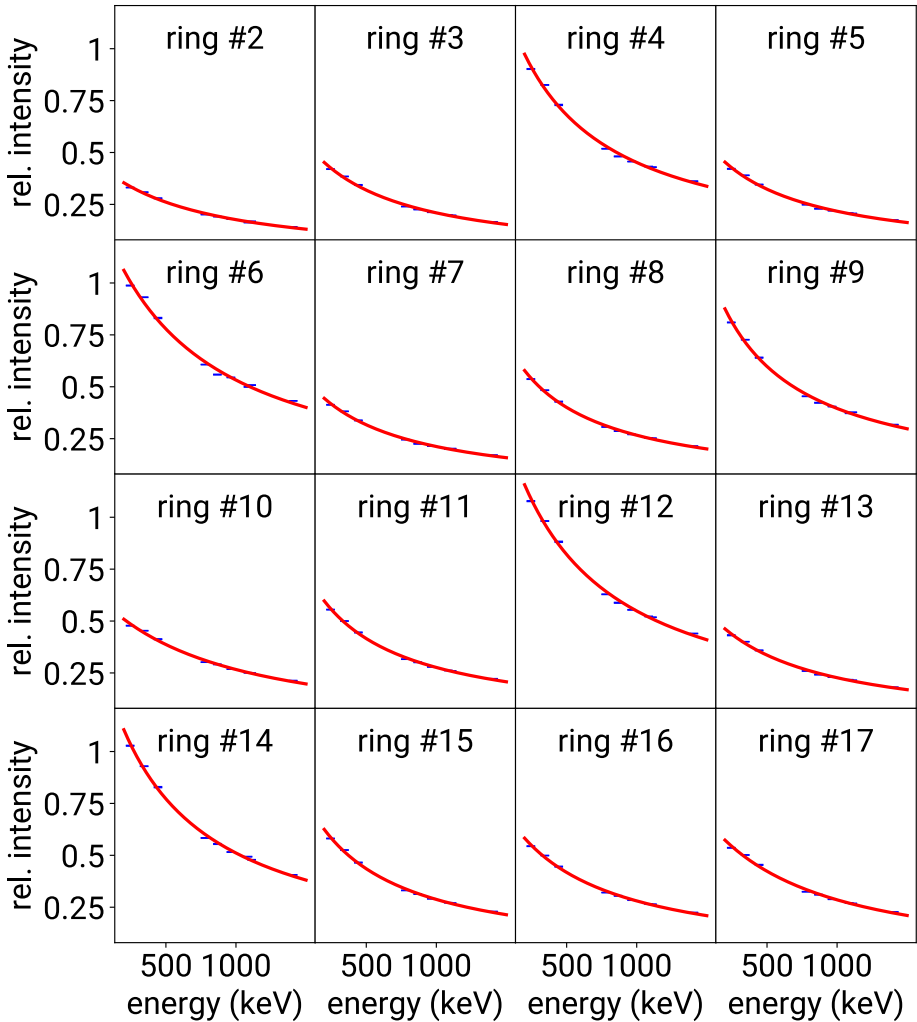


Figure C.2.: The ringwise efficiency calibration measurements of Gammasphere. A simple exponential decay function was used for the fit on the data from the ^{152}Eu source ($E_\gamma > 200$ keV).

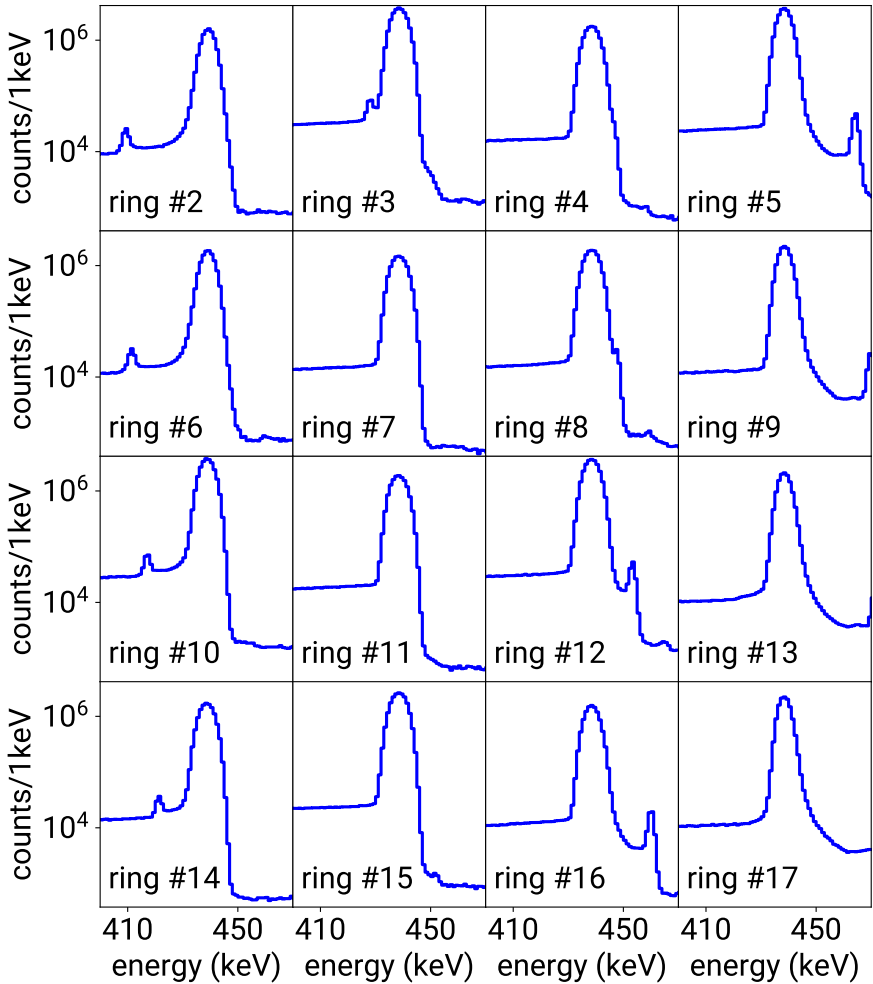


Figure C.3.: Ringwise γ -ray singles spectra zoomed to the $2_1^+ \rightarrow 0_1^+$ transition at 439 keV are shown. The determined peak areas are presented in Table C.2.

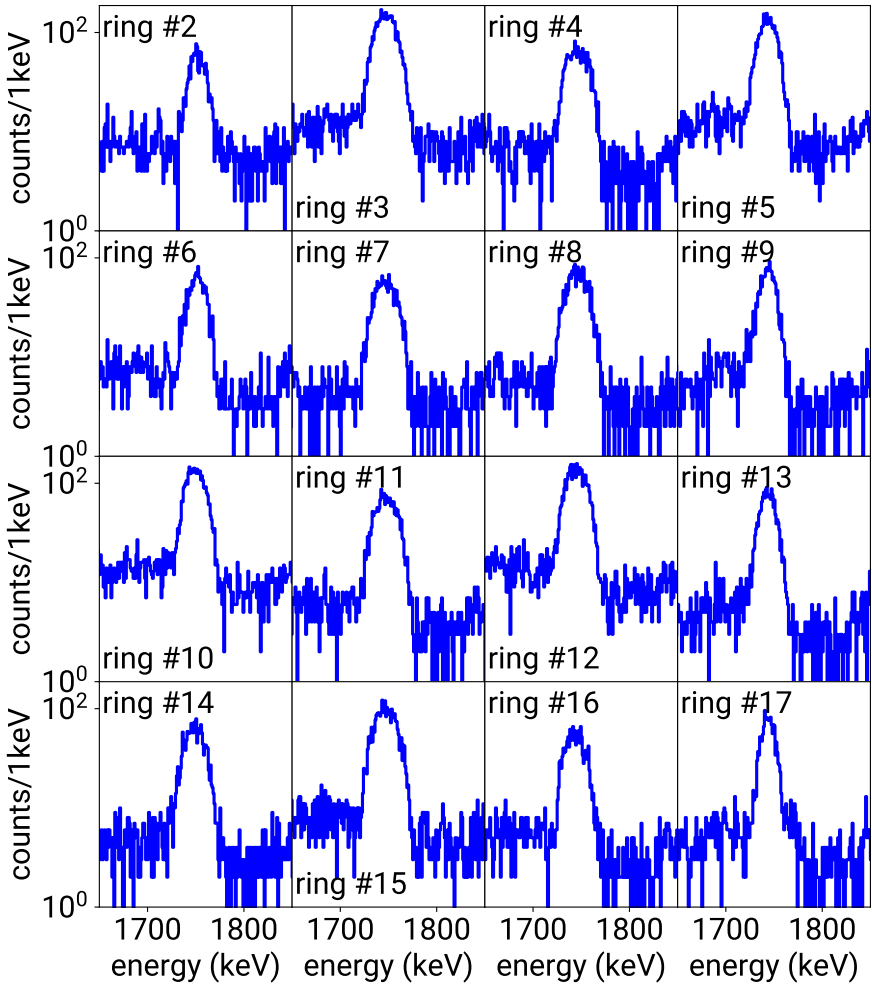


Figure C.4.: Ringwise γ -ray spectra gated on the $2_1^+ \rightarrow 0_1^+$ transition and zoomed to the $3_2^- \rightarrow 2_1^+$ transition at 1747 keV are shown. The determined peak areas are presented in Table C.2.

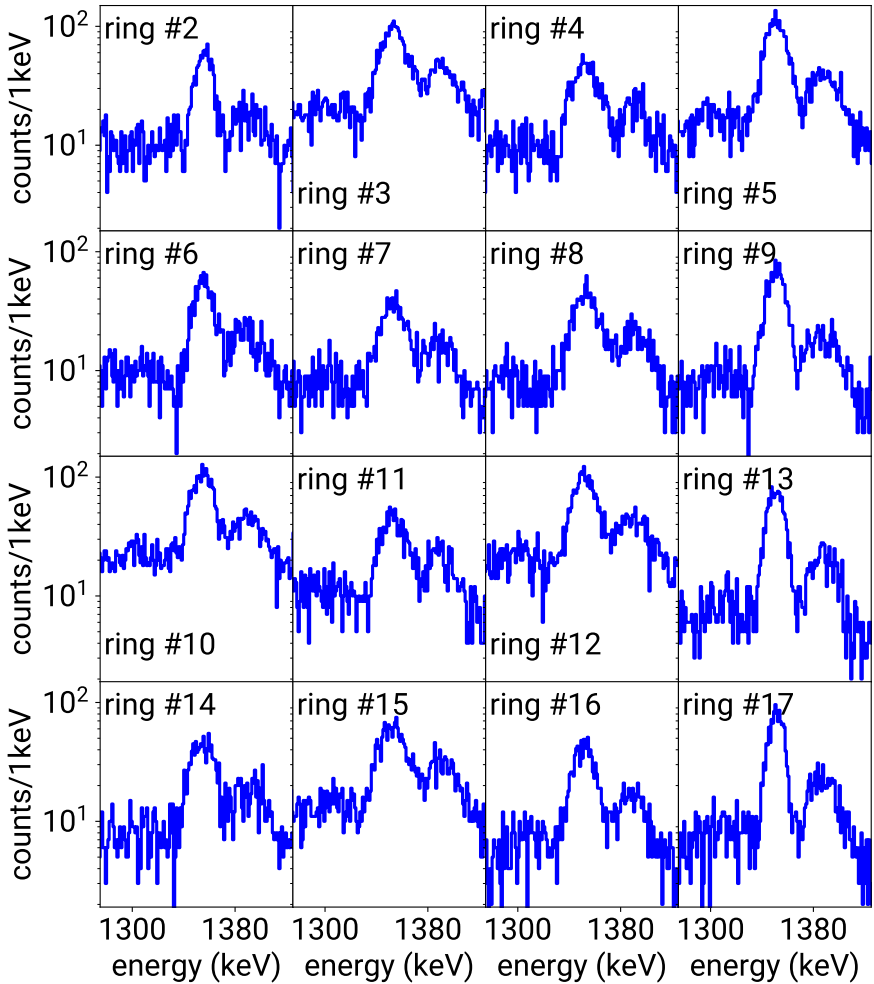


Figure C.5.: Ringwise γ -ray spectra gated on the $2_1^+ \rightarrow 0_1^+$ transition and zoomed to the $2_7^+ \rightarrow 2_1^+$ transition at 1354 keV are shown. The determined peak areas are presented in Table C.2.

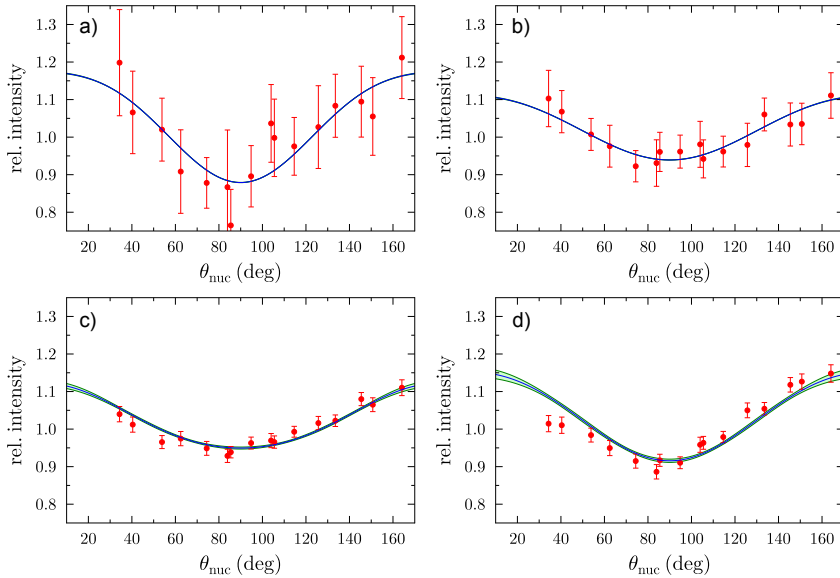


Figure C.6.: The angular distributions of the transitions $2_3^+ \rightarrow 2_2^+$, $2_3^+ \rightarrow 2_1^+$, $2_2^+ \rightarrow 2_1^+$ and $4_1^+ \rightarrow 2_1^+$ in coincidence with the $2_1^+ \rightarrow 2_1^+$ transition are shown in a), b), c) and d), respectively. The intensities are determined with the spectra from Figures C.7, C.8, C.9 and C.10.

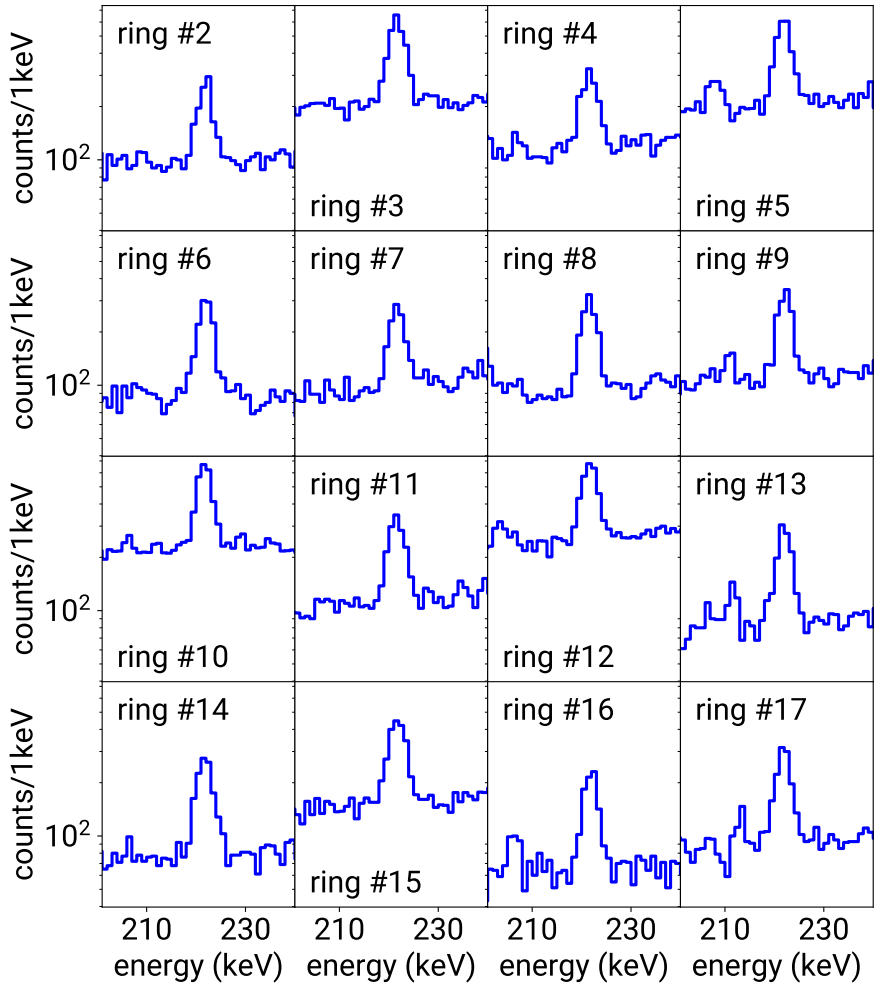


Figure C.7.: Ringwise γ -ray spectra gated on the $2_1^+ \rightarrow 0_1^+$ transition and zoomed to the $2_3^+ \rightarrow 2_2^+$ transition at 222 keV are shown. The determined peak areas are presented in Table C.2.

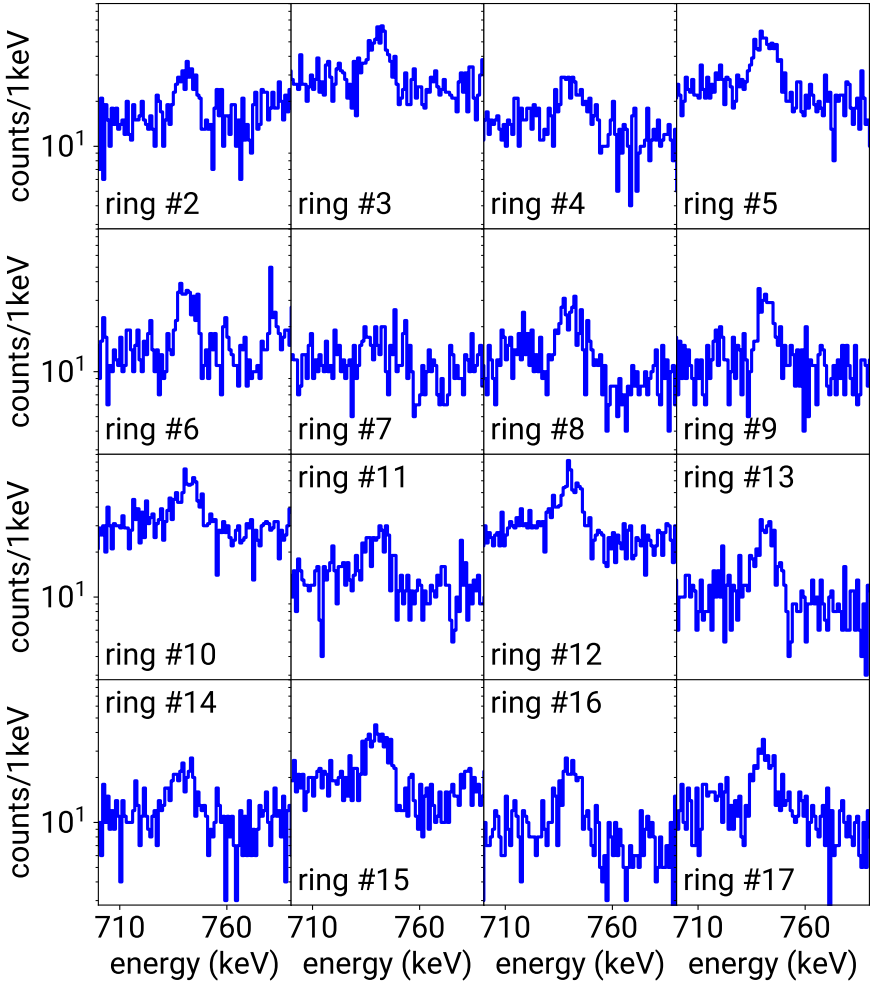


Figure C.8.: Ringwise γ -ray spectra gated on the $2_1^+ \rightarrow 0_1^+$ transition and zoomed to the $2_3^+ \rightarrow 2_1^+$ transition at 742 keV are shown. The determined peak areas are presented in Table C.2.

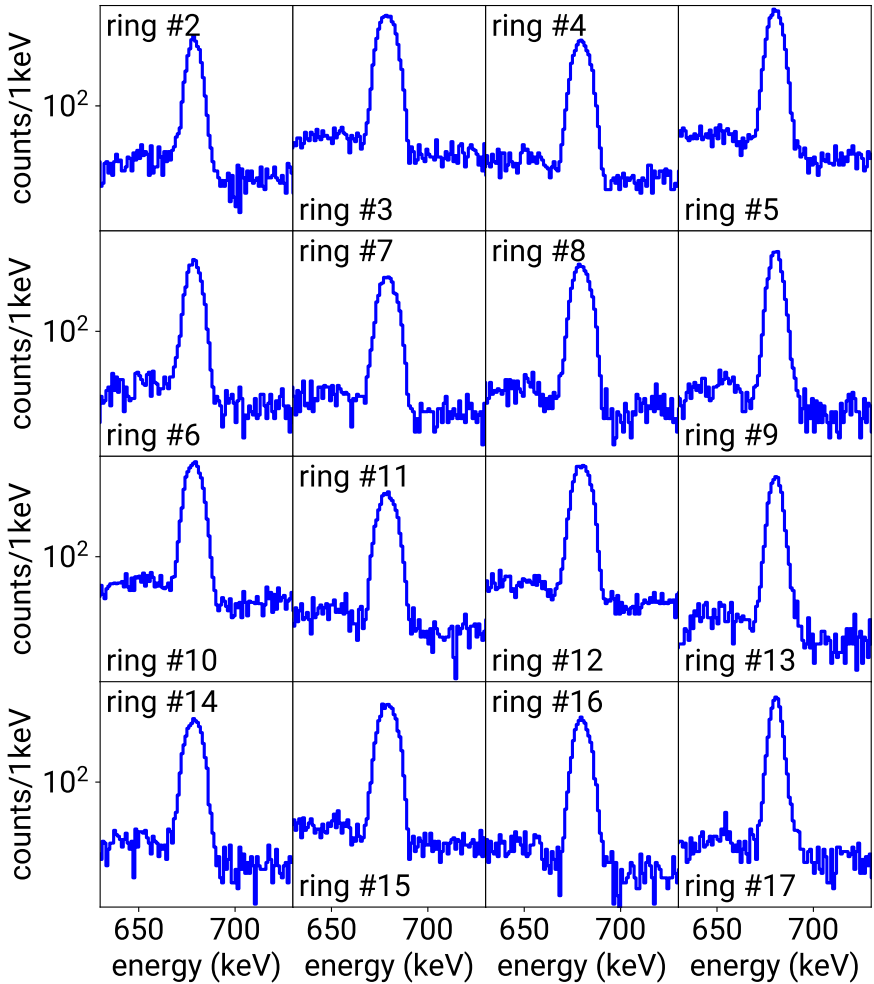


Figure C.9.: Ringwise γ -ray spectra gated on the $2_1^+ \rightarrow 0_1^+$ transition and zoomed to the $4_1^+ \rightarrow 2_1^+$ transition at 680 keV are shown. The determined peak areas are presented in Table C.2.

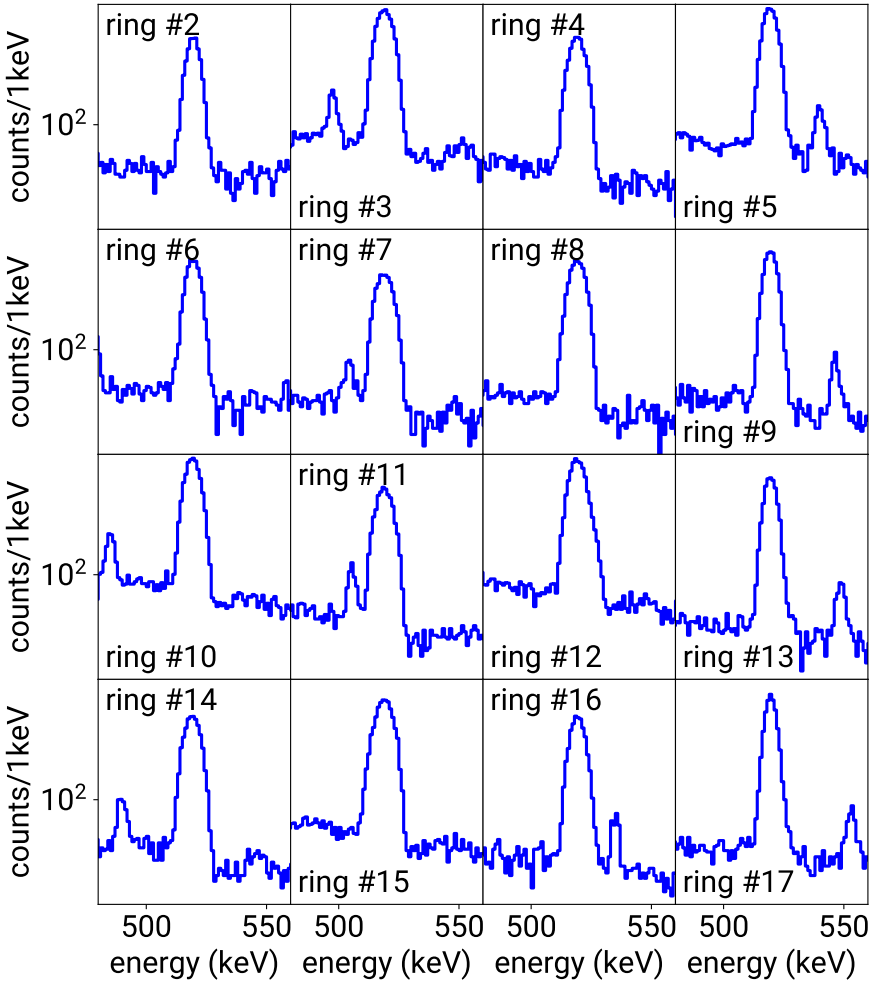


Figure C.10.: Ringwise γ -ray spectra gated on the $2_1^+ \rightarrow 0_1^+$ transition and zoomed to the $2_2^+ \rightarrow 2_1^+$ transition at 520 keV are shown. The determined peak areas are presented in Table C.2.

D. CLX Files

The CE code CLX was used to calculate the cross sections of excited states of ^{202}Hg in the $^{12}\text{C}(^{202}\text{Hg}, ^{202}\text{Hg}^*)^{12}\text{C}$ CE reaction. The input file consists of three parts. The header to define the experiment, the involved nuclear states and the transition matrix elements between the nuclear states.

Listing D.1: CLX-input file for the $^{12}\text{C}(^{202}\text{Hg}, ^{202}\text{Hg}^*)^{12}\text{C}$ CE experiment.

```
1 202Hg on 12C @890MeV Gammasphere !Title
2 11101111
3 24 0 6. !Max states inv=0—Max Value of Magnetic N
4 0. 0. 0. !Accuracy parameters
5 6 202 !Target Z projectile A
6 80 12 !Projectile Z target A
7 829 !Average beam energy (target thickness)
8 0.1 180 10 !Starting angle—stopping, step in cm sys
9 1 0 0.0 1 0 !Levels—Spin—energy(mev)—Parity
10 2 2 0.439 1 0
11 3 2 0.960 1 0
12 4 4 1.120 1 0
13 5 2 1.182 1 0
14 6 4 1.311 1 0
15 7 2 1.348 1 0
16 8 2 1.389 1 0
17 9 0 1.564 1 0
18 10 2 1.575 1 0
19 11 0 1.643 1 0
20 12 2 1.793 1 0
21 13 2 1.823 1 0
22 14 5 1.965 -1 0
23 15 2 1.966 1 0
24 16 6 1.988 1 0
25 17 2 2.133 1 0
26 18 4 2.293 1 0
27 19 3 2.356 -1 0
28 20 2 2.456 1 0
29 21 2 2.516 1 0
30 22 2 2.681 1 0
31 23 3 2.709 -1 0
32 24 3 3.166 -1 0
33
34 1 2 0.7815 2 !439keV B(E2) nndc
35 1 3 0.0366 2 !960 keV smaller than value from nndc
```

36	1	4	0.0001	4	!E4 excitation of 4+1 state =0
37	1	5	0.0001	2	
38	1	6	0.0001	4	!E4 excitation of 4+2 state =0
39	1	7	0.0001	2	
40	1	8	0.02158	2	
41	1	10	0.0001	2	
42	1	12	0.0691	2	
43	1	13	0.0429	2	
44	1	15	0.0001	2	
45	1	17	0.02961	2	
46	1	18	0.0001	4	!E4 excitation of 4+3 state =0
47	1	19	0.204	3	
48	1	20	0.02783	2	
49	1	21	0.0618	2	
50	1	22	0.0831	2	
51	1	23	0.5915	3	
52	1	24	0.1316	3	
53					
54	2	2	-1.33	2	!quadrupole moment from nndc
55	2	3	0.303	2	!520 keV smaller than value from nndc
56	2	4	1.297	2	!680 keV
57	2	5	0.2139	2	!predetermined from br and delta
58	2	6	0.2166	2	!
59	2	7	0.23145	2	!908 keV
60	2	8	0.168	2	!950 keV predetermined from br
61	2	9	0.203	2	
62	2	10	0.1295	2	!1135 keV predetermined from br
63	2	11	0.1349	2	
64	2	12	0.0499	2	!predetermined from br and delta
65	2	13	0.302	2	!1384 keV predetermined from br
66	2	14	0.4955	3	!excitation of the 5- state
67	2	15	0.592	2	!1527 keV
68	2	16	0.528	4	
69	2	18	0.467	2	!
70	2	20	0.0001	2	!gs excitation
71					
72	3	3	0	2	
73	3	5	0.882	2	!222 keV predetermined from br and delta
74	3	6	2.951	2	!351 keV predetermined from br
75	3	8	0.661	2	!429 keV predetermined from br
76	3	10	0.784	2	!616
77	3	12	0.470	2	!833 keV predetermined from br
78	3	13	0.630	2	!863 keV predetermined from br
79					
80	4	4	0	2	
81	4	16	1.52	2	!B(E2) nndc
82					
83	5	5	0	2	
84	5	6	3.82	2	!129 keV predetermined from br
85	5	8	2.94	2	!207 keV predetermined from br
86	5	13	0.853	2	!615 keV predetermined from br
87					
88	6	6	0	2	
89	6	15	1.39	2	!654 keV predetermined from br

Listing D.2: Python3 code using CLX to determine the uncertainties of the MEs.
 This code was designed for the $^{12}\text{C}(^{202}\text{Hg}, ^{202}\text{Hg}^*)^{12}\text{C}$ CE experiment.

```

1 import numpy as np
2 import math as mt
3 import random
4 import os
5
6
7 ##customized codes functions.py and yield_norm.py###
8 import functions as fn
9 import yield_norm as yn
10
11
12 max_iter = 100 ##number of iterations##
13
14 ##start of determination of the set of matrix elements###
15 for k in range(0,max_iter):
16
17     maxtrans = int(40) #number of transitions
18     maxlvl = int(23) #number of levels
19
20     ##production of the list of transitions , yields and the beam energy varied
21     ##inside the uncertainties of known quantities###
22     clxhgtrans = yn.clx_trans_rn()
23     hgyields = yn.clx_yields_rn()
24     beam_energy = yn.beam_energy_rn()
25
26     small_range = [0,13] #definition of the 2 fixed ME <0+1||E2||2+1> and <2+1||E2
27     ||2+1>
28     trans_final = np.zeros((maxtrans,4)) # definition of list for the final MEs
29     big_range = [j for j in range(0,maxtrans) if j not in yn.branching_rn()[0].nums
30     ] #definition of MEs, which will be varied excluding ME which are predetermine
31     by other MEs
32     big_iter = 0 #start value for big_iter
33
34     while big_iter < 25:
35         ##FILE and PATH definitions###
36         PATH_TO_CLX = "/home/ralli/Physik/clx_test/clx_source_code/clx"
37         NAME_OF_TEMP_CLX = "blubber.clx"
38         INPUT_HEADER = "input/rest_py.dat"
39         INPUT_LEVELS = "input/lvl_py.dat"
40         RANDOM_BEAM_E = "random/beamenergy_hg_rn.dat"
41         RANDOM_TRANSITIONS = "random/trans_hg_rn.dat"
42         PATH_TO_XSECS = "random/x_section_hg.dat"
43         PATH_TO_TAB3 = ".././tab3.awk"
44
45         os.system("rm "+NAME_OF_TEMP_CLX) #remove old CLX input
46         os.system("cat "+INPUT_HEADER+" "+RANDOM_BEAM_E+" "+INPUT_LEVELS+" "+
47         RANDOM_TRANSITIONS+" >> "+ NAME_OF_TEMP_CLX) # produce new CLX input
48         os.system(PATH_TO_CLX+" <"+NAME_OF_TEMP_CLX+" | "+PATH_TO_TAB3+" > "+
49         PATH_TO_XSECS) #execute new CLX file and save xsecs in PATH_TO_XSECS
50
51         clxhg = np.loadtxt(PATH_TO_XSECS, dtype={'names': ('lvl', 'xsec', 'rel')},

```

```

formats': (np.int, np.float, np.float)}, skiprows=3) #load CLX xsections
46
47 diff_yield_xsection = [(clxhgx[i][0], (clxhgx[i][2] - hgyields[i][1])/
hgyields[i][1], (clxhgx[i][2] - hgyields[i][1])/hgyields[i][2]) for i in range(
maxlvl)] #determine deviation of CLX and experimental relative xsections
48
49 error_sum1 = np.sum([abs(diff_yield_xsection[i][1]) for i in range(maxlvl)
])/maxlvl #normalized error sum
50
51 print(error_sum1, big_iter)
52 ##### start of the production of new set of matrix elements###
53 for i in big_range:
54     z = int(clxhgtrans[i][1]-2)
55     if i in small_range:
56         clxhgtran1 = clxhgtrans[i][2] #the two known ME are fixed
57     elif i == 2:
58         clxhgtran1 = 0.0 # that ME <2+3||E2||0+1> is defined to be 0, for
an upper limit that may change
59     else:
60         diff_temp = abs(diff_yield_xsection[z][1]) #deviation of CLX and
EXP
61         sign_diff = np.sign(diff_yield_xsection[z][1]) #increase or
decrease?
62         sign_me = np.sign(clxhgtrans[i][2])
63         #####crucial part#####
64         #the change of the ME is defined by the deviation of CLX
65         #and EXP yields and whether the CLX yields have to increase or
decrease.
66         #Furthermore, the change is randomized to prevent loopings and the
change decrease with rising iterations.
67         #####
68         clx_add = sign_me*sign_diff*np.random.normal(diff_temp, diff_temp
/100,1)[0]*clxhgtrans[i][2]/(big_iter+10)
69         clxhgtran1 = clxhgtrans[i][2] - clx_add
70         trans_final[i] = clxhgtrans[i][0], clxhgtrans[i][1], clxhgtran1,
clxhgtrans[i][3] #definition of new matrix element
71
72         #####The predetermined MEs are added to the list of MEs####
73         ###They are determined via branching ratios, deltas, energies.... and
another ME, e.g. of a ground state transition####
74         ###The quantities are saved in yields_norm.py and will be varied inside
their uncertainties#####
75         for obj in yn.branching_rn():
76             length_dec = len(obj.decay)
77             for i in range(length_dec):
78                 it = obj.decay[i][3]
79                 test = fn.multi_func(obj.decay[i][0], obj.delta, obj.decay[i][1],
trans_final[obj.num][2], obj.en, obj.decay[i][2], obj.br, obj.decay[i][4], obj.nL,
obj.decay[i][5])
80                 trans_final[it] = clxhgtrans[it][0], clxhgtrans[it][1], test,
clxhgtrans[it][3]
81
82
83         clxhgtrans = trans_final

```

```

84     np.savetxt(RANDOM_TRANSITIONS, trans_final, fmt=( '%-4d', '%-4d', '%1.8f', '%-4d'
85 ))#save set of MEs
86     big_iter += 1 #increase big_iter
87     if error_sum1 < 0.05: #convergence criterium
88         print('converged')
89         PATH_TO_MES = "mxe"
90         os.system("cp "+RANDOM_TRANSITIONS+" "+PATH_TO_MES+"/set"+str(k)) #copy
91         final set of MEs to a folder where all sets of successful minimization are
92         stored
93         break
94     elif error_sum1 > 1.25 or big_iter > 24: #failed to converge -> start new
95     print('failed to converge')
96     big_iter = 0
97     clxhgtrans = yn.clx_trans_rn()
98     hgyields = yn.clx_yields_rn()
99     eam_energy = yn.beam_energy_rn()
100    small_range = [0,13]

```

Listing D.3: Variation of known quantities inside their uncertainties in lists which are used in Listing D.2.

```

1  '''
2  Python script to vary the known quantities inside their uncertainties using normal
3  distributions
4  '''
5  import numpy as np
6  import math as mt
7  import random
8  import functions as fn
9
10 maxlvl = int(23)#number of levels
11 maxtrans = int(40)#number of transitions
12 def clx_yields_rn():#variation of the experimental yields inside their
13     uncertainties
14     filename_yield = "input/yields_hg.dat"
15     hgyields = np.loadtxt(filename_yield, dtype={'names': ('lvl_en', 'rel', 'deltarel')},
16         'formats': (np.int, np.float, np.float)}, skiprows=1)
17
18     return [[hgyields[i][0], np.random.normal(hgyields[i][1], hgyields[i][2], 1),
19         hgyields[i][2]] for i in range(maxlvl)]
20
21 def clx_trans_rn():#variation of the known MEs inside their uncertainties
22     filename_trans = "input/trans_hg_py.dat"
23     clxhg_trans = np.loadtxt(filename_trans, dtype={'names': ('lvl_d', 'lvlup', 'mx', 'L')},
24         'formats': (np.int, np.int, np.float, np.int)})
25     hgtrans_rn = []
26     for i in range(0, maxtrans):
27         if i == 0: #ME <2+1|E2|0+1>
28             hgtrans_iter = (clxhg_trans[i][0], clxhg_trans[i][1], np.random.normal(
29                 clxhg_trans[i][2], 0.0032, 1)[0], clxhg_trans[i][3])
30         elif i == 13: #ME <2+1|E2||2+1>
31             hgtrans_iter = (clxhg_trans[i][0], clxhg_trans[i][1], np.random.normal(
32                 clxhg_trans[i][2], 0.17, 1)[0], clxhg_trans[i][3])

```

```

26     else:#all other MEs
27         hgtrans_iter = (clxhg_trans[i][0],clxhg_trans[i][1],clxhg_trans[i][2],
28             clxhg_trans[i][3])
29         hgtrans_rn.append(hgtrans_iter)
30     RANDOM_TRANSITIONS = "random/trans_hg_rn.dat"
31     np.savetxt(RANDOM_TRANSITIONS, hgtrans_rn,fmt=( '%-4d', '%-4d', '%1.8f', '%-4d'))#
32     save MEs
33     return hgtrans_rn
34
35 def beam_energy_rn():#variation of the beam_energy, bc of the energy loss in the
36     target
37     beam_energy_rn = np.random.normal(829,6.5,1)
38     RANDOM_BEAM_E = "random/beamenergy_hg_rn.dat"
39     np.savetxt(RANDOM_BEAM_E, beam_energy_rn,fmt=( '%-4d'))
40
41 def branching_rn():#variation of the branching ratios
42     #520 960 keV
43     1960 = fn.level(960,1,np.random.normal(14, .2,1),2,0)
44     1960.add_decay(520,14,np.random.normal(100, .2,1),0,2,np.random.normal(.9,0.1,1))
45
46     #1182keV
47     11182 = fn.level(742,16,np.random.normal(51,2,1),2,np.random.normal(2.1,0.4,1))
48     11182.add_decay(222,29,np.random.normal(100,4,1),2,2,np.random.normal
49         (-.13,0.03,1))
50
51     #1311keV
52     11311 = fn.level(872,17,np.random.normal(51,4,1),2,0)
53     11311.add_decay(351,30,np.random.normal(100,3,1),1,2,0)
54     11311.add_decay(129,36,np.random.normal(17,5,1),1,2,0)
55
56     #1389keV
57     11389 = fn.level(1389,3,np.random.normal(11,4,1),2,0)
58     11389.add_decay(950,19,np.random.normal(100,4,1),1,2,0)
59     11389.add_decay(430,31,np.random.normal(29,3,1),1,2,0)
60     11389.add_decay(207,37,np.random.normal(15,4,1),1,2,0)
61
62     #1575keV
63     11575 = fn.level(1135,21,np.random.normal(58,19,1),2,0)
64     11575.add_decay(616,32,np.random.normal(100,16,1),1,2,0)
65
66     #1793
67     11794 = fn.level(1794,4,np.random.normal(2.8,1.3,1),2,0)
68     11794.add_decay(1354,23,np.random.normal(100,1,1),0,2,np.random.normal
69         (0.06,0.04,1))
70     11794.add_decay(833,33,np.random.normal(3.0, .6,1),1,2,0)
71
72     #1823
73     11823 = fn.level(1823,5,np.random.normal(8,3,1),2,0)
74     11823.add_decay(1384,24,np.random.normal(100,6,1),0,2,np.random.normal(0.1,0.1,1)
75         )
76     11823.add_decay(863,34,np.random.normal(41,4,1),1,2,0)
77     11823.add_decay(641,38,np.random.normal(17,2,1),1,2,0)

```



```

74
75 #1966keV
76 l1966 = fn.level(1527,26,np.random.normal(100,8,1),2,0)
77 l1966.add_decay(654,39,np.random.normal(8,3,1),1,2,0)
78
79 return [l1960,l1182,l1311,l1389,l1575,l1794,l1823,l1966]

```

Listing D.4: Conversions and relations used in Listing D.2.

```

1 import numpy as np
2 import weakref
3
4
5 class level(object):
6
7     nums = []
8     _instances = set()
9     #defining norm qualities of a level, i.e. of the dominant transition
10    def __init__(self, norm_energy, norm_number, norm_branching, norm_L, norm_delta):
11        self.en = norm_energy
12        self.num = norm_number
13        self.br = np.abs(norm_branching)#must be positive
14        self.nL = norm_L
15        self.delta = norm_delta
16        self.decay = []
17        self._instances.add(weakref.ref(self))
18    #add a second decay
19    def add_decay(self, energy, tnum, branching, decay_mode, L2, delta2):
20        self.decay.append([decay_mode, delta2, energy, tnum, np.abs(branching), L2])
21        self.nums.append(tnum)
22
23    @classmethod
24    def getinstances(cls):
25        dead = set()
26        for ref in cls._instances:
27            obj = ref()
28            if obj is not None:
29                yield obj
30            else:
31                dead.add(ref)
32        cls._instances -= dead
33
34    #constants of this experiment
35    Aint = 202 #mass number of 202hg
36    wuconv = [.06446*Aint**(2/3),.05940*Aint**(4/3),.05940*Aint**2] #conversion to W.u.
37    ce = [1.59*10**15, 1.22*10**9, 5.67**2] #conversion constant
38    cm = 1.76*10**13 #conversion constant
39
40    #conversion from eb to W.u.
41    def WuE(L,A):
42        return 1/(4*np.pi)*(3/(L+3))**2*1.2**(2*L)*A**(2*L/3)*10**(-2*L)
43
44    #calculation of B(EL) in W.u. from the ME

```

```

45 def BE(mxe, Ii , L) :
46     return mxe**2/(2*Ii +1)/WuE(L, Aint)
47
48 #calculation of the partial natural linewidth from B(EL)
49 def gammaE(L, E, B) :
50     return ce[L-1]*(E)**(2*L+1)*B*WuE(L, Aint)*10**4
51
52 #calculation of the partial natural linewidth from B(ML)
53 def gammaM(L, E, B) :
54     return cm*(E)**(2*L+1)*B
55
56 #determination of the ratio of 2 ME by the branching ratio, the multipolarities and
57   the energies (pure transition or no delta known)
58 def meratio1(br1 , br2 , L1 , L2 , E1 , E2) :
59     return np. sqrt ((br1*ce[L2-1]*E2**(2*L2 + 1)*wuconv[L2-1])/(br2*ce[L1-1]*E1**(2*L1
60   +1)*wuconv[L1-1]))
61
62 #the corresponding ME from the ratio meratio1
63 def melement(me1, br1 , br2 , L1 , L2 , E1 , E2) :
64     return me1/meratio1 (br1 , br2 , L1 , L2 , E1 , E2)
65
66 #The same when mixed transitions are involved, the electrical ME are returned
67 def conversionE(Delta , me, E1, E2, br) :
68     return np. sqrt (((Delta**2*gammaM(1, E2, gammaE(2, E1, BE(me, 2, 2)))/(br*(1+Delta**2)*cm
69   *E2**3)))/(ce[1]*E2**5*WuE(2, Aint)*10**4))*5*WuE(2, Aint))
70
71 #The same for L=2
72 def conversionE2(Delta1 , Delta2 , me, E1, E2, br) :
73     return np. sqrt (((E1/E2)**5) / br * ((1/Delta1)**2 + 1) / ((1 / Delta2)**2 + 1)*me
74   **2)
75
76 #Assignment of different cases to the three different possibilities
77 def multi_func(FLAG, Delta1 , Delta2 , me, E1, E2, br1 , br2 , L1 , L2) :
78     try :
79         if FLAG == 0:
80             return conversionE(Delta2 , me, E1/1000, E2/1000, br1/br2)
81         elif FLAG == 1:
82             return melement(me, br1 , br2 , L1 , L2 , E1 , E2)
83         elif FLAG == 2:
84             return conversionE2(Delta1 , Delta2 , me, E1/1000, E2/1000, br1/br2)
85     except :
86         print([FLAG, Delta1 , Delta2 , me, E1, E2, br1 , br2 , L1 , L2])
87         return None

```

Listing D.5: The header for the CLX-input file used in Listing D.2.

```
1 202Hg on 12C @890MeV Gammasphere !Title
2 11101111
3 24 0 6. !Max states inv-0-Max Value of Magnetic N
4 0. 0. 0. !Accuracy parameters
5 6 202 !Target Z projectile A
6 80 12 !Projectile Z target A
```

Listing D.6: The list of levels for the CLX-input file used in Listing D.2.

```
1 0.1 180 10 !Starting anglge-stopping,step in cm sys
2 1 0 0.0 1 0 !Levels-Spin-energy(mev)-Paritiy
3 2 2 0.439 1 0
4 3 2 0.960 1 0
5 4 4 1.120 1 0
6 5 2 1.182 1 0
7 6 4 1.311 1 0
8 7 2 1.348 1 0
9 8 2 1.389 1 0
10 9 0 1.564 1 0
11 10 2 1.575 1 0
12 11 0 1.643 1 0
13 12 2 1.793 1 0
14 13 2 1.823 1 0
15 14 5 1.965 -1 0
16 15 2 1.966 1 0
17 16 6 1.988 1 0
18 17 2 2.133 1 0
19 18 4 2.293 1 0
20 19 3 2.356 -1 0
21 20 2 2.456 1 0
22 21 2 2.516 1 0
23 22 2 2.681 1 0
24 23 3 2.709 -1 0
25 24 3 3.166 -1 0
```

Listing D.7: The list of transitions and MEs for the CLX-input file used in Listing D.2.

1	1	2	0.7815	2
2	1	3	0.0366	2
3	1	5	0.00	2
4	1	8	0.02158	2
5	1	12	0.0691	2
6	1	13	0.0429	2
7	1	17	0.02961	2
8	1	19	0.204	3
9	1	20	0.02783	2
10	1	21	0.0618	2
11	1	22	0.0831	2
12	1	23	0.5915	3
13	1	24	0.1316	3
14	2	2	-1.33	2
15	2	3	0.303	2
16	2	4	1.297	2
17	2	5	0.14	2
18	2	6	0.22	2
19	2	7	0.23145	2
20	2	8	0.168	2
21	2	9	0.203	2
22	2	10	0.1295	2
23	2	11	0.1349	2
24	2	12	0.0499	2
25	2	13	0.302	2
26	2	14	0.4955	3
27	2	15	0.592	2
28	2	16	0.528	4
29	2	18	0.467	2
30	3	5	4.882	2
31	3	6	2.951	2
32	3	8	0.661	2
33	3	10	0.784	2
34	3	12	0.470	2
35	3	13	0.630	2
36	4	16	1.52	2
37	5	6	3.82	2
38	5	8	2.94	2
39	5	13	0.853	2
40	6	15	1.39	2

E. HIL β^+/ϵ Decay Experiment

Listing E.1: Python code for the calculation of the activities of the β^+/ϵ -decay experiment at the HIL.

```
1 import numpy as np
2 import pandas as pd
3 import random
4 import time
5
6 ### Time ###
7 activity_total = []
8 timescale = 1 #1/timescale second: 1->s, 1000->ms, etc...
9 maximum = int(50000) #length of simulation in units of the timescale
10 xdata = np.linspace(0,maximum,maximum+1)
11 dx = xdata[1]-xdata[0] #needed for building gradients
12
13 ### Lifetimes ###
14 #A = 142
15 Tgd = 70*timescale #142Gd in units of timescale
16 Teu1 = 2.4*timescale #142Eu (short-lived isomer) in units of timescale
17 Teu2 = 1.223*60*timescale #142Eu (long-lived isomer) in units of timescale
18 Tsm = 70*60*timescale #142Sm in units of timescale
19 #A = 141
20 Teu141 = 2.7*timescale #141Eu
21 Tsm141 = 22.6*60*timescale #141Sm
22
23 #####
24 #cross section integrated over the interaction depth (mb * mg/cm^2)
25 #####
26
27 x_secs = pd.read_csv('./x_sec_140MeV.csv') #read-out of PACE4 output file
28 x_secs = x_secs.values #list manipulation
29 tot_xsec = x_secs[10][0] #values in mb
30
31 #####
32 #ratio of isotopes as reaction product
33 #at 140MeV 114Cd(32S)
34 #####
35
36 #mass 142
37 gd0 = x_secs[0][0]/tot_xsec #.121 142Gd
38 eu10 = 0 #0 142Eu s-l isomer
39 eu20 = x_secs[1][0]/tot_xsec #.232 142Eu l-l isomer
```

```

40 sm0 = x_secs[2][0]/tot_xsec #.139 142Sm
41 #mass 141
42 eu141 = x_secs[4][0]/tot_xsec #.137 141Eu
43 sm141 = x_secs[5][0]/tot_xsec #.112 141Sm
44 #mass139
45 sm139 = x_secs[7][0]/tot_xsec #.062 139Sm
46 pm139 = x_secs[8][0]/tot_xsec #.058 139Pm
47
48 #####
49 #beam and target specifications
50 #####
51
52 d_tar = 1 # 3.5 # in mg/cm^2, if the x_sec is already integrated over
53 the depth d_tar ==1 wo a unit
54 dens_tar = 8.65*10**3 #Cd in mg/cm^3
55 d_target = d_tar/(100*dens_tar) #thickness of target in [m]
56 Avogadro = 6.022*10**23 #Avogadro constant
57 mol_vol = 13*10**-6 #Sn: 16*10**-6 #molare volume m^3/mol
58 N_target = Avogadro * d_target / mol_vol #target particles per m^2
59
60 ### activation and measuring time ###
61 time_impl = 60 #time of implantation in units of the time scale
62 meas_time = 60 #time of stopped beam in units of the time scale
63
64 ### current in particles per second (pps) ###
65 pp_time = .5*27 * 10**9 * N_target * (tot_xsec*10**-31) / timescale #10**-31 is
66 used for the conversion von mb->m^2
67
68 ### Activation time at the start of the experiment ###
69 acti_time = 60*timescale
70
71 #####
72 #Definition of the functions for the activity and atom number
73 #####
74
75 ###
76 #atom number of directly produced isotopes
77 #N10 = number of produced isotopes per beam bunch
78 #T = half life
79 #t = time
80 ###
81 def N1(N10=1,T=2,t=3):
82     return N10*np.exp(-np.log(2)*t/T)
83
84 ###
85 #atom number of isotopes which are produced directly and through beta decay
86 #N20 = number of produced isotopes per beam bunch
87 #N10 = number of produced mother isotopes per beam bunch
88 #T2 = half life
89 #T1 = half life of mother nucleus
90 #t = time
91 ###
92 def N2(N20,T2,N10,T1,t):
93     return (N20+N10*(1-np.exp(-np.log(2)*t/T1)))*np.exp(-np.log(2)*t/T2)

```

```

92  ###
93
94  #atom number of isotopes which are produced directly and through beta decay of
    mother and grand mother
95  #N30 = number of produced isotopes per beam bunch
96  #N20 = number of produced mother isotopes per beam bunch
97  #N10 = number of produced grand mother isotopes per beam bunch
98  #T3 = half life
99  #T2 = half life of mother nucleus
100 #T1 = half life of grandmother nucleus
101 #t = time
102 ###
103 def N3(N30, T3, N20, T2, N10, T1, t):
104     N2temp = N20*(1-np.exp(-np.log(2)*t/T2))
105     N1temp = N10*(1-np.exp(-np.log(2)*t/T1)-np.exp(-np.log(2)*t/T2)+np.exp(-np.log
    (2)*t*(1/T1+1/T2)))
106     N3temp = (N30+N2temp+N1temp)*np.exp(-np.log(2)*t/T3)
107     return N3temp
108
109
110 ###
111 #corresponding activities
112 ###
113 def A1(N10, T1, t):
114     A = np.log(2)/T1*N10*2**(-t/T1)
115     return A
116
117 def A2(N20, T2, N10, T1, t):
118     A2temp = -np.gradient(N2(N20, T2, N10, T1, t), dx) + A1(N10, T1, t)
119     return A2temp
120
121 def A3(N30, T3, N20, T2, N10, T1, t):
122     A3temp = -np.gradient(N3(N30, T3, N20, T2, N10, T1, t), dx) + A2(N20, T2, N10, T1, t)
123     return A3temp
124
125 ###
126 #Sum of multiple beam implantations
127 ###
128 def sum_A_mult(N):
129
130     ylist_tot = np.zeros(maximum+1) #length of simulation
131     cyc = (meas_time+time_impl) #cycle of measuring and implantation
132
133     for i in range(acti_time): #implantation during activation time
134         ylist_tot += np.append(np.zeros(i), N[0:maximum+1-i])
135
136     for i in range(acti_time, maximum+1-cyc, cyc): #iteration from activation time
        till the end
137         for j in range(time_impl): #implantation during implantation time
138             ylist_tot += np.append(np.zeros(i+j), N[0:maximum+1-i-j])
139
140     return ylist_tot
141
142 #####

```

```

143 #reaction products
144 #####
145 ### A = 142 ###
146 #Gd
147 gdN = N1(gd0*pp_time ,Tgd ,xdata)
148 gd = A1(gd0*pp_time ,Tgd ,xdata)
149 #142Gd->142Eu, short-lived isomer
150 eu1N = N2(eu10*pp_time ,Teu1 ,gd0*pp_time ,Tgd ,xdata)
151 eu1 = A2(eu10*pp_time ,Teu1 ,gd0*pp_time ,Tgd ,xdata)
152 #142Eu, long-lived isomer
153 eu2N = N1(eu20*pp_time ,Teu2 ,xdata)
154 eu2 = A1(eu20*pp_time ,Teu2 ,xdata)
155 #142Sm, production channel via beta decay of the long-lived 142eu isomer
156 sm2N = N2(sm0*pp_time ,Tsm ,eu20*pp_time ,Teu2 ,xdata)
157 sm2 = A2(sm0*pp_time ,Tsm ,eu20*pp_time ,Teu2 ,xdata)
158 #142Sm, production channel via beta decays from 142Gd->142Eu
159 sm1N = N3(sm0*pp_time ,Tsm ,eu10*pp_time ,Teu1 ,gd0*pp_time ,Tgd ,xdata)
160 sm1 = A3(sm0*pp_time ,Tsm ,eu10*pp_time ,Teu1 ,gd0*pp_time ,Tgd ,xdata)
161 #Subtraction of the direct population to prevent double counting
162 smN = sm2N + sm1N - N1(sm0*pp_time ,Tsm ,xdata)
163 sm = sm1 + sm2 - A1(sm0*pp_time ,Tsm ,xdata)
164
165 ### A = 141 ###
166 #Eu
167 eu141N = N1(eu141*pp_time ,Teu141 ,xdata)
168 eu141A = A1(eu141*pp_time ,Teu141 ,xdata)
169 #Sm
170 sm141N = N2(sm141*pp_time ,Tsm141 ,eu141*pp_time ,Teu141 ,xdata)
171 sm141A = A2(sm141*pp_time ,Tsm141 ,eu141*pp_time ,Teu141 ,xdata)
172
173 #####
174 #Pulsed implantation over the maximum time (maximum * timescale) (1 implantation
    per time unit)
175 #Result is the activity after several implantations and the equilibrium activity
    can be determined
176 #####
177 ### A = 142 ###
178 #Gd
179 sumgdc = sA1_func(gd0 ,Tgd ,xdata)
180 sum_gdA = sum_A_mult(gd)
181 sumgd = sN1_func(gd0 ,Tgd ,xdata)
182 #Eu
183 sumeu2c = sA1_func(eu20 ,Teu2 ,xdata)
184 sum_eu2A = sum_A_mult(eu2)
185 sumeu1 = sN2_func(eu10 ,Teu1 ,gd0 ,Tgd ,xdata)
186 sumeu1c = sA2_func(eu10 ,Teu1 ,gd0 ,Tgd ,xdata)
187 sum_eu1A = sum_A_mult(eu1)
188 sumeu2 = sN1_func(eu20 ,Teu2 ,xdata)
189 #Sm
190 sumsmc = sA3_func(sm0 ,Tsm ,eu10 ,Teu1 ,gd0 ,Tgd ,xdata)+sA2_func(sm0 ,Tsm ,eu20 ,Teu2 ,xdata
    )
191 sum_smA = sum_A_mult(sm)
192 sumsm = sN3_func(sm0 ,Tsm ,eu10 ,Teu1 ,gd0 ,Tgd ,xdata)+sN2_func(sm0 ,Tsm ,eu20 ,Teu2 ,xdata)
193 ### A = 141 ###

```



```

194 #Eu
195 sumeu141 = sN1_func(eu141, Teu141, xdata)
196 sumeu141c = sA1_func(eu141, Teu141, xdata)
197 sum_eu141A = sum_A_mult(eu141A)
198 #Sm
199 sumsm141 = sN2_func(sm141, Tsm141, eu141, Teu141, xdata)
200 sumsm141c = sA2_func(sm141, Tsm141, eu141, Teu141, xdata)
201 sum_sm141A = sum_A_mult(sm141A)
202
203 #####
204 #####
205 #Different method, same result:
206 #Simulation of the implantation and decay process and the following activity
207 #####
208 #####
209
210 scale = 1      #time scale: 1->s, 1000->ms, etc...
211 loggi = np.log(2)  #ln(2)
212
213 ### Simulation of an exponential decay ###
214 #NO = Number of atoms
215 #T = half life
216 def decay(NO,T):
217     return np.random.exponential(T/loggi, NO)
218
219 #Function to count the decayed and undecayed atoms [decayed (=A), not decayed (=N)]
220 def decayN(NO,T, t):
221     dc = 0
222     ndc = 0
223     test = decay(NO,T)
224     testlen = len(test)
225     for i in range(testlen):
226         if test[i] <= t:
227             dc += 1
228         else:
229             ndc += 1
230     return np.array([dc, ndc])
231
232 #Definition of lists for numbers (*NS) and activities (*AS) for isotopes
233 gdAS, gdNS, euAS, euNS, eu2AS, eu2NS, sm1AS, sm1NS, sm2AS, sm2NS, smAS_sub, smNS_sub = np.
    zeros((12, maximum+1))
234
235 #####
236 #Simulations of the numbers of isotopes after one beam implantation
237 #####
238 ### A = 142 ###
239 #Gd
240 for i in range(maximum+1):
241     gdAS[i], gdNS[i] = decayN(int(gd0*scale*pp_time), Tgd, i)
242 #Eu short-lived
243 for i in range(maximum+1):
244     euAS[i], euNS[i] = decayN(decayN(int(gd0*scale*pp_time), Tgd, i)[0], Teu1, i)
245 #Eu long-lived
246 for i in range(maximum+1):

```

```

247     eu2AS[i], eu2NS[i] = decayN(int(eu20*scale*pp_time), Teu2, i)
248 #Sm from 2 different paths
249 for i in range(maximum+1):
250     sm1AS[i], sm1NS[i] = decayN(int(sm0*scale*pp_time)+decayN(int(gd0*scale*
251     pp_time), Tgd, i)[0], Teu1, i)[0], Tsm, i)
252 for i in range(maximum+1):
253     sm2AS[i], sm2NS[i] = decayN(int(sm0*scale*pp_time)+decayN(int(eu20*scale*pp_time
254     ), Teu2, i)[0], Tsm, i)
255 #to prevent double counting
256 for i in range(maximum+1):
257     smAS_sub[i], smNS_sub[i] = decayN(int(sm0*scale*pp_time), Tsm, i)
258 smNS = np.add(sm1NS, sm2NS-smNS_sub)
259 smAS = np.add(sm1AS, sm2AS-smAS_sub)
260 #####
261 #The activity is determined by the gradient of the decaying atoms
262 #####
263 #parameters of the determination of the gradient
264 step_size = 10
265 grad_size = 10
266 #resulting activity
267 gdASg = np.gradient([np.median(gdAS[i:i+step_size]) for i in range(maximum-
268     step_size)], grad_size*dx) # in Sekunden
269 euASg = np.gradient([np.median(euAS[i:i+step_size]) for i in range(maximum-
270     step_size)], grad_size*dx) # in Sekunden
271 eu2ASg = np.gradient([np.median(eu2AS[i:i+step_size]) for i in range(maximum-
272     step_size)], grad_size*dx) # in Sekunden
273 smASg = np.gradient([np.median(smAS[i:i+step_size]) for i in range(maximum-
274     step_size)], grad_size*dx) # in Sekunden
275 #shaping/rebin des gradienten
276 gd_rebin = [scale/grad_size*np.median(gd[i:i+step_size]) for i in range(maximum-
277     step_size)]
278 eu_rebin = [scale/grad_size*np.median(eu1[i:i+step_size]) for i in range(maximum-
279     step_size)]
280 eu2_rebin = [scale/grad_size*np.median(eu2[i:i+step_size]) for i in range(maximum-
281     step_size)]
282 sm_rebin = [scale/grad_size*np.median(sm[i:i+step_size]) for i in range(maximum-
283     step_size)]
284 #####
285 #Pulsed implantation over the maximum time (maximum * timescale) (1 implantation
286     per time unit)
287 #####
288 #length of simulation
289 sum_len = 1500
290 #sum of the activity of during on implantation interval
291 def sumASg(N):
292     sum_a = np.zeros(sum_len)
293     for i in range(time_impl):
294         sum_a[0+i:sum_len] += N[0+i:sum_len]

```

```

290     return sum_a
291
292 #application to A = 142 isotopes
293 sumgdASg = sumASg(gdASg)
294 sumsmASg = sumASg(smASg)
295 sumeuASg = sumASg(euASg)
296 sumeu2ASg = sumASg(eu2ASg)
297 #reshaped activities
298 sumgdrebin = sumASg(gd_rebin)
299 sumeu2rebin = sumASg(eu2_rebin)
300 sumeu2rebin = sumASg(eu2_rebin)
301 sumsmrebin = sumASg(sm_rebin)
302
303 #sum during several activation and measurement periods
304 def sum_sum(sum_a):
305     sum_sum_a = np.zeros(maximum)
306     for i in np.arange(0,maximum,time_impl+meas_time):
307         if maximum-i<sum_len:
308             sum_sum_a[i:maximum] += sum_a[:maximum-i]
309         else:
310             sum_sum_a[i:i+sum_len] += sum_a
311
312     return sum_sum_a
313
314 ### application to A = 142 isotopes ###
315 ### final activities over a time of many implementation and measurement cycles
316 sumsumgdASg = sum_sum(sumgdASg)
317 sumsumsmASg = sum_sum(sumsmASg)
318 sumsumeuASg = sum_sum(sumeuASg)
319 sumsumeu2ASg = sum_sum(sumeu2ASg)
320 #reshaped activities
321 sum_gd_rebin = sum_sum(sumgdrebin)
322 sum_sm_rebin = sum_sum(sumsmrebin)
323 sum_eu_rebin = sum_sum(sumeurebin)
324 sum_eu2_rebin = sum_sum(sumeu2rebin)

```

Listing E.2: Calculated integrated cross sections (mb) of the FE reaction of a ^{114}Cd target with a thickness of 4 mg/cm^2 and a ^{32}S beam with an energy of 140 MeV using PACE4. This file, is used as input in Listing E.1.

```

1 Integrated X section , Isotope
2 108.17815011743144, 142Gd
3 239.23057871606372, 142Eu
4 144.21788908287587, 142Sm
5 3.5756834157016515, 142Pm
6 45.693363639137885, 141Eu
7 34.00818056775048, 141Sm
8 6.443840112594604, 141Pm
9 40.229396829222814, 139Sm
10 39.503289696925115, 139Pm
11 5.450480232018972, 139Nd
12 748.5170866248407, TOTAL

```



Bibliography

- [1] *Nudat 2.8*, NNDC, <https://www.nndc.bnl.gov/nudat2/> (visited on 12/28/2020).
- [2] M. Goepfert-Mayer, *On Closed Shells in Nuclei*, *Physical Review* **74**, 235 (1948).
- [3] M. Goepfert-Mayer, *On Closed Shells in Nuclei. II*, *Physical Review* **75**, 1969 (1949).
- [4] O. Haxel et al., *On the “ Magic Numbers” in Nuclear Structure*, *Physical Review* **75**, 1766 (1949).
- [5] A. Bohr et al., *Nuclear Structure*, Vol. II (Benjamin, Reading, MA, 1975).
- [6] R. F. Casten, *Nuclear Structure from a Simple Perspective*, Vol. 23 (Oxford University Press on Demand, 2000).
- [7] T. Otsuka, *Boson Model of Medium-Heavy Nuclei*, PhD thesis (University of Tokyo (unpublished), 1978).
- [8] F. Iachello, *Electron Scattering in the Interacting Boson Model*, *Nuclear Physics A* **358**, 89–112 (1981).
- [9] F. Iachello et al., *The Interaction Boson Model*, Cambridge University Press (1987).
- [10] G. Rainovski et al., *Stabilization of Nuclear Isovector Valence-Shell Excitations*, *Physical Review Letters* **96**, 122501 (2006).
- [11] D. Radford et al., *Nuclear Structure Studies with Heavy Neutron-Rich RIBS at the HRIBF*, *Nuclear Physics A* **746**, 83 (2004).
- [12] M. Danchev et al., *One-Phonon Isovector $2_{1,ms}^+$ State in the Neutron-Rich Nucleus ^{132}Te* , *Physical Review C* **84**, 061306 (2011).
- [13] G. Jakob et al., *Evidence for Proton Excitations in $^{130,132,134,136}\text{Xe}$ Isotopes from Measurements of g Factors of 2_1^+ and 4_1^+ States*, *Physical Review C* **65**, 24316 (2002).

-
- [14] M. J. Bechara et al., *Quadrupole Moment of the First 2^+ Excited State in ^{136}Ba through the Reorientation Effect*, Physical Review C **29**, 1672–1677 (1984).
- [15] R. Stegmann et al., *Evolution of Quadrupole Collectivity in $N = 80$ Isotones toward the $Z = 64$ Subshell Gap: The $B(E2; 2_1^+ \rightarrow 0_1^+)$ Value of ^{142}Sm* , Physical Review C **91**, 054326 (2015).
- [16] C. Bauer et al., *Local Suppression of Collectivity in the $N = 80$ Isotones at the $Z = 58$ Subshell Closure*, Physical Review C **88**, 021302(R) (2013).
- [17] R. F. Casten et al., *The Evolution of Nuclear Structure: the Scheme and Related Correlations*, Journal of Physics G: Nuclear and Particle Physics **22**, 1521 (1996).
- [18] T. Ahn et al., *Evolution of the One-Phonon $2_{1,\text{ms}}^+$ Mixed-Symmetry State in $N = 80$ Isotones as a Local Measure for the Proton–Neutron Quadrupole Interaction*, Physics Letters B **679**, 19–24 (2009).
- [19] N. Pietralla et al., *Isvector Quadrupole Excitations in the Valence Shell of the Vibrator Nucleus ^{136}Ba : Evidence from Photon Scattering Experiments*, Physical Review C **58**, 796 (1998).
- [20] R. Kern et al., *Search for Isvector Valence-Shell Excitations in ^{140}Nd and ^{142}Sm via Coulomb Excitation Reactions of Radioactive Ion beams*, in EPJ Web of Conferences, **194** (2018), p. 03003.
- [21] R. Kern et al., *Restoring the Valence-Shell Stabilization in ^{140}Nd* , Physical Review C **110**, 011303(R) (2020).
- [22] R. Kern et al., *Coulomb Excitation of Proton-Rich $N = 80$ Isotones at HIE-ISOLDE*, in Journal of Physics: Conference Series, **1555** (2020), p. 012027.
- [23] N. Warr et al., *The Miniball Spectrometer*, The European Physics Journal A **49**, 40 (2013).
- [24] E. Williams et al., *Candidates for Low-Lying Mixed-Symmetry States in ^{140}Nd* , Physical Review C **80**, 054309 (2009).
- [25] K. Sieja et al., *Description of Proton-Neutron Mixed-Symmetry States near ^{132}Sn within a Realistic Large Scale Shell Model*, Physical Review C **80**, 054311 (2009).
- [26] K. P. Lieb et al., *Dopper Shift Attenuation Lifetime Measurement in ^{54}Cr Following Thermal Neutron Capture*, Physics Letters B **215**, 50–54 (1988).

-
- [27] G. Hartung et al., *Inelastic Electron Scattering off Mixed Symmetry $J^\pi = 2^+$ States in ^{56}Fe* , Physics Letters B **221**, 109–112 (1989).
- [28] S. A. A. Eid et al., *A Shared Mixed-Symmetry State in ^{56}Fe* , Physics Letters B **166**, 267–268 (1986).
- [29] A. Gade et al., *Isovector Dipole and Quadrupole Excitations in ^{66}Zn* , Physical Review C **65**, 054311 (2002).
- [30] P. E. Garrett et al., *First Observation of Mixed-Symmetry States in a Good $U(5)$ Nucleus*, Physical Review C **54**, 2259 (1996).
- [31] C. Fransen et al., *Comprehensive Studies of Low-Spin Collective Excitations in ^{94}Mo* , Physical Review C **67**, 024307 (2003).
- [32] C. Fransen et al., *Investigation of Low-Spin States in ^{92}Zr with the $(n, n'\gamma)$ Reaction*, Physical Review C **71**, 054304 (2005).
- [33] H. Klein et al., *Proton-Neutron Mixed-Symmetry 2_{ms}^+ and 3_{ms}^+ states in ^{96}Ru* , Physical Review C **65**, 044315 (2002).
- [34] S. W. Yates, *Mixed-Symmetry States in Weakly Deformed Nuclei from $(n, n'\gamma)$ Reaction Studies*, Journal of Radioanalytical and Nuclear Chemistry **265**, 291–295 (2005).
- [35] N. Pietralla et al., *Transition Rates between Mixed Symmetry States: First Measurement in ^{94}Mo* , Physical Review Letters **83**, 1303 (1999).
- [36] N. Pietralla et al., *Coulomb Excitation of the 2_{ms}^+ State of ^{96}Ru in Inverse Kinematics*, Physical Review C **64**, 031301 (2001).
- [37] N. Pietralla et al., *Proton-Neutron Structure of the Effective Quadrupole-Octupole Coupled $E1$ Transition Operator*, Physical Review C **68**, 031305 (2003).
- [38] V. Werner et al., *Proton-Neutron Structure of the $N = 52$ Nucleus ^{92}Zr* , Physics Letters B **550**, 140–146 (2002).
- [39] L. Coquard et al., *Evolution of the Mixed-Symmetry $2_{1,\text{ms}}^+$ Quadrupole-Phonon Excitation from Spherical to γ -soft Xe Nuclei*, Physical Review C **82**, 024317 (2010).
- [40] T. Ahn et al., *Identification of the $2_{1,\text{ms}}^+$ Mixed-Symmetry State in ^{136}Ce* , Physical Review C **86**, 014303 (2012).

-
- [41] J. R. Vanhoy et al., *Structural Characteristics of ^{142}Ce through Inelastic Neutron Scattering*, *Physical Review C* **52**, 2387 (1995).
- [42] B. Fazekas et al., *Level Scheme and Mixed-Symmetry States of ^{134}Ba from in-Beam ($n, n\gamma$) Measurements*, *Nuclear Physics A* **548**, 249–270 (1992).
- [43] I. Wiedenhöver et al., *2^+ Mixed-Symmetry State in the $O(6)$ -like Nucleus ^{128}Xe* , *Physical Review C* **56**, 2354(R) (1997).
- [44] S. F. Hicks et al., *Structural Characteristics of ^{144}Nd through γ -Ray Spectroscopy Following Inelastic Neutron Scattering*, *Physical Review C* **57**, 2264 (1998).
- [45] G. Molnár et al., *Search for Mixed-Symmetry States in the $O(6)$ Nucleus ^{134}Ba* , *Physical Review C* **37**, 898 (1988).
- [46] D. Kocheva et al., *Low-Lying Isovector Valence-Shell Excitations of ^{212}Po* , *Physical Review C* **93**, 011303(R) (2016).
- [47] A. Yaneva et al., *Experimental Evidence for Low-Lying Quadrupole Isovector Excitation of ^{208}Po* , *The European Physical Journal A* **56**, 1–7 (2020).
- [48] R. Stegmann et al., *Identification of the One-Quadrupole Phonon $2^+_{1,\text{ms}}$ state of ^{204}Hg* , *Physics Letters B* **770**, 77–82 (2017).
- [49] I. Lee, *The Gammasphere*, *Progress in Particle and Nuclear Physics* **28**, 473–485 (1992).
- [50] R. Kern et al., *Nuclear Isovector Valence-Shell Excitation of ^{202}Hg* , *Physical Review C* **99**, 011303(R) (2019).
- [51] A. Arima et al., *Collective Nuclear States as Symmetric Couplings of Proton and Neutron Excitations*, *Physics Letters B* **66**, 205–208 (1977).
- [52] W. R. Phillips et al., *Octupole Deformation in Neutron-Rich Barium Isotopes*, *Physical Review Letters* **57**, 3257–3260 (1986).
- [53] L. P. Gaffney et al., *Studies of Pear-Shaped Nuclei Using Accelerated Radioactive beams*, *Nature* **497**, 199–204 (2013).
- [54] B. Bucher et al., *Direct Evidence of Octupole Deformation in Neutron-Rich ^{144}Ba* , *Physical Review Letters* **116**, 112503 (2016).
- [55] P. A. Butler et al., *The Observation of Vibrating Pear-Shapes in Radon Nuclei*, *Nature communications* **10**, 1–6 (2019).

-
- [56] P. A. Butler et al., *Evolution of Octupole Deformation in Radium Nuclei from Coulomb Excitation of Radioactive ^{222}Ra and ^{228}Ra Beams*, *Physical Review Letters* **124**, 042503 (2020).
- [57] B. A. Brown, *The Nuclear Shell Model Towards the Drip Lines*, *Progress in Particle and Nuclear Physics* **47**, 517–599 (2001).
- [58] I. Shavitt et al., *Many-Body Methods in Chemistry and Physics: MBPT and Coupled-Cluster Theory* (Cambridge university press, 2009).
- [59] P. Navrátil et al., *Recent Developments in No-Core Shell-Model Calculations*, *Journal of Physics G: Nuclear and Particle Physics* **36**, 083101 (2009).
- [60] T. Otsuka et al., *Monte Carlo Shell Model for Atomic Nuclei*, *Progress in Particle and Nuclear Physics* **47**, 319–400 (2001).
- [61] E. Caurier et al., *Gamow-Teller Strength in ^{54}Fe and ^{56}Fe* , *Physical Review C* **52**, 1736(R) (1995).
- [62] P. O. Lipas et al., *Proton-Neutron Symmetry in Boson Models of Nuclear Structure*, *Reports on Progress in Physics* **53**, 1355 (1990).
- [63] N. Pietralla et al., *Experiments on Multiphonon States with Proton – Neutron Mixed Symmetry in Vibrational Nuclei*, *Progress in Particle and Nuclear Physics* **60**, 225–282 (2008).
- [64] D. Bohle et al., *New Magnetic Dipole Excitation Mode Studied in the Heavy Deformed Nucleus ^{156}Gd by Inelastic Electron Scattering*, *Physics Letters B* **137**, 27–31 (1984).
- [65] T. Otsuka et al., *Multiphonon Structure of γ -Unstable or $O(6)$ Nuclei*, *Physical Review C* **50**, 1768(R) (1994).
- [66] G. Siems et al., *Multiple Quadrupole “Phonon” excitations in ^{130}Ba* , *Physics Letters B* **320**, 1–6 (1994).
- [67] N. Pietralla et al., *Distribution of Low-Lying Quadrupole Phonon Strength in Nuclei*, *Physical Review Letters* **73**, 2962 (1994).
- [68] N. Pietralla et al., *Odd-Spin Yrast States as Multiple Quadrupole-Phonon Excitations*, *Physics Letters B* **349**, 1–6 (1995).
- [69] N. Pietralla et al., *2_1^+ and 2_2^+ states in Collective Nuclei as Multiple Q-Phonon Excitations*, *Physical Review C* **57**, 150 (1998).

-
- [70] C. McClelland et al., *Excitation of Heavy Nuclei by the Electric Field of Low-Energy Protons*, *Physical Review* **91**, 760 (1953).
- [71] K. Alder et al., *Study of Nuclear Structure by Electromagnetic Excitation with Accelerated Ions*, *Reviews of Modern Physics* **28**, 432 (1956).
- [72] K. Alder et al., *Coulomb Excitation: a Collection of Reprints* (Academic Press, 1966).
- [73] K. Alder et al., *Electromagnetic Excitation: Theory of Coulomb Excitation with Heavy Ions* (North-Holland Publishing Company, Amsterdam-Oxford, 1975).
- [74] D. Cline et al., *Nuclear Shapes Studied by Coulomb Excitation*, *Annual Review of Nuclear and Particle Science* **36**, 683 (1986).
- [75] J. Suhonen, *From Nucleons to Nucleus: Concepts of Microscopic Nuclear Theory* (Springer Science & Business Media, 2007).
- [76] K. S. Krane et al., *Directional Correlations of Gamma Radiations Emitted from Nuclear States Oriented by Nuclear Reactions or Cryogenic Methods*, *Atomic Data and Nuclear Data Tables* **11**, 351–406 (1973).
- [77] T. Yamazaki, *Tables of Coefficients of Angular Distribution of Gamma Rays from Aligned Nuclei*, *Nuclear Data Sheets* **3**, 1 (1967).
- [78] A. E. Stuchbery, *Gamma-Ray Angular Distributions and Correlations after Projectile-Fragmentation Reactions*, *Nuclear Physics A* **723**, 69–92 (2003).
- [79] <https://home.cern/science/accelerators/accelerator-complex/panoramas> (visited on 05/13/2020).
- [80] J. Mierzejewski et al., *EAGLE — the Central European Array for Gamma Levels Evaluation at the Heavy Ion Laboratory of the University of Warsaw*, *Nuclear Instruments and Methods in Physics Research Section A: Accelerators, Spectrometers, Detectors and Associated Equipment* **659**, 84–90 (2011).
- [81] <https://www.phy.anl.gov/atlas/facility/floorplan.html> (visited on 05/26/2020).
- [82] M. J. G. Borge et al., *HIE-ISOLDE, the Project and the Physics Opportunities*, *The European Physical Journal A* **52**, 334 (2016).
- [83] Y. Kadi et al., *Post-accelerated Beams at ISOLDE*, *Journal of Physics G: Nuclear and Particle Physics* **44**, 084003 (2017).

-
- [84] V. N. Fedosseev et al., *ISOLDE RILIS: New Beams, New Facilities*, Nuclear Instruments and Methods in Physics Research Section B: Beam Interactions with Materials and Atoms **266**, 4378–4382 (2008).
- [85] <https://rilis-web.web.cern.ch/training> (visited on 05/17/2021).
- [86] F. Ames et al., *Cooling of Radioactive Ions with the Penning Trap REXTRAP*, Nuclear Instrumentation and Methods in Physics Research A **538**, 17 (2005).
- [87] F. Wenander, *Charge Breeding of Radioactive Ions with EBIS and EBIT*, Journal of Instrumentation **5**, 33 (2010).
- [88] Y. Kadi et al., *HIE-ISOLDE – Technical Design Report for the Energy Upgrade*, tech. rep. (CERN, 2018).
- [89] N. Warr, *The Miniball Double-Sided Silicon Strip Detector (CD)*, (2015) <https://www.ikp.uni-koeln.de/~warr/doc/cd.pdf> (visited on 05/15/2020).
- [90] L. P. Gaffney et al., *MiniballCoulexSort*, (2019) <https://doi.org/10.5281/zenodo.1344355> (visited on 01/23/2020).
- [91] S. Y. F. Chu et al., *The Lund/LBNL Nuclear Data Search*, (1999) <http://nucleardata.nuclear.lu.se/toi/> (visited on 05/15/2020).
- [92] H. Weick, *ATIMA*, (2020) <https://web-docs.gsi.de/~weick/atima/> (visited on 05/27/2020).
- [93] J. Ziegler et al., *SRIM – The Stopping and Range of Ions in Matter*, Nuclear Instrumentation and Methods B **268**, 1823 (2010).
- [94] R. J. Casperson, *Experimental and Numerical Analysis of Mixed-Symmetry States and Large Boson Systems*, PhD thesis (Yale University, 2010).
- [95] N. Nica, *Nuclear Data Sheets for $A = 140$* , Nuclear Data Sheets **108**, 1287–1470 (2007).
- [96] V. Ponomarev et al., *Particle-Hole and Particle-Particle Correlations in Neodymium Isotopes*, Nuclear Physics A **601**, 1–40 (1996).
- [97] T. Kibedi et al., *Evaluation of Theoretical Conversion Coefficients using BrIcc*, Nuclear Instruments and Methods in Physics Research Section A: Accelerators, Spectrometers, Detectors and Associated Equipment **589**, 202–229 (2008).

-
- [98] D. Cline et al., *GOSIA User Manual for Simulation and Analysis of Coulomb Excitation Experiments*, Gosia Steering Committee **18**, 19–60 (2012).
- [99] M. Zielinska et al., *Analysis Methods of Safe Coulomb-Excitation Experiments with Radioactive Ion Beams Using the GOSIA Code*, European Physical Journal A **52**, 99 (2016).
- [100] D. Rosiak et al., *Enhanced Quadrupole and Octupole Strength in Doubly Magic ^{132}Sn* , Physical Review Letters **121**, 252501 (2018).
- [101] L. P. Gaffney et al., *Low-Energy Coulomb Excitation of ^{62}Fe and ^{62}Mn Following in-Beam Decay of ^{62}Mn* , The European Physical Journal A **51**, 1–9 (2015).
- [102] L. P. Gaffney et al., *Collectivity in the Light Radon Nuclei Measured Directly via Coulomb Excitation*, Physical Review C **91**, 064313 (2015).
- [103] K. Gladnishki et al., *Search for One-Phonon Mixed-Symmetry States in the Radioactive Nucleus ^{140}Nd* , Physical Review C **82**, 037302 (2010).
- [104] R. Stegmann, *One-Quadrupole-Phonon States of Heavy Vibrational Nuclei Studied in Coulomb Excitation*, PhD thesis (Technische Universität Darmstadt, 2017).
- [105] T. Johnson et al., *Nuclear Data Sheets for $A = 142$* , Nuclear Data Sheets **112**, 1949–2127 (2011).
- [106] M. A. Riley, *GAMMASPHERE – The Beginning...1993-1997*, (1998) <https://http://nucalf.physics.fsu.edu/~riley/gamma/> (visited on 08/12/2020).
- [107] R. Pardo et al., *ATLAS with CARIBU: a Laboratory Portrait*, Nuclear Physics News **26**, 1–5 (2016).
- [108] R. Geller, *Electron Cyclotron Resonance Ion Sources and ECR Plasmas* (Institute of Physics, Bristol, 1996).
- [109] T. Möller, *Aspects of Nuclear Collectivity Studied in Projectile Coulomb Excitation Experiments*, PhD thesis (Technische Universität Darmstadt, 2014).
- [110] W. Lewin et al., *Some Measurements on the Decay of ^{202}Tl* , Nuclear Physics **62**, 337–352 (1965).
- [111] H. Ower, *Coulombanregung von Hochspinzuständen in ^{232}Th , ^{234}U und ^{236}U* , PhD thesis (Goethe Universität Frankfurt, 1980).

-
- [112] A. Bockisch et al., *Reorientation Effect Measurements of Even Mercury Isotopes*, *Zeitschrift für Physik A Atoms and Nuclei* **291**, 245–254 (1979).
- [113] R. H. Spear et al., *Static Quadrupole Moments of the First Excited States of ^{200}Hg and ^{202}Hg* , *Nuclear Physics A* **345**, 252–262 (1980).
- [114] Y. K. Agarwal et al., *Multiple Coulomb Excitation of ^{202}Hg and ^{204}Hg* , *Zeitschrift für Physik A Atoms and Nuclei* **320**, 295–299 (1985).
- [115] C. S. Lim et al., *Measurements of $E3$ Transition Strength in the Stable Even-Mass Hg Isotopes*, *Nuclear Physics A* **522**, 635–647 (1991).
- [116] S. Zhu et al., *Nuclear Data Sheets for $A = 202$* , *Nuclear Data Sheets* **109**, 699–786 (2008).
- [117] R. B. Firestone et al., *Decay Studies of Neutron Deficient Nuclei near the $Z = 64$ Sub-Shell: ^{142}Dy , $^{140,142}\text{Tb}$, $^{140,142}\text{Gd}$, $^{140,142}\text{Eu}$, ^{142}Sm , and ^{142}Pm* , *Physical Review C* **43**, 1066 (1991).
- [118] G. G. Kennedy et al., *Structure of ^{142}Sm from the Decay of ^{142}Eu* , *Physical Review C* **12**, 553 (1975).
- [119] M. Piiparinen et al., *High-Spin Spectroscopy of the ^{142}Eu , ^{143}Eu and ^{144}Eu Nuclei*, *Nuclear Physics A* **605**, 191–268 (1996).
- [120] A. M. Bizzeti-Sona et al., *The g Factor of the 8^+ isomer of ^{142}Eu* , *Zeitschrift für Physik A Atoms and Nuclei* **346**, 181 (1993).
- [121] A. M. Bizzeti-Sona et al., *High-Spin Levels in the Odd-Odd Nucleus ^{142}Eu* , *Zeitschrift für Physik A Atoms and Nuclei* **A337**, 235 (1990).
- [122] O. B. Tarasov et al., *LISE++: Radioactive Beam Production with in-Flight Separators*, *Nuclear Instruments and Methods in Physics Research Section B: Beam Interactions with Materials and Atoms* **266**, 4657–4664 (2008).
- [123] A. Gavron, *Statistical Model Calculations in Heavy Ion Reactions*, *Physical Review C* **21**, 230 (1980).
- [124] I. K. Lemberg et al., *Modern Methods of Nuclear Spectroscopy* (Nauka, Leningrad, 1985).
- [125] J. Srebrny et al., *Transition Probabilities in Negative Parity Bands of the ^{119}I Nucleus*, *Nuclear Physics A* **683**, 21–47 (2001).
- [126] <http://slcj.uw.edu.pl/en/available-beams/> (visited on 12/11/2020).

-
- [127] M. Palacz, Private Communication, Nov. 2019.
- [128] N. L. Iudice et al., *Fine Structure of Proton-Neutron Mixed Symmetry States in Some $N = 80$ Isotones*, *Physical Review C* **77**, 044310 (2008).
- [129] D. Bianco et al., *Importance-Sampling Diagonalization Algorithm for Large-Scale Shell Model Calculations on $N = 80$ Isotones*, *Physical Review C* **85**, 034332 (2012).
- [130] E. Caurier et al., *The Shell Model as a Unified View of Nuclear Structure*, *Reviews of modern Physics* **77**, 427 (2005).
- [131] E. Caurier et al., *Collectivity in the Light Xenon Isotopes: A Shell Model Study*, *Physical Review C* **82**, 064304 (2010).
- [132] B. Singh, *Nuclear Data Sheets for $A = 130$* , *Nuclear Data Sheets* **93**, 33–242 (2001).
- [133] Y. Khazov et al., *Nuclear Data Sheets for $A = 132$* , *Nuclear Data Sheets* **104**, 497–790 (2005).
- [134] A. A. Sonzogni, *Nuclear Data Sheets for $A = 134$* , *Nuclear Data Sheets* **103**, 1–182 (2004).
- [135] A. A. Sonzogni, *Nuclear Data Sheets for $A = 138$* , *Nuclear Data Sheets* **98**, 515–664 (2003).
- [136] J. K. Tuli, *Nuclear Data Sheets for $A = 144$* , *Nuclear Data Sheets* **56**, 607–707 (1989).
- [137] Y. Khazov et al., *Nuclear Data Sheets for $A = 146$* , *Nuclear Data Sheets* **136**, 163–452 (2016).
- [138] K. Heyde et al., *Symmetric and Antisymmetric States: A General Feature of Two-Component Systems*, *Physical Review C* **33**, 1050 (1986).
- [139] L. Coquard, *Evolution of the One-Quadrupole Phonon $2_{1,ms}^+$ Mixed-Symmetry State in $^{124,126,128,130,132}\text{Xe}$* , PhD thesis (Technische Universität Darmstadt, 2010).
- [140] A. Giannatiempo et al., *Signatures for Mixed-Symmetry States in the $U(5)$ Limit of the Neutron-Proton Interacting Boson Model*, *Physical Review C* **48**, 2657 (1993).
- [141] K. Heyde et al., *Magnetic Dipole Excitations in Nuclei: Elementary Modes of Nucleonic Motion*, *Rev. Mod. Phys.* **82**, 2365–2419 (2010).

-
- [142] N. A. Smirnova et al., *Interrelation Between the Isoscalar Octupole Phonon and the Proton-Neutron Mixed-Symmetry Quadrupole Phonon in Near-Spherical Nuclei*, Nuclear Physics A **678**, 235–257 (2000).
- [143] P. D. Cottle et al., *Fragmentation of Octupole Strength in Even-A Pt Isotopes*, Physical Review C **38**, 2843 (1988).
- [144] N. V. Zamfir et al., *Octupole Fragmentation and $O(6)$ Symmetry in Even-A Pt Isotopes*, Physical Review C **48**, 1745 (1993).



List of Figures

1.1. Excitation energies of 2_1^+ states in the chart of nuclides.	1
1.2. Collective quadrupole excitations	3
1.3. Nuclear orbital occupation of ^{140}Nd and the $B(E2; 2_1^+ \rightarrow 0_1^+)$ strengths of the $N = 80$ isotones.	4
1.4. The previously known $B(M1; 2_{1,\text{ms}}^+ \rightarrow 2_1^+)$ strengths of the $N = 80$ isotones and in the vicinity of ^{208}Pb	6
2.1. Level schemes of vibrating and rotating nuclei.	10
2.2. Level scheme emerging from the nuclear shell model	16
2.3. $U(5)$ level scheme of low-lying FSSs and MSSs.	21
2.4. Two-state mixing scenario	23
2.5. F -spin mixing in a two-state mixing scenario	25
3.1. General scattering process of a Coulomb excitation.	28
3.2. Theoretical cross sections of CE of transitions with different multipolarities.	33
3.3. Two scenarios of measuring angular distributions of γ - γ and of particle- γ coincidences.	37
4.1. Overview of the beam lines of CERN.	41
4.2. Floorplan of the ATLAS facility	42
4.3. The functionality of RILIS	44
4.4. Schematic layout of the ion beam structure of HIE-ISOLDE	45
4.5. Schematic drawing and a picture of the DSSD.	47
4.6. Relative γ -ray efficiency of Miniball.	48
4.7. Time difference of particle- γ events detected by the DSSD and Miniball.	49
4.8. Overview of the kinematic of the ^{140}Nd CE experiment.	50
4.9. The beam-gated E_γ - E_γ matrix of the ^{140}Nd CE experiment.	52

4.10. Beam-gated γ -ray spectra of the ^{140}Nd CE experiment.	53
4.11. The partial level scheme of ^{140}Nd	54
4.12. Beam-gated γ -ray spectra of the ^{142}Sm CE experiment.	58
4.13. The partial level scheme of ^{142}Sm	59
4.14. Monitoring of the yields' deviations during the GOSIA minimization process of the ^{140}Nd CE experiment.	63
4.15. χ^2 -surface distributions to deduce the uncertainties of the MEs $\langle 2_4^+ E2 0_1^+ \rangle$ and $\langle 2_3^+ E2 0_1^+ \rangle$	64
4.16. Probing the sensitivity of the CE calculations on the signs of the MEs of ^{140}Nd	65
4.17. Monitoring of the yields' deviations during the GOSIA minimization process of the ^{142}Sm CE experiment.	69
4.18. A schematic drawing of the Gammasphere detectors and the effect of Compton suppression.	73
4.19. Time difference spectrum of the γ -ray incidents in respect to the beam frequency.	75
4.20. Reaction kinematics and the Doppler-shift-correction optimization.	76
4.21. The random-time-subtracted medium-energy γ -ray spectra of the $^{12}\text{C}(^{202}\text{Hg}, ^{202}\text{Hg}^*)$ CE experiment.	77
4.22. The random-time-subtracted high-energy γ -ray spectra of the $^{12}\text{C}(^{202}\text{Hg}, ^{202}\text{Hg}^*)$ CE reaction.	78
4.23. The E_γ - E_γ matrix of the ^{202}Hg CE experiment.	79
4.24. Angular distributions of selected transitions of ^{202}Hg	80
4.25. The partial level scheme of ^{202}Hg	83
4.26. The probability distributions of the transition matrix element using the python3 code which uses CLX, see Listing D.2.	88
4.27. Fusion-evaporation cross sections using the PACE4 and COMPA.	89
4.28. Activities of various produced radioactive isotopes.	90
5.1. $E2$ and $M1$ transition strength distributions of ^{140}Nd and ^{142}Sm	96
5.2. $B(M1; 2_{1,\text{ms}}^+ \rightarrow 2_1^+)$ systematic of the $N = 80$ isotones and the corresponding F -spin mixing matrix elements.	98
5.3. Evolution of the level energy and the $B(M1; 2_{1,\text{ms}}^+ \rightarrow 2_1^+)$ strength along the $N = 80$ isotonic chain.	100
5.4. Probing $U(5)$ symmetry for the $N = 80$ isotones with $B(E2)$ values.	102
5.5. $M1$ strength distributions $B(M1; 2_i^+ \rightarrow 2_1^+)$ of ^{202}Hg	105

5.6.	$B(M1; 2_{1,ms}^+ \rightarrow 2_1^+)$ strengths in the $A = 208$ mass region and V_{F-mix} of the $N, Z = 80$ isotopes.	107
5.7.	The $B(M1; 2_{1,ms}^+ \rightarrow 2_1^+)$ strengths of nuclei in the mass regions near doubly-magic nuclei.	108
A.1.	Overview of the kinematic of the ^{142}Sm CE experiment.	115
A.2.	The target-gated E_γ - E_γ matrix of the ^{140}Nd CE experiment.	116
A.3.	The target-gated γ -ray spectra of the ^{140}Nd CE experiment.	117
A.4.	The beam-gated E_γ - E_γ matrix of the ^{142}Sm CE experiment.	118
A.5.	The target-gated E_γ - E_γ matrix of the ^{142}Sm CE experiment.	119
A.6.	The target-gated γ -ray spectra of the ^{142}Sm CE experiment.	120
A.7.	Probing the sensitivity of the CE calculations on the sign of the MEs of ^{142}Sm	123
C.1.	Relative γ -ray efficiency of Gammasphere.	141
C.2.	Relative γ -ray efficiency of the rings of Gammasphere.	144
C.3.	Ringwise γ -ray singles spectra zoomed to the $2_1^+ \rightarrow 0_1^+$ transition at 439 keV are shown. The determined peak areas are presented in Table C.2.	145
C.4.	Ringwise γ -ray spectra gated on the $2_1^+ \rightarrow 0_1^+$ transition and zoomed to the $3_2^- \rightarrow 2_1^+$ transition at 1747 keV are shown. The determined peak areas are presented in Table C.2.	146
C.5.	Ringwise γ -ray spectra gated on the $2_1^+ \rightarrow 0_1^+$ transition and zoomed to the $2_7^+ \rightarrow 2_1^+$ transition at 1354 keV are shown. The determined peak areas are presented in Table C.2.	147
C.6.	The angular distributions of the transitions $2_3^+ \rightarrow 2_2^+$, $2_3^+ \rightarrow 2_1^+$, $2_2^+ \rightarrow 2_1^+$ and $4_1^+ \rightarrow 2_1^+$	148
C.7.	Ringwise γ -ray spectra gated on the $2_1^+ \rightarrow 0_1^+$ transition and zoomed to the $2_3^+ \rightarrow 2_2^+$ transition at 222 keV are shown. The determined peak areas are presented in Table C.2.	149
C.8.	Ringwise γ -ray spectra gated on the $2_1^+ \rightarrow 0_1^+$ transition and zoomed to the $2_3^+ \rightarrow 2_1^+$ transition at 742 keV are shown. The determined peak areas are presented in Table C.2.	150
C.9.	Ringwise γ -ray spectra gated on the $2_1^+ \rightarrow 0_1^+$ transition and zoomed to the $4_1^+ \rightarrow 2_1^+$ transition at 680 keV are shown. The determined peak areas are presented in Table C.2.	151



C.10. Ringwise γ -ray spectra gated on the $2_1^+ \rightarrow 0_1^+$ transition and zoomed to the $2_2^+ \rightarrow 2_1^+$ transition at 520 keV are shown. The determined peak areas are presented in Table C.2. 152

List of Tables

2.1. F -spin properties	19
4.1. An overview of the reported experiments.	43
4.2. Geometry of the Miniball array.	46
4.3. Measured γ -ray intensities in the beam-gated spectra of the ^{140}Nd CE experiment.	57
4.4. Measured γ -ray intensities of the ^{142}Sm CE experiment.	61
4.5. Measured properties of the levels and γ -ray transitions of ^{140}Nd	68
4.6. Measured properties of the levels and γ -ray transitions of ^{142}Sm	72
4.7. The polar angles of the 17 rings of Gammasphere in respect to the beam axis.	74
4.8. The coefficients $a_{2,4}$ and $E2/M1$ multipole-mixing ratios of selected γ -ray transitions of ^{202}Hg	81
4.9. Previously measured absolute transition strengths of ^{202}Hg	84
4.10. Measured properties of the levels and γ -ray transitions in ^{202}Hg	85
4.11. γ - γ coincidence rates estimation for the designed HIL experiment.	92
5.2. Orbital structure and $B(M1; 2^+_{1,ms} \rightarrow 2^+_1)$ of $^{202,204}\text{Hg}$ and $^{208,212}\text{Po}$	106
5.3. Comparison of previously measured $E2$ absolute transition strengths of ^{202}Hg from Refs. [112, 114] and this work.	109
A.1. The γ -ray transitions used for the energy and efficiency calibration for the HIE-ISOLDE experiments.	113
A.2. Measured γ -ray intensities in the target-gated spectra of the ^{140}Nd CE experiment.	121
A.3. Measured γ -ray intensities in the target-gated spectra of the ^{142}Sm CE experiment.	122



C.1. The measured counts with statistical uncertainties of identified transitions of the ^{202}Hg CE experiment determined in four γ -ray spectra. 142

C.2. Peak areas of selected transitions of ^{202}Hg determined in ring spectra in coincidence with the $2_1^+ \rightarrow 0_1^+$ transition unless otherwise noted. 143

Listings

B.1.	GOSIA-input file to define the HPGe detectors of Miniball.	125
B.2.	GOSIA-input file for the $^{208}\text{Pb}(^{140}\text{Nd}, ^{140}\text{Nd}^*)^{208}\text{Pb}^*$ CE experiment.	126
B.3.	Experimental yields of the excited nuclear states of ^{140}Nd	131
B.4.	GOSIA-input file for the $^{208}\text{Pb}(^{142}\text{Sm}, ^{142}\text{Sm}^*)^{208}\text{Pb}^*$ CE experiment.	132
B.5.	Experimental yields of the excited nuclear states of ^{142}Sm	137
B.6.	GOSIA-input file used for the iterative procedure to determine the statistical tensor of the 2_7^+ state and δ of the $2_7^+ \rightarrow 2_1^+$ transition of ^{202}Hg	138
D.1.	CLX-input file for the $^{12}\text{C}(^{202}\text{Hg}, ^{202}\text{Hg}^*)^{12}\text{C}$ CE experiment.	153
D.2.	Python3 code using CLX to determine the uncertainties of the MEs. This code was designed for the $^{12}\text{C}(^{202}\text{Hg}, ^{202}\text{Hg}^*)^{12}\text{C}$ CE experiment.	155
D.3.	Variation of known quantities inside their uncertainties in lists which are used in Listing D.2.	157
D.4.	Conversions and relations used in Listing D.2.	159
D.5.	The header for the CLX-input file used in Listing D.2.	161
D.6.	The list of levels for the CLX-input file used in Listing D.2.	161
D.7.	The list of transitions and MEs for the CLX-input file used in Listing D.2.	162
E.1.	Python code for the calculation of the activities of the β^+/ϵ -decay experiment at the HIL.	163
E.2.	Calculated integrated cross sections (mb) of the FE reaction of a ^{114}Cd target with a thickness of 4 mg/cm^2 and a ^{32}S beam with an energy of 140 MeV using PACE4. This file, is used as input in Listing E.1.	169



List of Publications

Publications

- J. Wiederhold et al., *Fast-timing Lifetime Measurement of ^{152}Gd* , Physical Review C **94**, 044302 (2016).
- **R. Kern** et al., *Nuclear Isovector Valence-Shell Excitation of ^{202}Hg* , Physical Review C **99**, 011303(R) (2019).
- J. Wiederhold et al., *Evolution of $E2$ strength in the rare-earth isotopes $^{174,176,178,180}\text{Hf}$* , Physical Review C **99**, 024316 (2019).
- M. Stoyanova et al., *Lifetimes of the 4_1^+ States of ^{206}Po and ^{204}Po : A Study of the Transition from Noncollective Seniority-like Mode to Collectivity*, Physical Review C **100**, 064304 (2019).
- A. Yaneva et al., *Experimental Evidence for Low-Lying Quadrupole Isovector Excitation of ^{208}Po* , The European Physical Journal A **56**, 246 (2020).
- P. Napiralla et al., *Approach to a Self-Calibrating Experimental γ -Ray Tracking Algorithm*, Nuclear Instruments and Methods in Physics Research Sec. A **955**, 163337 (2020).
- **R. Kern** et al., *Restoring the Valence-Shell Stabilization in ^{140}Nd* , Physical Review C **110**, 041304(R) (2020).

Conference Proceedings

- **R. Kern** et al., *Search for Isovector Valence-Shell Excitations in ^{140}Nd and ^{142}Sm via Coulomb Excitation Reactions of Radioactive Ion beams*, EPJ Web of Conferences. Vol. **194**, 03003 (2018).

-
- M. Stoyanova et al., *A Study on the Transition between Seniority-Type and Collective excitations in ^{204}Po and ^{206}Po* , EPJ Web of Conferences. Vol. **194**, 03002 (2018).
 - N. Pietralla et al., *Symmetry and Order in Nuclear Structure Originating from the Proton-Neutron Degree of Freedom*, AIP Conference Proceedings **2150**, 020004 (2019)
 - **R. Kern** et al., *Coulomb Excitation of Proton-Rich $N = 80$ Isotones at HIE-ISOLDE*, Journal of Physics: Conference Series. Vol. **1555**, 012027 (2020).
 - M. Stoyanova et al., *Evolution of the Structure of the 4_1^+ States in Po Isotopes*, Journal of Physics: Conference Series. Vol. **1555**, 012019 (2020).
 - D. Kocheva et al., *Lifetime Measurements of the Low-Lying Excited States of ^{208}Po* , Journal of Physics: Conference Series. Vol. **1555**, 012020 (2020).

Danksagung

Ich möchte mich bei allen Leuten bedanken, die mich auf den Weg zur Promotion begleitet und unterstützt haben, Freunde, Familie, Kollegen und Vorgesetzte.

Besonderer Dank gilt Prof. Dr. Dr. h.c. mult Norbert Pietralla, der mir diese Promotion ermöglicht hat, nachdem er die Finanzierung noch einmal "mit spitzer Feder" durchgerechnet hat und mich immer wieder mit fachlichem Rat durch die Zeit als Doktorand geführt hat.

Des Weiteren danke ich Dr. V. W., mit dem viele fachliche Diskussionen geführt wurden, die mir auf dem Weg zu dieser Doktorarbeit sehr halfen.

Meinem ehemaligen Kollegen Dr. R. S. danke ich für die Betreuung während meiner Masterarbeit und am Anfang meiner Zeit als Doktorand. Ich danke ihm für die Grundsteinlegung dieser Arbeit.

Für die schöne Zeit im Institut für Kernphysik danke ich den Kollegen aus meiner Arbeitsgruppe, Dr. P. K., T. S., U. G., J. K., O. P., Dr. O. M., Dr. P. C. R., Dr. P. R. J., Dr. W. W., R. Z., E. S. und A. W.. Weiterhin danke ich, Dr. T. K., Dr. L. J., Dr. J. W., U. A., K. I., Dr. A. D'A.. und allen anderen, die ausgiebige Mittagspausen am Kicker mit mir verbracht haben.

Besonderer Dank gilt auch meinen Freunden, T. B., P. D., Dr. U. S., J. S., J. T., S. W. und T. W., die das Studium mit Kartenspielen und anderen fröhlichen Aktivitäten stets unterhaltsam hielten. Ich bin auch meinem Bürokollegen und Freund Dr. P. N. für die gemeinsame und sehr amüsante Zeit im Büro 210 und darüberhinaus sehr dankbar.

Für das Korrekturlesen meiner Arbeit danke ich Dr. J. W., Dr. P. N., T. B., R. Z. und Dr. P. J..

I would like to thank Prof. Dr. G. R. for his scientific advice and for the fruitful discussions during experiments, conferences and via Skype. I would also like to thank Dr. L. P. G. for helping me with GOSIA and Miniball issues.

Ganz besonderer Dank gilt meiner unterstützenden Familie, meine Eltern, Ellen und Kurt, meinen Geschwistern, Sophia und Eric sowie meinen Großeltern, Adelheid und Erhard und Maria. Es ist ein gutes Gefühl eine Familie zu haben, die

einem immer den Rücken stärkt.

Selbstverständlich gilt ein großer Dank meiner Verlobten, Steffi, die mich auf diesem langen Weg und noch weiter mit ihrem Verständnis und ihrer Liebe unterstützt hat, und ihrer Familie, für die herzliche Aufnahme in jene.

Diese Arbeit wurde gefördert durch das Bundesministerium für Bildung und Forschung unter den Fördernummern 05P15RDCIA und 05P18RDCIA und durch die Helmholtz Graduate School for Hadron and Ion Research (HGS-HIRE).

Lebenslauf

Removed from online version